# Exploring Models of Supergravity Grand Unification with LHC and Dark Matter Phenomenology

by

Sujeet Akula

B.S. in Applied Mathematics & Physics, University of Wisconsin–Milwaukee
B.S. in Computer Science, University of Wisconsin–Milwaukee
M.S. in Physics, Northeastern University

A dissertation submitted to

The Faculty of the College of Science of
Northeastern University

In partial fulfillment of the requirements for the degree of
Doctor of Philosophy

April 15, 2014

Dissertation directed by

Pran Nath
Matthews Distinguished University Professor of Physics

## Abstract of Dissertation

Beginning with a review of the Standard Model of particle physics, as well as supersymmetry and supergravity, we explore the phenomenology of models built in the framework of supergravity grand unification. The models are studied by considering results from prominent experiments such as the search for exotic particles with the Large Hadron Collider, satellite telescopes that determine the anisotropy in the cosmic microwave background, and terrestrial searches for dark matter. In particular, the discovery and mass measurement of the Higgs boson is used to consider the implications for naturalness and discovery prospects of supergravity models.

## Acknowledgements

Most importantly, I am thankful for my advisor, Matthews Distinguished University Professor of Physics, Pran Nath, for his guidance, encouragement, and far-sighted intuition. His dedication and deep focus have allowed him to be a renowned and prolific researcher. In a mentor, this level of activity is usually quite intimidating to prospective students, but here it is entirely tempered by his patient and kind demeanor. Truly, he has inspired me both as an academic and as a person.

The role of serving on a thesis committee is an unnatural synthesis of copy-editing, excessively polite critiquing, and serving as a last line of defense against printing that which is asinine. It is also a largely unrewarding job, but I can at least thank Professors Haim Goldberg, Brent D. Nelson, and Toyoko Orimoto, for agreeing to do it.

Much of the work presented in this dissertation was completed in collaboration with other physicists including Baris Altunkaynak, Ning Chen, Dan Feldman, Mengxi Liu, Zuowei Liu, and Gregg Peim.

I am very grateful to my grad school instructors Alain Karma, Haim Goldberg (again!), Matthew D. Schwartz, Jeffrey Sokoloff, Armen Stepanyants, Andrew Strominger, Allan Widom, and Mark Williams, as well as the instructors from my undergraduate studies Luis A. Anchordoqui, Daniel Agterberg, Paul F. Lyman, Valerica Raicu, Richard S. Sorbello, Michael Weinert, and Robert L. Wood. I thank the other faculty at the Physics department, but especially Professors George Alverson, Oleg Batischev, Michael Vaughn and Darien Wood.

I have also benefited from useful discussions with the other grad students in high energy including Ross Altman, Vic Feng, David Francescone, and Bryan Kaufman.

Despite being a graduate student, I have managed to enjoy living in Brookline largely due to good friends: Gregg Peim, Julio Chapeton, Kate Foss, Michael Shannon, Matt Chasco, Darin Baumgartel,

David Nash, Dana Eisland, Benjamin Jurke, and Micah McCauley.

I thank my mother, Anisha, who is a real scientist–with beakers and everything–for her love, support, and putting up with me for some reason, and crucially, for making so much *dam oluv* and *rogan josh* for me. I also thank my brother, Brijeet for teaching me to be curious and getting me interested in science. Also, I have a cousin, Vibhuti, who will be starting college soon and will just take over the world some day. I thank her for being so very cool.

Of course, I also have to thank my amazing fiancée, Laura. Not only is she the love of my life and my favorite person in the world, she, more than anyone else (myself included) is responsible for this dissertation to be finished. She is so wonderful that I would consider writing another dissertation just so I can acknowledge her again.

# Dedication

*For my mother Anisha,*

*and my fiancée Laura*

# Table of Contents

# List of Figures

# List of Tables

# Chapter 1

# Introduction and Overview

The Standard Model can be thought to have begun in the late 1920s and early 1930s, as Dirac developed [1] and introduced [2] one of its core components, Quantum Electrodynamics. Since that time, the theory has evolved greatly, introducing new particles and structures of interactions, while being simultaneously verified by experiments that have similarly evolved with increasing ambition and precision. Now, with the apparent discovery of the final piece, the Higgs boson, the Standard Model can be considered to have been completed, in 2012.

Of course, particle physics itself is not complete as many unsolved questions remain; there is great interest in arriving at the correct theory of physics beyond the Standard Model. The reason for the success of the Standard Model is largely due to the apparent fact that the framework upon which the Standard Model is built, the relativistic mechanics of quantum fields and gauge invariance, allows one to correctly articulate aspects of nature. That is, the framework does not allow one to see what particles and interaction must exist, instead it allows one to accurately describe how they exist. In order to retain this success, it is sensible to retain the foundational underpinning of the Standard Model while adjusting and elaborating on its features.

This dissertation explores models of physics beyond the Standard Model developed within supergravity grand unification, a theoretically attractive framework that begins to solve some of the unresolved questions from the Standard Model. The models are studied with the use of empirical data and constraints from particle accelerators, deep underground nuclear recoil detectors, and satellite telescopes.

The dissertation is organized as follows. In Chapter 2, a basic introduction to the formalism and features of the Standard Model of particle physics is presented, along with a discussion of the open problems. In Chapter 3, the ideas and methods of supersymmetric field theories are introduced and motivated. In Chapter 4, relevant aspects of supergravity grand unification are studied for the models of interest. The impact of the very first searches for supersymmetric particles for the parameter space of the supergravity models and supersymmetric dark matter are given in Chapter 5 and Chapter 6. The impact of large scalar masses for naturalness is studied in Chapter 7. The allowed parameter space of minimal supergravity for the theoretically viable ranges of the Higgs boson mass is explored in Chapter 8. The first measurement of the Higgs boson mass is used to estimate the parameters of minimal supergravity using Bayesian methods in Chapter 9. A new class of supergravity grand unification models is proposed and explored in Chapter 10 that aim to simultaneously produce the accepted Higgs boson mass along with the anomalous magnetic moment of the muon.

# Chapter 2

# The Standard Model

## 2.1 Introduction

The Standard Model (SM) [3–11] is a Yang-Mills gauge field theory built on the spacetime symmetry of the Poincaré group and on the internal symmetry group of $SU(3)_C \times SU(2)_L \times U(1)_Y$, where $SU(3)_C$ is the gauge group of strong color interactions, $SU(2)_L$ is the gauge group of weak chiral interactions, and $U(1)_Y$ is the weak hypercharge factor. The coupling strength for these are taken to be $g_3$, $g$, and $g'$, respectively. The weak hypercharge is related to electric charge and $T_3$, a generator of $SU(2)_L$ by the relation

$$Q = T_3 + \frac{1}{2}Y\,. \tag{2.1}$$

The electroweak gauge symmetry of $SU(2)_L \times U(1)_Y$ is spontaneously broken to $U(1)_Q$, the electromagnetic gauge group, by the Brout-Englert-Higgs mechanism [12–15] where a scalar field, known as the Higgs field, with a potential that has a symmetry-breaking minimum is introduced, giving a non-zero vacuum expectation value (VEV) to the field. Gauge-invariant interactions with the Higgs field

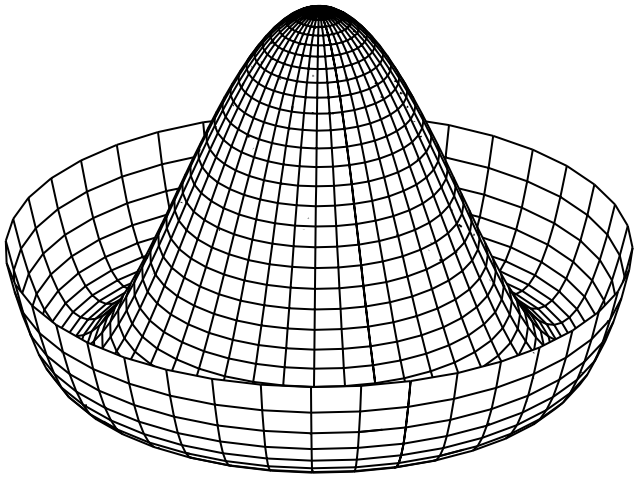

Figure 2.1: A schematic sketch of the shape of the symmetry-breaking Higgs potential. The height of the surface is the value of $V_H$ and the base is the complex plane of $H$.

produce mass terms for the fermions in the spontaneously broken SM. The extra degrees of freedom arising from the Nambu-Goldstone [16–18] scalars become the longitudinal polarizations of three linear combinations ($W^{\pm}$ and $Z^0$) of the four massless $SU(2)_L$ and $U(1)_Y$ gauge fields, making them massive in the unitary gauge. Thus it is said that the Higgs mechanism gives mass to the other particles of the SM.

## 2.2 Electroweak Symmetry Breaking

Spontaneous breaking of the electroweak gauge symmetry is crucial in the Standard Model as a length scale was observed in the weak nuclear force, a feature otherwise incompatible with Yang-Mills theories. This is achieved by means of the Higgs potential

$$V_H = -\mu^2 H^\dagger H + \lambda \left(H^\dagger H\right)^2 \tag{2.2}$$

where the relative sign of $\mu^2$ and $\lambda$ produces a potential with a symmetry-breaking minimum. A schematic sketch of the Higgs potential is given in Fig. 2.1.

The vacuum state will occupy any part of the circle in the complex plane which gives the minimum value of the potential. This means that the Higgs field acquires a non-zero vacuum expectation value, which can be written as

$$\langle H \rangle = \begin{pmatrix} 0 \\ v/\sqrt{2} \end{pmatrix} \tag{2.3}$$

with $v = \mu/\sqrt{\lambda}$. Then, the Lagrangian can be re-written perturbatively around this minimum with $H \to \langle H \rangle + h$.

The Higgs field is a doublet of $SU(2)_L$, and its weak hypercharge is arranged so that it has a neutral component, which will have the VEV. Additionally, its couplings to the electroweak gauge fields will guarantee that one linear combination of $W^a_\mu$ and $B_\mu$ fields which has no electric charge will not couple to the Higgs. That combination is the photon, and it is the vector boson that mediates the preserved $U(1)_Q$ factor for electromagnetic interactions. Also, the Higgs is a singlet of $SU(3)_C$ so the gluon does not interact with the Higgs either and remains massless as well.

## 2.3 Particle Content

The fields of the Standard Model can be divided into the spin-1 gauge fields, the spin-$^1/_2$ matter fields, and the scalar Higgs field.

In the adjoint representation of $SU(3)_C$ are the gluon fields $G^a_\mu(x)$, with $a = 1 \ldots 8$. Similarly for $SU(2)_L$, we have the $W^{1,2,3}_\mu(x)$ fields. Associated with the abelian hypercharge factor is the $B_\mu(x)$ field.

The matter fields of the SM all have spin-$^1/_2$ and transform either as $SU(2)_L$ singlets, in which case they are called right-handed or right-chiral, or they transform in the fundamental representation

| Field | Content | $SU(3)_C$ | $SU(2)_L$ | $U(1)_Y$ |
|---|---|---|---|---|
| | | Quarks | | |
| $Q_i$ | $(u_L, d_L)$ | $\square$ | $\square$ | $1/3$ |
| $u_i$ | $u_{Ri}$ | $\overline{\square}$ | $\mathbf{1}$ | $4/3$ |
| $d_i$ | $d_{Ri}$ | $\overline{\square}$ | $\mathbf{1}$ | $-2/3$ |
| | | Leptons | | |
| $L_i$ | $(\nu, e_L)_i$ | $\mathbf{1}$ | $\square$ | $-1$ |
| $e_i$ | $e_{Ri}$ | $\mathbf{1}$ | $\mathbf{1}$ | $-2$ |
| | | Higgs | | |
| $H$ | $(H^+, H_0)$ | $\mathbf{1}$ | $\mathbf{1}$ | $1$ |
| | | Gauge | | |
| $G$ | $G^a_\mu$ | Adj | $\mathbf{1}$ | $0$ |
| $W$ | $W^0_\mu, W^\pm_\mu$ | $\mathbf{1}$ | Adj | $0$ |
| $B$ | $B_\mu$ | $\mathbf{1}$ | $\mathbf{1}$ | $0$ |

Table 2.1: A listing of the fields and particle content of the Standard Model. The irreducible representations of the non-Abelian gauge groups that the fields belong to are indicated by Young tableaux, with "Adj" denoting the adjoint representation. The weak hypercharge factor is also listed. The index $i$ is for each of the 3 generation of quarks and leptons.

of $SU(2)_L$, and are called left-handed (or left-chiral). Quark fields transform as $SU(3)_C$ triplets, and lepton fields transform as singlets. There are three "generations" of quarks and leptons in the standard model.

The particle content of the SM is summarized in Table 2.1, with the Higgs also listed.

## 2.4 Lagrangian

The Lagrangian of the SM can be organized in a few parts:

$$\mathcal{L} = \mathcal{L}_{\text{YM}} + \mathcal{L}_{\text{Kinetic}} + \mathcal{L}_{\text{Yukawa}} + \mathcal{L}_{\text{Higgs}} \, . \tag{2.4}$$

The Yang-Mills Lagrangian, $\mathcal{L}_{\text{YM}}$, provides the kinetic terms of the gauge field strengths

$$-\mathcal{L}_{\text{YM}} = \frac{1}{4} G^a_{\mu\nu} G^{a\mu\nu} + \frac{1}{4} W^a_{\mu\nu} W^{a\mu\nu} + \frac{1}{4} B_{\mu\nu} B^{\mu\nu} \, , \tag{2.5}$$

where the gauge field strengths are defined by

$$G^a_{\mu\nu} = \partial_\mu G^a_\nu - \partial_\nu G^a_\mu - g_3 f^a_{bc} G^b_\mu G^c_\mu \, , \text{ with } a, b, c = 1, 2, \ldots, 8 \tag{2.6}$$

$$W^a_{\mu\nu} = \partial_\mu W^a_\nu - \partial_\nu W^a_\mu - g \epsilon^a_{bc} W^b_\mu W^c_\mu \, , \text{ with } a, b, c = 1, 2, 3 \tag{2.7}$$

$$B_{\mu\nu} = \partial_\mu B_\nu - \partial_\nu B_\mu \, . \tag{2.8}$$

In the equations above, $f^a_{bc}$ are the $SU(3)$ structure constants, and $\epsilon^a_{bc}$ are the $SU(2)$ structure constants.

The kinetic terms for matter fields are in $\mathcal{L}_{\text{Kinetic}}$, but it also provides the gauge–matter couplings by means of the covariant derivative. For a given Weyl spinor field[1], $\chi$, the covariant derivative $D_\mu \chi$ takes

[1] The spinor notations used are explained in Appendix A.1.

the form

$$D_\mu \chi = \left( \partial_\mu + i g_3 \frac{\lambda_a}{2} G^a_\mu(x) + i g T_a W^a_\mu(x) + i g' \frac{y}{2} B_\mu \right) \chi \,, \tag{2.9}$$

where $T_a$ are the generators of SU(2), $\lambda_a$ are the Gell-Mann matrices, and $y$ is the hypercharge of $\chi$. If $\chi$ is a singlet of $SU(3)_C$ or of $SU(2)_L$ then the $g_3$ term or the $g$ term vanishes, respectively. If $\chi$ is in the $\overline{\square}$ representation of $SU(3)_C$, then the $g_3$ term is conjugated. Then, we can write $\mathcal{L}_{\text{Kinetic}}$ as

$$\mathcal{L}_{\text{Kinetic}} = \bar{L}_i \sigma^\mu D_\mu L^i + \bar{e} \sigma^\mu D_\mu e^i + \bar{Q}_i \sigma^\mu D_\mu Q^i + \bar{u}_i \sigma^\mu D_\mu u^i + \bar{d}_i \sigma^\mu D_\mu d^i \,, \tag{2.10}$$

and $i$ is summed from 1 to 3 for each generation of quarks and leptons.

The Higgs coupling to matter, $\mathcal{L}_{\text{Yukawa}}$ is written as

$$\mathcal{L}_{\text{Yukawa}} = i Y_e^{ij} \bar{L}_i \sigma_2 H^* e_j + i Y_u^{ij} \bar{Q}_i \sigma_2 H u_j + i Y_d^{ij} \bar{Q}_i \sigma_2 H^* d_j + \text{ c.c.} \tag{2.11}$$

Here, $Y_e$, $Y_u$, and $Y_d$ are the Yukawa coupling matrices. They are in principle complex-valued and entirely arbitrary. Without electroweak symmetry breaking, the Yukawa Lagrangian describes the coupling of the Higgs field to the left- and right-chiral matter spinors. With electroweak symmetry breaking, the Higgs field in the interaction terms is replaced as

$$H \to \langle H \rangle + \frac{1}{\sqrt{2}} h \equiv \frac{1}{\sqrt{2}} (v + h) \tag{2.12}$$

where $v$, a c-number is the Higgs VEV, and $h$ is the Higgs boson. Then we are left with mass terms for the fermions as well as interactions between the Higgs boson and the fermions. The generated fermion mass parameters in the Lagrangian will have the form $m = yv/\sqrt{2}$, where $y$ is the corresponding Yukawa matrix element. Thus the otherwise arbitrary Yukawa coupling matrices are adjusted to reproduce the correct empirically observed mass, and offer no insight into the structure of the fermion mass spectrum.

The final piece of the Standard Model Lagrangian is the Higgs Lagrangian, which was introduced in Section 2.2. The Higgs Lagrangian includes the Higgs kinetic terms and couplings to gauge fields, as well as the Higgs potential responsible for electroweak symmetry breaking. Noting that

$$D_\mu H = \left(\partial_\mu + igT_a W_\mu^a + ig' y_H B_\mu\right) H \,, \tag{2.13}$$

where $y_H = 1$ is the Higgs hypercharge, we have

$$\mathcal{L}_{\text{Higgs}} = \left(D_\mu H\right)^\dagger \left(D_\mu H\right) + \mu^2 H^\dagger H + \lambda \left(H^\dagger H\right)^2 \,. \tag{2.14}$$

With this, we have constructed the full structure of the Standard Model Lagrangian.

## 2.5 Problems in the Standard Model

Despite the remarkable success of the Standard Model, it is quite clear that it must be extended for a variety of reasons. A sampling of these are enumerated here

- **Gravity** The Standard Model does not include the gravitational interaction. We cannot hope to conclude a fundamental theory of particles and interactions without mention of gravity, thus this is perhaps the most glaring omission.
- **Neutrino Masses** The absence of right-handed neutrinos precludes one from writing any dimension-4 operator for neutrino mass, and higher-dimensional operators are not within the SM framework.
- **Flavor** There is an extraordinary disparity in the magnitudes of the quark and lepton masses. This hierarchy in the Yukawa couplings is completely arbitrary in the SM.
- **Matter–antimatter Asymmetry** Assuming an equal amount of matter and anti-matter in the

early universe, as is natural in the SM, no sufficient source of CP violation exists to account for the vast asymmetry in the amount of matter and antimatter today.

- **Higgs Hierarchy** The nature of scalar field theory implies that the Higgs boson mass receive corrections from matter that it couples to, and in the SM, these corrections are divergent. If a cut-off scale $\Lambda$ is established, then the corrections diverge as $\Lambda^2$. If the cut-off scale is taken to be the Planck mass, where the SM is not sensible anyway, then the Higgs mass parameter must be tuned to a bewildering 32 digits.
- **Dark Matter** Cosmological data indicates that the matter in the SM accounts for roughly 4.9% of the mass-energy in the universe. An otherwise unexplained form of matter called Dark Matter apparently accounts for 26.8% while the cosmological constant contains the remaining 68.3% of the universe. A particle theory of dark matter is an essential starting point for physics beyond the Standard Model.

Thus it is essential that physics beyond the Standard Model be developed. We will introduce supersymmetry in the next chapter which addresses some, but certainly not all of the issues raised here.

# Chapter 3

# Supersymmetry

## 3.1 Origins of Supersymmetry

Supersymmetry (SUSY) was discovered by Ramond [19] in 1971, while writing the string Dirac equation. It was further applied towards the development of a superstring theory by Neveu and Schwarz [20], followed by Gervais and Sakita [21]. The first 4-dimensional Poincaré superalgebra came from Gol'fand and Likhtman [22], and independently, the first 4-dimensional interacting supersymmetric QFT came from Wess and Zumino [23]. Additionally, Volkov and Akulov [24] produced the earliest theory of spontaneously broken supersymmetry, where they identified the neutrino (then thought to be massless) as the Goldstone fermion. Salam and Strathdee [25] introduced the superspace in 1974, giving the easiest way to produce field representations of supersymmetry. In 1975, Haag, Łopuszański, and Sohnius showed [26] that by relaxing the assumptions of the Coleman-Mandula theorem [27] to include both commuting and anti-commuting generators, one finds that the Poincaré superalgebra is the most general nontrivial symmetry of the S-matrix.

## 3.2 Formulation

### 3.2.1 Superalgebra

Superalgebra [28–38] (also called a graded Lie algebra) generalizes the notion of a commutator to the so-called supercommutator by alternating between commutation and anti-commutation, based on the "grading" of the generators. Specifically, one defines the supercommutator by

$$\left[t_a, t_b\right\} \equiv t_a t_b - (-1)^{\eta_a \eta_b} t_b t_a = i C^c_{ab} t_c \tag{3.1}$$

where $\eta_a$ is the grading of the generator $t_a$, and $C^c_{ab}$ are the structure constants. The gradings serve as a parity between even (bosonic) and odd (fermionic) generators. Conventionally, even generators have $\eta = 0$ and odd generators have $\eta = 1$. Operators formed by the product of graded generators in turn have a grading equal to the modulo-2 sum of the gradings of the generator factors. Additionally, one obtains a super-Jacobi identity of the form

$$(-1)^{\eta_a \eta_c} \left[t_a, \left[t_b, t_c\right\}\right\} + (-1)^{\eta_b \eta_c} \left[t_c, \left[t_a, t_b\right\}\right\} + (-1)^{\eta_a \eta_b} \left[t_b, \left[t_c, t_a\right\}\right\} = 0 \,. \tag{3.2}$$

In supersymmetry, the even generators of the Poincaré group are combined with a collection of $\mathcal{N}$ odd Weyl spinor generators, $Q^A_\alpha$, where $A = 1 \ldots \mathcal{N}$ and $\alpha$ is the spinor index, using the supercommutator. Then, the Coleman-Mandula theorem along with a conventional choice of basis determines the form of the superalgebra. Using the gradings of the generators, one resolves the supercommutator into an explicit form, giving the following commutation and anti-commutation relations of the supersymmetry algebra

$$\left\{Q^A_\alpha, \bar{Q}_{B\dot{\beta}}\right\} = 2\sigma^\mu_{\alpha\dot{\beta}} P_\mu \delta^A_B \tag{3.3}$$

$$\left[M_{\mu\nu}, Q_\alpha^A\right] = i\left(\sigma_{\mu\nu}\right)_\alpha^{\ \beta} Q_\beta^A \tag{3.4}$$

$$\left[M_{\mu\nu}, \bar{Q}^{A\dot{\alpha}}\right] = i\left(\bar{\sigma}_{\mu\nu}\right)^{\dot{\alpha}}_{\ \dot{\beta}} \bar{Q}^{A\dot{\beta}} \tag{3.5}$$

$$\left[P_\mu, Q_\alpha^A\right] = \left[P_\mu, \bar{Q}_{B\dot{\beta}}\right] = 0 \tag{3.6}$$

$$\left\{Q_\alpha^A, Q_\beta^B\right\} = \varepsilon_{\alpha\beta} Z^{AB} \tag{3.7}$$

$$\left\{\bar{Q}_\alpha^A, \bar{Q}_\beta^B\right\} = \varepsilon_{\alpha\beta} Z^{*AB} \tag{3.8}$$

where the usual 2-component notation has been used[1]. Further, $P_\mu$ and $M_{\mu\nu}$ are the generators of the Poincaré group; $\bar{Q}$ denotes the complex conjugate of $Q$. The elements $Z$ and $Z^*$ are called central charged as they belong to an abelian invariant subalgebra of the superalgebra, and commute with every element of the superalgebra. However, since they are anti-symmetric, they do not appear for $\mathcal{N} = 1$.

We see that the generator of translations $P_\mu$ commutes with $Q$ and $\bar{Q}$, and $P^2$ is a Casimir operator, thus fields within an irreducible representation, a "supermultiplet", must have equal mass. This is in contradiction to experiment; if supersymmetry is realized in nature it must be spontaneously broken.

In contrast to mass, the spin of the fields need not be equal, instead, the fermionic degrees of freedom must equal the boson degrees of freedom. For this reason, only if $\mathcal{N} = 1$ does one find it possible to write a chiral theory. Thus, we will restrict our discussion in the $\mathcal{N} = 1$ case. Additionally, all fields within a supermultiplet belong to the same representation of the gauge group.

An important result of supersymmetry is that from Eq. (3.3), we can obtain a set of $\mathcal{N}$ equations for the vacuum energy in terms of the SUSY generators, by inspecting the $2 \times 2$ trace, for each $A$, and simply adding them all. The resulting expression for the Hamiltonian operator is

$$P_0 = \frac{1}{4\mathcal{N}} \sum_{A,\alpha} \left[Q_\alpha^A \bar{Q}_{\dot{\alpha}}^A + \bar{Q}_{\dot{\alpha}}^A Q_\alpha^A\right] \tag{3.9}$$

[1]The spinor notations used are explained in Appendix A.1.

We can find its expectation value for any given state $|\psi\rangle$,

$$\langle\psi|P_0|\psi\rangle = \frac{1}{4\mathcal{N}}\sum_{A,\alpha,k}\left[\langle\psi|Q^A_\alpha|\phi_k\rangle\langle\phi_k|\bar{Q}^A_{\dot{\alpha}}|\psi\rangle + \langle\psi|\bar{Q}^A_{\dot{\alpha}}|\phi_k\rangle\langle\phi_k|Q^A_\alpha|\psi\rangle\right] \tag{3.10}$$

$$= \frac{1}{2\mathcal{N}}\sum_{A,\alpha}\left|\langle\phi_k|Q^A_\alpha|\psi\rangle\right|^2 \tag{3.11}$$

Thus, it is guaranteed that $\langle\psi|P_0|\psi\rangle \geqslant 0$. Now, any state that gives a zero expectation value must be the vacuum; if there is no such state then the vacuum spontaneously breaks supersymmetry.

### 3.2.2 Superspace and Superfields

In this section, we develop the superspace formulation for the case $\mathcal{N} = 1$. Supermultiplets may be obtained by repeated use of the super-Jacobi identity. However, the superspace formalism allows one to write expressions that are manifestly supersymmetric. This is achieved by adding to spacetime coordinates, a pair of Grassmann coordinates $\theta^\alpha$ and its complex conjugate $\bar{\theta}^{\dot{\alpha}}$:

$$\text{Spacetime: } x^\mu \longrightarrow \text{Superspace: } \left\{x^\mu, \theta^\alpha, \bar{\theta}^{\dot{\alpha}}\right\} \tag{3.12}$$

Because the Grassmann coordinates[2] anti-commute, all polynomials in a Grassmann variable must be truncated at the quadratic term. This means that any given function in superspace has an exact finite Taylor expansion in the Grassmann coordinates:

$$\begin{aligned}\mathbf{S}\left(x^\mu, \theta^\alpha, \bar{\theta}_{\dot{\alpha}}\right) = \phi(x) + \theta\xi(x) + \theta^2 f(x) + \bar{\theta}\bar{\chi}(x) + \bar{\theta}\bar{\sigma}^\mu\theta A_\mu(x) \\ + i\theta^2\bar{\theta}\bar{\lambda}(x) + \bar{\theta}^2 g^*(x) + i\bar{\theta}^2\theta\eta(x) + \theta^2\bar{\theta}^2 d(x)\end{aligned} \tag{3.13}$$

[2]For more details on Grassmann coordinates, see Appendix A.2.

here the "superfield" $\mathbf{S}$ is a Lorentz scalar with 4 scalar components: $\phi$, $f$, $g$, and $d$, 4 Weyl spinor components: $\xi$, $\chi$, $\lambda$, and $\eta$, and 1 vector: $A$. Indeed, we could promote the rank of the superfield to e.g. $\mathbf{S}_\nu$ by additionally increasing the rank of its components. One may also add a spinor index to the superfield, but that will change the expansion slightly.

Transformations of the superfields are constructed by finding a form for the SUSY generators that satisfy

$$\exp\left(-i\epsilon Q - i\bar{\epsilon}\bar{Q}\right)\mathbf{S}\left(x^\mu, \theta^\alpha, \bar{\theta}^{\dot{\alpha}}\right) = \mathbf{S}\left(x^\mu + \Delta^\mu, \theta^\alpha + \epsilon^\alpha, \bar{\theta}_{\dot{\alpha}} + \bar{\epsilon}_{\dot{\alpha}}\right) \tag{3.14}$$

where $\epsilon$ is an arbitrary spinor parameter of the transformation and $\Delta^\mu = i\epsilon\sigma^\mu\bar{\theta} + i\bar{\epsilon}\bar{\sigma}^\mu\theta$. We note that translations in the spinor coordinate are accompanied by a translation of the scalar coordinate. One finds

$$Q_\alpha = i\frac{\partial}{\partial\theta^\alpha} - \left(\sigma^\mu\bar{\theta}\right)_\alpha \partial_\mu, \text{ and, } \bar{Q}^{\dot{\alpha}} = i\frac{\partial}{\partial\theta_{\dot{\alpha}}} - (\sigma^\mu\theta)^{\dot{\alpha}}\,\partial_\mu \tag{3.15}$$

satisfy the Poincaré superalgebra. The effect of the transformation on $\mathbf{S}$ can be explicitly determined [38] in terms of its components:

$$\delta\phi = \xi\epsilon + \bar{\chi}\bar{\epsilon} \tag{3.16}$$

$$\delta\xi = 2f\epsilon - (A_\mu + i\partial_\mu\phi)\sigma^\mu\bar{\epsilon} \tag{3.17}$$

$$\delta f = \bar{\lambda}\bar{\epsilon} + \frac{i}{2}\partial_\mu\xi\bar{\sigma}^\mu\epsilon \tag{3.18}$$

$$\delta\bar{\chi} = 2g^*\bar{\epsilon} + (A_\mu - i\partial_\mu\phi)\bar{\sigma}^\mu\epsilon \tag{3.19}$$

$$\delta A_\mu = \bar{\lambda}\bar{\sigma}_\mu\epsilon - \eta\sigma_\mu\bar{\epsilon} + \frac{i}{2}\partial_\nu(\xi\sigma_\mu\bar{\sigma}^\nu\epsilon - \bar{\chi}\bar{\sigma}_\mu\sigma^\nu\bar{\epsilon}) \tag{3.20}$$

$$\delta\bar{\lambda} = 2d\bar{\epsilon} - i\partial_\mu f\bar{\sigma}^\mu\bar{\epsilon} + \frac{i}{2}\partial_\mu A_\nu\bar{\sigma}^\nu\sigma^\mu\bar{\epsilon} \tag{3.21}$$

$$\delta g^* = \epsilon\eta + \frac{i}{2}\partial_\mu\bar{\chi}\bar{\sigma}^\mu\epsilon \tag{3.22}$$

$$\delta\eta = 2d\epsilon - i\partial_\mu g^*\sigma^\mu\bar{\epsilon} - \frac{i}{2}\partial_\mu A_\nu\sigma^\nu\bar{\sigma}^\mu\epsilon \tag{3.23}$$

$$\delta d = \frac{i}{2}\partial_\mu \left(\bar{\lambda}\bar{\sigma}^\mu \epsilon + \eta\sigma^\mu \bar{\epsilon}\right) \tag{3.24}$$

Crucially, we see that at translation in superspace of the "highest component" $d$ is a divergence in spacetime, and will not contribute to the action.

In order to create superfields using derivatives that transform correctly, it is convenient to introduce the covariant derivative:

$$D_\alpha = \frac{\partial}{\partial\theta_\alpha} - i\left(\sigma^\mu\bar{\theta}\right)_\alpha \partial_\mu, \text{ and, } \bar{D}^{\dot{\alpha}} = \frac{\partial}{\partial\theta^{\dot{\alpha}}} - i\left(\sigma^\mu\theta\right)^{\dot{\alpha}} \partial_\mu \tag{3.25}$$

yielding the relation

$$\left\{D_\alpha, \bar{D}^{\dot{\alpha}}\right\} = 2i\sigma^\mu_{\alpha\dot{\beta}}\partial_\mu \, . \tag{3.26}$$

The covariant derivative is a crucial aspect of superspace as it lets us project out any component of a given superfield. E.g., we may obtain the highest component (the $\theta^2\bar{\theta}^2$ component) of $\mathbf{S}$:

$$d = \frac{1}{16}D^2\bar{D}^2\mathbf{S}\Big|_{\theta=\bar{\theta}=0} \, . \tag{3.27}$$

Now, we saw from Eq. (3.24) that the $d$ component transforms as a total divergence, which will not contribute to the action. This means that we can use the covariant derivative to write a SUSY-invariant action (ensuring that the Lagrangian is Hermitian) from a generic superfield $\mathbf{S}$

$$S = \int d^4x \, \frac{1}{16}D^2\bar{D}^2\mathbf{S}\Big|_{\theta=\bar{\theta}=0} + \text{ H.c.} = \int d^4x \, d^4\theta \, \mathbf{S} + \text{ H.c.} \tag{3.28}$$

The covariant derivative also allows us to both define and build an irreducible representation of the

$\mathcal{N} = 1$ SUSY algebra, the chiral superfield[3], defined by

$$\text{Chiral superfield: } \bar{D}_{\dot{\alpha}} \mathbf{\Phi} = 0 \, . \tag{3.29}$$

Thus any superfield $\mathbf{S}$ may be turned into a chiral superfield $\mathbf{\Phi}$ using $\bar{D}$ as

$$\bar{D}_{\dot{\alpha}} \mathbf{\Phi} \equiv \bar{D}_{\dot{\alpha}} \left[ \bar{D}^2 \mathbf{S} \right] = 0 \, . \tag{3.30}$$

When working with chiral superfields, it becomes useful to define a new variable

$$y^{\mu} \equiv x^{\mu} + i\theta\sigma^{\mu}\bar{\theta} \tag{3.31}$$

so that chiral superfields may now be written simply as arbitrary functions of $y^{\mu}$ and $\theta_{\alpha}$, which in general has the form[4]

$$\mathbf{\Phi}(y^{\mu}, \theta^{\alpha}) = \phi(y) + \sqrt{2}\theta\xi(y) + \theta^2 F(y) \tag{3.32}$$

where $F$ is an auxiliary (non-dynamic) scalar to be eliminated by the field equations (similar to $d$ in $\mathbf{S}$). The superspace translation acts on the components of $\mathbf{\Phi}$ by

$$\delta\phi = \sqrt{2}\epsilon\xi \tag{3.33}$$

$$\delta\chi = -i\sqrt{2}\sigma^{\mu}\bar{\epsilon}\partial_{\mu}\phi + \sqrt{2}\epsilon F \tag{3.34}$$

$$\delta F = -i\sqrt{2}\bar{\epsilon}\bar{\sigma}^{\mu}\partial_{\mu}\chi \, . \tag{3.35}$$

We now see that in the case of the chiral superfield, once again, the highest component transforms under SUSY by a total derivative (just like $d$). This means that we have another way of constructing a

[3] This is a *left* chiral superfield–the right chiral superfield is constructed by $\bar{D} \to D$

[4] For a right chiral superfield, instead of $y^{\mu}$ one uses $\bar{y}^{\mu} \equiv x^{\mu} - i\bar{\theta}\bar{\sigma}^{\mu}\theta$; additionally $\theta \to \bar{\theta}$, with $\theta\xi \to \bar{\theta}\bar{\chi}$.

SUSY-invariant action, based on chiral superfields; for an arbitrary chiral superfield $\mathbf{\Phi}$,

$$\mathbf{S} = -\frac{1}{4}\int d^4x\, D^2\mathbf{\Phi}\Big|_{\theta=\bar{\theta}=0} + \text{H.c.} = \int d^4x\, d^2\theta\, \mathbf{\Phi} + \text{H.c.} \tag{3.36}$$

Thus, we have two ways of constructing SUSY invariant actions. Actions such as Eq. (3.28) are due to D-terms and actions such as Eq. (3.36) are due to F-terms. Note that the D-term is in essence an F-term since it is based on $\bar{D}^2\mathbf{S}$, which is in fact a chiral superfield.

Another important irreducible representation is the gauge superfield. It begins with the condition for a vector superfield and adds to it the requirement of belonging to the gauge algebra

$$\text{Vector superfield: } \mathbf{V} = \mathbf{V}^\dagger \ . \tag{3.37}$$

Thus, from the notation of Eq. (3.13), $\chi = \xi$, $f = g$, and $\eta = \lambda$. Also, $\phi$, $A_\mu$ and $d$ must be real. Gauge freedom allows us to zero the components $\phi$, $\xi = \chi$, and $f = g$, as is done in the Wess-Zumino gauge wherein the gauge superfield is written as

$$\mathbf{V}\left(x^\mu, \theta^\alpha, \bar{\theta}^{\dot{\alpha}}\right) = \bar{\theta}\bar{\sigma}^\mu A_\mu(x) + i\theta^2\bar{\theta}\bar{\lambda}(x) - i\bar{\theta}^2\theta\lambda(x) + \frac{1}{2}\theta^2\bar{\theta}^2 d(x) \ . \tag{3.38}$$

Here, $A_\mu$ is the usual gauge field, $\lambda$ is its "superpartner" which is called the gaugino field, and $d$ is the auxiliary field.

### 3.2.3 Supersymmetric Lagrangians

Starting with a set of chiral superfields $\mathbf{\Phi}^i$, we note that any holomorphic function $\mathcal{W}(\mathbf{\Phi}^i)$ satisfies

$$\bar{D}_{\dot{\alpha}}\mathcal{W}(\mathbf{\Phi}^i) = 0 \ , \tag{3.39}$$

meaning that it in turn is also a chiral superfield. We know from the previous section (cf. Eq. (3.36)) that we can build an F-term from it to have a supersymmetric Lagrangian term

$$\mathcal{L}_{\mathcal{W}} = \int d^2\theta\, \mathcal{W}(\mathbf{\Phi}^i) + \text{H.c.} \tag{3.40}$$

which can be rewritten as

$$\mathcal{L}_{\mathcal{W}} = F^i \frac{\partial \mathcal{W}}{\partial \phi^i} - \frac{1}{2}\xi^i \xi^j \frac{\partial^2 \mathcal{W}}{\partial \phi^i \partial \phi^j} + \text{H.c.} \tag{3.41}$$

Here, $F^i$, $\phi^i$, and $\xi^i$ refer to the corresponding components of $\mathbf{\Phi}^i$. The holomorphic function $\mathcal{W}$ is called the superpotential.

For supersymmetric gauge theories, we already have the gauge superfield $\boldsymbol{V}$ that allows us to embed the massless spin-1 gauge boson along with its superpartner gaugino field. In order to write gauge-invariant kinetic terms for $\boldsymbol{V}$ it is useful to define the supersymmetric field strength. For the case of an Abelian gauge theory,

$$\boldsymbol{W}_\alpha \equiv -\frac{1}{4}\bar{D}^2 D_\alpha \boldsymbol{V} \tag{3.42}$$

which is a gauge-invariant chiral superfield, which carries a spinor index from the super derivative. Now, to finally obtain the gauge kinetic term, we obtain the F-term in the bilinear of the super field strength [29]

$$\mathcal{L}_{\text{Abelian}} = \int d^2\theta\, \boldsymbol{W}^\alpha \boldsymbol{W}_\alpha = 2i\bar{\lambda}\bar{\sigma}^\mu \partial_\mu \lambda + d^2 - \frac{1}{2}F^{\mu\nu}F_{\mu\nu} + \frac{i}{4}\varepsilon^{\mu\nu\lambda\sigma}F_{\mu\nu}F_{\lambda\sigma} \tag{3.43}$$

where $F_{\mu\nu}$ is the usual gauge field strength.

In the case of a non-Abelian gauge theory, the super field strength must be changed to accommodate the change in the form of gauge transformations, and one finds that for a non-Abelian gauge group

with generators $T^a$ gauge superfields $\boldsymbol{V}_a$, and coupling $g$,

$$\boldsymbol{W}_\alpha \equiv -\frac{1}{4}\bar{D}^2\left(e^{-T^a\boldsymbol{V}_a}D_\alpha e^{T^a\boldsymbol{V}_a}\right) \tag{3.44}$$

where it is conventional to have scaled $\boldsymbol{V} \to 2g\boldsymbol{V}$. The gauge kinetic terms in this case arise from

$$\mathcal{L}_{\text{non-Abelian}} = \frac{1}{4g^2}\int d^2\theta\, \boldsymbol{W}^{a\alpha}\boldsymbol{W}^a_\alpha + \text{ H.c.} \tag{3.45}$$

In principle, it is not necessary that the gauge kinetic terms be limited to the trace. We can obtain a more general form that can also include higher-dimensional operators by introducing the gauge kinetic function so that

$$\mathcal{L}_{\text{gauge}} = \int d^2\theta\, f_{ab}\left(\boldsymbol{\Phi}^i\right)\boldsymbol{W}^{a\alpha}\boldsymbol{W}^b_\alpha \tag{3.46}$$

where $f_{ab}$ is (like the superpotential) a chiral superfield that is a holomorphic function of chiral superfields. The gauge kinetic function for Eq. (3.45) is of course

$$f_{ab} = \frac{1}{4g^2}\delta_{ab}\,. \tag{3.47}$$

The gauge–matter Lagrangian terms are due to the so-called Kähler potential, $\mathcal{K}$. Here, the left and right chiral and gauge superfields are combined into a gauge-invariant vector superfield, and the Lagrangian terms are obtained from the D-term

$$\mathcal{L}_{\text{Kähler}} = \int d^4\theta\, \mathcal{K}\left(\boldsymbol{\Phi}^{\bar{i}\dagger}, e^{2\boldsymbol{V}}\boldsymbol{\Phi}^j\right) \tag{3.48}$$

where the barred index runs over right-chiral superfields while the un-barred index is over the left-chiral superfields.

It is worth pointing out that the formalism of the superpotential, gauge kinetic function, and the Kähler potential were brought into global supersymmetry by way of local supersymmetry. I.e., they were first discovered in the development of supergravity, a key topic in Chapter 4. Indeed, the formalism of the Kähler potential become more elaborate in supergravity, and the reader is referred to [29] for more details.

## 3.3 Spontaneous Supersymmetry Breaking

As already mentioned, the prediction of equal-mass superpartners in SUSY does not agree with experiment, thus SUSY can only exist if spontaneously broken. The idea is similar to electroweak symmetry breaking, but here SUSY cannot be broken by radiative corrections–if it is not broken at tree-level it will not be broken at the loop-level [39–42].

Now, we have already seen that non-zero vacuum energy means that supersymmetry is spontaneously broken. Since essentially the scalar potential is made up of F-terms and D-terms, as long as we can arrange them to not both be zero on average, we will have spontaneous breaking.

### 3.3.1 F-term breaking

Spontaneously breaking SUSY with an F-term can be achieved by the O'Raifeartaigh [43] mechanism. Here, one begins with the superpotential of 3 chiral superfields written as

$$\mathcal{W} = m\Phi_2\Phi_3 + \lambda\Phi_1\left(\Phi_3^2 - \mu^2\right) \tag{3.49}$$

which yields the scalar potential

$$V = \left|\mathcal{F}_1\right|^2 + \left|\mathcal{F}_2\right|^2 + \left|\mathcal{F}_3\right|^2 \text{, where } \mathcal{F}_i = \frac{\partial \mathcal{W}}{\partial \phi_i}\text{, and} \tag{3.50}$$

$$\mathcal{F}_1 = -\lambda\left(\phi_3^{*\,2} - \mu^2\right) \tag{3.51}$$

$$\mathcal{F}_2 = -m\phi_3^* \tag{3.52}$$

$$\mathcal{F}_3 = -m\phi_2^* - 2\lambda\phi_1^*\phi_3^* \,. \tag{3.53}$$

One can see that it is not possible to simultaneously have every $\mathcal{F}_i = 0$. Thus the minimum value of the potential will be non-zero, indicating broken supersymmetry.

### 3.3.2 D-term breaking

If there is a U(1) gauge invariance, one can also have D-term breaking without F-term breaking by the Fayet-Iliopoulos [44] mechanism. This is achieved by arranging the scalar potential to have term linear in the gauge multiplet's auxiliary field:

$$\mathcal{L}_{\text{FI}} = \int d^2\theta\, \boldsymbol{W}^\alpha \boldsymbol{W}_\alpha - \int d^4\theta\, \kappa^2 \boldsymbol{V} \tag{3.54}$$

$$\Longrightarrow V = \frac{1}{2}d^2 - \kappa^2 d + g d q_i |\phi^i|^2 \tag{3.55}$$

where $g$ is the gauge coupling of the U(1) group with charges $q_i$ for the scalars $\phi_i$, and $\kappa$ is a parameter with $[\kappa] = 1$. If the scalars each have[5] $\langle\phi_i\rangle = 0$ then one will have the vacuum energy be $V \sim \kappa^4$.

It turns out that in minimal phenomenological models of SUSY (such as the one discussed in Chapter 3), if the weak hypercharge group is used, it can lead to spontaneous breaking of electromagnetism. Thus it would only be sensible to use this mechanism with an otherwise undetermined U(1). Though,

[5] This typically only happens with accompanying terms in the superpotential omitted from the discussion.

as we will see next, this will still not be sufficient for phenomenology.

### 3.3.3 Supertrace Sum Rule

If SUSY is broken by an elementary superfield, we get the phenomenologically desired result of having different masses for the component fields of different spin. However, there remains a strict constraint relating [45] these masses. For a given superfield with mass $M$, let $M_j$ be the mass matrix of the component spin-j field. Then one finds the so-called "supertrace" sum rule[6],

$$\mathrm{STr}\, M^2 = \sum_j (-1)^{2j}(2j+1)\,\mathrm{Tr}\, M_j^2 = 0\ . \tag{3.56}$$

This constraint leads to severe conflict with empirical data, but remains a feature of most theories of spontaneously broken global supersymmetry.

Typically, the supertrace sum rule is avoided by introducing a set of additional superfields that are neutral gauge singlets of the Standard Model gauge group and are very massive, so that they do not affect low energy physics. Then, these fields are free to break supersymmetry, and the breaking of supersymmetry will be communicated to the elementary superfields by some additional mechanism. We will consider the breaking of local supersymmetry in Chapter 4, where these problems are neatly avoided.

## 3.4 The Minimal Supersymmetric Standard Model

Beginning with the Standard Model: the 3 generation of fermions, the electroweak and strong interactions, and the electroweak symmetry breaking via the Higgs mechanism, the simplest $\mathcal{N} = 1$

[6] The value of the supertrace can be adjusted by introducing an anomalous gauge group.

| Superfield | Bosons | Fermions | $SU(3)_C$ | $SU(2)_L$ | $U(1)_Y$ |
|---|---|---|---|---|---|
| | | Chiral Superfields | | | |
| $\mathbf{Q}_i$ | $(\tilde{u}_L, \tilde{d}_L)_i$ | $(u_L, d_L)$ | $\square$ | $\square$ | $1/3$ |
| $\bar{\mathbf{u}}_i$ | $\tilde{u}^*_{R,i}$ | $\bar{u}_i = u^\dagger_{Ri}$ | $\overline{\square}$ | $\mathbf{1}$ | $-1/3$ |
| $\bar{\mathbf{d}}_i$ | $\tilde{d}^*_{R,i}$ | $\bar{d}_i = d^\dagger_{Ri}$ | $\overline{\square}$ | $\mathbf{1}$ | $2/3$ |
| $\mathbf{L}_i$ | $(\tilde{\nu}, \tilde{e}_L)_i$ | $(\nu, e_L)_i$ | $\mathbf{1}$ | $\square$ | $-1$ |
| $\bar{\mathbf{e}}_i$ | $\tilde{e}^*_{R,i}$ | $\bar{e}_i = e^\dagger_{Ri}$ | $\mathbf{1}$ | $\mathbf{1}$ | $1$ |
| $\mathbf{H}_u$ | $(H^+_u, H^0_u)$ | $\left(\widetilde{H}^+_u, \widetilde{H}^0_u\right)$ | $\mathbf{1}$ | $\square$ | $1$ |
| $\mathbf{H}_d$ | $(H^0_d, H^-_u)$ | $\left(\widetilde{H}^0_d, \widetilde{H}^-_u\right)$ | $\mathbf{1}$ | $\square$ | $-1$ |
| | | Gauge Superfields | | | |
| $\mathbf{G}^a$ | $G^a_\mu$ | $\widetilde{G}^a$ | Adj | $\mathbf{1}$ | $0$ |
| $\boldsymbol{W}^i$ | $W^0_\mu, W^\pm_\mu$ | $\widetilde{W}^0, \widetilde{W}^\pm$ | $\mathbf{1}$ | Adj | $0$ |
| $\mathbf{B}$ | $B_\mu$ | $\tilde{B}$ | $\mathbf{1}$ | $\mathbf{1}$ | $0$ |

Table 3.1: A listing of the superfields and particle content within the MSSM. The irreducible representations of the non-Abelian gauge groups that the superfields belong to are indicated by Young tableaux–"Adj" is for the adjoint representation. The weak hypercharge factor is also listed. The index i is for each of the 3 generation of quarks and leptons.The chiral superfields are divided into the three groups. The first group has the squark bosons and quark fermions; the second group has the slepton bosons and lepton fermions; the third group has the Higgs bosons and the Higgsino fermions. The gauge superfields contain gauge bosons and gaugino fermions.

supersymmetric extension is called the Minimal Supersymmetric Standard Model (MSSM).

### 3.4.1 Particle Content

Here, the quarks and leptons are situated in chiral superfields, which additionally have new scalar (sfermion) superpartners: the squarks and sleptons. The chiral superfields belong to the same representations of the gauge group as in the SM. As expected, the gauge fields are within gauge superfields, along with Majorana gaugino fields.

It is not possible to have only one multiplet for the Higgs field. This is because the Higgs-fermion Yukawa couplings arise in SUSY from the superpotential, which must be holomorphic. As the SM builds the Higgs Lagrangian by using the Hermitian conjugate of the Higgs to obtain the opposite hypercharge, only one Higgs doublet is needed there. In the MSSM, two Higgs doublets are necessary: one that couples to up-like quarks and one that couples to down-type quarks and leptons. Thus, there are two chiral superfields for the Higgs scalars, and with them are two Weyl Higgsino spinors. In Table 3.1, a summary of the MSSM supermultiplets and its particle content is presented, with the representation of each multiplet within the gauge group indicated by Young tableaux.

### 3.4.2 The Lagrangian

The MSSM Lagrangian consists of the usual SUSY-invariant D-terms and F-terms in $\mathcal{L}_{\text{SUSY}}$, but additionally, one adds to the Lagrangian "soft" terms that explicitly break supersymmetry. For the purposes of the MSSM, one assumes they are generated by some mechanism that effectively generate $\mathcal{L}_{\text{soft}}$. Thus is MSSM Lagrangian is composed of two parts [35]

$$\mathcal{L}_{\text{MSSM}} = \mathcal{L}_{\text{SUSY}} + \mathcal{L}_{\text{soft}} \, . \tag{3.57}$$

The supersymmetric part is the result of supersymmetrizing the SM Lagrangian, noting that there are two chiral superfields for the Higgs. The Lagrangians for the gauge sector is given by the F-term for the field strengths

$$\mathcal{L}_{\text{gauge}} = \frac{1}{4}\int d^2\theta \, \left(\mathbf{G}^{a\,\alpha}\mathbf{G}^{a}_{\alpha} + \mathbf{W}^{i\,\alpha}\mathbf{W}^{i}_{\alpha} + \mathbf{B}^{\alpha}\mathbf{B}_{\alpha}\right) + \text{ H.c.} \tag{3.58}$$

where $\mathbf{G}^{\alpha}$ and $\mathbf{W}^{\alpha}$ are the non-Abelian supersymmetric field strengths for the $SU(3)_C$ and $SU(2)_L$ gauge superfields, respectively. And, $\mathbf{B}^{\alpha}$ is the Abelian supersymmetric field strength of the $U(1)_Y$ gauge superfield. The $a$ and $i$ are the group adjoint indices.

The kinetic terms for the chiral superfields reside in the matter Lagrangian, and arise from the D-term of the gauge-invariant Kähler potential, $\mathcal{K}$. In the MSSM, the simplest form of the Kähler potential is used, giving

$$\mathcal{L}_{\text{matter}} = \int d^4\theta \left( \mathbf{Q}_i^\dagger e^{\mathbf{\Omega}_Q} \mathbf{Q}_i + \bar{\mathbf{u}}_i^\dagger e^{\mathbf{\Omega}_u} \bar{\mathbf{u}}_i + \bar{\mathbf{d}}_i^\dagger e^{\mathbf{\Omega}_d} \bar{\mathbf{d}}_i + \mathbf{L}_i^\dagger e^{\mathbf{\Omega}_L} \mathbf{L}_i + \bar{\mathbf{e}}_i^\dagger e^{\mathbf{\Omega}_e} \bar{\mathbf{e}}_i \right), \tag{3.59}$$

where $i$ is the index of the generation of matter, and for a given chiral superfield $\mathbf{\Phi}$,

$$e^{\mathbf{\Omega}} \mathbf{\Phi} = \exp\left[ g_3 \mathbf{G}_a \lambda^a + g \boldsymbol{W}_i T^i + g' y \mathbf{B} \right] \mathbf{\Phi} \, . \tag{3.60}$$

In the above, if $\mathbf{\Phi}$ is a singlet of $SU(3)_C$ or of $SU(2)_L$ then the $g_3$ term and/or the $g$ term vanish, respectively. If $\mathbf{\Phi}$ is in the $\overline{\square}$ representation of $SU(3)_C$, then the $g_3$ term is conjugated. The factor $y$ is the weak hypercharge of $\mathbf{\Phi}$.

The Higgs–matter Yukawa terms come from the MSSM superpotential,

$$\mathcal{W}_{\text{MSSM}} = \mu H_u H_d + Y_u^{ij} \bar{\mathbf{u}}_i Q_j H_u + Y_d^{ij} \bar{\mathbf{d}}_i Q_j H_d + Y_e^{ij} \bar{\mathbf{e}}_i L_j H_d \tag{3.61}$$

where the $SU(2)_L$ indices are implicitly contracted. Further, $[\mu] = 1$ is a new dimensional parameter, while we also have the familiar Yukawa coupling matrices in generation space. The Higgs Lagrangian is built from this superpotential and the D-term of the Higgs–gauge coupling giving

$$\mathcal{L}_{\text{Higgs}} = \int d^4\theta \left( \mathbf{H}_u^\dagger e^{g \boldsymbol{W}_i T^i + g' y_H \mathbf{B}} \mathbf{H}_u + \mathbf{H}_d^\dagger e^{g \boldsymbol{W}_i T^i - g' y_H \mathbf{B}} \mathbf{H}_d \right) + \int d^2\theta \, \mathcal{W}_{\text{MSSM}} + \text{ H.c.} \tag{3.62}$$

With this we have the SUSY-invariant portion of the MSSM Lagrangian

$$\mathcal{L}_{\text{SUSY}} = \mathcal{L}_{\text{gauge}} + \mathcal{L}_{\text{matter}} + \mathcal{L}_{\text{Higgs}} \tag{3.63}$$

The "soft" SUSY-breaking Lagrangian consists of the Higgs–sfermion trilinear terms, the scalar mass terms, and the gaugino mass terms

$$\begin{aligned}
-\mathcal{L}_{\text{soft}} = \epsilon_{\alpha\beta} \Big( & A_u^{ij} Y_u^{ij} H_u^{\alpha} \tilde{Q}_i^{\beta} \tilde{u}_j + A_d^{ij} Y_d^{ij} H_d^{\alpha} \tilde{Q}_i^{\beta} \tilde{d}_j + A_e^{ij} Y_d^{ij} H_d^{\alpha} \tilde{L}_i^{\beta} \tilde{e}_j + \text{ H.c} \Big) \\
& + m_{H_u}^2 |H_u|^2 + m_{H_d}^2 |H_d|^2 + (\mu B_0 H_u H_d + \text{ H.c.}) \\
& + \left( M_Q^2 \right)_{ij} \tilde{Q}^{\dagger i} \tilde{Q}^j + \left( M_u^2 \right)_{ij} \tilde{u}^{\dagger i} \tilde{u}^j + \left( M_d^2 \right)_{ij} \tilde{d}^{\dagger i} \tilde{d}^j \\
& + \left( M_L^2 \right)_{ij} \tilde{L}^{\dagger i} \tilde{L}^j + \left( M_e^2 \right)_{ij} \tilde{e}^{\dagger i} \tilde{e}^j \\
& + \frac{1}{2} \left( M_1 \tilde{B} \cdot \tilde{B} + M_2 \tilde{W}^i \tilde{W}_i + M_3 \tilde{G}^a \tilde{G}_a + \text{ H.c.} \right)
\end{aligned} \tag{3.64}$$

where the trilinear couplings $[A_f] = 1$, the parameter $\mu$ is the same as in the superpotential, $M_f^2$ is the squared mass matrix of sfermion $\tilde{f}$, and the $M_1$, $M_2$, and $M_3$ are the masses of the bino, wino, and gluino, respectively. The massive parameter $B$ arises also from the breaking.

# Chapter 4

# Supergravity Grand Unification

## 4.1 Historical Introduction

A major issue with the global supersymmetry introduced in Chapter 3 is the difficulty with breaking SUSY and producing a spectrum of new sparticles consistent with observations. In the MSSM formalism, one simply adds to the Lagrangian a collection of terms that explicitly break SUSY, and all of the couplings in these terms are arbitrary parameters. By promoting supersymmetry to be a local symmetry, i.e., allowing the superspace translations to depend on the spacetime coordinate solves this issue, we are able to break supersymmetry in a phenomenologically viable way and realistic models can be constructed.

The first theory of local supersymmetry was super-gauge symmetry (or gauge supersymmetry) proposed in 1975 by Arnowitt and Nath [46, 47]. This was done by introducing the concept of gauge-completion in superspace, a method for constructing a covariant tensor for an arbitrary transformation group. The theory necessarily included Einstein gravity, and thus was later called supergravity (SUGRA). A different approach to supergravity was developed in 1976 by Freedman, Ferrara, and van

Nieuwenhuizen [48] and further simplified by Deser and Zumino [49]. In 1981, Witten elaborated the nature of dynamical breaking of supersymmetry [42] and van Nieuwenhuizen gave an extensive paper on the details of SUGRA [28]. In 1979, Cremmer *et al.* constructed [50] a supergravity Lagrangian coupled to a single chiral supermultiplet, a first step towards a realistic model of supergravity. In 1982, Chamseddine, Arnowitt, and Nath presented [51–54] the first realistic model of supergravity by coupling an arbitrary number of chiral superfields to supergravity, allowing for the presence of the quarks and leptons, and the Higgs bosons. This model came to be known as minimal supergravity (mSUGRA), and today it is also referred to in the literature as the constrained MSSM (CMSSM).

## 4.2 Essential Supergravity

### 4.2.1 Pure Supergravity

The discussion here is limited to 4-dimensional $\mathcal{N} = 1$ supergravity, and only a brief overview of the formalism is provided. The reader is directed to [28–32, 34] for excellent expositions of the formal aspects.

Here, supersymmetry becomes a local symmetry, generated by $M_{\mu\nu}$ and $P_\mu$ of the Poincaré group, which must have corresponding gauge fields

$$M_{ab} \longrightarrow \omega^{\mu}_{ab} \quad \text{the spin connection} \tag{4.1}$$

$$P_a \longrightarrow e^{\mu}_{a} \quad \text{the vierbein} , \tag{4.2}$$

where Latin characters are now used for the group indices, though they still run from $a = 0, 1, 2, 3$. The super field strengths of these gauge fields are given by the Riemann curvature tensor and the torsion tensor, which give the kinetics of supergravity.

Of course, in supersymmetry we do not have Poincaré group but the super-Poincaré group, which includes the spinor generators $Q_\alpha$, which must also have an associated gauge field, called the gravitino

$$Q_\alpha \longrightarrow \psi^\mu_\alpha \quad \text{the gravitino.} \tag{4.3}$$

As a vector-spinor, the gravitino has spin-$^3/_2$. Now, considering that the vierbein of course has spin-2, we realize that its superpartner must have spin-$^3/_2$ or spin-$^5/_2$. Since we cannot couple a spin-$^5/_2$ field to matter, it is natural to arrange the vierbein and the gravitino into the so-called gravity supermultiplet. The action for pure supergravity is then the sum of the action for the vierbein with the Rarita-Schwinger action [55] for the gravitino

$$S = \frac{1}{2\kappa^2}\int d^4x \left|\det e^a_\mu\right| R + \frac{i}{4}\int d^4x\, \varepsilon^{\mu\nu\rho\sigma}\bar{\psi}_\mu\gamma_5\gamma_\nu D_{\rho\sigma} \tag{4.4}$$

where[1] $\kappa^2 \equiv 8\pi G$, with $[\kappa] = -1$ and $G$ is the Newtonian gravitational constant. Additionally $R$ is the curvature scalar, $\gamma_\mu$ and $\gamma_5$ are Dirac matrices, and $D_{\rho\sigma\alpha}$ is the field strength of the gravitino. In the above, the contracted spinor indices are omitted.

### 4.2.2 Supergravity Coupled to Matter

The development of supergravity lead to the formalism used to construct the chiral Lagrangian, which depends on three functions: the superpotential $\mathcal{W}$, the Kähler potential $\mathcal{K}$, and the gauge kinetic function $f_{ab}$, where $a$ and $b$ are indices in the adjoint representation. The Lagrangian has the form

$$\mathcal{L} = \int d^4\theta\, \mathcal{K}\left(\mathbf{\Phi}^{\bar{\imath}\dagger}, e^{2V}\mathbf{\Phi}^j\right) + \left[\int d^2\theta\, f_{ab}\left(\mathbf{\Phi}^i\right)\mathbf{W}^{a\alpha}\mathbf{W}^b_\alpha + \int d^2\theta\, \mathcal{W}\left(\mathbf{\Phi}^i\right) + \text{ H.c.}\right] \tag{4.5}$$

[1] The inverse of $\kappa$ has dimensions of mass, and is called the Planck mass, $M_{Pl}$.

Here, $\boldsymbol{W}$ are super field strengths, $\mathcal{W}$ and $f$ are holomorphic functions, and $f$ transforms as a symmetric product of two adjoint representations in the gauge group. This Lagrangian includes non-renormalizable terms, and all higher-dimensional operators are suppressed by a factor of $\kappa$. It turns out that the Lagrangian only depends on $\mathcal{K}$ and $\mathcal{W}$ in the combination

$$\mathcal{G} = \kappa^2 \mathcal{K} - \ln\left(\kappa^6 |\mathcal{W}|^2\right) \tag{4.6}$$

where $\mathcal{G}$ is known as the Kähler function. This is because the Kähler transformation, where for some function $f$ of the scalar components of the chiral superfields,

$$\mathcal{K} \to \mathcal{K} + f(\phi^i) + f^\dagger(\phi^{\bar{\imath}\dagger}) \tag{4.7}$$

$$\mathcal{W} \to e^{-f(\phi^i)} \mathcal{W} \tag{4.8}$$

leaves $\mathcal{G}$ invariant. Note that this is only valid at the classical level, and is in fact anomalous at the quantum level [56–60].

The Kähler metric is defined by

$$g_{i\bar{\jmath}} \equiv \frac{\partial^2 \mathcal{K}}{\partial \phi^i \partial \phi^{\bar{\jmath}\dagger}} \, . \tag{4.9}$$

In the simplest case, $g_{i\bar{\jmath}} = \delta_{ij}$ is called a flat Kähler metric.

The full Lagrangian involves many terms suppressed by $\kappa^n$, which can be neglected. Some of the important terms are presented here [35, 61, 62], beginning with the scalar potential

$$-\mathcal{L}_V = \frac{1}{2} \sum_i g_i^2 \Re\left[f_{ab}^{-1}\right] \left(\mathcal{G}_{,i} T^{aij} \phi_j\right) \left(\mathcal{G}_{,k} T^{bkl} \phi_l\right) - \kappa^{-4} e^{-\mathcal{G}} \left(g^{i\bar{\jmath}} \mathcal{G}_{,i} \mathcal{G}_{,\bar{\jmath}} + 3\right) \tag{4.10}$$

where we see that the potential is not positive-definite any longer. However, for suitable choices of $f$, $\mathcal{K}$, and $\mathcal{W}$, in the limit $\kappa \to 0$, we recover the scalar potential of global SUSY.

The Lagrangian will also have terms bilinear in the gaugino fields

$$-\mathcal{L}_{\text{gaugino}} = \left[\frac{1}{4\kappa} e^{-\mathcal{G}/2} g^{i\bar{j}} \mathcal{G}_{,i} f^{\dagger}_{ab,i}\right] \bar{\lambda}^{a} \lambda^{b} \ . \tag{4.11}$$

The idea here is that SUSY breaking will cause the factor in brackets to grow a VEV, making the gauginos massive.

We also have a bilinear in the gravitino field

$$-\mathcal{L}_{\text{gravitino}} = \left[\kappa^{-1} e^{\mathcal{G}/2}\right] \bar{\psi}_{\mu} \sigma^{\mu\nu} \psi_{\nu} \tag{4.12}$$

and once again the VEV growth in the bracketed factor will give a mass term, this time for the gravitino.

## 4.3 Gravity-mediated Supersymmetry Breaking

In supergravity, the scalar potential is no longer positive semi-definite. However, we still cannot break SUSY by elementary fields due to the supertrace sum rule. In gravity mediation, the local supersymmetry is broken by a super-Higgs field, in analogy to electroweak symmetry breaking. Since the broken symmetry is generated by a spinor, in place of a Goldstone boson, there will be a Goldstone fermion, or goldstino. This will be absorbed by the gravitino, making it massive. The SUSY breaking is communicated to the elementary fields by operators suppressed by $\kappa$. This is achieved by additively separating the superpotential into a "visible" sector of elementary fields, and a "hidden" sector of SUSY breaking fields.

As a sketch, let $z$ be a super-Higgs field, and let $\phi_i$ be the physical fields. If $z$ is a gauge singlet, there

will be no gauge interactions with $\phi_i$. Additionally, if $\mathcal{W}$ has the form

$$\mathcal{W} = \mathcal{W}_{\text{visible}}(\phi^i) + \mathcal{W}_{\text{hidden}}(z) \tag{4.13}$$

then in the Lagrangian, the only couplings between $z$ and $\phi_i$ will be scaled by powers of $\kappa$. Then, $z$ is free to grow a VEV

$$\langle z \rangle = \mathcal{O}\left(\kappa^{-1}\right) = \mathcal{O}\left(M_{\text{Pl}}\right) \tag{4.14}$$

and the matter fields will not become super-heavy due to the $\kappa$ suppression of the couplings to $z$. Now, the fermionic partner to the scalar $z$ is absorbed by the gravitino, and its mass is a useful parametrization of SUSY breaking

$$m_{3/2} = \kappa^{-1} e^{-\langle \mathcal{G} \rangle/2} = \kappa^2 e^{\langle z \rangle^2/2} \left| \langle \mathcal{W}_{\text{hidden}} \rangle \right| \ . \tag{4.15}$$

Essentially, we have $m_{3/2} \sim \kappa m^2$. To obtain $m_{3/2} \sim 1$ TeV, we should choose $m \sim 10^{10}$ GeV.

The resulting effective scalar potential will now include terms of the form

$$-\mathcal{L} = m_0^2 |\phi^i|^2 + \frac{1}{2} m_{1/2} \bar{\lambda}_a \lambda_a + \mu B_0 H_u H_d + A_0 \mathcal{W}^{(3)} \tag{4.16}$$

exactly matching the form of the soft breaking Lagrangian given in Eq. (3.64). A key difference being the $\sim 100$ arbitrary parameters are now replaced by 4: $m_{3/2} \sim m_0$, $m_{1/2}$, $A_0$, $\mu$, and $B_0$. The reason why the number of parameters is so few is to do with assumptions that are made, including a flat Kähler metric, which treats all of the chiral superfields symmetrically, and choosing the gauge kinetic function to be

$$f_{ab} \sim \delta_{ab} + \mathcal{O}(\kappa) \ . \tag{4.17}$$

We noted earlier that the $f_{ab}$ transforms as the symmetric product of two adjoint representations. In the case that we choose the singlet, then the mass of all three gauginos will be equal, $m_{1/2}$. For any other

choice, we can have three independent masses

$$m_{1/2} \to M_1,\ M_2,\ M_3\ . \tag{4.18}$$

Similarly, adjustments can be made to the Kähler potential and the trilinear superpotential terms to allow for more flexible models.

## 4.4 Grand Unification

In the Standard Model, the three gauge couplings when evolved to high energies tend toward, but do not quite converge to a single point. Their unification would have been remarkable–showing that the seemingly disparate forces have a common origin. Remarkably, with the renormalization group equations in supersymmetry, the couplings do unify, within uncertainties. The RG evolution of the couplings in the SM and the MSSM are displayed in Fig. 4.1, and it is observed that the MSSM case does unify at a scale $\mu \sim 2 \times 10^{16}$ GeV, while in the SM the couplings do not unify.

The scale at which the gauge couplings unify in supersymmetry is called the grand unification scale, $M_{GUT}$. This can easily be interpreted as the scale at which a higher gauge symmetry group, $G_{GUT}$ is broken to the gauge group of the Standard Model,

$$G_{SM} = SU(3)_C \times SU(2)_L \times U(1)_Y\ . \tag{4.19}$$

The first grand unified theories were developed without supersymmetry. Pati and Salam [63, 64] introduced the notion of lepton number as the fourth color in

$$SU(4)_C \times SU(2)_L \times SU(2)_R \tag{4.20}$$

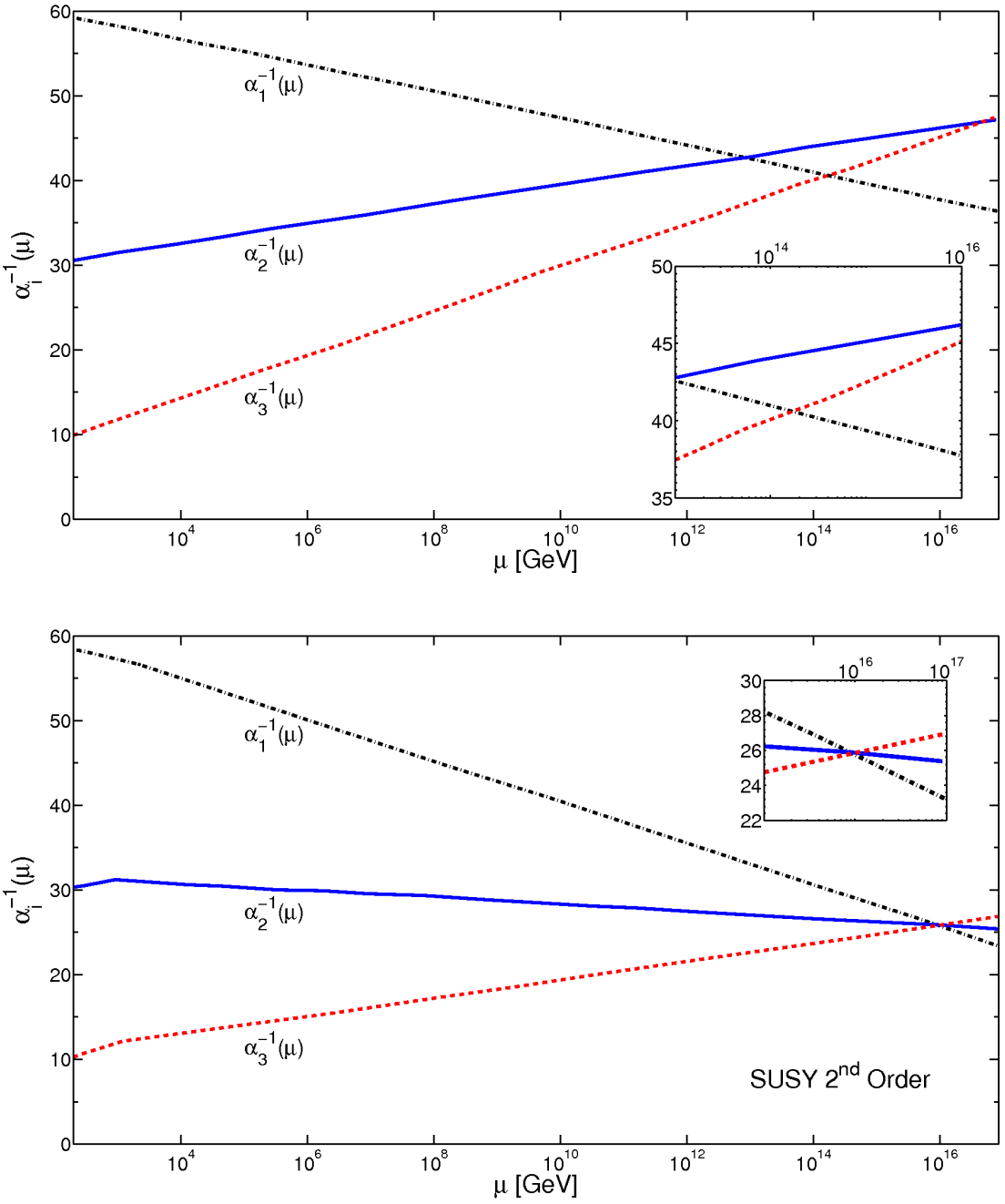


Figure 4.1: The renormalization group evolution of the gauge coupling constants $1/\alpha_i$, where $\alpha_i = g_i^2/4\pi$. In the top panel is evolution under the Standard Model RGEs. In the bottom panel is evolution under the MSSM RGEs. One can see that the couplings do not unify in the SM, but do unify in the MSSM at a scale $\mu \sim 2 \times 10^{16}$ GeV.

and the differences between quarks and leptons are obtained once the symmetry is spontaneously broken to $G_{SM}$. An attractive feature of this is the emergence of electric charge quantization. However, this did not unify $G_{SM}$ into a single grand unified group.

Georgi and Glashow [65–67] unified $G_{SM}$ into SU(5), a particular case of

$$SU(n) \supset SU(p) \times SU(n-p) \times U(1) \text{ , for } p > 1 \text{ , and } n > p+1 \text{ .} \tag{4.21}$$

Some of the main drawbacks in non-supersymmetric GUTs include the particles without some intervention would be of order $M_{GUT}$ in mass. Additionally, the scale of unification itself is low enough to cause grave problems in proton decay.

We note that the first supersymmetric grand unified theories (SUSY GUTs) were presented in [68, 69]. The first formulation of supergravity grand unification (SUGRA GUT) was given in [51, 52].

In the framework of a SUGRA GUT, it is natural to write the effective Lagrangian including soft-breaking terms, generated by gravity-mediated SUSY breaking at the scale $M_{GUT}$. Then, one RG evolves the high scale parameters to the electroweak scale, where phenomenological effects are determined.

### 4.4.1 Radiative Electroweak Symmetry Breaking

A highly attractive feature of SUGRA GUTs is the origin of electroweak symmetry breaking. While in the SM, the Higgs mechanism is the result of inserting a negative mass-squared into the Higgs potential to precipitate the breaking, in SUGRA GUTs the process emerges due to radiative corrections [70–72]. In fact, it is the breaking of supersymmetry itself, at the Planck scale that causes the radiative corrections that break electroweak symmetry.

Taking $V_H = V_0 + \Delta V_1$ to be the Higgs potential, tree-level plus loop-correction, one finds

$$V_0 = m^2_{H_u}|H_u|^2 + m^2_{H_d}|H_d|^2 + \mu B_0(H_u H_d + \text{ H.c.}) + \frac{1}{8}(g^2 + g'^2)(|H_u|^2 + |H_d|^2)^2 \tag{4.22}$$

and at the 1-loop level [73, 74]

$$\Delta V_1 = \frac{1}{64\pi^2}\sum_a (-1)^{2s_a} n_a M_a^4 \ln\left[\frac{M_a^2}{e^{3/2}Q^2}\right] \tag{4.23}$$

where for some particle labeled by $a$, $M_a$ is its tree-level mass, $s_a$ its spin, and $n_a$ the number of its helicity states. The running scale is indicated at $Q$.

As there are now two Higgs fields that shall have VEVs, it is convenient to define an angle to parametrize their ratio by

$$v_u \equiv \langle H_u \rangle \,,\, v_d \equiv \langle H_d \rangle \,, \text{ and } \tan\beta \equiv \frac{v_u}{v_d} \,. \tag{4.24}$$

Due to the presence of new scalars (with respect to the SM), constraints are established on the soft parameters by requiring that QED and QCD remain unbroken. The minimization conditions which require $\partial V_h/\partial v_i = 0$, with $i = u, d$ gives two relations

$$\sin 2\beta = \frac{2\mu B_0}{2|\mu|^2 + \bar{m}^2_{H_u} + \bar{m}^2_{H_d}} \tag{4.25}$$

$$\mu^2 + \frac{1}{2}M_Z^2 = \frac{\bar{m}^2_{H_d} - \bar{m}^2_{H_u}\tan^2\beta}{\tan^2\beta - 1} \,. \tag{4.26}$$

In the above, $\bar{m}_{H_i}$ is the loop-corrected mass of $H_i$. These relations allow us to determine $B_0$ and $\mu$. However, the sign of $\mu$ remains undetermined as it only enters into the constraints as $\mu^2$. Additionally, we are left with the new parameter $\tan\beta$.

These means that our SUGRA GUT formalism has led us to a model with 4 parameters and 1 sign

$$m_0,\ m_{1/2},\ , A_0,\ \tan\beta,\ \mathrm{sgn}\,(\mu)\ . \tag{4.27}$$

This model is referred to as mSUGRA–the minimal supergravity model.

### 4.4.2 Sparticle Masses

The mass matrices of the sfermions can be more or less read off directly from $\mathcal{L}_{\text{soft}}$, as there is only L-R mixing. The Higgs sector and the gaugino sector are not as straightforward, as the Higgs potential must be minimized for EWSB, and there is mixing between gauginos and Higgsinos.

In the Higgs sector, there are 5 massive Higgs bosons after EWSB, $h^0$, $H^0$, $A^0$, and $H^\pm$. The two neutral CP-even bosons are $h^0$, and $H^0$ where the mass of $h^0$ is lower than that of $H^0$. The other neutral Higgs boson $A^0$ has odd CP-parity. Finally, we have the charged Higgs $H^\pm$. At tree-level there masses are

$$m^2_{h,H} = \frac{1}{2}\left(m^2_A + M^2_Z \mp \sqrt{(m^2_A - M^2_Z)^2 + 4M^2_Z m^2_A \sin^2 2\beta}\ \right) \tag{4.28}$$

$$m^2_A = 2|\mu|^2 + m^2_{H_u} + m^2_{H_d} \tag{4.29}$$

$$m^2_{H^\pm} = m^2_A + M^2_W\,. \tag{4.30}$$

An important result from the Higgs boson mass formulae is that lighter CP-even neutral Higgs, $h^0$, behaves very similarly to lone Higgs boson of the Standard Model. Further, the mass of $h^0$ at tree-level does not exceed $M_Z$ and in fact, without additional structure, there is an upper limit of roughly 130 GeV on the mass of $h^0$ in SUSY. This is phenomenologically crucial and will be studied more carefully in Chapter 8 and Chapter 9.

The gauginos and the Higgsinos mix to form mass eigenstates, with the exception of the color-octet gluinos. They mix with neither the other gauginos nor the Higgsinos, and have mass $M_3$. Discounting the gluinos, the electrically neutral gauginos and Higgsinos mix to create a $4 \times 4$ symmetric mass matrix for the "neutralinos", $\tilde{\chi}_i^0$, in the basis $(\tilde{B}^0, \tilde{W}^0, \tilde{H}_d^0, \tilde{H}_u^0)$:

$$M_{\tilde{\chi}^0} = \begin{pmatrix} M_1 & \cdot & \cdot & (\text{sym.}) \\ 0 & M_2 & \cdot & \cdot \\ -\frac{g' v_d}{\sqrt{2}} & \frac{g v_d}{\sqrt{2}} & 0 & \cdot \\ \frac{g' v_u}{\sqrt{2}} & -\frac{g v_u}{\sqrt{2}} & -\mu & 0 \end{pmatrix} . \tag{4.31}$$

The charged gauginos and Higgsinos create the mass matrix for the "charginos", $\tilde{\chi}^{\pm}$, in the basis $(\tilde{W}^{\pm}, \tilde{H}^{\pm})$:

$$M_{\tilde{\chi}^{\pm}} = \begin{pmatrix} M_2 & g_2 v_2 \\ g_2 v_1 & \mu \end{pmatrix} . \tag{4.32}$$

At the tree-level, we can obtain from these mass matrices sum rules for the squared masses of the neutralinos and charginos

$$m^2_{\tilde{\chi}^0_1} + m^2_{\tilde{\chi}^0_2} + m^2_{\tilde{\chi}^0_3} + m^2_{\tilde{\chi}^0_4} - 2M_Z^2 = \mu^2 + M_1^2 M_2^2 \tag{4.33}$$

$$m^2_{\tilde{\chi}^{\pm}_1} + m^2_{\tilde{\chi}^{\pm}_2} - 2M_W^2 = \mu^2 + M_2^2 . \tag{4.34}$$

These equations are quite useful as the charginos and neutralinos do not receive large loop corrections to their masses.

# Chapter 5

# First LHC Searches for Supersymmetry

## 5.1 Introduction

In this chapter, the first searches [75–77] by CMS and ATLAS for supersymmetric particles are considered in the context of the mSUGRA model. The experimental collaborations have used $35\,\mathrm{pb}^{-1}$ of integrated luminosity in p on p collisions at the LHC, operating at $\sqrt{s} = 7\,\mathrm{TeV}$, to provide limits on mSUGRA in the $m_0$–$m_{1/2}$ plane, fixing the other parameters. Remarkably, the limits have immediately surpassed those set by DØ and CDF at the Tevatron [78].

We begin by reproducing the expected limits as given by CMS and ATLAS using Monte Carlo event generation for the signal (supersymmetric) processes, and a simulation of the detector response. Expected limits are then determined by supposing that the number of observed events in the defined signal regions are exactly equal to the expected background (Standard Model) yield, based on our own simulations [79–81]. We next determine how the limits are expected to change if the parameters $A_0$ and $\tan\beta$ are adjusted. Then, we will use other constraints on the mSUGRA parameter space arising from high-precision flavor physics experiments and the measured relic density of dark matter to view

the impact of the LHC searches on global fits to mSUGRA. In this larger context, we will discuss the naturalness of mSUGRA.

## 5.2 Reach plots with 35 pb$^{-1}$ of integrated luminosity

The ATLAS collaboration has released two analyses, one with 1 lepton [76] and the other with 0 leptons [77] both of which are considered in our analysis. For the 1 lepton analysis we follow the selection requirements that ATLAS reports in [76]. The pre-selection requirements for events are that a jet must have $p_T > 20\,\text{GeV}$ and $|\eta| < 2.5$, electrons must have $p_T > 20\,\text{GeV}$ and $|\eta| < 2.47$ and muons must have $p_T > 20\,\text{GeV}$ and $|\eta| < 2.4$. Further, we veto the "medium" electrons[1] in the electromagnetic calorimeter transition region, $1.37 < |\eta| < 1.52$. An event is considered if it has a single lepton with $p_T > 20\,\text{GeV}$ and its three hardest jets have $p_T > 30\,\text{GeV}$, with the leading jet having $p_T > 60\,\text{GeV}$. The distance, $\Delta R = \sqrt{(\Delta\eta)^2 + (\Delta\phi)^2}$, between each jet with the lepton must satisfy $\Delta R\,(j_i, \ell) > 0.4$, and events are rejected if the reconstructed missing energy, $\not{E}_T$, points in the direction of any of the three leading jets, $\Delta\phi\,(j_i, \not{E}_T) > 0.2$. Events are then classified into 2 channels, depending on whether the lepton is a muon or an electron. These are then further classified into four regions based on the missing energy and $m_T$ cuts, where we reconstruct the missing transverse momentum using the selected lepton plus jets with $p_T > 20\,\text{GeV}$ and $|\eta| < 4.9$ following ATLAS analysis, and $m_T = \sqrt{2p_T(\ell)\not{E}_T\left(1 - \cos\left(\Delta\phi\left(\ell, \not{E}_T\right)\right)\right)}$ is the transverse mass between the lepton and the missing transverse momentum vector. The four regions alluded to above are labeled the "signal region", the "top region", the "W region" and the "QCD region". For the "signal region" events were required to pass the additional cuts of $m_T > 100\,\text{GeV}$, $\not{E}_T > 125\,\text{GeV}$, $\not{E}_T > 0.25 M_{\text{eff}}$ and $M_{\text{eff}} > 500\,\text{GeV}$. Here the effective mass, $M_{\text{eff}}$, is the scalar sum of the missing energy with the $p_T$'s of the selected visible objects (in this case the lepton and the 3 jets). The number of events were then compared to the 95% CL

[1] See [82] for a definition of "loose", "medium" and "tight" electrons

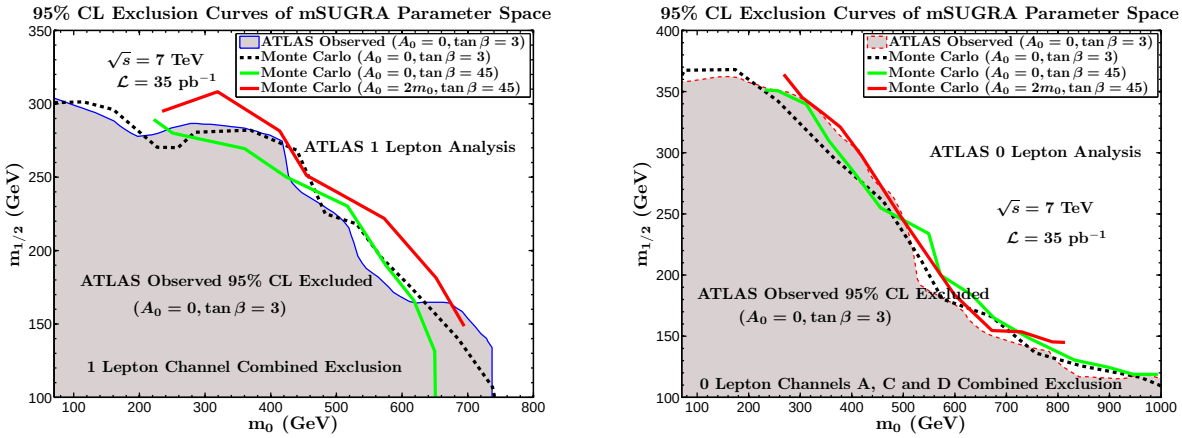


Figure 5.1: Left: Reach plot with 35 pb$^{-1}$ of integrated luminosity using the ATLAS cuts [76] [77] with different $\tan\beta$ and $A_0$: $A_0 = 0$ and $\tan\beta = 3$ (dashed line); $A_0 = 0$ and $\tan\beta = 45$ (solid green line); $A_0 = 2m_0$ and $\tan\beta = 45$ (solid red line). For comparison we give the ATLAS observed limit ($A_0 = 0$ and $\tan\beta = 3$) (solid blue line). Right: Reach plot with 35 pb$^{-1}$ of integrated luminosity of data using the ATLAS 0 lepton cuts. For comparison we give the ATLAS observed limit (red dashed line).

upper bounds that ATLAS found ($N_e < 2.2$ events and $N_\mu < 2.5$ events) [76]. The "top region" and "W region" are defined by events with $30\,\text{GeV} < \not{E}_T < 80\,\text{GeV}$ and $40\,\text{GeV} < m_T < 80\,\text{GeV}$, where the "top region" requires at least one of the three hardest jets to be b-tagged and the "W region" requires none of the three hardest jets to be b-tagged. The "QCD region" was required to have $m_T, \not{E}_T < 40\,\text{GeV}$ and was purely data driven. For our analysis events were rejected if they contaminated the three control regions. Using the standard model background from [80] we reproduced the ATLAS results.

For the 0 lepton analysis we follow the selection requirements that ATLAS reports in [77] where the pre-event selection is the same as for the 1 lepton case except that leptons are identified to have $p_T > 10\,\text{GeV}$. Here the events are classified into 4 regions "A", "B", "C" and "D"; where regions A and B have at least 2 jets and regions C and D have at least 3 jets. When referring to different cuts in these regions we define cuts on the "selected" jets to mean that the bare minimum number of jets in this region must satisfy the following requirement: For regions A and B "selected" jets mean that they are

the first two hardest jets and for regions C and D "selected" jets mean that they are the first three hardest jets. Events are required to have $\not{E}_T > 100\,\text{GeV}$ and the selected jets must each have $p_T > 40\,\text{GeV}$ with the leading jet $p_T > 120\,\text{GeV}$. As in the case with 1 lepton, events are rejected if the missing energy points in the direction of any of the selected jets, $\Delta\phi\,(j_i, \not{E}_T) > 0.4$, where $i$ is over the selected jets. Region A requires events to have $\not{E}_T > 0.3M_{\text{eff}}$ and $M_{\text{eff}} > 500\,\text{GeV}$ and regions C and D require events to have $\not{E}_T > 0.25M_{\text{eff}}$ with region C requiring $M_{\text{eff}} > 500\,\text{GeV}$ and region D requiring $M_{\text{eff}} > 1\,\text{TeV}$. In this case $M_{\text{eff}}$ is defined in terms of selected jets, i.e. for regions A and B it is the scalar sum of the first two hardest jets and for regions C and D it is the scalar sum of the first three hardest jets. For the analysis here we do not apply the cut for region B, i.e. $m_{T\,2} > 300\,\text{GeV}$, since the models excluded in this region are already excluded in region D [83].

Following the framework of the ATLAS Collaboration [76] we have carried out a set of three parameter sweeps in the $m_0$–$m_{1/2}$ plane taking $m_{1/2} \leqslant 500\,\text{GeV}$ and $m_0 \leqslant 1\,\text{TeV}$. Two of the parameter sweeps were a $10\,\text{GeV} \times 10\,\text{GeV}$ grid scan in the $m_0$–$m_{1/2}$ plane having a fixed universal trilinear parameter, $A_0 = 0$, and fixed $\tan\beta$; one set with $\tan\beta = 3$ and the other with $\tan\beta = 45$. A third parameter scan was done with $A_0 = 2m_0$ and $\tan\beta = 45$. Throughout the analysis we take $\mu > 0$ and $m_{\text{top}}^{\text{pole}} = 173.1\,\text{GeV}$. For the simulation of the mSUGRA models, renormalization group evolution and computation of the physical masses of the sparticles was performed using SuSpect [84] and we implement both MadGraph and PYTHIA for event generation [85, 86]. A comparison of our reach to the reach done by the ATLAS Collaboration is shown in Fig. 5.1.

In Fig. 5.2 we plot the number of signal events for electrons in the $m_0$–$m_{1/2}$ plane where the reach plot from ATLAS is also exhibited and where the ATLAS reach plot corresponds to the number of observed events and those that have a larger number predicted by the model. For the 1 lepton analysis, we first present the models excluded by the muon channel, colored by $N_{\text{events}}^{\mu}$ (indicated by squares). Next, we overlay from the remaining models, those that have been excluded by the electron channel,

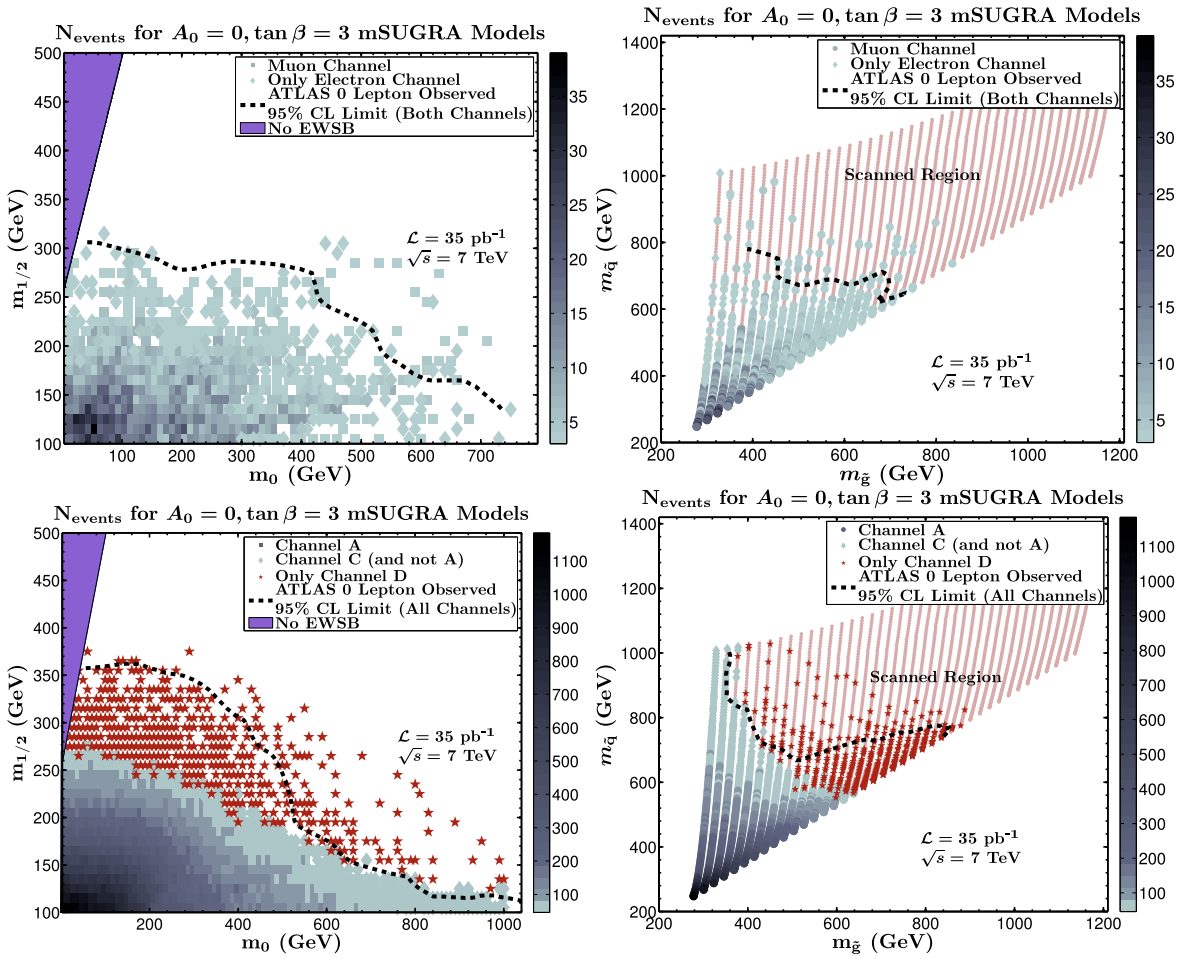


Figure 5.2: Top left panel: Number of signal events in the $m_0$–$m_{1/2}$ plane for the case $A_0 = 0$, $\tan\beta = 3$ using the 1 lepton ATLAS cuts in the $m_0$–$m_{1/2}$ plane. The dark areas correspond to number of events greater than 2 with the actual numbers indicated along the vertical line to the right while the white areas are filled with models but have number of events less than 2. Top right panel: Same as the left panel except that the plot is $m_{\tilde{g}}$ (gluino)–$m_{\tilde{q}}$ (squark) mass plane for the lightest squark of the first 2 generations. The square region in the left panel becomes squeezed into the polygon-like region in the physical mass plane in the right panel. One may note that the ATLAS constraints do not rule out a low mass gluino on the scale of order 400 GeV for heavy squarks. Bottom left panel: The same as the top left panel except that the analysis is done using 0 lepton ATLAS cuts. Bottom right panel: Same as the top right panel except that the analysis is done using the 0 lepton ATLAS cuts. The (red) stars correspond to channel D. In channel D we find maximally 51 events over the space scanned after a requirement that the number of events be at least 15 before cuts. However, when only considering models not already excluded by channels A and C, the number of events in channel D is maximally 18.

and colored by $N^{e}_{\text{events}}$ (indicated by diamonds). Similarly for the 0 lepton analysis, we begin with models excluded by channel A, colored by $N^{A}_{\text{events}}$ (indicated by squares); overlay models excluded by C (but not A) and colored by $N^{C}_{\text{events}}$ (indicated by diamonds). Next, we overlay models excluded by channel D alone in a single color (stars), as $N^{D}_{\text{events}}$ are not comparable with $N^{A}_{\text{events}}$ or $N^{C}_{\text{events}}$. We also show the number of signal events for electrons in the $m_{\tilde{g}}$–$m_{\tilde{q}}$ plane. An ATLAS reach curve is also exhibited.

The upper left panel of Fig. 5.2 gives us a more quantitative description of the electron and muon channels in putting constraints on the $m_0$–$m_{1/2}$ parameter space with 35 $\text{pb}^{-1}$ of data. As expected the largest number of single $e$ and $\mu$ events arise at low mass scales, i.e., for low values of $m_0$ and of $m_{1/2}$ and the number of signal events decrease and we approach the boundary after which they fall below 2 for the 1 lepton ATLAS analysis. It is also instructive to examine the signal events in the gluino-squark mass plane where the squark mass corresponds to the average first two generation squark mass. This is done in the upper right panel of Fig. 5.2. Here the polygon shape of the region is a simple mapping of the allowed parameter in the $m_0$–$m_{1/2}$ plane of the upper left panel. The plot is useful as it directly correlates squark and gluino model points that are either excluded or allowed by the 1 lepton ATLAS analysis. The 0 lepton analysis of the lower panels in Fig. 5.2 is very similar to the analysis of the upper panels except for different array of cuts. There is a general consistency in the analysis of the 1 lepton and the 0 lepton analysis, although the 0 lepton cuts appear more constraining as they appear to exclude a somewhat larger region of the parameter space. Together the analysis of the upper and lower panels of Fig. 5.2 gives us a more analytical understanding of the relative strengths of the 1 lepton and 0 lepton cuts.

## 5.3 Implications of Constraints

In the analysis of the reach plots experimental constraints were not imposed beyond those that arise from the ATLAS analyses. Next we include these constraints and in our analysis we will consider the larger parameter space when all four parameters $m_0$, $m_{1/2}$, $A_0$, $\tan\beta$ are varied. In doing so, we apply various constraints from searches on the sparticle mass limits, B-physics and from $g_\mu - 2$. Next we explore the constraint from upper bound on the relic density from WMAP only, and then with combination of all of the above. These indirect constraints were calculated using MICROMEGAs [87], with the Standard Model contribution in the $\mathcal{B}r(b \to s\gamma)$ corrected using the NNLO analysis of Misiak *et al.* [88, 89]. We now describe this more general analysis. In the upper left panel of Fig. 5.3 we apply the following "collider/flavor constraints" [90] $m_{h^0} > 93.5$ GeV, $m_{\tilde{\tau}_1} > 81.9$ GeV, $m_{\widetilde{\chi}_1^\pm} > 103.5\,\text{GeV}$, and $m_{\tilde{t}_1} > 100$ GeV, along with $(-11.4 \times 10^{-10}) \leqslant \delta\left(g_\mu - 2\right) \leqslant (9.4 \times 10^{-9})$, see [91], $\mathcal{B}r\left(B_s^0 \to \mu^+\mu^-\right) \leqslant 4.7 \times 10^{-8}$ (90 % C.L.) [92], and $(2.77 \times 10^{-4}) \leqslant \mathcal{B}r(b \to s\gamma) \leqslant (4.27 \times 10^{-4})$ [93]. These collider/flavor constraints by themselves have an effect, but the effect is quite small in terms of reducing the density of models that are already constrained by the ATLAS results.

We note that our scans of the parameter are very dense with $10^6$ models after EWSB alone. In the $m_0$–$m_{1/2}$ plane the collider/flavor cuts eliminate 12% of the models. However because $A_0$ and $\tan\beta$ are not fixed to specific values, but are allowed to run over their full natural ranges, a model point which is eliminated for say, large $\tan\beta$ by $b \to s\gamma$ or $B_s^0 \to \mu^+\mu^-$ at a specific point in the $m_0$–$m_{1/2}$ plane can correspond to a model point with a smaller value of $\tan\beta$ for the same $(m_0, m_{1/2})$ which is not eliminated. Thus the $m_0$–$m_{1/2}$ plane appears densely filled. This is contrary to what one would observe for fixed values of $(A_0, \tan\beta)$. For example, for $(A_0, \tan\beta) = (0, 45)$ the $b \to s\gamma$ constraint would remove models at large $m_0$ up to close to 2 TeV and $m_{1/2}$ up to about 750 GeV. As another example, for $(A_0, \tan\beta) = (0, 3)$ (the space looked at by ATLAS, and in the previous section) a strict limit of $m_{h^0} < 102\,\text{GeV}$ for light CP even Higgs removes all model points below the ATLAS limits. However

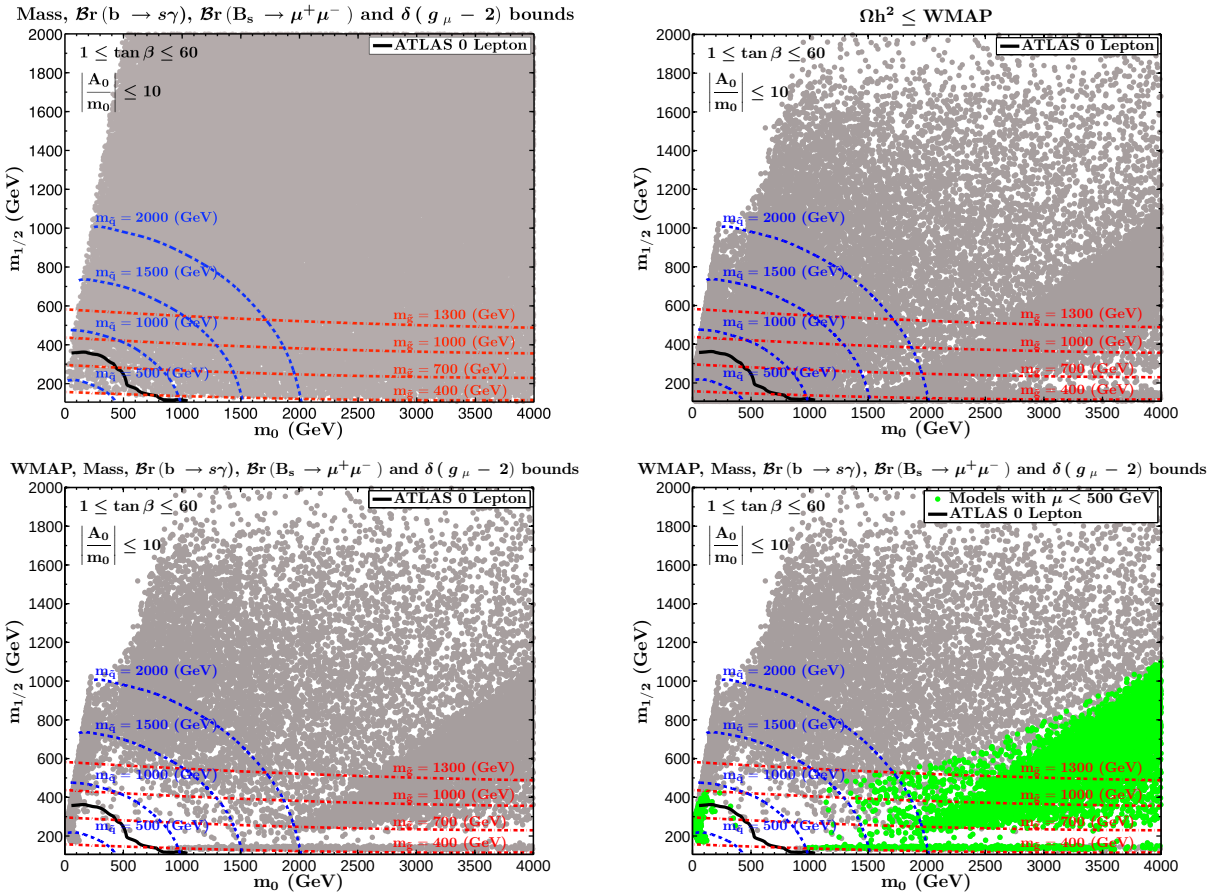


Figure 5.3: Upper left panel: An exhibition of the allowed models indicated by grey (dark) dots in the $m_0$–$m_{1/2}$ plane when only flavor and collider constraints are imposed. The region excluded by ATLAS (as well as CMS) lies below the thick black curve in the left hand corner. Upper right panel: same as the left upper panel except that only an upper bound on relic density of $\Omega h^2 \leqslant 0.14$ is imposed. Lower left panel: Same as the upper left panel except that the relic density constraint as in the upper right panel is also applied. This panel exhibits that most of the parameter space excluded by ATLAS is already excluded by the collider/flavor and relic density constraints. The dark region below the ATLAS curve is the extra region excluded by ATLAS which was not previously excluded by the indirect constraints. Lower right panel: The analysis of this figure is similar to the lower left panel except that models with $|\mu| < 500$ GeV are exhibited in green.

because one is varying $(A_0, \tan\beta)$ the area below the ATLAS limit is filled in this case.

Continuing on we next consider the "cosmological constraint" in the upper right panel of Fig. 5.3 where we apply only an upper bound on the relic density of the thermally produced neutralino dark

matter of $\Omega h^2 \leqslant 0.14$ [94, 95]. The WMAP upper bound constraint removes 96.5% of the models alone, thus this cosmological constraint is very severe eliminating a large fraction of models, but again the ATLAS constraints remain quite strong.

Next we consider the "combined collider/flavor and cosmological constraints" and find that together these constraints are generally much more severe than the ATLAS constraints. This is shown in the lower left panel of Fig. 5.3. Here models that were separately allowed by previously known collider/flavor constraints, and models that were separately allowed by just the upper bound from WMAP, are now eliminated under the imposition of the combined constraints. There is, however, a new region that ATLAS appears to exclude above and beyond what the indirect constraints exclude and this region is a region for low $m_0$ and for $m_{1/2}$ around 350 GeV. Thus it would require a larger integrated luminosity to move past the barren region, which is above the ATLAS bound, to get into the fertile region of the parameter space, where the fertile region is the area above the white patch in the lower panel of Fig. 5.3.

Finally in lower right panel of Fig. 5.3 we show the value of $\mu$ (at the electroweak symmetry breaking scale) in the $m_0$–$m_{1/2}$ plane where $\mu$ is the Higgsino mass parameter that enters in the Higgs bilinear term in the superpotential. The analysis is given under the "combined constraints" discussed in the lower left panel of Fig. 5.3. We note that essentially all of the natural region of the parameter space corresponding to small $\mu$, most of which lies close to the hyperbolic branch (Focus point) (HB/FP) [96–98] of radiative breaking of the electroweak symmetry or near the vicinity of the light CP even Higgs pole region [99] remains untouched by the CMS and LHC exclusion limits as illustrated in the lower right panel of Fig. 5.3 and remains to be explored. Further, as pointed out in [100], low mass gluinos as low as even 420 GeV in mSUGRA are allowed for the region for large $m_0$ where relic density can be satisfied on the light CP even Higgs pole [99]. This can be seen from Fig. 5.3 as the gluino and squark masses are exhibited in the plots. Along the Higgs pole region, electroweak symmetry breaking can also be natural, i.e., one has a small $\mu$. It is also seen that this region is not constrained by CMS and

ATLAS since their limits taper off at large $m_0$ as $m_{squark}$ gets heavy and the jets from squark production are depleted (see [100]).

## 5.4 Conclusion

The CMS and ATLAS analyses on the search for supersymmetry are impressive in that with only 35 $pb^{-1}$ of data their reach plots already exceed those from CDF and DØ experiments at the Tevatron. Both CMS and ATLAS have given reach plots in the $m_0$–$m_{1/2}$ plane for the case $A_0 = 0, \tan\beta = 3$ with the ATLAS analysis presenting more stringent limits compared to CMS. Because of the more stringent limits from ATLAS we adopted the ATLAS cuts in our analysis presented in this work. In our analysis we find consistency with the 1 lepton and 0 lepton results of ATLAS for the case analyzed by ATLAS, i.e., $A_0 = 0, \tan\beta = 3$. We have also investigated reach plots for other values of $A_0, \tan\beta$, i.e., $A_0 = 0, \tan\beta = 45$ and $A_0 = 2, \tan\beta = 45$. Another interesting question explored in this work is a relative study of the constraints on the $m_0$–$m_{1/2}$ parameter space by the CMS and ATLAS experiments vs the constraints that arise from Higgs mass limits, flavor physics, and from the dark matter constraints from WMAP. One finds that the current CMS and ATLAS limits are consistent with such constraints. Specifically a significant part of the parameter space excluded by the CMS and ATLAS 35 $pb^{-1}$ data is already excluded by the indirect constraints. We emphasize that low gluino masses (even as low as 400 GeV) remain unconstrained in mSUGRA, and this conclusion holds generically for other high scale models of soft breaking, for the case when the squark masses are significantly larger than the gluino mass. Of interest to the model at hand, is that such situation arises on the hyperbolic branch of radiative breaking of the electroweak symmetry where typically $\mu$ is relatively small, and the region is very dense in the allowed set of parameter points.

# Chapter 6

# First Searches for Neutralino Dark Matter at the LHC

## 6.1 Introduction

In this chapter, constraints on dark matter from the first CMS and ATLAS SUSY searches are investigated. It is shown that within the minimal supergravity model, the early search for supersymmetry at the LHC has depleted a large portion of the signature space in dark matter direct detection experiments. In particular, the prospects for detecting signals of dark matter in the XENON and CDMS experiments are significantly affected in the low neutralino mass region. Here the relic density of dark matter typically arises from slepton co-annihilations in the early universe. In contrast, it is found that the CMS and ATLAS analyses leave untouched the Higgs pole and the Hyperbolic Branch/Focus Point regions, which are now being probed by the most recent XENON results. Analysis is also done for supergravity models with non-universal soft breaking where one finds that a part of the dark matter signature space depleted by the CMS and ATLAS cuts in the minimal SUGRA case is repopulated. Thus, observation

of dark matter in the LHC depleted region of minimal supergravity may indicate non-universalities in soft breaking.

CMS and ATLAS have recently reported their first results for supersymmetry searches [75–77] and have put new constraints on the parameter space of the $\mathcal{N} = 1$ supergravity unified model [51, 52] which, with universal boundary conditions on the soft breaking parameters at the unification scale, is the model mSUGRA [51–53, 101]. In a subsequent work [102], the implications of the CMS and ATLAS searches on the mSUGRA parameter space was analyzed in the context of indirect constraints from LEP and Tevatron searches, from the Brookhaven $g_\mu - 2$ experiment, from FCNC constraints in B-physics, i.e., $b \to s\gamma$ and $B_s^0 \to \mu^+\mu^-$ and from WMAP.

In this chapter, we analyze the impact of the first results from CMS and ATLAS SUSY searches on the direct detection of dark matter [103–107]. It is found that the LHC results have a large impact on the signature space available for the low mass slepton co-annihilation region, depleting a significant region where direct detection experiments are sensitive to detecting a signal. Thus, we explore the effect of the recent LHC data on the prospects for directly detecting cold dark matter in experiments such as XENON and CDMS in supergravity unified models. We will discuss both minimal supergravity models, and SUGRA models with non-universal soft breaking terms at the grand unification scale.

For completeness, we begin with a brief summary of the independent parameters generated by softly broken supergravity theories which are needed to test such models at colliders and in dark matter experiments. The conditions under which the soft breaking in the minimal supergravity model are derived are summarized as follows: (i) supersymmetry is broken through a super Higgs effect giving mass to the gravitino through the presence of a hidden sector (singlet); (ii) the hidden and the visible interact only gravitationally; (iii) the Kähler potential is generation independent; (iv) the gauge kinetic function is minimally linear in the hidden sector singlet. This then gives rise to soft terms of the

form [51, 52]

$$L_{soft} = -\frac{1}{2}(M_a \lambda^a \lambda^a + \text{ H.c.}) - m_\alpha^2 C^{*\alpha} C^\alpha - \left(\frac{1}{6} A_{\alpha\beta\gamma} Y_{\alpha\beta\gamma} C^\alpha C^\beta C^\gamma + \mu B_0 H_1 H_2 + \text{ H.c.}\right) \quad (6.1)$$

where $\lambda^a$ are the gauginos, $H_{i=1,2}$ are Higgs doublets, and $C^\alpha$ are the slepton, squark and Higgs fields of the minimal supersymmetric standard model. For the case of universal boundary conditions at the unification (GUT) scale, $m_\alpha = m_0$ is the universal scalar mass, $M_a = m_{1/2}$ is the universal gaugino mass, $A_{\alpha\beta\gamma} = A_0$ is the universal trilinear coupling, and $B_0\mu$ is the bilinear coupling where $\mu$ is the Higgs mixing parameter that enters the superpotential in the form $\mu H_1 H_2$ (all at the GUT scale). Thus, the minimal supergravity models are specified by the following set of GUT scale parameters $(m_0, m_{1/2}, A_0, B_0, \mu)$. The renormalization group improved scalar potential at the electroweak symmetry breaking scale Q is given by

$$V = m_1^2|H_1|^2 + m_2^2|H_2|^2 + \mu B_0(H_1 H_2 + h.c.) + \frac{(g_2^2 + g_Y^2)}{8}(|H_1|^2 - |H_2|^2)^2 + \Delta V_1, \quad (6.2)$$

$$\Delta V_1 = \frac{1}{64\pi^2} \sum_a (-1)^{2s_a}(2s_a + 1) M_a^4 \left[\ln \frac{M_a^2}{Q^2} - \frac{3}{2}\right], \quad (6.3)$$

where the term $\Delta V_1$ is the one loop correction to the effective potential in the MSSM [97, 108, 109], and $s_a$ is the spin of particle a. The gauge couplings are subject to boundary conditions at the unification scale $\alpha_2(0) = \alpha_G = \frac{5}{3}\alpha_Y(0)$, while if the soft parameters are universal one has $m_i^2(0) = m_0^2 + \mu^2$, $i = 1, 2$. The breaking of electroweak symmetry occurs when (a) the determinant of the Higgs squared-mass matrix turns negative and (b) the potential is bounded from below; i.e. (a) $m_1^2 m_2^2 + (\mu B_0)^4 < 0$, and (b) $m_1^2 + m_2^2 - 2|\mu B_0^2| > 0$. Minimization of the potential then yields the following relations (I) $M_Z^2 = 2(\mu_1^2 - \mu_2^2 \tan^2\beta)(\tan^2\beta - 1)^{-1}$ and (II) $\sin 2\beta = 2(\mu B_0)(m_1^2 + m_2^2)^{-1}$, where $\mu_i^2 = m_i^2 + \Sigma_i$, where $\Sigma_i$ are the loop corrections [97, 109]. Here $\tan\beta = v_2/v_1$ is the ratio of the Higgs VEVs. (I) can be used to fix $\mu$ using the experimental value of $M_Z$, and the constraint (II) can be used to eliminate $B_0$

in favor of $\tan\beta$. The supergravity model at low energy can then be parametrized by [101]

$$m_0,\ m_{1/2},\ A_0,\ \tan\beta,\ \mathrm{sgn}(\mu)\ . \tag{6.4}$$

After specifying the high scale soft breaking parameters, one implements renormalization group analysis (see [110] for the two loop analysis) and is then able to predict all 32 sparticles masses as well as their couplings and interactions. The full analysis can be done using SuSpect [84].

## 6.2 ATLAS and CMS Constraints on Dark Matter Direct Detection in minimal Supergravity

We discuss now the implications of ATLAS and CMS results on dark matter. SUGRA models predict a dark matter candidate which over much of the parameter space is the lightest neutralino, the lightest (R-parity odd) superpartner (LSP). The LSPs are traveling with non relativistic speed order $0.001c$ in the galactic halo. This then translates into the fact that their momentum transfer is very small (order 100 MeV for LSP masses of order 100 GeV) in collisions with nuclei in a terrestrial detector. As such, the relevant interactions for the direct detection of LSP dark matter is calculated in the limit of zero momentum transfer in collisions with nuclei. For SUGRA models the interaction Lagrangian is given by [113–116]

$$\mathcal{L} = \bar{\chi}\gamma^\mu\gamma^5\chi\bar{q}_i\gamma_\mu(\alpha_{1i}+\alpha_{2i}\gamma^5)q_i + \alpha_{3i}\bar{\chi}\chi\bar{q}_i q_i + \alpha_{4i}\bar{\chi}\gamma^5\chi\bar{q}_i\gamma^5 q_i + \alpha_{5i}\bar{\chi}\chi\bar{q}_i\gamma^5 q_i + \alpha_{6i}\bar{\chi}\gamma^5\chi\bar{q}_i q_i\ . \tag{6.5}$$

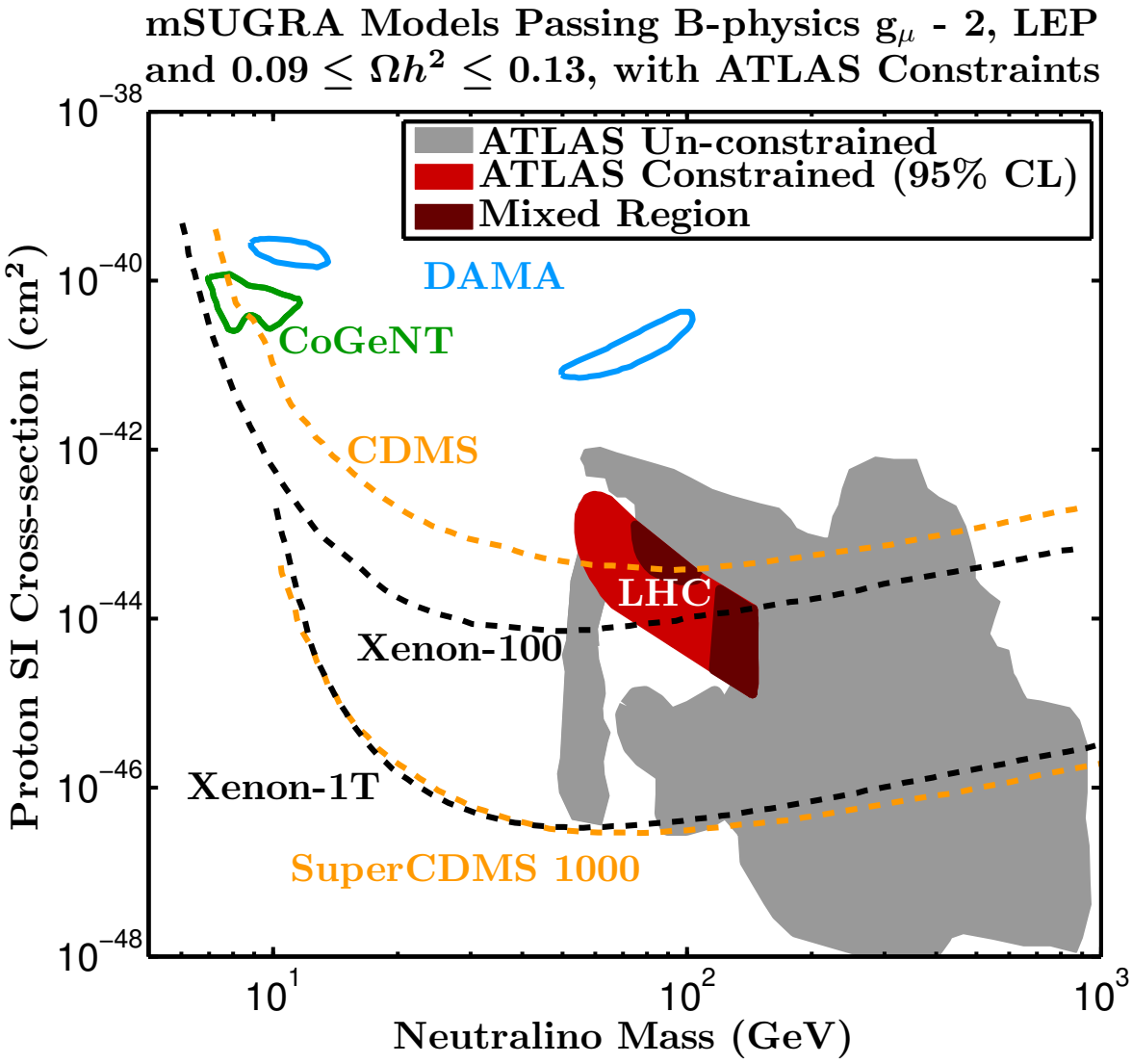


Figure 6.1: A plot of spin independent neutralino-proton cross section vs neutralino mass for mSUGRA under experimental constraints. The search for supersymmetry at LHC with 35 pb$^{-1}$ luminosity has excluded a significant number of models in this signature space which are marked by red color. In the red region, all the models in our scans have been constrained by the ATLAS search, while in the mixed region (maroon), about 60% of the models in our scans are constrained by the ATLAS search. Both the red and maroon regions satisfy the WMAP constraints. We also display the present CDMS [106, 107] and XENON-100 [103–105] curves as well as the future projected experimental curves [111, 112].

The spin independent (SI) cross section for neutralinos scattering elastically off target nuclei is mostly governed by the operator $\alpha_{3i}\bar{\chi}\chi\bar{q}_i q_i$. For heavy nucleus targets, the SI cross section add up coherently

$$\sigma_{\chi T} = \frac{4\mu_{\chi T}^2}{\pi}(Zf_p + (A-Z)f_n)^2 \,, \tag{6.6}$$

where $\mu_{\chi T}$ is the reduced mass of the neutralino and the target system, and $(Z, A)$ are the atomic (number, mass) of the nucleus. The interactions between the LSP and the target nuclei occur dominantly via t-channel CP-even Higgs exchange, and s-channel squark exchange. The relevant interactions are given in terms of

$$f_{p/n} = \sum_{q=u,d,s} f_{T_q}^{(p/n)} a_q \frac{m_{p/n}}{m_q} + \frac{2}{27} f_{TG}^{(p/n)} \sum_{q=c,b,t} a_q \frac{m_{p/n}}{m_q} \,. \tag{6.7}$$

Here $f_{T_u}^{(p/n)}$, $f_{T_d}^{(p/n)}$, $f_{T_s}^{(p/n)}$ are the nucleon parameters which can be obtained from the measurements of the pion-nucleon sigma term, and $f_{TG}^{(p/n)} \equiv 1 - f_{T_u}^{(p/n)} - f_{T_d}^{(p/n)} - f_{T_s}^{(p/n)}$. Numerical values and further details are given in, for example, in Ref. [87]. The spin independent cross section depends sensitively on LSP neutralino decomposition in terms of its Bino, Wino and Higgsino eigen-components $((\tilde{B}, \tilde{W}^3) \equiv (\lambda_Y, \lambda^3))$

$$\chi \equiv \chi_1^0 = n_{11}\tilde{B} + n_{12}\tilde{W}^3 + n_{13}\tilde{H}_1 + n_{14}\tilde{H}_2 \,. \tag{6.8}$$

The relevant couplings that enter in the spin independent cross section are [113–116]

$$\begin{aligned} a_q \equiv a_{3i} = &-\frac{1}{2\left(m_{1i}^2 - m_\chi^2\right)} \Re\left[(X_i)\,(Y_i)^*\right] - \frac{1}{2\left(m_{2i}^2 - m_\chi^2\right)} \Re\left[(W_i)\,(V_i)^*\right] \\ &- \frac{g_2 m_q}{4 m_W B}\left[\Re\left(\delta_1[g_2 n_{12} - g_Y n_{11}]\right) DC\left(-\frac{1}{m_H^2} + \frac{1}{m_h^2}\right)\right. \\ &\left. + \Re\left(\delta_2[g_2 n_{12} - g_Y n_{11}]\right)\left(\frac{D^2}{m_h^2} + \frac{C^2}{m_H^2}\right)\right] \,. \end{aligned} \tag{6.9}$$

Here the various quantities $X_i, Y_i, W_i$ etc. are defined in [113–116], where the full forms of $a_q$ can also be found. The first two terms arise from squark $(m_{1i}, m_{2i})$ exchange while the remaining terms arise from Higgs exchange which are almost always dominant in the models we discuss. The parameters $\delta_{1,2}$ depend on eigen components of the LSP wave function and $B, C, D$ depend on VEVs of the Higgs fields and the Higgs mixing parameter $\alpha$ and are given by

$$\begin{aligned} &\text{for } u \text{ quarks: } \delta_1 = n_{13}\ ,\ \delta_2 = n_{14}\ ,\ B = \sin\beta\ ,\ C = \sin\alpha\ ,\ D = \cos\alpha\ , \\ &\text{for } d \text{ quarks: } \delta_1 = n_{14}\ ,\ \delta_2 = -n_{13}\ ,\ B = \cos\beta\ ,\ C = \cos\alpha\ ,\ D = -\sin\alpha\ . \end{aligned} \tag{6.10}$$

In Fig. 6.1 we give the spin independent cross sections vs the neutralino mass after experimental constraints are applied (discussed in Section 6.4) as well as constraints from the LHC SUSY searches [102]. We describe the simulations further in what follows. Also shown are the XENON-100 [103–105], CDMS II [106, 107] and projected XENON and SuperCDMS limits for comparison [111, 112]. The direct mapping of the parameter space constrained by the recent CMS and ATLAS searches is substantial in the spin independent scattering cross section - dark matter mass plane. This is achieved by simulating the LHC SUSY production of the models and SM backgrounds under CMS and ATLAS cuts. We extend their results by considering a larger class of models over the parameter space relevant to early SUSY searches. In Fig. 6.1, we identify the region in this plane that the LHC data constrains. We will see that this corresponds to the low mass branch of the slepton co-annihilation region, defined by $(m_{\tilde{l}} - m_{\tilde{\chi}_1^0})/m_{\tilde{\chi}_1^0} \lesssim 0.2$. Thus, observation of dark matter in the LHC depleted region may indicate the presence of non-universalities. We discuss now the CMS and ATLAS analyses, and their generalizations and implications in more detail.

## 6.3 LHC Analysis

Here, we analyze the nature of the NLSP in the regions of the parameter space depleted by the CMS and ATLAS results as well as the SUSY event rates in the region that would be accessible to both the dark matter direct detection experiments and the LHC in the next rounds of data. As evident from the results of [75–77] the 0 lepton ATLAS analysis is the most stringent, so we mainly focus on this search in our analysis, but we have still checked these models with the 1 lepton ATLAS search and the CMS $\alpha_T$ jet search. We discuss in detail the 0 lepton ATLAS search only; the reader is directed to [75, 76] for a more detailed discussion on the other LHC SUSY searches.

We follow the pre-selection requirements that ATLAS reports in [77, 82]. Jet candidates must have $p_T > 20\,\text{GeV}$ and $|\eta| < 4.9$ and electron candidates must have $p_T > 10\,\text{GeV}$ and $|\eta| < 2.47$. Events are vetoed if a "medium" electron [82] is in the electromagnetic calorimeter transition region, $1.37 < |\eta| < 1.52$. Muon candidates must have $p_T > 10\,\text{GeV}$ and $|\eta| < 2.4$. Further, jet candidates are discarded if they are within $\Delta R = \sqrt{(\Delta\eta)^2 + (\Delta\phi)^2} = 0.2$ of an electron. For the analysis, the (reconstructed) missing energy, $\not{E}_T$, for an event is the negated vector sum of the $p_T$ of all the jet and lepton candidates.

The analysis is made up of 4 regions, "A", "B", "C" and "D", each having 0 lepton candidates. When referring to different cuts in these regions we define cuts on the "selected" jets to mean that the "selected" jet candidate has $|\eta| < 2.5$ and the bare minimum number of jets in this region must satisfy the requirement. For regions A and B "selected" jets refers to the first two hardest jets in the $|\eta| < 2.5$ region and for regions C and D "selected" jets refers to the first three hardest jets in the $|\eta| < 2.5$ region. Events are required to have $\not{E}_T > 100\,\text{GeV}$ and the selected jets must each have $p_T > 40\,\text{GeV}$ with the hardest jet $p_T > 120\,\text{GeV}$. Further, events are rejected if the missing energy points along the same direction as any of the selected jets., i.e. we require $\Delta\phi\left(j_i, \not{E}_T\right) > 0.4$, where $i$ is over the "selected"

jets. Region A requires events to have $\not{E}_T > 0.3 M_{\rm eff}$ with $M_{\rm eff} > 500\,{\rm GeV}$ and regions C and D both require events to have $\not{E}_T > 0.25 M_{\rm eff}$ with region C requiring $M_{\rm eff} > 500\,{\rm GeV}$ and region D requiring $M_{\rm eff} > 1\,{\rm TeV}$. In this case $M_{\rm eff}$ is defined to be the scalar sum of the missing energy and the $p_T$ of the "selected" jets. As in the analysis of [102] we do not apply the cut for region B, i.e. $m_{T2} > 300\,{\rm GeV}$, since the models constrained in this region are already constrained in region D [83].

For our analysis, we use the simulated SM background of [80] which was generated with MadGraph [85] for parton level processes, PYTHIA [86] for hadronization and PGS [117] for detector simulation. A more thorough discussion on the details of this background can be found in [80, 81], (see also [79, 118] for discussions on SM background for $2 \to N$ processes). After applying the LHC SUSY analysis to our SM background we are able to reproduce their reported standard model Monte Carlo results.

## 6.4 Result of dark matter analysis with CMS-ATLAS Constraints

We discuss now the implications of the data from CMS and ATLAS on dark matter. To this end we first carry out a survey of the mSUGRA parameter space as follows: $m_0 \in (10, 4000)\,{\rm GeV}$, $m_{1/2} \in (10, 2000)\,{\rm GeV}$, $A_0 \in (-10, 10) \cdot m_0$, $\tan\beta \in (1, 60)$. Performing a general survey of the mSUGRA model space we simulate the models that satisfy radiative electroweak symmetry breaking (REWSB) as well as direct and indirect experimental constraints including sparticle mass limits, B-physics constraints, and constraints from $g_\mu - 2$. We further require that the relic density be within the observed WMAP limit [94, 95], $0.0896 < \Omega_\chi h^2 < 0.1344$. These indirect constraints were calculated using MicrOMEGAs [87], with the Standard Model contribution in the $\mathcal{B}r(b \to s\gamma)$ corrected using the NNLO analysis of Misiak *et al.* [88, 89]. We apply the following "collider/flavor constraints" [90] $m_h > 93.5$ GeV, $m_{\tilde{\tau}_1} > 81.9$ GeV, $m_{\widetilde{\chi}_1^\pm} > 103.5\,{\rm GeV}$, $m_{\tilde{\tau}_1} > 100$ GeV, $m_{\tilde{b}_1} > 89$ GeV, $m_{\tilde{e}_R}, m_{\tilde{e}_L} > 107$ GeV,

$m_{\tilde{\mu}_R}, m_{\tilde{\mu}_L} > 94$ GeV, and $m_{\tilde{g}} > 400$ GeV, along with $(-11.4 \times 10^{-10}) \leqslant \delta\left(g_\mu - 2\right) \leqslant (9.4 \times 10^{-9})$, see [91], $\mathcal{B}r\left(B_s \to \mu^+\mu^-\right) \leqslant 4.2 \times 10^{-8}$ (90% C.L.) [119], and $(2.77 \times 10^{-4}) \leqslant \mathcal{B}r\left(b \to s\gamma\right) \leqslant (4.37 \times 10^{-4})$ [93].

To investigate the constraints from the LHC SUSY search on the dark matter detection signals, we scanned over 20 million models in the mSUGRA parameter space. After imposing the various experimental constraints as previously discussed, we simulate the models with the ATLAS 0-lepton analysis. It is found that there exists a large portion of the signature space in the spin independent cross section-neutralino plane which is being excluded by the ATLAS 0-lepton search. This excluded region which is marked by red color as shown in Fig. 6.1 was populated by mSUGRA models before considering the new LHC data. We further divide the excluded region into the red region where all the mSUGRA models scanned are excluded by the LHC data, and the two maroon regions each with about 60% of the models excluded by the LHC. (Note that ATLAS carried out their analysis for a few fixed values of $\tan\beta$ and $A_0$ while our analysis allow these to vary.) Next, by considering the NLSP, we find that essentially all of the region that is depleted by the LHC at 95% CL is the low mass region of the slepton co-annihilation branch.

This is shown more clearly in Fig. 6.2 where we display the number of SUSY events vs the neutralino mass for a subset of models in the two panels corresponding to the regions A and D with low neutralino masses. We do not display region C since it gives results similar to region A and we do not display region B since it is subsumed in region D. The dashed black lines in Fig. 6.2 can be viewed as the 95% C.L. limit in each signal region, as they correspond to the event thresholds reported by ATLAS. Indeed, most of the model points being constrained by the LHC are those where the stau is the NLSP appropriate for the slepton coannihilation branch. Further, very few of the model points are constrained by the ATLAS analysis which lie on the Hyperbolic Branch (HB) (Focus Point region) [96–98] of REWSB. The NLSP on the HB is mostly the light chargino and from Fig. 6.1 we find that very few of the chargino NLSP

models are currently constrained by the ATLAS analysis.

In contrast, the higher mass HB/FP region is becoming constrained by the XENON data [103–105]. This effect can be seen in Fig. 6.3 where we show the $m_0$–$m_{1/2}$ plane for the mSUGRA case denoted by their NLSP where the models on the left panel are constrained by XENON-100 and the models on the right panel are unconstrained by XENON-100.

Thus, we come to the conclusion that the ATLAS constraints are very severe for the low $m_0$ region, while the XENON constraints are very severe for the large $m_0$ region as shown. As can be seen from Ref. [102], the region which is now being constrained by XENON corresponds to $\mu \lesssim 400\,\text{GeV}$ and here the LSP wavefunction has a significant Higgsino component. We add here that bulk region and the Higgs pole region (the latter being the horizontal strip of essentially fixed $m_{1/2} \sim \mathcal{O}\,(100\text{–}150)$ GeV) remain largely untouched by either experiments.

More generally while the recent XENON analysis [103–105] has presented plots along with mSUGRA [101] (see Eq. (6.4)) model points on top of the data – we suggest that the XENON collaboration include the 50 GeV to 65 GeV mass range of mSUGRA in their constraint plots as this is the region where the XENON data shows its greatest present sensitivity. We also remark that in the analysis of the spin independent cross section we used the default values of the form factors as given in Ref. [87]. It is well known, the predictions for the SI cross section are sensitive to the precise knowledge of the form factors and in particular the strange quark form factor. In addition, variations on the order of 5 or larger have been reported in [115] and in [87] over a reasonable range of the pion-nucleon sigma term (for which the above form factors depend on). These uncertainties should be kept in mind while interpreting the results of dark matter direct detection experiments on the parameter space of models. Thus, while we have shown in Fig. 6.3 the regions which lie below and above the reported XENON limits one does need to factor in more generally the uncertainties in the hadronic matrix elements as well as the uncertainties in astrophysical quantities to have a more precise account of the constrained

region of parameter space. However, such an analysis goes beyond the scope of this chapter. Thus our aim here is to emphasize that the sensitivity of the XENON detector is encroaching on a new part of the space of SUGRA models, and it is beginning to provide more stringent constraints on the larger $m_0$ region for which the Higgsino component of the LSP wavefunction can become significant.

## 6.5 SUGRA models with non-universal breaking

The analysis for the mSUGRA case highlighted in Fig. 6.1 shows a deficit of models after the LHC constraints are applied in the region under the XENON-100 curve in the neutralino mass range of 50 GeV to 100 GeV corresponding to the slepton coannihilation region. While the assumption of universal boundary conditions on soft breaking in supergravity grand unification [51, 52] is the simplest possibility leading to the model mSUGRA, the framework of supergravity unification [51, 52] allows for non-universalities in the soft parameters which occurs generically for several classes of string motivated models (see [120–127]).

Non-universal gaugino masses can arise in two ways (a) from tree level supergravity with a gauge kinetic function dependent on singlets or products of singlets and fields which transform under the gauge groups of the standard model (b) from loop induced gaugino masses dependent on the beta function coefficient for each group. For tree level gaugino masses, one has

$$M_a = \frac{1}{2\Re(f_a)} F^I \partial_I f_a \ ,$$

where $F^I$ are the order parameters of SUSY breaking, $I$ denotes the hidden sector (singlet) fields responsible for the breaking of SUSY and $f_a$ is a diagonal gauge kinetic function, where $a$ is an adjoint index

for each gauge group. In addition for loop induced gaugino masses one has [54, 120, 121, 128]

$$M_a^1|_{adj} = -b_a^0 g_a^2 m_{3/2} + ...$$

where the higher order terms are given in [128] and the beta function coefficient is given in terms of $C_a, C_a^i$ ; the quadratic Casimir operators for the gauge group $G_a$ respectively in the adjoint representation

$$b_a^0 = \frac{1}{16\pi^2}(3C_a - \sum_i C_a^i) \ .$$

Thus we now consider the case of non-universal supergravity (NUSUGRA) models to see if the region depleted in the mSUGRA case can become populated when non-universalities are included. Here we will keep the analysis rather general and parametrize the non-universalities as in the gaugino masses which can be sourced from tree level supergravity, from loop induced gaugino masses, and most generally a combination of both as

$$M_a = m_{1/2} \ (1 + \delta_a) \ , \tag{6.11}$$

at the GUT scale for the gauge groups U(1), $SU(2)_L$, $SU(3)_C$ corresponding to $a = 1, 2, 3$. The ranges chosen are $\delta_a = (-1, 1)$ with the ranges for the remaining parameters as in the mSUGRA case.

The result of the analysis is shown in Fig. 6.4 where we exhibit the allowed set of models over a broad range of neutralino masses which satisfy all the experimental constraints, but do not yet have the LHC SUSY search constraints applied to them. The area depleted by the LHC for the mSUGRA case lies within the red boundary and is shown for comparison. One observes that the presence of non-universalities in the gaugino sector repopulates a significant part of the region of the signature space in the spin independent scattering cross section-neutralino mass plane that is constrained by the LHC SUSY searches relative to the case of minimal SUGRA. This region of re-population is found to produce a consistent relic density via multiple coannihilation channels.

In particular, because the chargino mass can be split from the LSP mass with non-universalities in the gaugino sector consistent with the LEP bound on the chargino mass, the low mass region below the light CP even Higgs pole, which is largely the Z-pole region, is now allowed by the relic density constraint. Thus one can have a dark matter mass as low as

$$m_{\tilde{\chi}_1^0} \gtrsim 40\,\text{GeV (NUSUGRA–gauginos)}, \tag{6.12}$$

in the NUSUGRA case, where the lower limit is higher in the mSUGRA case to be consistent with the LEP data.

The top panel of Fig. 6.5 gives the analysis with a focus on the 50 GeV to 100 GeV neutralino mass region where we also apply the LHC analysis as already described. From Fig. 6.4 and the top panel of Fig. 6.5, it is apparent that the gaugino mass non-universalities produce a significant re-population of the region with models specifically in the 50 GeV to 100 GeV neutralino mass range. Also shown in the bottom two panels of Fig. 6.5 are the gluino mass and the lightest second generation squark mass. We note that a gluino mass as low as 400 GeV and a squark mass as low as 600 GeV are unconstrained by the present ATLAS data. Similar results are obtained when non-universalities in both the gaugino sector and the Higgs sector [126, 127] are present. In this case the analysis gives results similar to those of Fig. 6.5 with a larger density of allowed models which populate the region depleted by the LHC SUSY searches.

## 6.6 Conclusion

The implications of the first SUSY analysis by CMS and ATLAS on supersymmetric dark matter are analyzed. It is found that the CMS and ATLAS constraints deplete a significant branch of the slepton coannihilation regions in the mSUGRA parameter space where dark matter can originate in the

early universe while the Higgs pole region and the Hyperbolic Branch (focus point region) are not constrained. However, a large portion of the Hyperbolic Branch region is now becoming constrained by the recent XENON data. The effect of non-universalities in the gaugino masses are analyzed and it is found that a part of the region in the spin-independent cross section vs the LSP mass plane depleted by the CMS and ATLAS analysis for mSUGRA is repopulated when non-universalities are included, i.e., for the NUSUGRA case. Thus observation of dark matter in the mSUGRA region depleted by the ATLAS constraints could point to supergravity models with non-universal soft breaking.

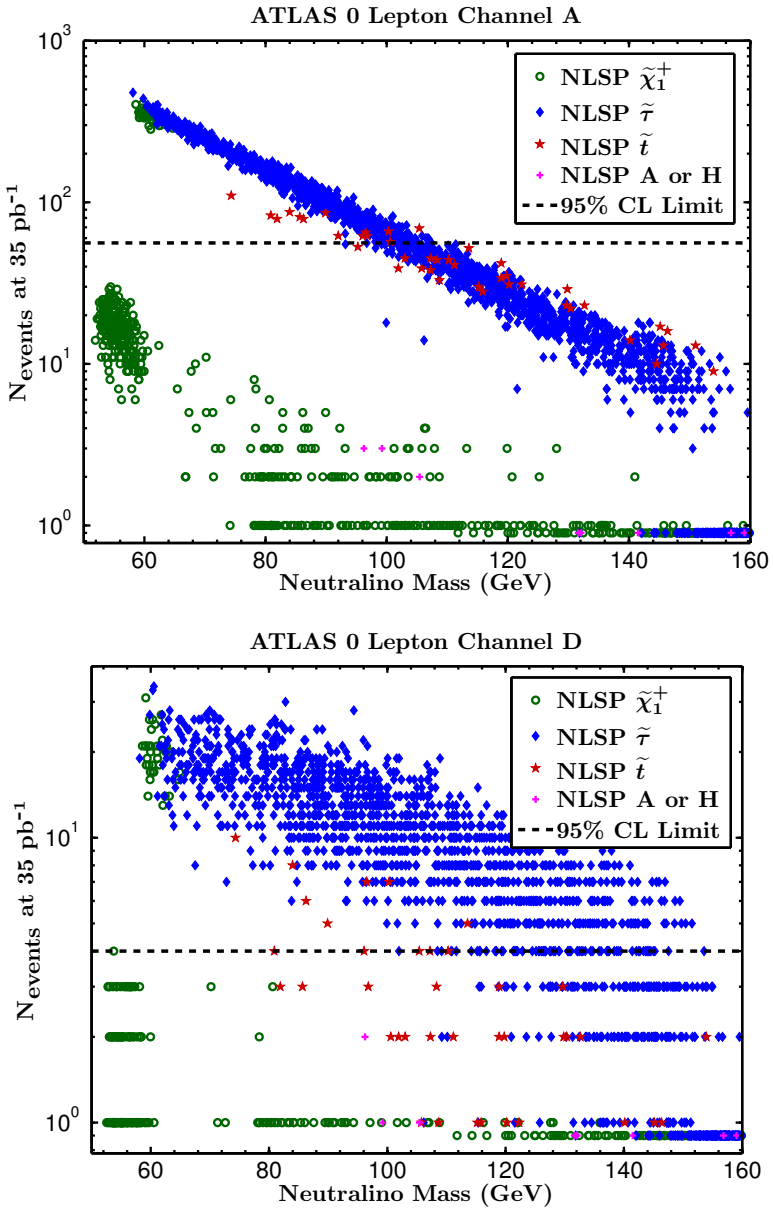


Figure 6.2: Exhibition of the number of SUSY events in the ATLAS 0 lepton analysis and the corresponding NLSPs against the neutralino mass with 35 pb$^{-1}$ of integrated luminosity for a subset of models around the LHC excluded region of Fig. 6.1. Left panel: Region A [77]; Right panel: Region D [77]. The dashed black lines can be viewed as the 95% C.L. limit in each signal region, as they correspond to the event thresholds reported by ATLAS along the $m_0$–$m_{1/2}$ boundaries [83]. Essentially, the models being eliminated by the ATLAS results (above the dashed black line) are those with the stau as the NLSP.

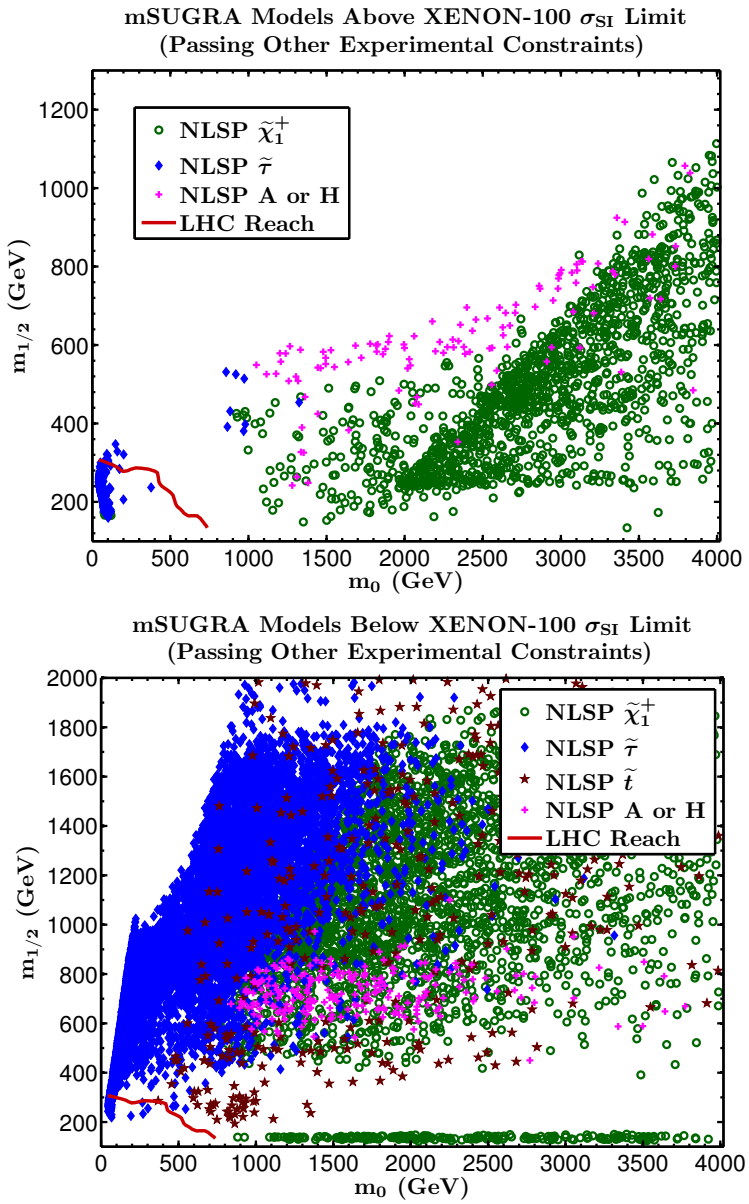


Figure 6.3: Exhibition of models in the $m_0$–$m_{1/2}$ plane denoted by their NLSPs and the ATLAS 0 lepton curve (red) is drawn for comparison (see Fig. 6.1). The left panel corresponds to the models that have been constrained by XENON-100 [103–105] and the right panel corresponds to the models that are unconstrained by XENON-100. All models have the same constraints as Fig. 6.1. From this analysis we see explicitly that the reported XENON constraints are severe in the larger $m_0$ region constraining the hyperbolic branch, while the low $m_0$ region, which are the low mass slepton co-annihilation regions, are being constrained by both XENON and the LHC.

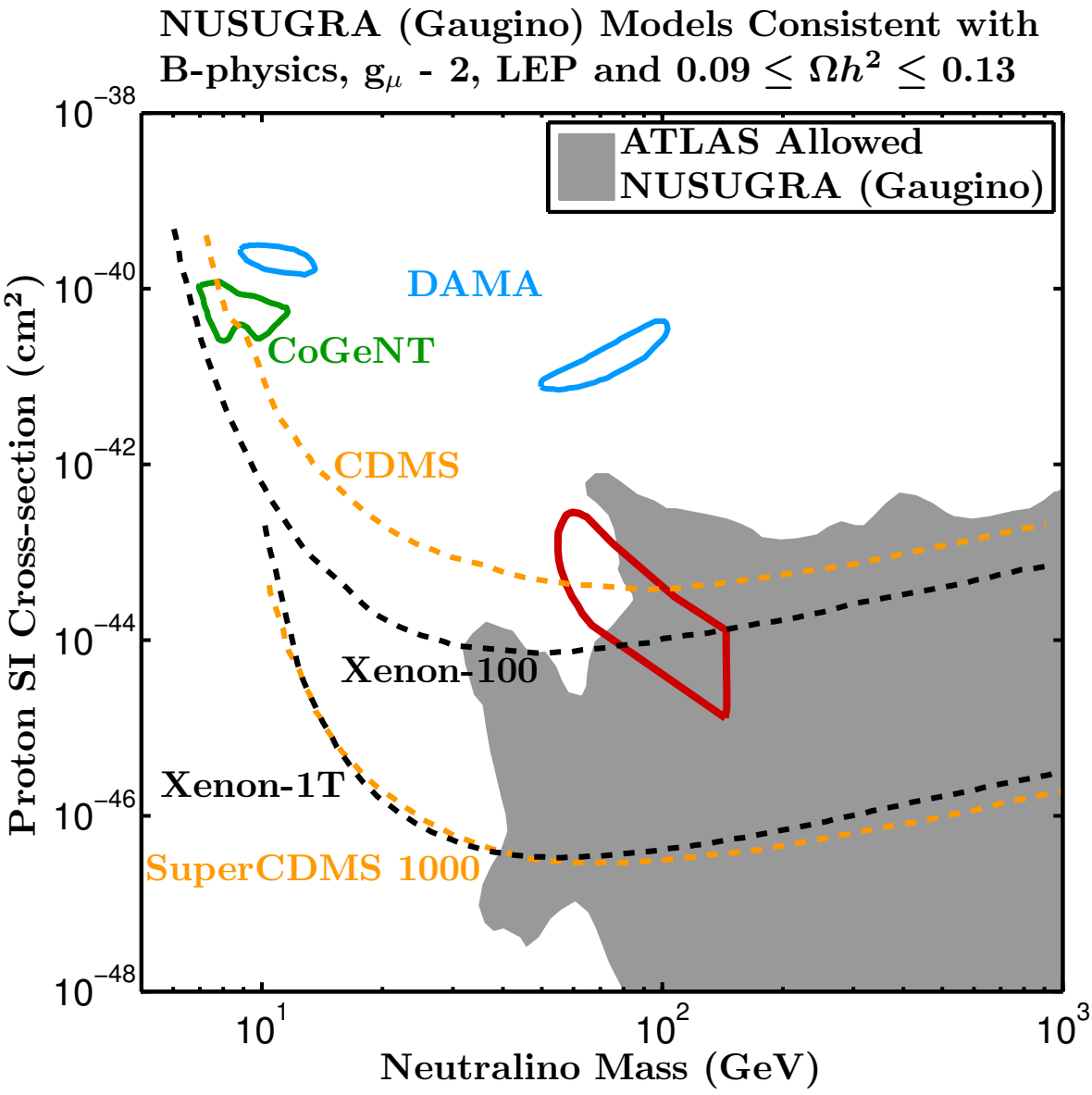


Figure 6.4: Analysis of models with non-universalities in the gaugino masses with the LEP, Tevatron, $g_\mu - 2$, FCNC and WMAP constraints. The red contour is the region depleted for mSUGRA by the ATLAS results and is shown for comparison. While this random scan does not emphasize the mSUGRA parameter region, a more intensive scan would include all of the gray area of Fig. 6.1.

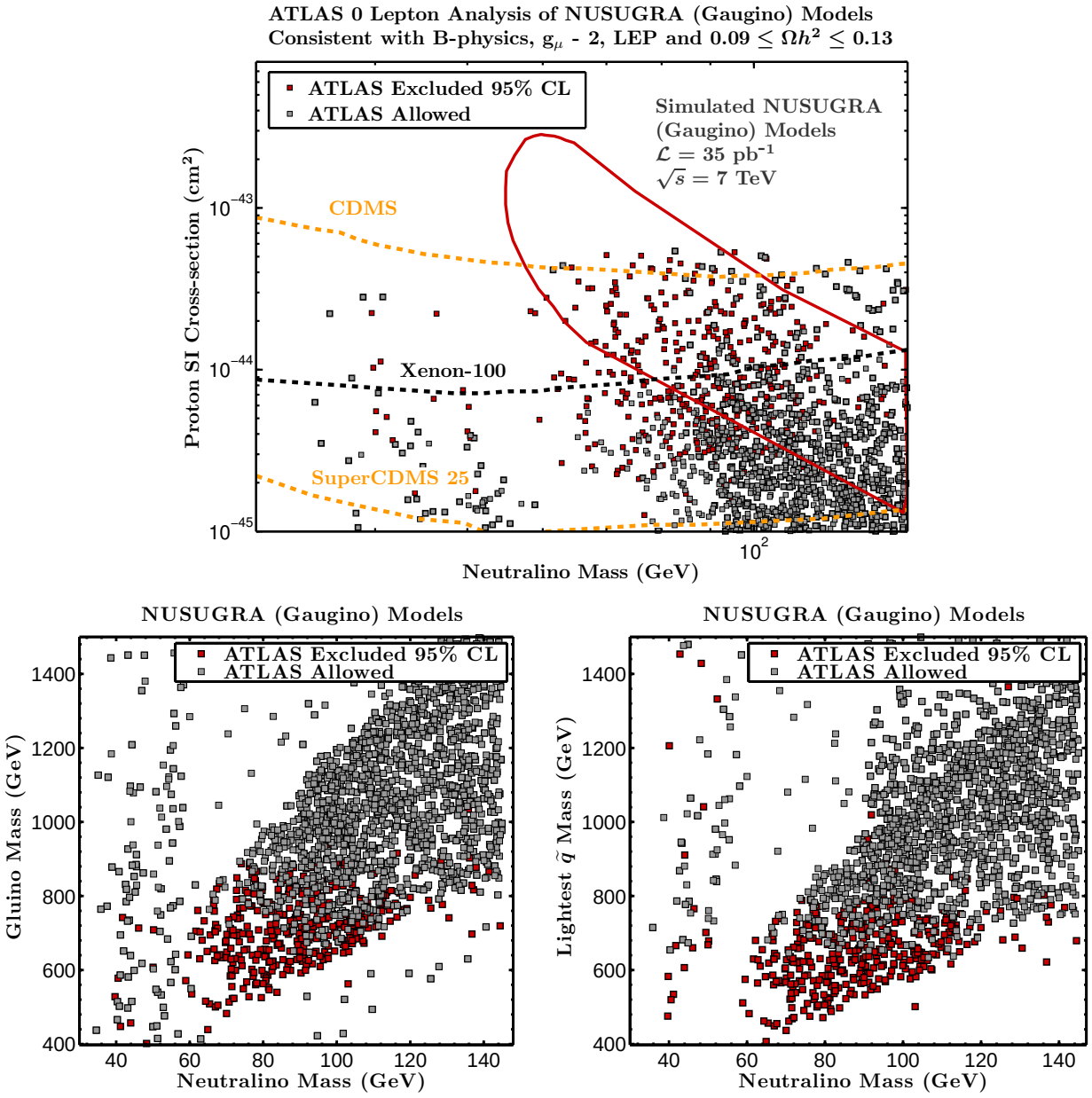


Figure 6.5: Re-population of the region depleted by ATLAS. Shown are NUSUGRA models, where the red contour is the ATLAS constrained region in mSUGRA. The non-universal gaugino models simulated (a subset of models in Fig. 6.4) under the ATLAS 0 lepton cuts that are constrained by the analysis indicated by red squares. The bottom two panels show the gluino mass and the lightest second generation squark mass where we note a gluino mass as low as 400 GeV and squark masses as low as 600 GeV are unconstrained by the present ATLAS data.

# Chapter 7

# Hyperbolic Branch of Minimal Supergravity and Naturalness

## 7.1 Introduction

In this chapter, it is shown that the Hyperbolic Branch of radiative breaking of the electroweak symmetry contains in it three regions: the Focal Point, Focal Curves, and Focal Surfaces. Further, the Focal Point is shown to lie on the boundary of Focal Curves. These focal regions allow for a small $\mu$ while scalar masses can become large. It is shown that for the mSUGRA model the current LHC-7 constraint depletes the Focal Point region while regions on Focal Curves and Focal Surfaces remain intact. The LHC implications for models which lie on Focal Curves are briefly discussed as well as the implications of dark matter constraints for the Focal Point, Focal Curves and Focal Surfaces are discussed.

Several naturalness, hierarchy, and, fine-tuning problems exist in particle physics: some big and some small. The most severe one relates to the smallness of the vacuum energy in units of the Planck mass, followed by the smallness of the ratio $M_W/M_{\rm Pl}$. There are several other small-to-moderate size

hierarchies such as the ratio $M_{GUT}/M_{Pl}$ and the ratios in the fermion mass spectra such as $m_u/m_t$. Also, there are hierarchy problems of a more technical nature, such as in the Higgs sector of the standard model, where the Higgs boson mass receives a loop correction which is quadratically dependent on the cutoff. This problem is resolved in supersymmetric models with a cancellation between the fermionic and super-fermionic loops which results in the quadratic dependence on the cutoff being replaced by a logarithmic dependence. A similar problem at a much smaller scale often called the little hierarchy problem appears for supersymmetric models if the scalar masses turn out to be large. In fact, in certain models of soft breaking the scalar masses can get large, as is the case in supergravity grand unified models [51] with hierarchical breaking of supersymmetry [129] and for certain string motivated models [125]. Large scalar masses have also been considered in other contexts [130].

The little hierarchy problem can be roughly described as follows: in the radiative breaking of the electroweak symmetry (REWSB) one has $\frac{1}{2}M_Z^2 \simeq -\mu^2 - m_{H_2}^2$ where $\mu$ is the Higgs mixing parameter and $m_{H_2}$ is the mass of the Higgs boson that couples to the top quark. Naively $m_{H_2}$ gets large as the universal scalar mass $m_0$ gets large and a large cancellation is needed between $\mu$ and $m_{H_2}$ to get a small $M_Z$. A more practical approach is to view the REWSB relation as a determination of $\mu$ which is the view point we adopt here. From this perspective, if $m_0$ is large the accessibility of sparticles at the LHC rests on the size of $m_{1/2}$ and $\mu$ and thus a small $\mu$ (and a small $m_{H_2}$) is desirable.

The question then is how one may achieve a small $\mu$ for the above class of models in the context of radiative breaking of the electroweak symmetry. The basic mechanism for achieving the above was first realized in [96]. In the analysis of [96] it was found that there exist two natural regions of radiative breaking, one where there is an upper bound on the soft parameters $m_0$, $m_{1/2}$, $A_0$ for a fixed $\mu$ (the Ellipsoidal Branch, EB), and the other where one or more soft parameters can get very large for fixed $\mu$ (the Hyperbolic Branch, HB). In a later work, [98], it was shown that there exists a region where the value of the Higgs mass squared, $m_{H_2}^2$, becomes essentially independent of the values of the input

parameter $m_0$ at the GUT scale. Such a region was then labeled the Focus Point.

In this chapter, we classify the solutions of the Hyperbolic Branch in Section 7.2 and show that it contains three main regions: (1) Focal Points (HB/FP): This region lies at the boundary between the Ellipsoidal and the Hyperbolic Branches where $\mu^2$ becomes independent of $m_0^2$ and thus $m_0$ can get large while $\mu$ remains fixed with the other soft parameters being held fixed. In this definition we do not include the Focal Point on the EB. The Focal Point is technically different from the Focus Point [98] but for $\tan\beta \gg 1$ they are essentially the same as will be made clear in Section 7.2 and Section 7.3. The HB/FP region, however, is only a small part of HB and the larger parts of HB are Focal Curves and Focal Surfaces as discussed below, and in detail in Section 7.2 and Section 7.4. (2) Focal Curves (HB/FC): Focal Curves are where two soft parameters are comparable and can get large while $\mu$ is fixed. We define HB/FC such that the HB/FP region is excluded. (3) Focal Surfaces (HB/FS): Here one may have a fixed (and small) $\mu$ while the three dimensional soft parameters may get large. The HB/FS region is the set of all Focal Curves, thus does not include the HB/FP region.

In Section 7.5, we carry out a numerical analysis considering experimental constraints including from the LHC-7 data, to observe its effect on the HB region. We will show that the combined constraints severely deplete the Focal Point region, while the Focal Curves and thus Focal Surfaces largely remain intact. We also explore implications for LHC and dark matter searches.

Concluding remarks are presented in Section 7.6.

## 7.2 Focal Points, Curves, Surfaces of the Hyperbolic Branch

In this section we will discuss in detail the classification of HB into the three broad regions mentioned in the last section. We begin with the equation for the radiative breaking of the electroweak symmetry

$$\mu^2 + \frac{1}{2}M_Z^2 = \frac{\overline{m}_{H_1}^2 - \overline{m}_{H_2}^2 \tan^2\beta}{\tan^2\beta - 1}\ , \tag{7.1}$$

where we have $\overline{m}_{H_i}^2 = m_{H_i}^2 + \Sigma_i$ and $\Sigma_i$ is the contribution arising from the loop corrections to the effective potential for $i = 1, 2$ [97]. In this section we will focus on the supergravity grand unification model with universal boundary conditions [51–53] whose soft breaking sector is described by

$$\Big(m_0,\ m_{1/2},\ A_0,\ \tan\beta,\ \mathrm{sgn}(\mu)\Big)\ , \tag{7.2}$$

where $m_0$ is the universal scalar mass, $m_{1/2}$ is the universal gaugino mass, $A_0$ is the universal trilinear coupling and $\mu$ is the Higgs mixing parameter in the superpotential. The model of Eq. (7.2) is referred to as mSUGRA or sometimes as the constrained minimal supersymmetric model, CMSSM. The analysis is done using the techniques given in [101] where one starts with universal boundary conditions given by Eq. (7.2) for the soft parameters at the GUT scale and evolves the sparticle masses downwards using renormalization group equations. For illustration in the text, we consider one loop evolution where we neglect the Yukawa couplings except for the top quark. The simulations presented later are done using numerical codes which include the effects of the $b$ and $\tau$ Yukawa couplings. In this model the radiative breaking of the electroweak symmetry allows for a determination of $\mu^2$ in terms of the soft parameters as [96, 126]

$$\mu^2 = -\frac{1}{2}M_Z^2 + m_0^2 C_1 + A_0^2 C_2 + m_{1/2}^2 C_3 + m_{1/2} A_0 C_4 + \Delta\mu_{\rm loop}^2\ , \tag{7.3}$$

where

$$C_1 = \frac{1}{\tan^2\beta - 1}\left(1 - \frac{3D_0 - 1}{2}\tan^2\beta\right) , \tag{7.4}$$

$$C_2 = \frac{\tan^2\beta}{\tan^2\beta - 1}k , \tag{7.5}$$

$$C_3 = \frac{1}{\tan^2\beta - 1}\left(g - e\tan^2\beta\right) , \tag{7.6}$$

$$C_4 = -\frac{\tan^2\beta}{\tan^2\beta - 1}f , \tag{7.7}$$

and the functions $e.f$, $g$, $k$ are as defined in [131]. $D_0(t)$ is defined by

$$D_0(t) = \left(1 + 6Y_0F(t)\right)^{-1} \tag{7.8}$$

$$\text{with, } Y_0 = h_t(0)^2/(4\pi^2) . \tag{7.9}$$

Here, $h_t(0)$ is the top Yukawa coupling at the GUT scale, $M_G \simeq 2 \times 10^{16}$ GeV. Further,

$$F(t) = \int_0^t E(t')dt' , \tag{7.10}$$

where

$$E(t) = \left(1 + \beta_3 t\right)^{16/3b_3}\left(1 + \beta_2 t\right)^{3/b_2}\left(1 + \beta_1 t\right)^{13/9b_1} . \tag{7.11}$$

Here $\beta_i = \alpha_i(0)b_i/(4\pi)$ and $b_i = (-3, 1, 11)$ for SU(3), SU(2) and U(1) and $t = \ln\left(M_G^2/Q^2\right)$ where $Q$ is the renormalization group point. Our normalizations are such that $\alpha_3(0) = \alpha_2(0) = \frac{5}{3}\alpha_1(0) = \alpha_G(0)$. Further, $\Delta\mu^2_{\text{loop}}$ is the loop correction [97].

As is well known, the tree value of $\mu^2$ (Eq. (7.3) without $\Delta\mu^2_{\text{loop}}$), is sensitive to the renormalization group scale and the same is true of the loop correction. However, the sum of the tree and the loop term is relatively insensitive to variations in $Q$ [96].

Further, one of the interesting phenomena observed in [96] is the following: suppose one goes to a renormalization group point Q where the loop contribution $\Delta\mu^2_{\rm loop}$ is minimized (this typically occurs at $Q \sim \mathcal{O}\left(\sqrt{M_{\tilde{t}_1} M_{\tilde{t}_2}}\right)$, where $M_{\tilde{t}_1}$ and $M_{\tilde{t}_2}$ are the stop masses). Now at low values of $\tan\beta$ and Q it is observed that the co-efficients $C_i$ $(i = 1 - 4)$ continue to be all positive. In this case it is clear that for any fixed $\mu$ the soft parameters have well defined upper limits. However, for larger values of $\tan\beta$, $C_1$ can vanish or even turn negative as Q increases. We will call the region where $C_1$ either vanishes or is negative as the Hyperbolic Branch. In this case it is possible to have large soft parameters while $\mu$ remains relatively small.

The HB of REWSB contains three regions: (1) The Focal Point (HB/FP): We define the points where $C_1$ vanishes as Focal Points. From Eq. (7.3) and Eq. (7.4) we find that when $C_1 = 0$, $m_0$ can get large without affecting $\mu$. For practical purposes, for a fixed $\tan\beta$, we will take a small region around $C_1 = 0$, and call it the Focal Point region, specifically

$$|C_1| < \delta\left(Q, m_t\right), \quad \delta\left(Q, m_t\right) \ll 1\,. \tag{7.12}$$

In determining $\delta\left(Q, m_t\right)$ we are guided by the experimental error in the top quark mass from $m_t = (173.1 \pm 1.3)\,\text{GeV}$. Now, for a fixed $\tan\beta$, $C_1 = C_1(m_t, Q)$ where $Q \sim \mathcal{O}\left(\sqrt{M_{\tilde{t}_1} M_{\tilde{t}_2}}\right)$ and thus, Q depends on the top mass via the dependence of the stop masses on $m_t$. However, this implicit dependence on $m_t$ via Q is rather weak and effectively $\delta C_1 = \frac{\delta C_1}{\delta m_t}\delta m_t$. A direct analysis gives the following approximate result

$$\delta C_1 \simeq 3\left(1 - D_0\right)\frac{\delta m_t}{m_t}\,. \tag{7.13}$$

This result agrees with the one loop analysis in Fig. 7.1 where $\delta C_1$ can be interpreted as the vertical spacing between the curves in the right panel of Fig. 7.1. In the full numerical analysis presented later

in identifying the parameter points that lie in the Focal Point region, we calculate $\delta C_1$ numerically for each point by calculating the variation in $C_1$ for variations in $m_t$. (2) Focal Curves (HB/FC): The region where $C_1 < 0$ allows for two soft parameters to get large while $\mu$ remains small is the Focal Curve region. In fact, in this case there are two general possibilities: HB/FC1 and HB/FC2. In the case of HB/FC1 (HB/FC2), we have $C_1 < 0$ and $m_{1/2}$ ($A_0$) as well as $\mu$ are held fixed with $m_0$ and $A_0$ ($m_{1/2}$) allowed to vary. These two cases can be combined into a single form HB/FC$_\alpha$ defined by $C_1 < 0$ and the constraint $m_{1/2} = \alpha(1-\alpha)^{-1}A_0$ where $0 < \alpha < 1$. We note that HB/FC$_\alpha$ reduces to HB/FC1 when $\alpha \sim 0$ and reduces to HB/FC2 when $\alpha \sim 1$. (3) The Focal Surface (HB/FS): is the region of HB where $C_1 < 0$ while all the soft parameters (except $\tan\beta$), i.e, $m_0$, $m_{1/2}$, $A_0$ vary and may get large while $\mu$ remains fixed. In terms of HB/FC$_\alpha$, varying $\alpha$ creates a Focal Surface.

We discuss now briefly the issue of fine-tuning. Often one uses the criterion of fine-tuning to designate some regions of the parameters as preferred over others. However, such criteria are necessarily subjective and widely different results can be attained by different choices. For example, one criteria used is to look at the sensitivity of $M_Z$ to variations in the parameters that enter in Eq. (7.1). Let us define the set of such parameters to be $a_i$, then the sensitivities $f_i$ and the fine tuning parameter $f$ are taken to be as in [98]:

$$f_i = \left|\frac{\partial \ln M_Z^2}{\partial \ln a_i}\right| , \quad f = \max\{f_i\} \ . \tag{7.14}$$

Using the above criteria it has been argued that certain regions of the parameter space (such as when $A_0 \neq 0$) are less natural than the $A_0 = 0$ region [98]. However, such an argument appears to us as hasty in suppressing parts of the parameter space based purely on a theoretical prejudice. For example, as already noted in [98] inclusion of the top Yukawa in the list $\{a_i\}$ would lead to very different conclusions. It may turn out that nature chooses a parameter point which one might consider 'unnatural' from a criteria such as of Eq. (7.14) but is perhaps the natural consequence of a more unified approach. In our analysis we will not rely on criteria such as Eq. (7.14) as a selection principle for the parameter space,

since the subjectivity of such criteria is their weakness. Rather, we take the more pragmatic approach regarding exploration of the entire parameter from a phenomenologically desirable view point. Such a view point requires that we explore the small $\mu$ region of the parameter space while one or more of the other soft parameters (such as $m_0$ and $A_0$) could become large. Effectively our naturalness criteria will be simply regions of small $\mu$ as in the analysis of [96]. Thus solutions of this type appear desirable for phenomenological reasons regarding the detectability of new physics at the LHC. Further, as mentioned earlier situations of this type arise in theory models [125, 129].

## 7.3 The Focus Point region of HB

While the Hyperbolic Branch [96] and the Focus Point [98] both allow for large values of $m_0$ while $\mu$ remains small, the exact relationship of the Hyperbolic Branch and of the Focus Point has not been elucidated in the literature; this is the focus of this section. We show that the Focus Point is the boundary point of a Focal Curve on the Hyperbolic Branch. Again for illustration we will consider one loop evolution, and among the Yukawa couplings retain only the top quark coupling. Here the scalar masses $m^2_{H_2}$, $m^2_{\tilde{U}}$ and $m^2_{\tilde{Q}}$ satisfy the following set of coupled equations

$$\frac{dm^2_{H_2}}{dt} = -3Y_t\Sigma - 3Y_tA_t^2 + \left(3\tilde{\alpha}_2M_2^2 + \tilde{\alpha}_1M_1^2\right) \ , \tag{7.15}$$

$$\frac{dm^2_{\tilde{U}}}{dt} = -2Y_t\Sigma - 2Y_tA_t^2 + \left(\frac{16}{3}\tilde{\alpha}_3M_3^2 + \frac{16}{9}\tilde{\alpha}_1M_1^2\right) \ , \tag{7.16}$$

$$\frac{dm^2_{\tilde{Q}}}{dt} = -Y_t\Sigma - Y_tA_t + \left(\frac{16}{3}\tilde{\alpha}_3M_3^2 + 3\tilde{\alpha}_2M_2^2 + \frac{1}{9}\tilde{\alpha}_1M_1^2\right) \ . \tag{7.17}$$

Here $\Sigma = (m^2_{H_2} + m^2_{\tilde{Q}} + m^2_{\tilde{U}})$, $Y_t = h_t^2/(16\pi^2)$, and where $h_t$ is the Yukawa coupling at scale Q. The analysis of [98] made the observation that the solution to Eq. (7.15), can be written in the form

$m_i^2 = (m_i^2)_p + \delta m_i^2$ where $(m_i^2)_p$ is the particular solution and the $\delta m_i^2$ obey the homogeneous equation

$$\frac{d}{dt}\begin{pmatrix} \delta m_{H_2}^2 \\ \delta m_U^2 \\ \delta m_Q^2 \end{pmatrix} = -Y_t \begin{pmatrix} 3 & 3 & 3 \\ 2 & 2 & 2 \\ 1 & 1 & 1 \end{pmatrix} \begin{pmatrix} \delta m_{H_2}^2 \\ \delta m_U^2 \\ \delta m_Q^2 \end{pmatrix} . \tag{7.18}$$

The solution to the above with the universal boundary conditions at the GUT scale is given by

$$\begin{pmatrix} \delta m_{H_2}^2 \\ \delta m_U^2 \\ \delta m_Q^2 \end{pmatrix} = \frac{1}{2} m_0^2 \begin{pmatrix} 3J(t) - 1 \\ 2J(t) \\ J(t) + 1 \end{pmatrix} , \tag{7.19}$$

where $J$ is an integration factor defined by

$$J(t) \equiv \exp\left[-6\int_0^t Y_t(t')dt'\right] . \tag{7.20}$$

As $Q \to M_G$, one has $J(t) \to 1$ and the universality of the masses is recovered at the GUT scale. Noting that $Y(t)$ at the one loop level satisfies the equation

$$\frac{dY_t}{dt} = \left(\frac{16}{3}\tilde{\alpha}_3 + 3\tilde{\alpha}_3 + \frac{13}{9}\tilde{\alpha}_1\right) Y_t - 6Y_t^2 , \tag{7.21}$$

one finds $Y_t$ so that

$$Y_t(t) = \frac{Y(0)E(t)}{1 + 6Y(0)F(t)} . \tag{7.22}$$

where $F(t)$ and $E(t)$ are defined after Eq. (7.8), one can inspect $J(t)$ to find that $J(t) = D_0(t)$, where $D_0(t)$ is defined by Eq. (7.8). Thus $\delta m^2_{H_2}$ takes the form

$$\delta\overline{m}^2_{H_2} \equiv \frac{\delta m^2_{H_2}}{m_0^2} = \frac{1}{2}\left(3D_0 - 1\right) \ . \tag{7.23}$$

and $C_1$ can be expressed in terms of $\delta\overline{m}^2_{H_2}$

$$C_1 = \frac{1}{\tan^2\beta - 1}\left(1 - \delta\overline{m}^2_{H_2}\tan^2\beta\right) \ . \tag{7.24}$$

From Eq. (7.23) we see that the correction $\delta m^2_{H_2}$ becomes independent of $m_0$ when $D_0 = 1/3$, which corresponds to the so called Focus Point region [98], and from Eq. (7.24) one finds that $\delta\overline{m}^2_{H_2} \to 0$ implies that $C_1$ also vanishes, for $\tan\beta \gg 1$. Thus for large $\tan\beta$, i.e. $\tan\beta \gtrsim 5$, the Focal Point and the Focus Point essentially merge. More explicitly, the Focus Point implies the vanishing of $\delta\overline{m}^2_{H_2}$ while the Focal Point requires the vanishing of $C_1$. A numerical analysis of the behavior of $C_1$ as a function of $Q$ for a set of fixed $\tan\beta$'s is given in Fig. 7.1 as well as a graphical representation of the different branches. Fig. 7.1 shows that the Focal Point is the boundary point of HB or, in other words, the transition point between EB and HB.

## 7.4 Focal Curves and Surfaces

*Focal Curves (HB/FC):* To exhibit the emergence of a Focal Curve we rewrite Eq. (7.1) in the following form

$$\mu^2 = -\frac{1}{2}M_Z^2 + m_0^2 C_1 + \overline{A}_0^2 C_2 + m_{1/2}^2\overline{C}_3 + \Delta\mu^2_{\text{loop}} \ , \tag{7.25}$$

$$\text{with, } \overline{A}_0 \equiv A_0 + \frac{C_4}{2C_2}m_{1/2} \ , \text{ and } \ \overline{C}_3 \equiv C_3 - \frac{C_4^2}{4C_2} \ . \tag{7.26}$$

Now, suppose we go to the renormalization group point Q where the loop corrections are minimized and, further, we are in a region of $\tan\beta$ and Q where $C_1$ is negative. In this case one finds that there exist curves where $m_0$ and $A_0$ get large while $m_{1/2}$ is held fixed and $\mu$ is relatively small compared to $m_0$ and $A_0$. Thus we can rewrite Eq. (7.25) in the form

$$\left(\overline{A}_0\sqrt{C_2}\right)^2 - \left(\sqrt{|C_1|}\, m_0\right)^2 = \pm|\mu_1|^2 \ \ \text{(HB/FC1)}, \tag{7.27}$$

where $\pm|\mu_1|^2 \equiv \mu^2 + \frac{1}{2}M_Z^2 - m_{1/2}^2\overline{C}_3 - \Delta\mu^2_{\rm loop}$ , where $\pm$ indicates the overall sign of the right hand side. Thus one has two branches corresponding to the two signs. We can interpret Eq. (7.27) as an equation of a Focal Curve in the $m_0$–$\bar{A}_0$ plane (or in the $m_0$–$A_0$ plane around a shifted origin in $A_0$) such that as $m_0$ and $A_0$ get large, $\mu$ remains fixed for fixed $m_{1/2}$ (this is Focal Curve HB/FC1 as defined in Section 7.2). In the limit when $m_0$, $|A_0|$ (and Q) are much larger than $\mu$ and $m_{1/2}$ one gets the result

$$\frac{\bar{A}_0}{m_0} \longrightarrow \frac{A_0}{m_0} \longrightarrow \pm\sqrt{\frac{|C_1|}{C_2}} \longrightarrow\sim \pm 1\ . \tag{7.28}$$

where the last entry in Eq. (7.28) arises from a numerical evaluation of $C_1$ and $C_2$ as given by Eq. (7.4) and Eq. (7.5) as shown in Fig. 7.2.

In order to identify which points lie on Focal Curves we compute the $C_i$ for each point and then subject them to the conditions necessary for them to lie on a Focal Curve. Thus for the case presented above we consider $m_{1/2}$ fixed while $m_0$ and $A_0$ vary with $C_1 < 0$ and outside the Focal Point region. An analysis illustrating Focal Curves in this case is given in Table 7.1. For this analysis and subsequent figures and tables we use both SuSpect [84] and SoftSUSY [132] which include the two loop renormalization group equations and the two loop corrections to the Higgs sector. The analysis is done for the case when $m_0$ lies in the range 500 GeV to 4000 GeV and $A_0$ lies in the range $-500$ GeV to $-3000$ GeV with $\tan\beta = 15$ and $\mu$ remaining within 10% of 600 GeV. A similar analysis is shown pictorially in the

| $m_0$ (GeV) | $A_0$ (GeV) | Q (GeV) | $\mu$ (GeV) |
|---|---|---|---|
| 500 | -482 | 750 | 597 |
| 1000 | -550 | 940 | 599 |
| 1500 | -650 | 1195 | 599 |
| 2000 | -800 | 1484 | 596 |
| 2500 | -1050 | 1790 | 600 |
| 3000 | -1350 | 2105 | 601 |
| 3500 | -1700 | 2428 | 602 |
| 4000 | -2080 | 2754 | 599 |
| 4500 | -2500 | 3083 | 600 |
| 5000 | -2950 | 3413 | 605 |

Table 7.1: Display of HB/FC1 for $m_{1/2} = 400$ GeV and $\tan\beta = 15$. This is an example of HB/FC1 with $A_0 < 0$ solution with $\mu = (600 \pm 6)$ GeV. The values of $\mu$ have been calculated with both SuSpect [84] and SoftSUSY [132].

left panel of Fig. 7.3, where we have displayed the Focal Curves for $m_{1/2} = 500\,\text{GeV}$, $\tan\beta = 45$ and $\mu = (465 \pm 35)$ GeV. We see that for $m_0$ and $|A_0|$ large, there is good agreement with Eq. (7.28), i.e., one finds $A_0/m_0 \to \pm 1$ asymptotically for large $m_0$. We note that the limit $A_0/m_0 \sim 1$ consistent with small $\mu$ was noticed and discussed recently in the analysis of [133] in the context of a string motivated model. From the left panel of Fig. 7.3 we note that this limit is part of HB and is specifically the end point of the Focal Curve HB/FC1. The left panel of Fig. 7.4 shows model points with $m_{1/2} < 1\,\text{TeV}$ and $m_0 > 10\,\text{TeV}$ with $\mu < 2\,\text{TeV}$. The result of $m_0$ up to 10 TeV were exhibited in [96], and up to 30 TeV in [133], and here we exhibit $m_0$ up to 50 TeV and beyond for $\mu < 2\,\text{TeV}$, i.e., $\mu/m_0 \ll 1$.

Now there is also another possibility of achieving a Focal Curve which can be illustrated by writing Eq. (7.3) in the form

$$\mu^2 + \frac{1}{2}M_Z^2 = m_0^2 C_1 + A_0^2 \overline{C}_2 + \overline{m}_{1/2}^2 C_3 + \Delta\mu_{\text{loop}}^2 \,. \tag{7.29}$$

$$\overline{m}_{1/2} \equiv m_{1/2} + \frac{C_4}{2C_3}A_0, \quad \overline{C}_2 \equiv C_2 - \frac{C_4^2}{4C_3} \, . \tag{7.30}$$

As before, we can write this equation in the form

$$\left(\overline{m}_{1/2}\sqrt{C_3}\right)^2 - \left(m_0\sqrt{|C_1|}\right)^2 = \pm|\mu_2|^2 \ \ \text{(HB/FC2)}, \tag{7.31}$$

where $\pm|\mu_2|^2 \equiv \mu^2 + \frac{1}{2}M_Z^2 - A_0^2\overline{C}_2 - \Delta\mu^2_{\rm loop}$ . Thus again one has two branches depending on the sign. Here one keeps $A_0$ fixed while $m_0$ and $m_{1/2}$ get large and $\mu$ is relatively small (this is Focal Curve HB/FC2 as defined in Section 7.2). For the case when $|\mu_2|$ is small relative to $m_0$ and $\overline{m}_{1/2}$ one finds the following relationship asymptotically

$$\frac{\overline{m}_{1/2}}{m_0} \longrightarrow \frac{m_{1/2}}{m_0} \longrightarrow \sqrt{\frac{|C_1|}{C_3}} \longrightarrow \approx 0.4 \, . \tag{7.32}$$

where the last entry in Eq. (7.32) is obtained by using Eq. (7.4) and Eq. (7.6) as shown in Fig. 7.2. An illustration of this case is given in the right panel of Fig. 7.3 where $m_{1/2}$ gets very large. For these curves we see that we can still have models with $\mu$ small ($\mu \lesssim 450\,\text{GeV}$) and $m_{1/2}$ large ($m_{1/2} \gtrsim 1500\,\text{GeV}$), which leads to the gluino mass being on the order of a few TeV or larger.

To show that there exists a larger set of Focal Curves than the cases we have discussed above we exhibit a whole set of parametric Focal Curves which we label as HB/FC$_\alpha$. To do this we define $m_{1/2} = \frac{\alpha}{1-\alpha}|A_0|$, where $0 \leqslant \alpha < 1$. This allows us to rewrite Eq. (7.3) as

$$\pm\,|\mu_\alpha|^2 = -\left(\sqrt{|C_1|}\right)^2 m_0^2 + C_\alpha A_0^2 \, . \tag{7.33}$$

where $\pm|\mu_\alpha|^2 = \mu^2 + \frac{1}{2}M_Z^2 - \Delta\mu^2_{\rm loop}$. Further,

$$C_\alpha = C_2 + \frac{\alpha^2}{(1-\alpha)^2}C_3 + \frac{\alpha}{1-\alpha}C_4 \ \ {\rm sgn}\,(A_0) \ \ , \tag{7.34}$$

Eq. (7.33) shows that there exists parametric Focal Curves, parameterized by $\alpha$, where one can get the same value of $\mu$ which can be taken to be small, while $\alpha$ can take on values in the range $[0,1)$. This phenomenon illustrated in the right panel of Fig. 7.4 displays several Focal Curves for constant $\mu$. One finds that as $\alpha$ decreases the asymptotic form of the curves in the $A_0 - m_0$ plane become more steep. This result is in agreement with the theoretical prediction at one loop for the asymptotic ratio $A_0/m_0$ which is

$$A_0/m_0 \rightarrow \pm\sqrt{\left|C_1\right|/C_\alpha} \ . \tag{7.35}$$

Focal regions in mSUGRA Hyperbolic Branch

| Focal Region | Symbol | Varying Parameters | Fixed Parameters |
|---|---|---|---|
| Focal Point | HB/FP | $m_0$ | $m_{1/2}$, $A_0$ |
| Focal Curve | HB/FC1 | $m_0$ $A_0$ | $m_{1/2}$ |
| Focal Curve | HB/FC2 | $m_0$ $m_{1/2}$ | $A_0$ |
| Focal Curve | HB/FC$_\alpha$ | $m_0$, $A_0$ or $m_{1/2}$ | $m_{1/2} = \frac{\alpha}{1-\alpha}\lvert A_0\rvert$ |
| Focal Surface | HB/FS | $m_0$, $m_{1/2}$, $A_0$ | |

Table 7.2: A summary of the classification of focal regions in mSUGRA. The focal regions are those where $\mu$ remains constant while one or more soft parameters may get large. $\tan\beta$ is assume fixed in each of the cases discussed and $\alpha$ has the range $0 \leqslant \alpha < 1$.

*Focal Surfaces HB/FS:* We consider next the radiative breaking of the electroweak symmetry where all the three parameters $m_0$, $m_{1/2}$, or $A_0$ can get large while $\mu$ remains small. This solution is again valid in the region of the parameter space where $C_1$ turns negative at the value of renormalization group point which minimizes the loop correction. This is the Focal Surface HB/FS as defined in Section 7.2

and we can express it in the following two forms

$$\pm |\mu_s|^2 = -\left(\sqrt{|C_1|}\, m_0\right)^2 + \left(\overline{A}_0\sqrt{C_2}\right)^2 + \left(m_{1/2}\sqrt{\overline{C}_3}\right)^2 \tag{7.36}$$

where $\pm|\mu_s|^2 = \mu^2 + \frac{1}{2}M_Z^2 - \Delta\mu^2_{\rm loop}$. A summary of focal regions is given in Table 7.2. An exhibition of a Focal Surface for the case $\mu = (0.465 \pm 0.035)$ TeV is given in Fig. 7.5. We note that on the Focal Surface shown in Fig. 7.5 $m_0$, $m_{1/2}$, or $A_0$ can all be seen to get large in certain regions while $\mu$ remains relatively constant. We note in passing that another way to generate a Focal Surface is to consider a Focal Curve HB/FC$_\alpha$ and let $\alpha$ vary over its allowed range $0 \leqslant \alpha < 1$. Thus a Focal Surface can be viewed as a collection of Focal Curves as in the right panel of Fig. 7.4.

## 7.5 LHC and Dark Matter Implications

*Constraints of LHC-7 data on Focal Regions:* We now investigate the implications of the recent LHC data [75–77, 134–136] on the focal regions constituted of the Focal Point, Focal Curves and Focal Surfaces. To this end we first generate mSUGRA parameter points using a uniformly distributed random scan over the soft parameters with $m_0 < 4$ TeV, $m_{1/2} < 2$ TeV, $A_0/m_0 \in (-10, 10)$, and $\tan\beta \in (1, 60)$. After the constraint of REWSB roughly 22 million mSUGRA parameter points are collected. These are then subject to experimental constraints which include the LEP and Tevatron [90] limits on the Higgs mass and on the sparticle masses as discussed in [137, 138] and $\mathcal{B}r\left(B_s^0 \to \mu^+\mu^-\right) \leqslant 1.1 \times 10^{-8}$ [139]. These constraints will be referred to as the *general constraints*. In imposing these constraints we use MicrOMEGAs [87] for the computation of the relic density and SuSpect for the computation of the sparticle mass spectrum and $\mu$ at the scale at which electroweak symmetry breaks, $Q_{\rm EWSB}$. A more statistically rigorous procedure for the implementation of the constraints would be to use $\chi^2$ or maximum likelihoods, but for the purpose of this analysis it is unnecessary.

CMS and ATLAS have reported results for supersymmetry searches [75–77, 134–136] based on about 1 fb of data. The implications of these results (as well as dark matter results) have been considered for the parameter space of SUSY models in a number of works [100, 102, 137, 140–151] and some discussion on the collider implications on naturalness can be found in [152–155]. Here we use the constraint arising from the recent the ATLAS 1 fb search [135, 136] and the CMS 1 fb search [75] to explore their implications on the focal region. The implications of the LHC data for the Ellipsoidal Branch and for the Hyperbolic Branch are exhibited in Fig. 7.6. The top left panel gives the parameter space in EB and here one finds that most of the model points being constrained by LHC-7 lie in the low $m_0$ region. The top right panel gives the corresponding analysis for HB/FP and HB/FC. In the analysis here we have assumed that $m_{1/2}/m_0 \leqslant 0.1$ for HB/FC1 and $A_0/m_0 \leqslant 0.1$ for HB/FC2. The middle left panel exhibits the same set of parameter points on HB/FP and HB/FC as the top left panel except that the regions are now labeled according to the sparticle landscape picture [123, 156–158] by the next to lightest particle beyond the Standard Model (NLP) in the mass hierarchy (note that this includes all of the sparticles and Higgs sector particles, but omits the Standard Model-like $h^0$). Here one finds that most of the region being constrained by the LHC-7 data is the high $m_0$ region. The HB region contains the Focal Point, Focal Curves and Focal Surfaces as discussed in the preceding sections. Of these we display just the Focal Point region in the middle right panel. Here one finds that the Focal Point region is highly depleted and is further constrained by the LHC-7 data. The bottom panels of Fig. 7.6 show the parameter points on the entire HB region consisting of the HB/FP, HB/FC and HB/FS, where the left panel displays the parameter points where the NLP is either a $\tilde{\chi}_1^{\pm}$ or $\tilde{\tau}_1$, and the right hand panel shows the parameter points where the NLP is $\tilde{t}$, A or H. Thus the analysis of Fig. 7.6 shows that the HB/FP is almost empty and most of the parameter space remaining on HB lies in the region of Focal Curves or Focal Surfaces, i.e., it lies on HB/FC and HB/FS.

*LHC signals on HB/FC1:* We discuss now an important phenomenon related to HB/FC1, which

arises from the constraint that $m_{1/2}$ and $\mu$ are fixed even though $A_0$ and $m_0$ get large. This can lead to observable leptonic signatures, specifically the trileptonic signature [159–163], even when $m_0$ lies in the several TeV region (For a recent work on the trileptonic signal see [164]). The reason for this is rather obvious, in that the chargino and the neutralino masses are held relatively constant along the Focal Curve HB/FC1. Thus the production cross-section for the charginos and neutralinos will be essentially independent of $m_0$. We are specifically interested in the production cross-section of the light chargino $\tilde{\chi}_1^\pm$ and the second lightest neutralino $\tilde{\chi}_2^0$, i.e., $\sigma_{\tilde{\chi}_1^\pm \tilde{\chi}_2^0}$ which can lead to a trileptonic signal from the decay of $\tilde{\chi}_1^\pm, \tilde{\chi}_2^0$ so that $\tilde{\chi}_1^\pm \to l^\pm + \nu_l + \tilde{\chi}_1^0$ and $\tilde{\chi}_2^0 \to l^+ l^- \tilde{\chi}_1^0$ (important contributions can also arise from the production of $\tilde{\chi}_1^\pm \tilde{\chi}_i^0$ ($i = 3, 4$) depending on the part of the parameter space one is in). The chargino and neutralino final state can arise at tree level from two main processes in pp collisions. Thus, for example, $\tilde{\chi}_a^+ \tilde{\chi}_i^0$ can arise from the s-channel fusion diagram $u + \bar{d} \to W^{+*} \to \tilde{\chi}_a^+ + \tilde{\chi}_i^0$ and from the t-channel exchange diagram of a $\tilde{d}_L$ squark. The latter diagram is suppressed when $m_0$ is large so that the main production cross-section proceeds via the s-channel off -shell $W^\pm$ production [159–163]. Thus the $\tilde{\chi}_1^\pm \tilde{\chi}_i^0$ production cross-section is expected to be independent of $m_0$ for large $m_0$. The constancy of $\sigma_{\tilde{\chi}_1^\pm \tilde{\chi}_2^0}/\sigma_{\text{total}}$ is exhibited in Fig. 7.7 for HB/FC1 defined by $m_{1/2} = 0.35\,\text{TeV}$, $\tan\beta = 45$ and $\mu = (0.20 \pm 0.01)\,\text{TeV}$. The branching ratio into trileptons is also computed. In the analysis we use SUSY-HIT [165] for the computation of decays, PYTHIA [86] for event generation, and PGS [117] for detector simulation. For the case of models exhibited in Fig. 7.7 the $\tilde{\chi}_1^\pm \tilde{\chi}_2^0$ production cross-section is $(164.3 \pm 9.97)$ fb and the $\tilde{\chi}_1^\pm \tilde{\chi}_3^0$ production cross-section is $(112.1 \pm 8.53)$ fb, which leads to roughly 50 raw trilepton events at 10 fb where we have included $\tau$'s in the definition of leptons. The number of events will be reduced when off-line cuts are imposed and a more detailed analysis would require further knowledge of the cuts used in the experimental multileptonic search at that luminosity. Of course a much larger number of events is expected at higher $\sqrt{s} = 10\,\text{TeV}$, or $\sqrt{s} = 14\,\text{TeV}$ at the same luminosity. Similarly, the $\tilde{\chi}_1^\pm \tilde{\chi}_2^0$ and $\tilde{\chi}_1^\pm \tilde{\chi}_3^0$ production states can decay hadronically. For the hadronic analysis we use the cuts as outlined in Ref. 1 of [135, 136] by ATLAS and find

that our effective cross-sections are $(5.2 \pm 0.15)$ fb, $(0.7 \pm 0.16)$ fb, $(1.6 \pm 0.33)$ fb, $(0.6 \pm 0.18)$ fb and $(0.5 \pm 0.15)$ fb which can be compared to the reported 95% C.L. upper bounds at 1.04 fb of 22 fb, 25 fb, 429 fb, 27 fb and 17 fb, respectively. Typically these points produce hard jet signatures, but with low jet multiplicity. Thus the hadronic signals on HB/FC1 may become visible if a luminosity in excess of 20 fb can be achieved at LHC-7. Another possible channel for discovery would be a combination of jets and leptons, but such an analysis is outside the scope of the current work.

*Dark Matter in the EB and the Focal Domains:* It is interesting to investigate the prediction for dark matter searches in EB vs HB domains. We begin by considering first the full parameter space of mSUGRA which, after general constraints, is exhibited in the top left panel of Fig. 7.8 where the LHC-7 constraint with 1 fb of data is also exhibited. The spin-independent cross-section vs the neutralino mass corresponding to the parameter space in the top left panel is exhibited in the top right panel where we have also exhibited the experimental exclusion from XENON-100 experiment. Next, in the bottom-left panel of Fig. 7.8, we exhibit the spin-independent neutralino-proton cross-section vs the neutralino mass for EB while the bottom right panel exhibits the same for the full HB domain consisting of HB/FP, HB/FC and HB/FS. The HB/FP region indicated by the red area is rather small while most of the remaining parameter space is constituted of HB/FC and HB/FS.

## 7.6 Conclusion

It is shown that the Hyperbolic Branch of radiative breaking of the electroweak symmetry consists of several regions of the parameter space where $\mu$ is small. These regions consist of the Focal Points, Focal Curves and Focal Surfaces. The Focal Point (HB/FP) region is where $m_0$ can get large with fixed $m_{1/2}$ and $A_0$ while $\mu$ remains small. A small $\mu$ can also be achieved on Focal Curves and on Focal Surfaces. There are two possible Focal Curves: HB/FC1 and HB/FC2 such that on HB/FC1, $m_0$ and $A_0$ both

may get large, while $m_{1/2}$ and $\mu$ remain fixed, while on HB/FC2, $m_0$ and $m_{1/2}$ may get large while $A_0$ remains fixed. These two general categories can be unified by the parameter $\alpha$ defining the Focal Curve mode HB/FC$_\alpha$. An explicit illustration of these regions is given for mSUGRA where it is shown that the HB/FP region is significantly depleted when the current constraints from the LHC-7 data are applied. Thus the remaining parameter points in this region lie on Focal Curves (or more generally, on Focal Surfaces). The possible signatures arising from the HB region were briefly discussed. On the HB/FC1 region one can get scalar masses to lie in the several TeV region and still have light gauginos. This region gives a significant enhancement to proton lifetime [166] because of the smallness of the gaugino masses and relative heaviness of the squark masses.

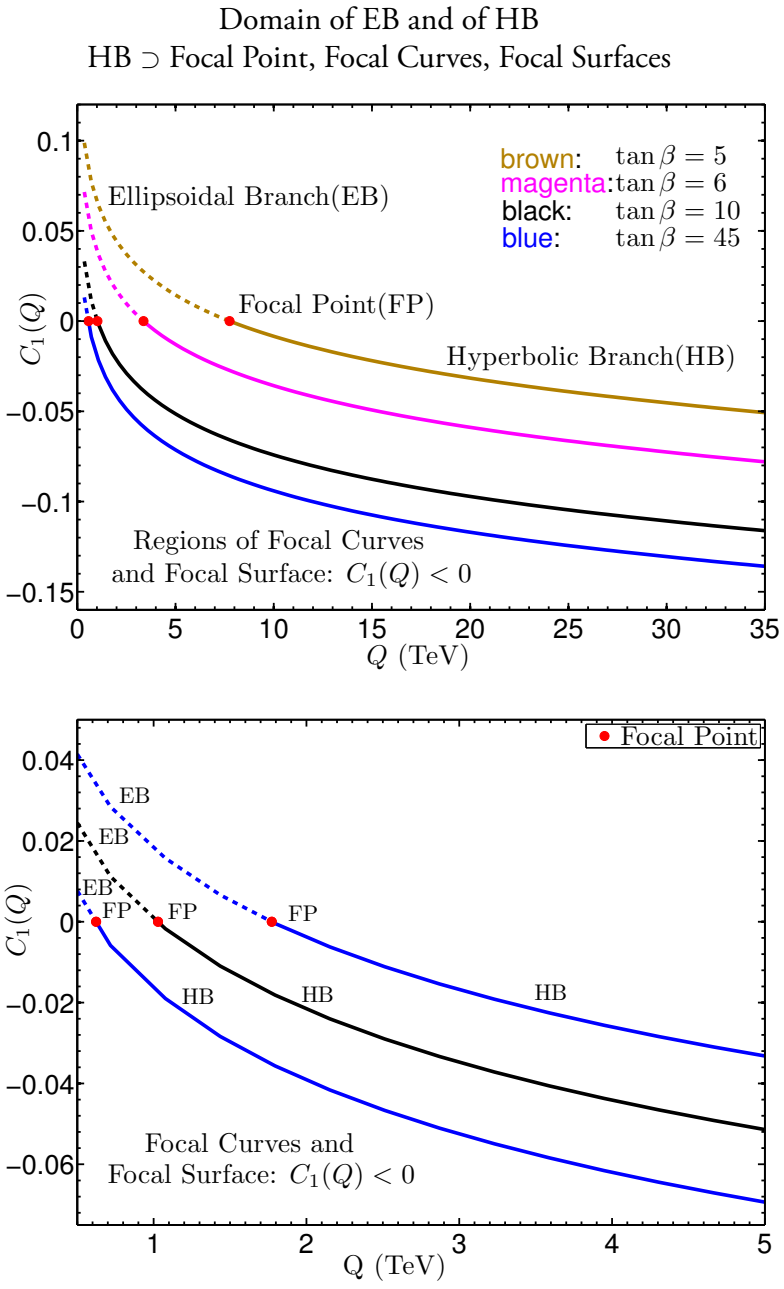


Figure 7.1: Left panel: A display of $C_1$ as a function of Q for different values of tan β, i.e., tan β = 5 (brown), tan β = 6 (magenta), tan β = 10 (black) and tan β = 45 (blue). For larger values of tan β, $C_1$ is positive for Q $\lesssim$ 1 TeV. Right panel: A display of the sensitivity of $C_1$(Q) to the top quark mass. The dashed blue lines correspond to $\pm 1\sigma$ in the top pole mass around the black solid line which corresponds to the central value, where the pole mass is taken to be $m_t = (173.1 \pm 1.3)$ GeV.

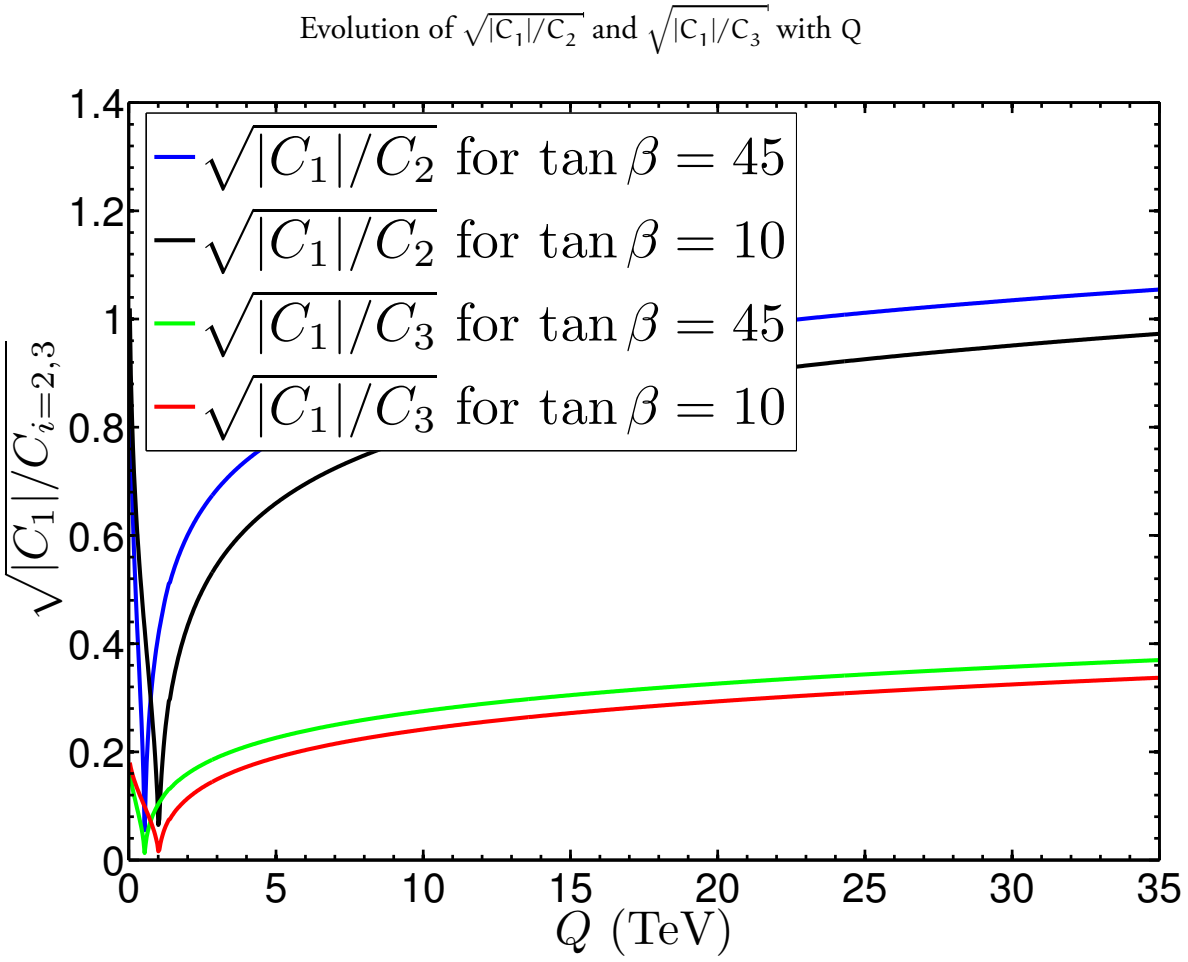


Figure 7.2: A numerical analysis of the evolution of $\sqrt{|C_1|/C_2}$ and $\sqrt{|C_1|/C_3}$ using Eq. (7.4), Eq. (7.5), and Eq. (7.6). Here one finds that $\sqrt{|C_1|/C_2}$ tends to ~ 1 and $\sqrt{|C_1|/C_3}$ tends to ~ 0.4 as Q becomes large. The analysis is shown for $\tan\beta = 10$ and $\tan\beta = 45$.

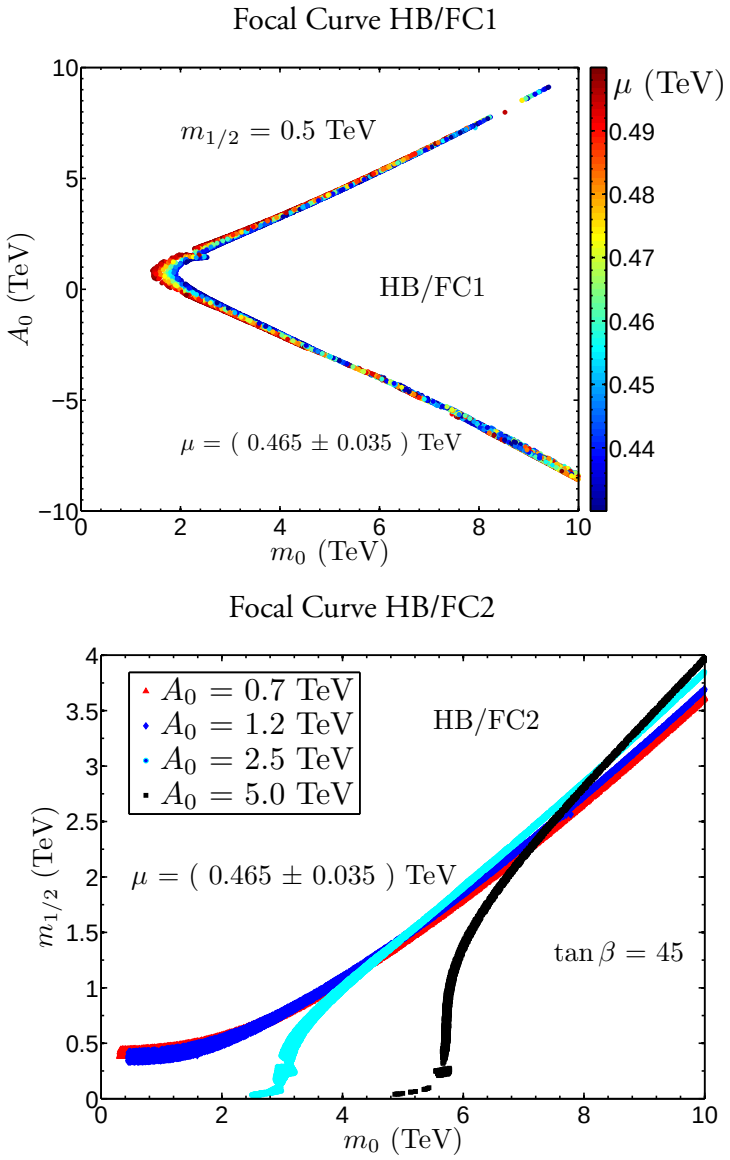


Figure 7.3: Left panel: Exhibition of Focal Curves HB/FC1 with $m_{1/2} = 0.5$ TeV and $\tan\beta = 45$ where $\mu$ lies in the range $\mu = (0.465 \pm 0.035)$ TeV. Points are displayed by $\mu$ value. Right panel: An illustration of Focal Curves HB/FC2 which arise when $m_0$ and $m_{1/2}$ are free to vary while $A_0$ is fixed and $\mu$ is held relatively constant. The analysis is for $\tan\beta = 45$ and for four values of $A_0$ which are $A_0 = 0.7$ TeV (red), $A_0 = 1.2$ TeV (blue), $A_0 = 5.0$ TeV (cyan) and $A_0 = 2.5$ TeV (black). The analysis above shows that on the Focal Curve HB/FC1 and HB/FC2 one has good agreement with the asymptotic behavior as predicted by Eq. (7.28) and Eq. (7.32).

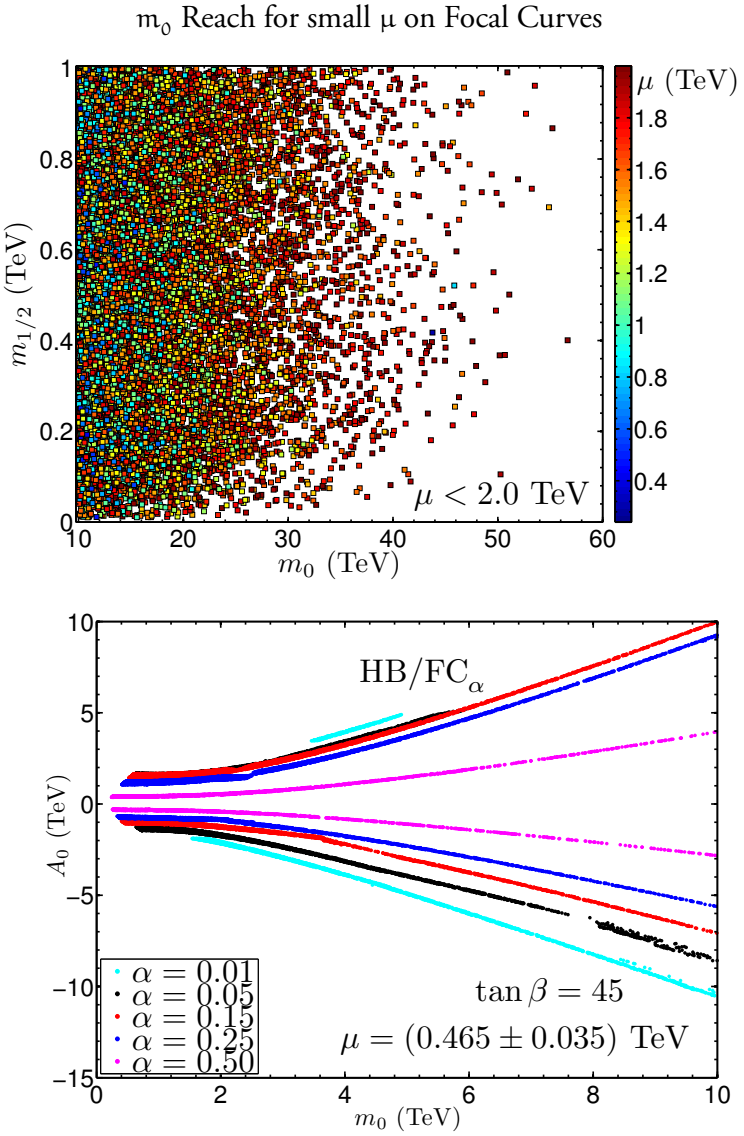


Figure 7.4: Left panel: An exhibition of the reach in $m_0$ on Focal Curves HB/FC1 and HB/FP with $\mu < 2$ TeV consistent with radiative breaking of the electroweak symmetry where points are displayed by their $\mu$ value in units of TeV. It is seen that an $m_0$ as large as 50 TeV and above can be reached in this region. Essentially all models lie on HB/FC1, but there are a few (0.1% of the displayed models) that are HB/FP. Models were found by doing a uniformly distributed parameter scan of $m_0$, $m_{1/2}$, $A_0$ and $\tan\beta$. Right Panel: Exhibition of Focal Curves HB/FC$_\alpha$ using $m_{1/2} = \frac{\alpha}{1-\alpha}|A_0|$ for $\tan\beta = 45$ and $\mu = (0.465 \pm 0.035)$ TeV with $m_0$ between 10 GeV and 10 TeV and $A_0$ between $-8m_0$ and $8m_0$. We display the cases where $\alpha = 0.01, 0.05, 0.15, 0.25, 0.50$ and notice that for smaller $\alpha$ the asymptotic behavior is more steep.

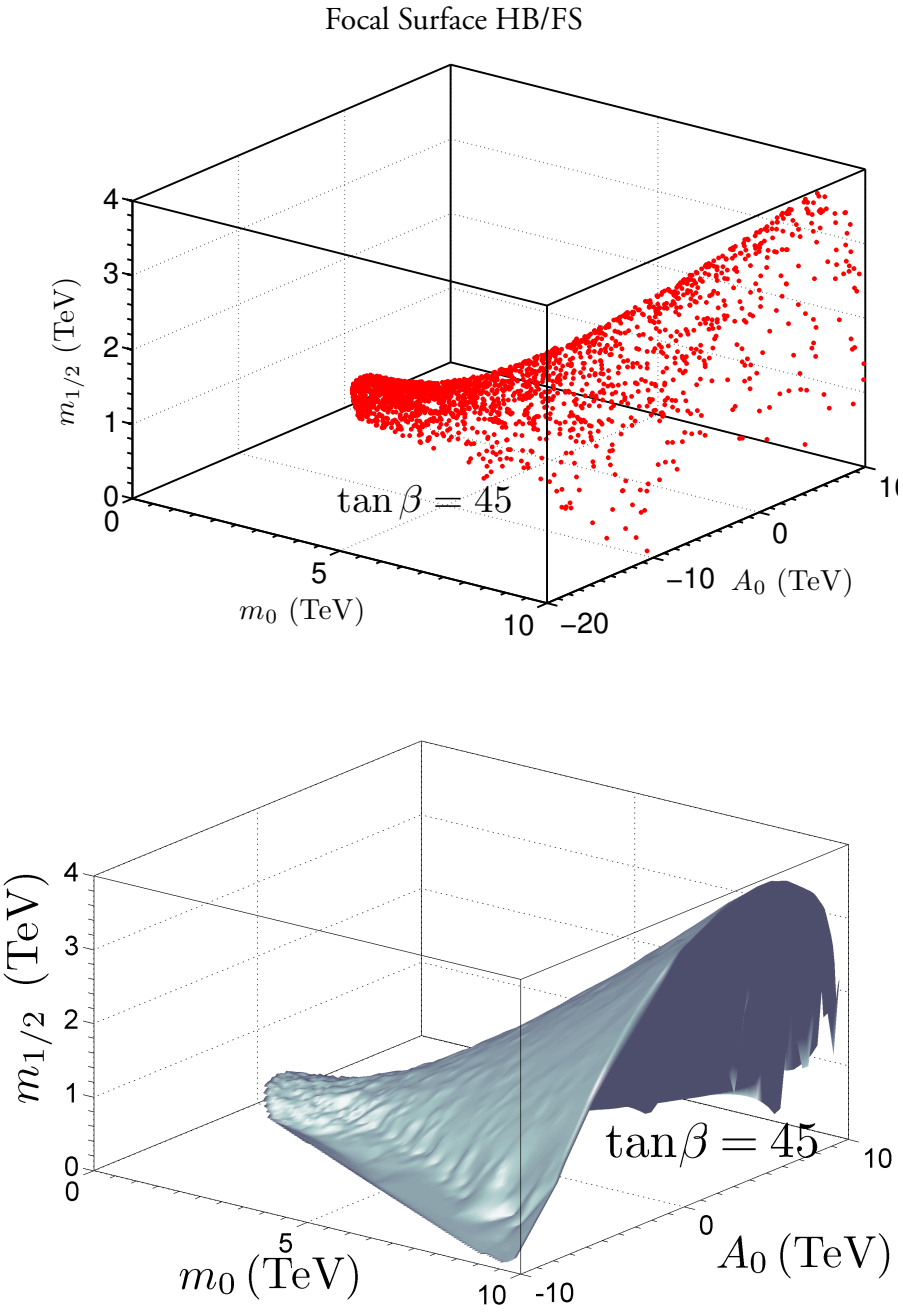


Figure 7.5: Exhibition of a Focal Surface when $\tan\beta = 45$ and $\mu = (0.465 \pm 0.035)$ TeV while $m_0$, $m_{1/2}$, and $A_0$ can all get large. The left panel shows a scatter plot of model points lying on a Focal Surface. The right panel shows the same Focal Surface using an interpolation of the points presented in the left panel.

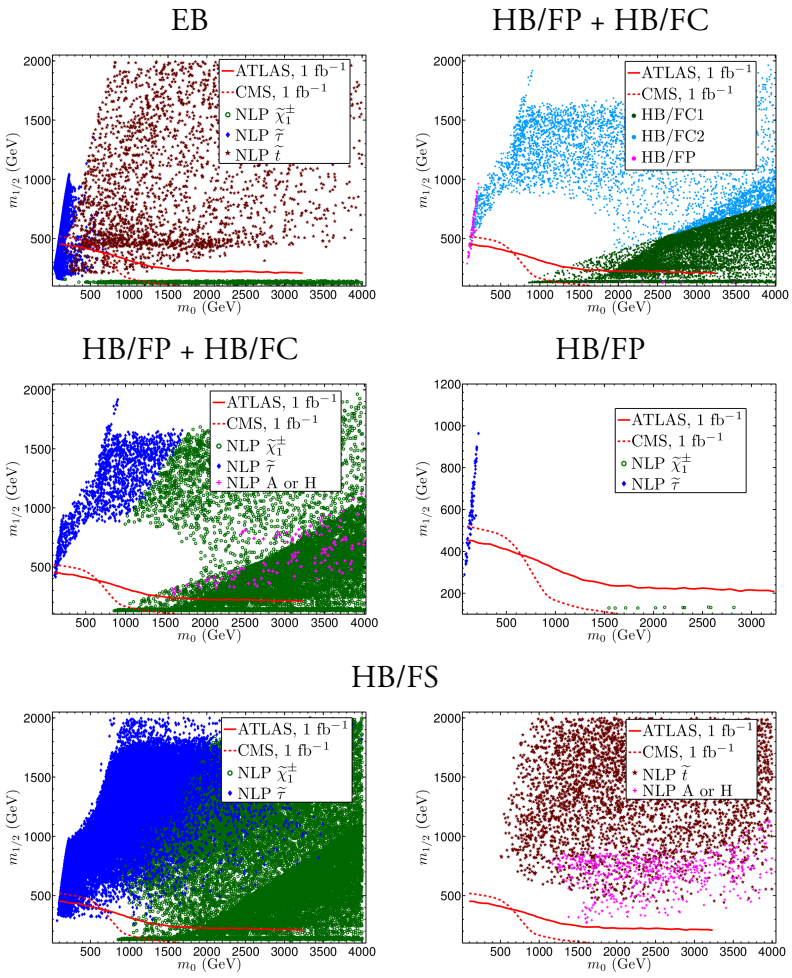


Figure 7.6: Top Left: The mSUGRA parameter points passing the general constraints in the $m_0$–$m_{1/2}$ plane that are a part of the Ellipsoidal Branch, labeled by the NLP. Please note in the definition of EB we have excluded the HB/FP region. Top Right: The mSUGRA parameter points in the $m_0$–$m_{1/2}$ plane passing the general constraints that are a part of HB/FC1, HB/FC2, or HB/FP, labeled as such. Middle Left : An exhibition of the mSUGRA parameter points passing general constraints that also lie on HB/FC1 or HB/FC2, labeled by the NLP. Middle Right: The mSUGRA parameter points passing the general constraints that arise from the Focal Point (HB/FP) region. Bottom Left: A display of the mSUGRA parameter points containing the $\tilde{\chi}_1^{\pm}$ and the $\tilde{\tau}_1$ NLPs passing the general constraints and including the parameters in HB/FS, i.e., the entire Hyperbolic Branch except for HB/FP. Bottom Right: Same as Bottom Left except the NLPs displayed are $\tilde{t}_1$, A, H.

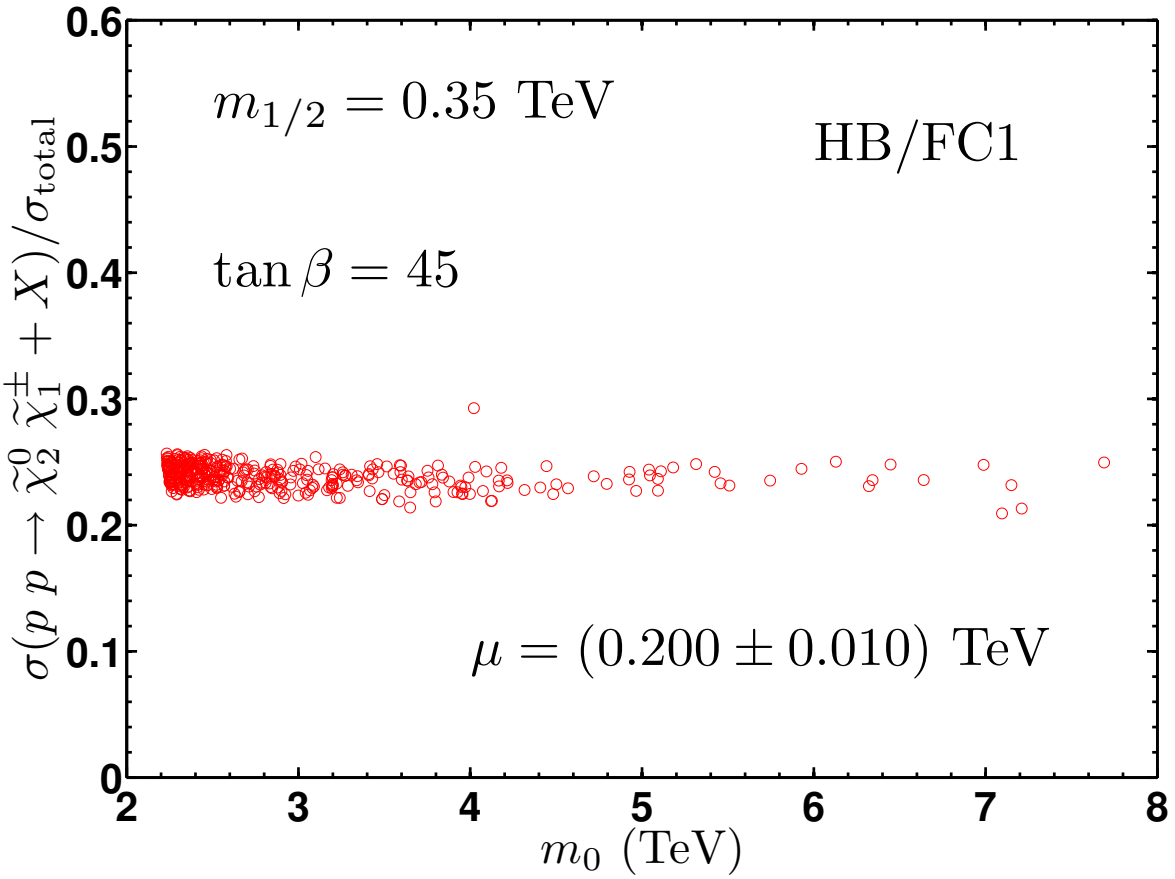


Figure 7.7: Fraction of the total cross-section that is made up by $\tilde{\chi}_1^{\pm}\tilde{\chi}_2^0$ production as a function of $m_0$ at $\sqrt{s} = 7$ TeV. The analysis shows that the production cross-section is rather insensitive to $m_0$ which implies the signatures from HB/FC1 such as the trileptonic signal could be visible even in the asymptotic region when $m_0$ and $A_0$ are very large.

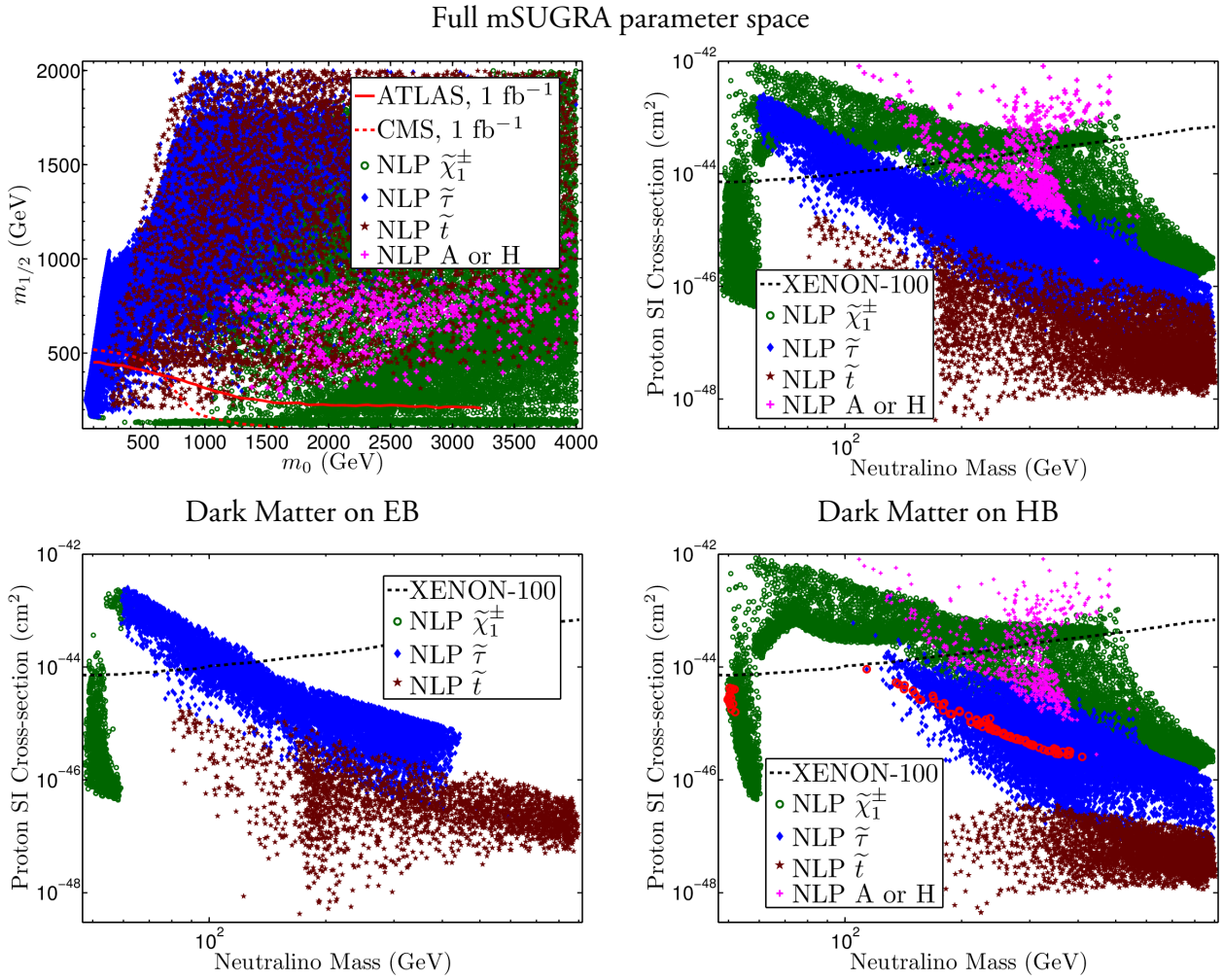


Figure 7.8: Top left: A display for the mSUGRA model points in the $m_0$–$m_{1/2}$ plane that pass the general constraints as discussed in text. Top right: A display of the spin-independent neutralino-proton cross-section $\sigma^{SI}_{\widetilde{\chi}_1^0,p}$ for the parameter points in the top left panel. Bottom left: A display of the spin-independent neutralino-proton cross-section, $\sigma^{SI}_{\widetilde{\chi}_1^0 p}$, for the EB region. Bottom right: Same as the bottom left except that the analysis is for HB which contains the Focal Point as well as Focal Curves and Focal Surfaces.

# Chapter 8

# Higgs Mass Predictions in Supergravity Unification

## 8.1 Introduction

LHC-7 has narrowed down the mass range of the light Higgs boson. This result is consistent with the supergravity unification framework, and the current Higgs boson mass window implies a rather significant loop correction to the tree value, pointing to a relatively heavy scalar sparticle spectrum with universal boundary conditions. It is shown that the largest value of the Higgs boson mass is obtained on the Hyperbolic Branch of radiative breaking. The implications of light Higgs boson in the broader mass range of 115 GeV to 131 GeV and a narrower range of 123 GeV to 127 GeV are explored in the context of the discovery of supersymmetry at LHC-7 and for the observation of dark matter in direct detection experiments.

In models based on supersymmetry the light Higgs boson [12–15] has a predictive mass range, and recently LHC-7 has stringently constrained the light Higgs boson to lie in the 115 GeV to 131 GeV

range (ATLAS) and the 115 GeV to 127 GeV range (CMS) at the 95% C.L. [167, 168] with possible hints of evidence within a few GeV of 125 GeV. This mass window lies in the range predicted by supergravity unification (SUGRA) [51, 169]. In this chapter, we investigate supergravity model points that are consistent with the mass range given by the new LHC-7 data [167, 168].

LHC-7 has made great strides in exploring the parameter space of supersymmetric models. Indeed, early theoretical projections for the expected reach in sparticle masses and in the $m_0$–$m_{1/2}$ plane for LHC-7 [79, 80, 170] have been met and exceeded by the 1 fb and 2 fb LHC-7 data [75–77, 134–136]. The implications of the new LHC results have been analyzed by a number of authors in the context of lower limits on supersymmetric particles and in connection with dark matter [100, 102, 137, 138, 140–152]. Now the most recent results from CERN [167, 168] indicate that the two detectors, ATLAS and CMS, have collected as much as 5 fb of data. One of the most interesting implications of the LHC-7 data concerns the constraints it imposes on the Higgs boson mass.

As mentioned above we will work within the framework of a supergravity grand unification model with universal boundary conditions [51–53, 169]. Here we discuss the dependence of the light Higgs boson mass on the parameter space, i.e., on $m_0$, $m_{1/2}$, $A_0$, $\tan\beta$ [97, 101], where $m_0$, $m_{1/2}$, and $A_0$ are the parameters at the GUT scale, where the GUT scale, $M_{\rm GUT} \sim 2 \times 10^{16}$ GeV is defined as the scale at which the gauge couplings unify, and where $m_0$ is soft scalar mass, $m_{1/2}$, the gaugino mass, $A_0$, the trilinear coupling and $\tan\beta$, the ratio of the two Higgs VEVs in the minimal supersymmetric standard model.

An important aspect of SUGRA models is that the radiative electroweak symmetry breaking, REWSB, is satisfied for $A_0/m_0$ typically in the $-5$ to 5 range. The renormalization group evolution then leads to a value of the trilinear coupling, $A_t$, at the electroweak scale to also be $\mathcal{O}$(TeV). The relevance of this observation is that quite generically supergravity unification leads to a sizable $A_t$ which is needed to give a substantial leading order loop correction to the Higgs Boson mass for any fixed $\mu$, $\tan\beta$ and $m_0$,

where $\mu$ is the Higgs mixing parameter in the superpotential. Thus a generic prediction of SUGRA models under radiative electroweak symmetry breaking for a sizable $A_0/m_0$ is that there would be a substantial loop correction to the Higgs boson mass, and it is well known that the light Higgs mass at the tree level has the value $m_{h^0} \leqslant M_Z$ and there is a significant loop correction $\Delta m_{h^0}$ to lift it above $M_Z$ [171–180].

The dominant one loop contribution arises from the top/stop sector and is given by

$$\Delta m_{h^0}^2 \simeq \frac{3m_t^4}{2\pi^2 v^2} \ln \frac{M_S^2}{m_t^2} + \frac{3m_t^4}{2\pi^2 v^2} \left( \frac{X_t^2}{M_S^2} - \frac{X_t^4}{12 M_S^4} \right) , \tag{8.1}$$

where $v = 246\,\mathrm{GeV}$, $M_S$ is an average stop mass, and $X_t$ is given by

$$X_t \equiv A_t - \mu \cot\beta . \tag{8.2}$$

From Eq. (8.1) one finds that the loop correction is maximized when

$$X_t \sim \sqrt{6} M_S . \tag{8.3}$$

We note that there can be important loop corrections also from the b-quark sector and a correction similar to Eq. (8.1) can be written where $X_t$ is replaced by $X_b = A_b - \mu \tan\beta$ along with other appropriate replacements. Thus when $\mu \tan\beta$ becomes large, the b-quark contribution to the loop correction, which is proportional to powers of $X_b$, becomes large and is comparable to the top contribution which implies that a high Higgs mass can also result in stau-coannihilation models where typically $m_{1/2}$ is large and $m_0$ is relatively small.

Further, we note that the approximation of Eq. (8.3) would not hold if the off-diagonal elements of the stop mass squared matrix are comparable to the diagonal elements which can happen for very

large $A_t$. In addition, it is well known that the two loop corrections are substantial (see e.g. [181] for a numerical analysis). While the correction at the one loop level has the symmetry $X_t \to -X_t$, this symmetry is lost when the two loop corrections are included and then sgn $(A_0/m_0)$ plays an important role in the corrections to the Higgs boson mass. As seen later this observation is supported by the full numerical analysis which includes the two loop corrections. We note in passing that the theoretical predictions for the light Higgs boson mass depend sensitively on the input parameters which include the gauge coupling constants as well as the top mass with their experimental errors. Additionally, there are also inherent theoretical uncertainties which together with the uncertainties of the input parameters allow theoretical predictions of the light Higgs boson mass accurate to only within an error corridor of a few GeV (see e.g. [181]).

Since the loop corrections involve the sparticle spectrum, a large loop correction implies a relatively heavy sparticle spectrum and specifically heavy scalars. Such a possibility arises in REWSB which allows for scalars heavier than 10 TeV [96]. Specifically, with scalars approaching 10 TeV, the Higgs boson mass can remain heavy while the gaugino sector is free to vary. This occurs within the minimal SUGRA framework and similar situations arise in other works of radiative breaking [133, 182, 183].

Indeed, quite generally in SUGRA and string models with the MSSM field content, the analysis of the Higgs mass with loop corrections under the constraints of REWSB gives an upper limit on the light Higgs boson mass of about 135 GeV for a wide range of input parameters.[1] A very interesting aspect of the recent LHC-7 data concerns the fact that a large portion of the Higgs boson mass window has been excluded and what remains is consistent with the range predicted by the SUGRA models.

[1] We note that heavier Higgs boson masses can be obtained in a variety of different models such as hierarchical breaking models [129, 184, 185] or by addition of vector like multiplets [186].

## 8.2 Higgs Mass in minimal SUGRA

We discuss now the dependence of the light Higgs boson mass on the SUGRA parameter space. The numerical analysis was done using a uniformly distributed random scan over the soft parameters with $\mathrm{sgn}(\mu) = 1$, $m_{1/2} < 5\,\mathrm{TeV}$, $\left|A_0/m_0\right| \leqslant -8$, $\tan\beta \in (1, 60)$ and two different ranges for $m_0$. One scan was done sampling over lower values of $m_0$, i.e. $m_0 \leqslant 4\,\mathrm{TeV}$, and has roughly 10 million mSUGRA model points (where a model point is defined as 1 set of the mSUGRA input parameters). The other scan was done sampling over larger values of $m_0$, i.e. $m_0 \geqslant 4\,\mathrm{TeV}$, and contains approximately 24 million mSUGRA model points. For the scan sampling over large values of $m_0$ we have imposed the upper bound of $m_0 = 100\,\mathrm{TeV}$.

Experimental constraints were then applied to these mSUGRA model points which include the limits on sparticle masses from LEP [90]: $m_{\tilde{\tau}_1} > 81.9\,\mathrm{GeV}$, $m_{\widetilde{\chi}_1^\pm} > 103.5\,\mathrm{GeV}$, $m_{\tilde{t}_1} > 95.7\,\mathrm{GeV}$, $m_{\tilde{b}_1} > 89\,\mathrm{GeV}$, $m_{\tilde{e}_R} > 107\,\mathrm{GeV}$, $m_{\tilde{\mu}_R} > 94\,\mathrm{GeV}$, and $m_{\tilde{g}} > 308\,\mathrm{GeV}$. Additionally, we apply the WMAP [94, 95] $4\sigma$ upper bound, i.e. $\Omega_\chi h^2 < 0.1344$. We define $(\Omega_\chi h^2)_{\mathrm{WMAP}} \equiv 0.1120$, the central value from the WMAP-7 data. Only taking the WMAP upper limit allows for the possibility of multicomponent dark matter [187]. Other constraints applied to the mSUGRA parameter points include the $g_\mu - 2$ [91] constraint $\left(-11.4 \times 10^{-10}\right) \leqslant \delta\left(g_\mu - 2\right) \leqslant \left(9.4 \times 10^{-9}\right)$ and constraints from B-physics measurements [93, 119, 139] which yield flavor constraints from the data, i.e. $\left(2.77 \times 10^{-4}\right) \leqslant \mathcal{B}r\left(b \to s\gamma\right) \leqslant \left(4.37 \times 10^{-4}\right)$ (where this branching ratio has the NNLO correction [88]) and $\mathcal{B}r\left(B_s \to \mu^+\mu^-\right) \leqslant 1.1 \times 10^{-8}$. As done in [138, 188], we will refer to these constraints as the *general constraints*. These constraints were imposed using MicrOMEGAs [87, 189] for the relic density as well as for the indirect constraints and SoftSUSY [132] for the sparticle mass spectrum. The model points are generated with SoftSUSY version 3.2.4 which includes an important bug fix for heavy scalars when computing $m_{h^0}$.

We display the model points consistent with the *general constraints* in Fig. 8.1 and in Fig. 8.3. In the left panel of Fig. 8.1 we exhibit the Higgs boson mass as a function of $m_0$ for the case when $\tan\beta > 20$ and in the right panel we exhibit it for the case when $\tan\beta < 20$. In both cases we see a slow logarithmic rise of $m_{h^0}$ with $m_0$ for large $m_0$. In the left and middle panels of Fig. 8.3 we show the distribution of the light Higgs boson mass in the $\tan\beta - A_0/m_0$ plane. One finds that a large part of the parameter space exists where the Higgs boson mass lies in the range $m_{h^0} > 115\,\text{GeV}$ (left panel) or in the narrower range $m_{h^0} > 123\,\text{GeV}$ (middle panel). In the right panel of Fig. 8.3, we show the distribution of $\log(m_0)$ (where $m_0$ is in GeV units) in the $m_{h^0} - A_0/m_0$ plane.

Our analysis shows a range of possibilities where a heavier Higgs boson, i.e. $m_{h^0} \gtrsim 125\,\text{GeV}$, can arise in the minimal supergravity model. Thus for values of $m_0 < 4\,\text{TeV}$ a heavier Higgs boson mass can be gotten for a large $A_0/m_0$ (typically of size $\pm 2$ with a significant spread). There may be a fine-tuning cost associated with producing this mass range for $h^0$, involving implicit cancellations which we demonstrate in Fig. 8.2, by displaying the tree-level mass term for $H_2$ and the correction to its mass from its coupling to the top quark. For values of $m_0 > 4\,\text{TeV}$ a heavier Higgs boson mass for relatively smaller values of $A_0/m_0$ is also allowed. For this case the first and second generation sfermions may be difficult to observe while the third generation sfermions would still be accessible. However, for the first case where a Higgs mass $m_{h^0} \gtrsim 125\,\text{GeV}$ arises for low $m_0$ and relatively larger $|A_0/m_0|$, the observation of signals arising from the production of first and second generation sfermions and heavier SUSY Higgs bosons remain very much within reach of the LHC with sparticles of relatively low mass in the spectrum, and variable mass hierarchies present [190] . This will be shown in more detail in the next section.

| Mass | $m_{h^o} > 115$ | $m_{h^o} > 117$ | $m_{h^o} > 119$ | $m_{h^o} > 121$ | $m_{h^o} > 123$ | $m_{h^o} > 125$ | $m_{h^o} > 127$ |
|---|---|---|---|---|---|---|---|
| $m_{H^o} \sim m_{A^o}$ | 212 | 216 | 273 | 324 | 1272 | 1517 | 2730 |
| $m_{H^\pm}$ | 230 | 234 | 288 | 337 | 1275 | 1520 | 2732 |
| $m_{\widetilde{\chi}_1^o}$ | 81 | 81 | 81 | 88 | 193 | 218 | 236 |
| $m_{\widetilde{\chi}_1^\pm} \sim m_{\widetilde{\chi}_2^o}$ | 104 | 104 | 104 | 111 | 376 | 424 | 459 |
| $m_{\widetilde{g}}$ | 800 | 800 | 803 | 803 | 1133 | 1264 | 1373 |
| $m_{\tilde{t}_1}$ | 156 | 197 | 228 | 230 | 231 | 246 | 260 |
| $m_{\tilde{\tau}_1}$ | 142 | 161 | 201 | 232 | 321 | 576 | 1364 |
| $m_{\tilde{q}}$ | 729 | 796 | 995 | 1126 | 1528 | 2235 | 2793 |
| $m_{\tilde{\ell}}$ | 163 | 194 | 265 | 325 | 475 | 1631 | 2557 |
| $\mu$ | 107 | 107 | 107 | 120 | 1418 | 1863 | 2293 |

| Mass | $m_{h^o} > 115$ | $m_{h^o} > 117$ | $m_{h^o} > 119$ | $m_{h^o} > 121$ | $m_{h^o} > 123$ | $m_{h^o} > 125$ | $m_{h^o} > 127$ |
|---|---|---|---|---|---|---|---|
| $m_{H^o} \sim m_{A^o}$ | 287 | 287 | 287 | 338 | 367 | 548 | 644 |
| $m_{H^\pm}$ | 301 | 301 | 301 | 349 | 378 | 555 | 646 |
| $m_{\widetilde{\chi}_1^o}$ | 91 | 91 | 91 | 91 | 91 | 91 | 256 |
| $m_{\widetilde{\chi}_1^\pm} \sim m_{\widetilde{\chi}_2^o}$ | 104 | 104 | 104 | 104 | 104 | 104 | 261 |
| $m_{\widetilde{g}}$ | 802 | 802 | 802 | 802 | 925 | 1006 | 1813 |
| $m_{\tilde{t}_1}$ | 229 | 229 | 229 | 229 | 229 | 360 | 360 |
| $m_{\tilde{\tau}_1}$ | 911 | 911 | 911 | 911 | 1186 | 1186 | 1186 |
| $m_{\tilde{q}}$ | 4035 | 4035 | 4035 | 4035 | 4215 | 4493 | 4493 |
| $m_{\tilde{\ell}}$ | 3998 | 3998 | 3998 | 4002 | 4085 | 4308 | 4308 |
| $\mu$ | 118 | 118 | 118 | 118 | 138 | 140 | 251 |

Table 8.1: Display of the lower limits on the sparticle masses as a function of a lower bound on the light Higgs mass for the mSUGRA models. The top panel shows the sparticle lower bounds for the small $m_0$ scan and the lower panel shows the sparticle lower bounds for the large $m_0$ sampling. The model points in both cases pass the *general constraints* as well as an additional constraint that the gluino mass exceed 800 GeV. We note that the lower bound limits for the sparticles are not necessarily for the same model point. All masses are in GeV. A remarkable aspect of the analysis is that a stop mass as low as 300 GeV can be obtained for parameter points with $m_0 > 4$ TeV. We further note that in this region one has the possibility of the first two neutralinos and the light chargino being degenerate as seen above when $\mu$ is smaller than the electroweak gaugino masses $M_1$ and $M_2$.

| Benchmark | $m_0$ | $m_{1/2}$ | $A_0/m_0$ | $\tan\beta$ |
|---|---|---|---|---|
| Light Stop | 5108 | 764 | 2.549 | 33.29 |
| Light Gauginos, Low $\mu$ | 3340 | 306 | -0.395 | 29.521 |
| Light Stau | 248 | 548 | -6.834 | 14 |

| Benchmark | $m_{h^0}$ | $m_{\widetilde{\chi}_1^0}$ | $m_{\widetilde{\chi}_1^\pm}$ | $m_{\widetilde{g}}$ | $m_{\tilde{t}_1}$ | $m_{\tilde{\tau}_1}$ | $m_{\widetilde{q}}$ | $m_{\tilde{\ell}}$ | $\mu$ |
|---|---|---|---|---|---|---|---|---|---|
| Light Stop | 125 | 321 | 621 | 1828 | 334 | 3604 | 5240 | 5108 | 3887 |
| Light Gauginos, Low $\mu$ | 121 | 91 | 115 | 832 | 1974 | 3070 | 3352 | 3335 | 125 |
| Light Stau | 121 | 228 | 438 | 1254 | 569 | 232 | 1126 | 325 | 1072 |

Table 8.2: Benchmark mSUGRA points that show the regions of parameter space that give masses near the minima presented, which shows how some but not all of the lower limits may be obtained by specific points. All masses are in GeV.

## 8.3 Sparticle Spectra and Higgs Mass

There are some interesting correlations between the light Higgs and the sparticle spectrum. As noted already a larger light Higgs boson mass typically indicates a relatively heavier sparticle spectrum. We give now a more quantitative discussion using the two scans discussed in the previous section after imposing the *general constraints*. In Table 8.1 we present the lower limits on some of the sparticles as the light Higgs mass gets progressively larger between $m_{h^0} = 115$ GeV and $m_{h^0} = 127$ GeV showing the results of the two scans (upper and lower tables). The top panel of the table is for the low value sampling of $m_0$, i.e. the scan with $m_0 \leqslant 4$ TeV, and the middle panel is for the large value sampling of $m_0$, i.e. the scan with $m_0$ between 4 TeV and 100 TeV. In the bottom panel, we give benchmark points with the sparticle masses near the lower limits presented. Thus, after applying an additional 800 GeV gluino cut on the models, for the low $m_0$ scan we find that a light Higgs boson mass of $m_{h^0} = 115$ GeV allows for a lightest neutralino mass of around 80 GeV, but $m_{h^0} = 125$ GeV indicates a lightest neutralino mass of around 220 GeV. The value of 220 GeV is consistent with independent constraints coming from the search for squarks and gluinos at the LHC (see [137, 138]). For the cases $m_{h^0} = 115$ GeV

and $m_{h^0} = 125\,\text{GeV}$ corresponding masses for the lightest chargino, $\tilde{\chi}_1^{\pm}$, (degenerate with the second lightest neutralino, $\tilde{\chi}_2^0$) are 100 GeV and 425 GeV; for the gluino, $\tilde{g}$, 800 GeV and 1.3 TeV; for the first and second generation squarks, $\tilde{q}$, 730 GeV and 2.2 TeV, and for the first and second generation sleptons, $\tilde{\ell}$, 150 GeV and 1.6 TeV. Thus for the low $m_0$ scan the shifts in lower limits are dramatic for the gluino and for the first generation sfermions. The stop, $\tilde{t}_1$, and the stau, $\tilde{\tau}_1$, however, continue to be relatively light. The $\tilde{\tau}_1$ mass, though is very sensitive to the higher mass bins in the light Higgs mass, i.e. bins greater then 123 GeV.

For the large $m_0$ scan the sparticle lower limits are modified in a significant way. Most noticeably, the electroweak gaugino spectrum can remain light at higher Higgs mass relative to what one finds in the more restrictive low $m_0$ scan. Further we observe that as the Higgs mass grows, the value of $\mu$ can remain a few times the $Z$ mass, where as in the low $m_0$ scan this does not occur. In addition we can see that the sfermion bounds do not change as drastically as the Higgs mass changes as they did with the low $m_0$ scan, and in particular the masses of the other Higgs bosons $A^0, H^0, H^{\pm}$ can remain much lighter.

More graphically, in Fig. 8.4 we compare ranges on the sparticle masses distributed by a light Higgs mass. Thus the left panel of Fig. 8.4 gives a plot of the stop mass vs. the gluino mass and the middle panel gives a plot of the stop mass vs the stau mass. These correlations of the light Higgs mass with the respective sparticle masses show directly how a determination of the Higgs mass at the LHC will constrain the masses of the R-parity odd particles. The right panel of Fig. 8.4 gives a display of the gluino mass vs $\mu$ (the Higgsino mass parameter at the scale $Q$ where electroweak symmetry breaking occurs). Here one finds that a $\mu$, as small as a 200 GeV, can generate a Higgs boson mass up to about 122 GeV. However, the larger Higgs masses, i.e., Higgs masses above 125 GeV can also have $\mu$ of size that is sub-TeV. Thus, one can have a heavier Higgs, scalars in the several TeV region, but still have a light $\mu$ [96, 123, 133].

## 8.4 Hyperbolic Branch of REWSB and Focal Surfaces

It is known that the radiative electroweak symmetry breaking carries in it a significant amount of information regarding the parameter space of SUGRA models. Thus REWSB allows for a determination of $\mu^2$ in terms of the soft parameters [96, 126] so that the breaking of electroweak symmetry is encoded in the following expression

$$\mu^2 = -\frac{1}{2}M_Z^2 + m_0^2 C_1 + A_0^2 C_2 + \overline{m}_{1/2}^2 C_3 + m_{1/2} A_0 C_4 + \Delta\mu_{\rm loop}^2 \,, \tag{8.4}$$

where $C_i$, $i$ running from 1 to 4, depend on the top mass, $\tan\beta$ and $Q$. It was shown in [96] that one can classify regions of Eq. (8.4) in the following two broad classes: the Ellipsoidal Branch, denoted EB, where $C_1 > 0$, and the Hyperbolic Branch, denoted HB, where $C_1 \leqslant 0$. More recently in [188] it was shown that HB can be further classified into three regions. One such region was defined as the Focal Point, HB/FP, where $C_1 = 0$. It was further shown that the HB/FP limits to the Focus Point [98] when $\tan\beta \gg 1$. Another region defined was the Focal Curve, HB/FC, where $C_1 < 0$ and two soft parameters are free to get large, i.e., either $m_0, A_0$ or $m_0, m_{1/2}$. The last region was defined to be the Focal Surface, HB/FS, where $C_1 < 0$ and three soft parameters were free to get large, i.e., $m_0, A_0, m_{1/2}$. It was further shown in [188] that HB/FC was a subset of HB/FS and that the HB/FP was mostly depleted after imposing constraints from flavor physics, WMAP, sparticle mass lower limits and LHC-7. However, other regions of the parameter space were found to be well populated.

In Fig. 8.5 we give an analysis of the Higgs mass ranges lying on the EB and on the Focal Regions with a comparison to the LHC-7 curves (Ref. 1 of [135, 136] and Ref. 2 of [75]). In the top two panels we consider the Higgs mass range upwards of 115 GeV. The left panel is for the Ellipsoidal Branch and the middle left panel is for the Focal Point region. In the EB region one finds that the majority of light Higgs boson masses do not exceed 124 GeV, while in the HB/FP region the Higgs masses do not get

beyond 120 GeV except perhaps for some isolated points. Further the HB/FP region is highly depleted as can be seen by the paucity of allowed model points in the middle left panel of Fig. 8.5. The largest Higgs boson masses are achieved on HB/FS, which includes HB/FC, shown in the right two panels of Fig. 8.5 where the region above a Higgs boson mass of 115 GeV (middle right) and between 123 GeV and 127 GeV (right) are shown. The right panel shows that the Higgs mass region within a few 125 GeV is well populated.

## 8.5 Higgs boson and dark matter

There is a strong correlation between the light Higgs mass and dark matter. It has already been pointed out that annihilation via the Higgs pole can generate the relic density to be consistent with WMAP [191]. In this case the neutralino mass would be roughly half the light Higgs boson mass. For heavier neutralino masses other annihilation mechanisms become available. We would be interested in the cases which include large $m_0$ and specifically in the spin independent proton-neutralino cross section in this domain. For this case when $m_0$ is large the s-channel squark exchange which contributes to the spin independent proton-neutralino cross section becomes suppressed while the t-channel Higgs exchange dominates. The scattering cross section in this case is given by

$$\sigma^{SI}_{\tilde{\chi}^0_1 N} = \left(4\mu^2_{\tilde{\chi}^0_1 N}/\pi\right)\left(Zf_p + (A-Z)f_n\right)^2 \ . \tag{8.5}$$

Here $f_{p/n} = \sum_{q=u,d,s} f^{(p/n)}_{T_q} C_q \frac{m_{p/n}}{m_q} + \frac{2}{27} f^{(p/n)}_{TG} \sum_{q=c,b,t} C_q \frac{m_{p/n}}{m_q}$, where the form factors $f^{(p/n)}_{T_q}$ and $f^{(p/n)}_{TG}$ are given in [87, 113, 114, 189] and the couplings $C_i$ are given by [113, 114]

$$C_q = -\frac{g_2 m_q}{4 m_W \delta_3}\left[(g_2 n_{12} - g_Y n_{11}])\,\delta_1\delta_4\delta_5\left(-\frac{1}{m_H^2}+\frac{1}{m_h^2}\right)\right.$$
$$\left. + (g_2 n_{12} - g_Y n_{11})\,\delta_2\left(\frac{\delta_4^2}{m_H^2}+\frac{\delta_5^2}{m_h^2}\right)\right]. \qquad (8.6)$$

For up quarks one has $\delta_i = (n_{13}, n_{14}, s_\beta, s_\alpha, c_\alpha)$ and for down quarks $\delta_i = (n_{14}, -n_{13}, c_\beta, c_\alpha, -s_\alpha)$, where $i$ runs from 1 to 5, $\alpha$ is the neutral Higgs mixing parameter, $n_{1j}$ is the neutralino eigen-content, $c_\alpha$ denotes $\cos\alpha$ and $s_\alpha$ denotes $\sin\alpha$. The above approximation holds over a significant part of the parameter space specifically for large $m_0$ and we have checked that it compares well with the full analysis where the full theory calculation is done with MicrOMEGAs. In the analysis presented here, however, we exhibit only the results of the full analysis. In Fig. 8.6 we give a plot of the proton-neutralino spin-independent cross section, $\sigma^{SI}_{\tilde{\chi}^0_1 p}$ times $\mathcal{R}$ plotted as a function of the neutralino mass where we have corrected $\sigma^{SI}_{\tilde{\chi}^0_1 p}$ by a factor $\mathcal{R} \equiv (\Omega h^2) / (\Omega h^2)_{WMAP}$ to take into account the possibility of multi-component dark matter. The points are shaded according to the Higgs boson masses and we show the XENON-100 [103, 104] exclusion curve as well as the XENON-1T [111] and the SuperCDMS [112] projections.

It is important to observe that when the Higgs mass region 123 GeV to 127 GeV is considered, nearly all of the mSUGRA parameter points that lie in this region which are also consistent with the *general constraints* (from our low $m_0$ and high $m_0$ scans) give rise to neutralino mass and proton-neutralino spin-independent cross section (scaled by $\mathcal{R}$), that lies just beyond what the most recent results from the XENON collaboration have probed. However, a vast majority of this region is projected to be explored by XENON-1T and SuperCDMS. This point is clearly seen in the right panel of Fig. 8.6.

## 8.6 Conclusion

Recent data from LHC-7 indicates a narrow window on the light Higgs mass. This allowed mass window is consistent with the range predicted by SUGRA models and specifically by the mSUGRA model. Here we discussed the implications of the indicated mass range for the light Higgs mass for the sparticle mass spectrum and for dark matter. Using the allowed Higgs mass range above 115 GeV the corresponding ranges for the soft masses and couplings, as well as the ratio of the vacuum expectation values of the Higgs doublets and the Higgsino mass parameter were found. We then investigated the ranges for the sparticle masses correlated to the predicted value of the Higgs Boson mass, specifically for the chargino, the neutralino, the gluino, the stop, the stau, for the first and second generation squarks and sleptons and for the heavier Higgs of the minimal supersymmetric standard model, i.e., the CP-odd Higgs $A^0$, the CP-even Higgs $H^0$, and the charged Higgs $H^{\pm}$.

Our conclusions are that the largest Higgs masses are realized on the Focal Surface of the Hyperbolic Branch of radiative electroweak symmetry breaking. We also point out that low values of $\mu \sim 150$ GeV are consistent with heavy squarks and sleptons in the 10 TeV region or larger. We find that $m_{h^0} \in (123 - 127)$ GeV does allow for light third generation stop as low as $m_{\tilde{t}_1} > 230$ GeV, though the second generation squarks are at least $m_{\tilde{q}} > 1.5$ TeV and second generation sleptons are at least 475 GeV. Thus, the restriction of the light Higgs boson to the mass window $m_{h^0} \in (123 - 127)$ GeV provides further constraints on the sparticle spectrum that are complimentary to the direct searches for sparticles at the LHC.

Further, we find precise predictions for dark matter if the light Higgs boson mass lies between 123 GeV and 127 GeV. For these light Higgs boson masses, the corresponding range of the lightest neutralino mass would be accessible in the next generation of direct detection dark matter experiments. The light Higgs boson in the 123 GeV and 127 GeV range was shown to be generic for the case of heavy

scalars in minimal supergravity with $|A_0/m_0| \sim \mathcal{O}(1)$.

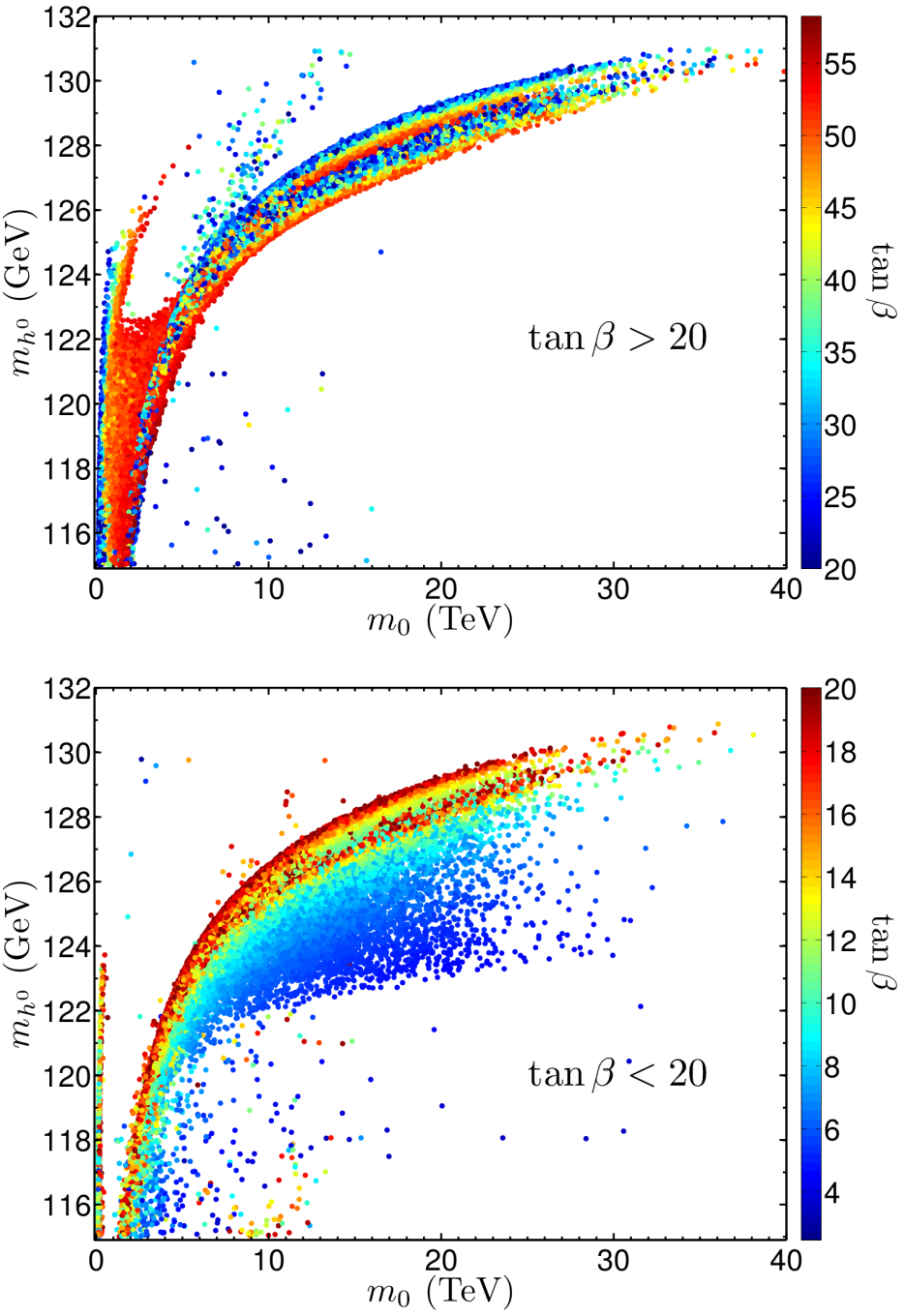


Figure 8.1: Left: Exhibition of the light Higgs mass as a function of $m_0$ for $\tan\beta > 20$. Right: Same as the left panel except that $\tan\beta < 20$. The data analyzed passes the *general constraints* and are generated with both scans of $m_0$.

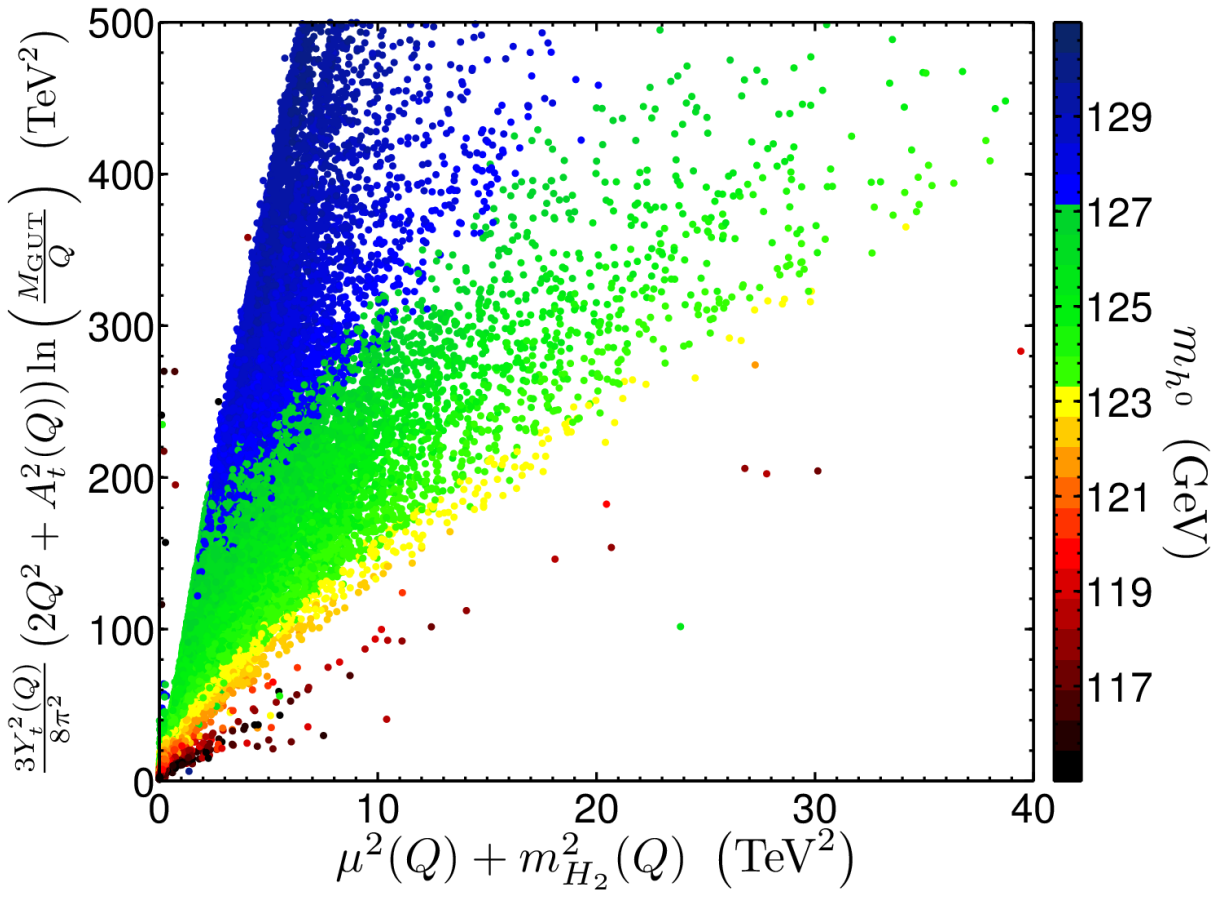


Figure 8.2: Here we display the tree-level mass term of the $H_2$ doublet, $\mu^2(Q)+(m^{\rm tree}_{H_2}(Q))^2$ and the loop correction resulting from the coupling to the top quark, $\frac{3Y_t^2(Q)}{8\pi}\left(3Q^2 + A_t^2(Q)\right)\ln\left(\frac{M_{\rm GUT}}{Q}\right)$, arising from parameter points that satisfy the general constraints and have $m_{h^0} \in (115, 131)$ GeV, as an indication of the fine-tuning from implicit cancellations.

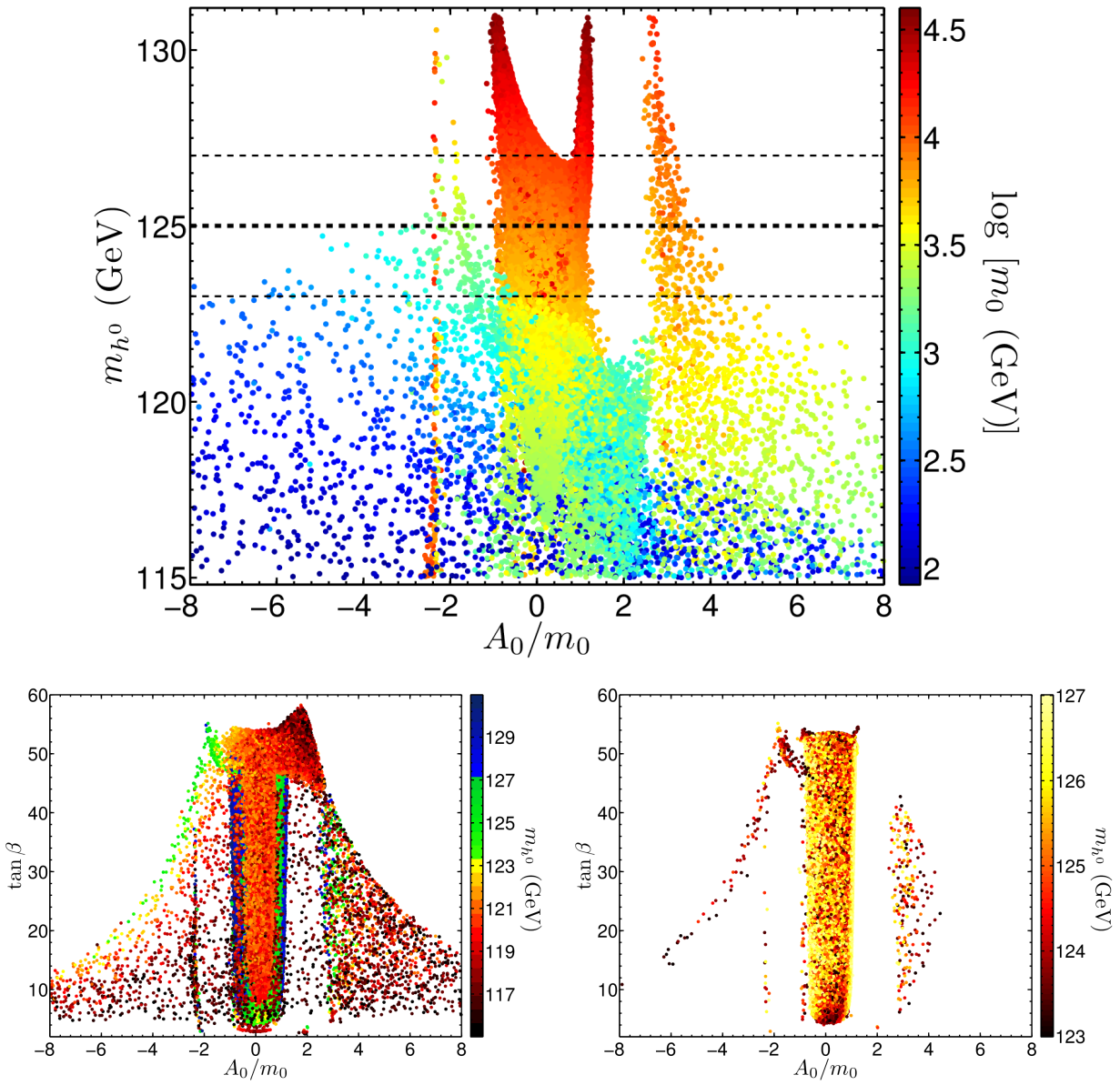


Figure 8.3: Left: A display of the model points in the $\tan\beta - A_0/m_0$ plane when $m_{h^0} > 115$ GeV. Model points are shaded according to their light Higgs boson mass, $m_{h^0}$. Middle: Same as the left panel except that $m_{h^0} > 123$ GeV . Right: Exhibition of the model points in the $m_{h^0} - A_0/m_0$ plane displayed by $\log(m_0)$ with $m_0$ in GeV units. It is seen that for low values of $|A_0/m_0|$ larger $m_0$ corresponds to a heavier light Higgs boson. The data analyzed passes the *general constraints* and are generated with both scans of $m_0$ as discussed in the text.

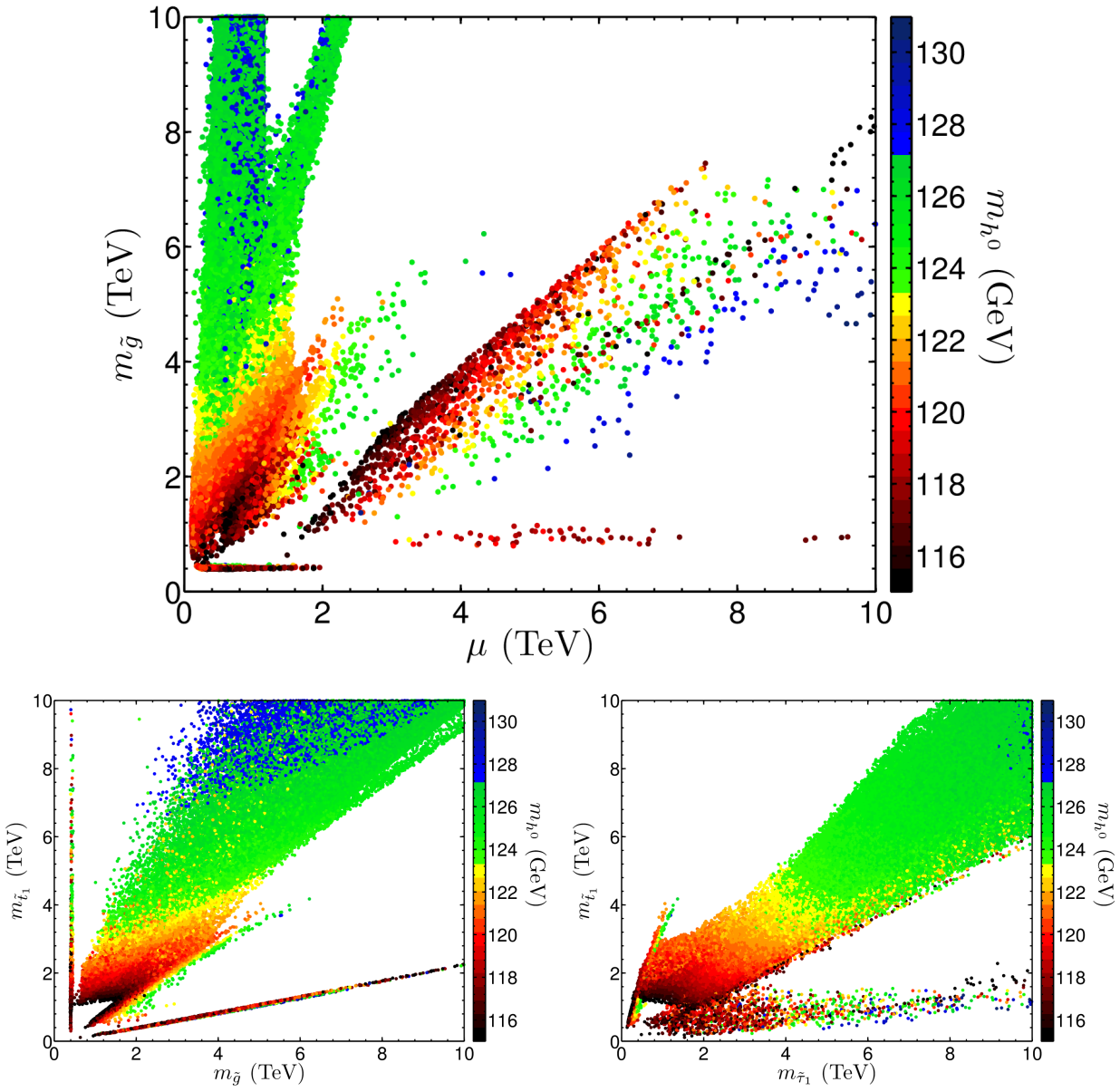


Figure 8.4: Analysis is based on the *general constraints* discussed in the text and for both scans of $m_0$. Left panel: Exhibition of the stop vs the gluino mass in the mass window where both the stop and the gluino masses run till 10 TeV. Middle panel: Exhibition of stop mass vs stau mass. Right panel: Exhibition of the gluino mass vs $\mu$.

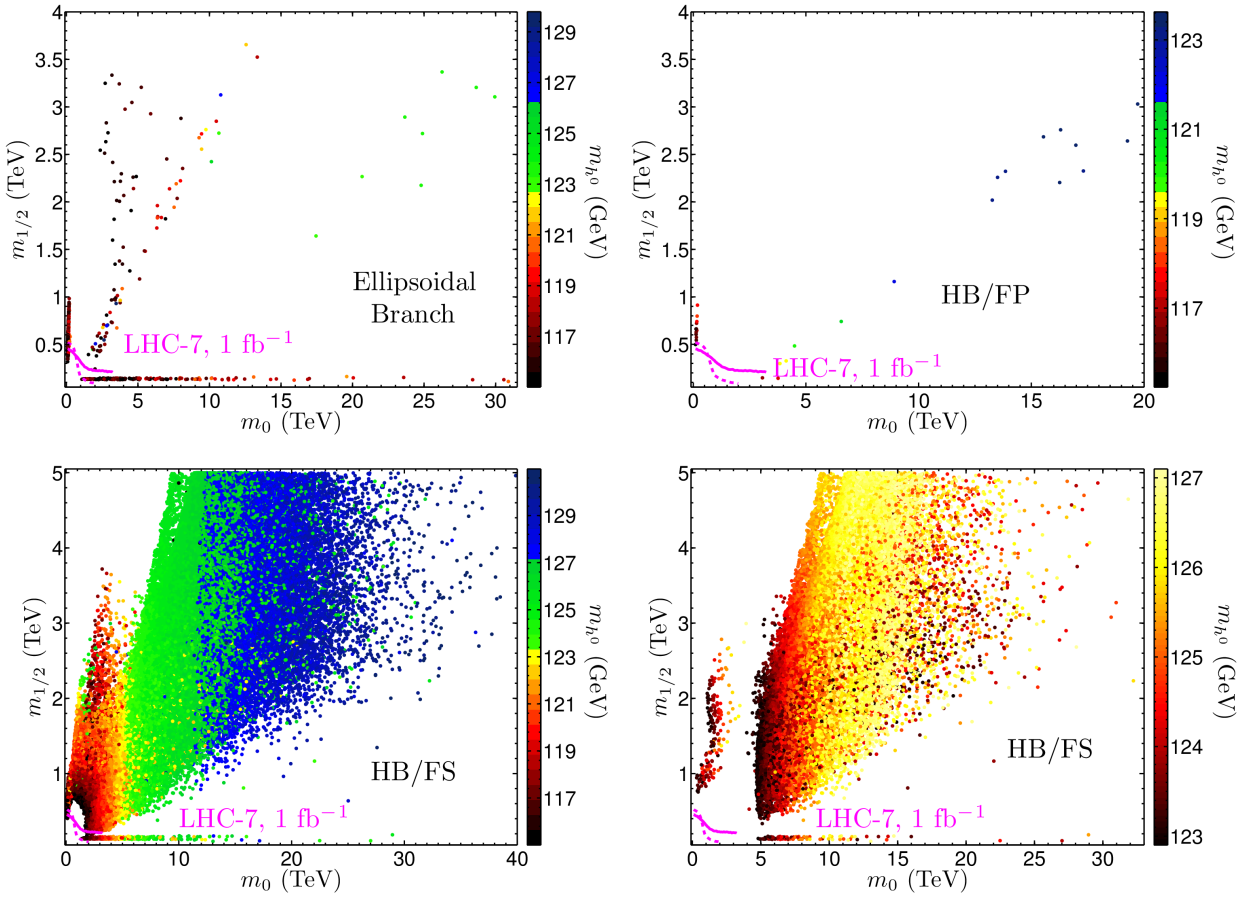


Figure 8.5: Analysis of the Higgs boson mass in Focal Regions. The analysis is done for the model points that satisfy the low $m_0$ sampling and the *general constraints*. Left: Shows the EB region with the light Higgs boson mass greater than 115 GeV. We see that the majority of these points are not in the heavy Higgs boson region. Middle Left: Displays the HB/FP where we see that there are no Higgs masses greater then 120 GeV. In the right two panels we display the HB/FS (which include HB/FC) as follows: in the middle right panel we exhibit the HB/FS model points for the Higgs mass range above 115 GeV and in the right panel we exhibit the HB/FS model points that have the light Higgs boson mass between 123 GeV and 127 GeV. In all panels the dotted magenta line corresponds to the curve CMS given in Ref. 2 of [75] and the solid magenta line corresponds to the ATLAS curve of Ref. 1 of [135, 136].

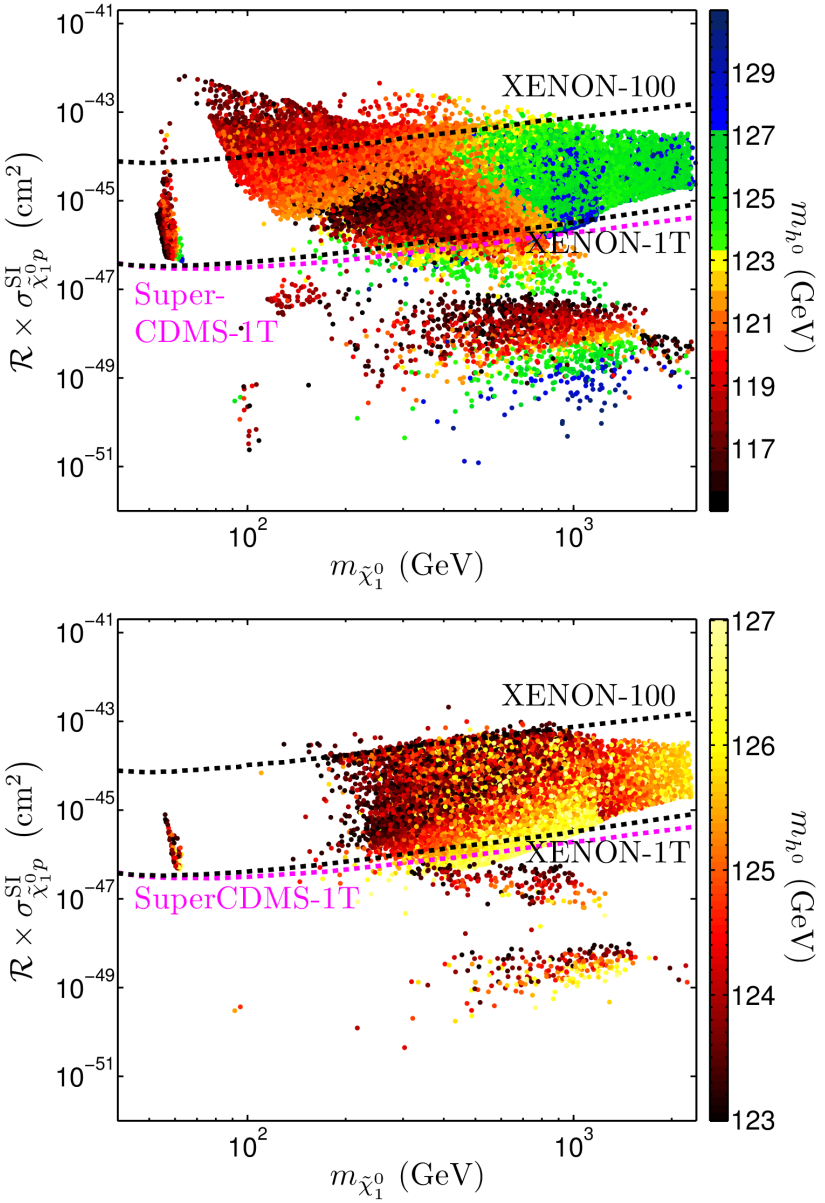


Figure 8.6: Exhibition of proton-neutralino spin-independent cross section against the neutralino mass. Here we see that models with a Higgs Boson mass in the range consistent with the results from LHC-7 will be probed in the next round of dark matter experiments. In the plots the proton-neutralino spin-independent cross section was corrected by $\mathcal{R} \equiv (\Omega h^2) \,/\, (\Omega h^2)_{\text{WMAP}}$ to allow for multicomponent dark matter. The analysis is done for the model points passing the *general constraints* from the low $m_0$ sampling. The left panel gives the full light Higgs boson mass range, i.e. 115 GeV to 131 GeV and the right panel only deals with the sensitive region between 123 GeV to 127 GeV.

# Chapter 9

# Implications of the Higgs Boson Discovery for Minimal Supergravity

## 9.1 Introduction

A Bayesian analysis is carried out to identify the consistent regions of the mSUGRA parameter space, where the newly-discovered Higgs boson's mass is used as a constraint, along with other experimental constraints. It is found that $m_{1/2}$ can lie in the sub-TeV region, $A_0/m_0$ is mostly confined to a narrow strip with $|A_0/m_0| \leqslant 1$, while $m_0$ is typically a TeV or larger. Further, the Bayesian analysis is used to set 95% CL lower bounds on sparticle masses. Additionally, it is shown that the spin independent neutralino-proton cross section lies just beyond the reach of the current sensitivity but within the projected sensitivity of the SuperCDMS-1T and XENON-1T experiments, which explains why dark matter has thus far not been detected. The light sparticle spectrum relevant for the discovery of supersymmetry at the LHC are seen to be the gluino, the chargino and the stop with the gluino and the chargino as the most likely candidates.

The most recent search at the LHC [192–198] for the Higgs boson [12–15] with the combined 7 TeV and 8 TeV data indicates a signal for the Higgs boson with mass $125.3 \pm 0.4\,(\text{stat.}) \pm 0.5\,(\text{syst.})$ GeV for CMS with a local significance of $5.0\,\sigma$ and with mass $126.0 \pm 0.4\,(\text{stat.}) \pm 0.4\,(\text{syst.})$ GeV for ATLAS with local significance of $5.9\,\sigma$. As is well known the Higgs boson mass at the tree level lies below the $Z^0$ boson mass, but it can be made larger by inclusion of loop corrections. However, in supergravity grand unification [51–53] there is another upper limit, i.e., of about 130 GeV due to the constraint of radiative breaking of the electroweak symmetry (for a review see [199]) as well as other experimental constraints (for a recent analysis see [200, 201]). The correction to the Higgs boson mass is given by [171–179][1].

$$\Delta m^2_{h^0} \simeq \frac{3m_t^4}{2\pi^2 v^2} \ln \frac{M_S^2}{m_t^2} + \frac{3m_t^4}{2\pi^2 v^2} \left( \frac{X_t^2}{M_S^2} - \frac{X_t^4}{12 M_S^4} \right) , \tag{9.1}$$

where $X_t \equiv A_t - \mu \cot\beta$, where $A_t$ is the $A_0$ parameter run down to the weak scale (see Eq. (9.2)), $v = 246\,\text{GeV}$, and $M_S$ is an average stop mass. The loop correction in Eq. (9.1) is maximized when $X_t \sim \sqrt{6} M_S$. There are also additional loop corrections from, e.g., the b-quark sector as well as from higher loops. The early searches at the LHC-7 gave a possible hint of the Higgs boson in the mass range $\sim (117-129)$ GeV [135] and the combined Tevatron analysis reported an excess between $(115-140)$ GeV [203]. These findings have led to significant activity [200, 204–209] to investigate the implications of the results for supersymmetry.

## 9.2 Implications for mSUGRA

We note that the scale $M_S$ in Eq. (9.1) which is determined by the soft parameters depends sensitively on the Higgs mass. In the analysis we use the Higgs boson mass constraint within the Bayesian statistical framework to estimate the soft parameters of mSUGRA (sometimes referred to as CMSSM) which are

[1] For reviews, see [180, 202]

given by [51–53]

$$m_0, m_{1/2}, A_0, \tan\beta, \mathrm{sgn}(\mu) \tag{9.2}$$

where $m_0$ is the universal scalar mass, $m_{1/2}$ is the universal gaugino mass, $A_0$ is the trilinear couplings and $\tan\beta$ is the ratio of the two Higgs VEVs in MSSM, and $\mu$ is the Higgs mixing parameter. The soft parameters of Eq. (9.1) define our model's parameter set, $\theta = \left\{m_0, m_{1/2}, A_0, \tan\beta\right\}$, and additionally we consider a set of the most sensitive standard model nuisance parameters, $\psi = \left\{m_t, m_b(m_b)^{\overline{MS}}, \alpha_s(m_Z)^{\overline{MS}}, \alpha_{EM}(m_Z)^{\overline{MS}}\right\}$. These together form the basis parameter set: $\Theta = \{\theta, \psi\}$. Using Bayes's theorem, the posterior probability density function (PDF) for the theory described by $\Theta$, which may be mapped to observables, $\xi(\Theta)$ to be compared against experimental data, $d$ is given by:

$$p(\Theta|d) = \frac{p(d|\xi(\Theta))\pi(\Theta)}{p(d)}\,, \tag{9.3}$$

where $\mathcal{L} \equiv p(d|\xi(\Theta))$ is the likelihood function–the terms of which are described in Table 9.1, $\pi(\Theta)$ is the distribution in $\Theta$ prior to considering experimental results, and $\mathcal{Z} \equiv p(d)$ is the Bayesian evidence which can be used in model selection. However, in our goal of parameter estimation, it serves only as a normalization factor. We present results obtained by considering both the 2D marginalized posterior PDF (where the full N-dimensional posterior PDF of Eq. (9.3) has been integrated over the other parameters), as well as the profile likelihoods (where the confidence levels are determined by comparison to the global best-fit point). (For a more detailed description see [210].)

The analysis was done by using SusyKit [211], which employs the MultiNest [210, 212, 213] package for sampling parameter points efficiently, and uses SoftSUSY [132] for spectrum calculation, and MicrOMEGAs [87, 189] to calculate the relic density as well as for the indirect constraints. The credible intervals, marginalized posterior PDFs, and profile likelihood distributions were calculated using the plotting routines of SuperBayes [214, 215], which is largely based on the tools provided by

CosmoMC [216]. The constraint from the $g_\mu - 2$ measurement is not imposed in this analysis and this issue will be discussed later in the text.

In our analysis, we took our prior knowledge of the parameters to be either flat linear distributions or flat logarithmic distributions, with $m_0 \in (0.05, 8)$ TeV (log), $m_{1/2} \in (0.05, 5)$ TeV (log), $A_0 \in (-30, 30)$ TeV (linear), and $\tan\beta \in (3, 60)$ (linear). We have fixed $\mathrm{sgn}(\mu)$ to be positive. The Standard Model nuisance parameters were allowed to vary in $2\,\sigma$ windows of their central values, as quoted in Table 9.1. Our MultiNest sampling parameters, as defined in [210, 212, 213], were $n_{\rm live} = 20,000$ and $\mathtt{tol} = 0.0001$. It has been shown in [217] and in [213] that these parameters are not only sufficient to provide a map of the posterior PDF, but also to find the true best-fit point which is essential for the profile likelihood analysis.

In our likelihood analysis we use the CMS result since that result was available earlier [192]. We report our fits to the data, including the Higgs mass, in Fig. 9.1 in the form of 2D posterior PDF maps (left panels) as well as the profile likelihood maps (right panels). The posterior mean is marked with a large dot and the global best-fit is marked with a circled 'X'. (Note that while the best-fit point is crucial in Frequentist likelihood-ratio tests, it has no significance in the Bayesian framework.) The top panels exhibit the constraint in the $m_0 - m_{1/2}$ plane and show that $m_0$ is typically a TeV or larger, while $m_{1/2}$ can lie below 500 GeV. The middle panels exhibit the constraint in the $A_0/m_0 - \tan\beta$ plane, and here one finds that most of the allowed parameter space lies in the narrow strip $|A_0/m_0| \leqslant 1$ with a small strip in the range $|A_0/m_0| \in (-2, -6)$. The bottom panels exhibit the constraint in the $m_A - \tan\beta$ plane, and here one finds that the majority of the allowed range of $m_A$ lies above 1 TeV. Thus $m_A \gg m_{h^0}$ for the majority of the parameter space and thus we are in the so-called decoupling limit.

It was pointed out in [188] that most of the experimentally consistent parameter space of mSUGRA lies on the Hyperbolic Branch (HB) [96, 98] of radiative breaking of the electroweak symmetry under the LHC-7 constraints. The HB region has sub-regions which we may label as Focal Point (HB/FP),

| Observable | Central value | Exp. Error | Theory Error | Distribution | Ref. |
|---|---|---|---|---|---|
| | | SM Nuisance Parameters | | | |
| $m_t$ | 173.5 GeV | 1.0 GeV | — | Gaussian | [218] |
| $m_b(m_b)^{\overline{MS}}$ | 4.18 GeV | 0.03 GeV | — | Gaussian | [218] |
| $\alpha_s(m_Z)^{\overline{MS}}$ | 0.1184 | $7 \times 10^{-4}$ | — | Gaussian | [218] |
| $1/\alpha_{EM}(m_Z)^{\overline{MS}}$ | 127.944 | 0.014 | — | Gaussian | [218] |
| | | Measured | | | |
| $\mathcal{B}r(b \to s\gamma) \times 10^4$ | 3.21 | 0.33 | 0.21 | Gaussian | [88, 93] |
| $\Omega h^2$ | 0.1126 | 0.0036 | 10% | Upper-Gaussian | [94] |
| $m_{h^0}$ | 125.3 GeV | 0.6 GeV | 1.1 GeV | Gaussian | [192] |
| | | Limits (95% CL) | | | |
| $\mathcal{B}r(B_s^0 \to \mu^+\mu^-)$ | $4.5 \times 10^{-9}$ | — | 14% | Upper — Error Fn | [139] |
| $m_{h^0}$ | 122.5 GeV | — | — | Lower — Step Fn | [219] |
| $m_{h^0}$ | 129 GeV | — | — | Upper — Step Fn | [219] |
| $m_{\tilde{\chi}_1^0}$ | 46 GeV | — | 5% | Lower — Error Fn | [218] |
| $m_{\tilde{\chi}_2^0}$ | 62.4 GeV | — | 5% | Lower — Error Fn | [218] |
| $m_{\tilde{\chi}_3^0}$ | 99.9 GeV | — | 5% | Lower — Error Fn | [218] |
| $m_{\tilde{\chi}_4^0}$ | 116 GeV | — | 5% | Lower — Error Fn | [218] |
| $m_{\tilde{\chi}_1^\pm}$ | 94 GeV | — | 5% | Lower — Error Fn | [218] |
| $m_{\tilde{e}_R}$ | 107 GeV | — | 5% | Lower — Error Fn | [218] |
| $m_{\tilde{\mu}_R}$ | 94 GeV | — | 5% | Lower — Error Fn | [218] |
| $m_{\tilde{\tau}_1}$ | 81.9 GeV | — | 5% | Lower — Error Fn | [218] |
| $m_{\tilde{b}_1}$ | 89 GeV | — | 5% | Lower — Error Fn | [218] |
| $m_{\tilde{t}_1}$ | 95.7 GeV | — | 5% | Lower — Error Fn | [218] |
| $m_{\tilde{g}}$ | 500 GeV | — | 5% | Lower — Error Fn | [218] |
| $m_{\tilde{q}}$ | 1100 GeV | — | 5% | Lower — Error Fn | [218] |

Table 9.1: Summary of the observables used to estimate the mSUGRA parameters. Only the upper-half of the Gaussian is used in the consideration of $\Omega h^2$, i.e., there is only a penalty for values larger than the central value which allows for multicomponent dark matter [187]. The 95% CL limits have been evaluated under the assumption of only theoretical uncertainty, so the distribution used here is based on the error function, given explicitly in the fourth reference of [214].

Focal Curves (HB/FCi, i=1,2), and Focal Surfaces (HB/FS). It was shown in [188, 200] that the HB/FP is mostly depleted while the remaining parameter space lies on HB/FCi or HB/FS. Specifically we note

here that the right edge of $A_0/m_0$ in Fig. 9.1 is $\sim 1$. The value $|A_0/m_0| = 1$ was argued as string-motivated in [133] and was shown to be the asymptotic limit on the focal curve HB/FC1 in [188].

In Fig. 9.2 we present the 2D posterior PDF's (left panels) and the profile likelihoods (right panels) in the planes of the phenomenologically important sparticle masses. The top panels present the results in the gluino–squark mass plane, and indicate that the gluino can be below a TeV. The second row is plotted in the squark–chargino mass plane and demonstrates that the chargino masses are only bounded from below by the direct searches at LEP. The next row exhibits our fit in the stau–stop mass plane. Here one finds that the stau and stop masses are typically large except for a small strip where the stop mass can lie below a TeV. This is largely to be expected as we rely on a heavy stop to provide a sizable loop correction to the Higgs mass. The bottom panels show the analysis in the $\mu - m_{\tilde{g}}$ plane. One finds that $\mu$ is typically quite light, i.e., $\mu$ can be significantly below 500 GeV.

Using the marginalized 1D posterior PDF we are able to set lower limits on the sparticle masses from the $2\,\sigma$ credible regions. We present those limits here: $m_{\tilde{g}} > 1.39\,\text{TeV}$, $m_{\tilde{\chi}_1^\pm} > 196\,\text{GeV}$, $m_{A_0} \sim m_{H_0} \sim m_{H^\pm} > 1.3\,\text{TeV}$, $m_{\tilde{t}_1} > 3.1\,\text{TeV}$, $m_{\tilde{\tau}_1} > 3.1\,\text{TeV}$, $m_{\tilde{q}} > 5\,\text{TeV}$, and $m_{\tilde{\ell}} > 4.8\,\text{TeV}$. The profile likelihood analysis yields different results. Here, we find the 95% CL sparticle lower limits to be $m_{\tilde{g}} > 690\,\text{GeV}$, $m_{\tilde{\chi}_1^\pm} > 95\,\text{GeV}$, $m_{A_0 \sim H_0 \sim H^\pm} > 540\,\text{GeV}$, $m_{\tilde{t}_1} > 580\,\text{GeV}$, $m_{\tilde{\tau}_1} > 310\,\text{GeV}$, $m_{\tilde{q}} > 1.5\,\text{TeV}$, and $m_{\tilde{\ell}} > 580\,\text{GeV}$. We note that as expected the lower limits given by the profile likelihood analysis lie lower than the limits given by the PDF analysis. The analysis thus indicates that the light particles in mSUGRA in view of the Higgs mass measurement are the neutralino, the chargino, the gluino, the stau and the stop. Among these the most likely candidates for discovery in the next phase of CERN experiment are the gluino, the chargino and the stop.

## 9.3 125 GeV Higgs boson and dark matter

Neutralino-proton spin independent cross section $\sigma^{SI}_{\tilde{\chi}^0_1 p}$ depends sensitively on the Higgs boson mass (for a discussion see [200]). Thus considering the $\sim$ 125 GeV Higgs mass leads to a more constrained prediction for dark matter. In Fig. 9.3 we give a plot of $\mathcal{R} \times \sigma^{SI}_{\tilde{\chi}^0_1 p}$ as a function of the lightest neutralino mass $m_{\tilde{\chi}^0_1}$ where the factor $\mathcal{R}$ is defined by $\mathcal{R} \equiv (\Omega h^2) \,/\, (\Omega h^2)_{WMAP}$, and $(\Omega h^2)_{WMAP}$ is the central value of the WMAP-7 data. By only applying a likelihood penalty for points that are above the WMAP-7 limit, we have taken into account the possibility that there may be additional components of dark matter beyond the neutralino [187]. Quite remarkably, the bulk of the credible region of mSUGRA falls essentially exclusively between the current limits on dark matter by XENON-100 [103–105, 220] and the projected sensitivity of SuperCDMS [112] and XENON-1T [111].

We discuss now the constraint from $g_\mu - 2$. In supersymmetric theories, sparticle loops make significant contributions to the anomalous magnetic moment of the muon [221] if the relevant sparticles (charginos, neutralinos, smuons, sneutrinos) entering the loops are relatively light. The experimental determination of $\delta a_\mu = a_\mu^{exp} - a_\mu^{SM}$ where $a_\mu = (g_\mu - 2)/2$, depends sensitively on the hadronic correction to the standard model value. There are two main procedures for the estimation of the hadronic correction, which are either using the $e^+e^-$ annihilation cross section or from $\tau$ decay. The result using the $e^+e^-$ annihilation gives $\delta a_\mu = (28.7 \pm 8.0) \times 10^{-10}$ $(3.6\,\sigma)$ while for $\tau$-based hadronic contributions one has $\delta a_\mu = (19.5 \pm 8.3) \times 10^{-10}$ $(2.4\,\sigma)$ [222, 223]. In any case, within the universal soft SUSY-breaking paradigm there would be tension between the $g_\mu - 2$ result (specifically the one using $e^+e^-$ annihilation cross section) and the 125 GeV Higgs boson mass since the $m_0$ scale is rather high. If the $g_\mu - 2$ results stay, then there are at least two avenues open to make compatible the $g_\mu - 2$ results and the Higgs boson mass. The first possibility is that we stay within the universal soft breaking paradigm and additional contributions to the Higgs mass arise due to the presence of extra matter which can generate new loop corrections to the Higgs mass, or from extra gauge groups under which the Higgs is charged

yielding corrections to the Higgs mass through D-terms. Alternatively, one could give up universality of soft parameters and consider non-universal or flavored SUGRA models [126]. For instance, to satisfy the $g_\mu - 2$ constraint one may consider the soft scalar mass for the first two generations much smaller than for the third generation, or the sleptons being lighter than the squarks. These possibilities require further investigation.

## 9.4 Conclusion

In this work we have analyzed the implications of the Higgs boson discovery at CERN for supersymmetry. Specifically we analyzed the mSUGRA model to delineate constraints on soft parameters and identified the light particles that are prime candidates for discovery in the next phase of runs at the LHC. The analysis presented here explains why supersymmetric dark matter has not been seen thus far since essentially all of the parameter space lies below the current sensitivity of dark matter experiments due to the high Higgs mass. The analysis also points to excellent prospects for the discovery of dark matter at SuperCDMS and XENON-1T as well as the possibility of light neutralinos, charginos and gluinos, and possibly light stops and staus.

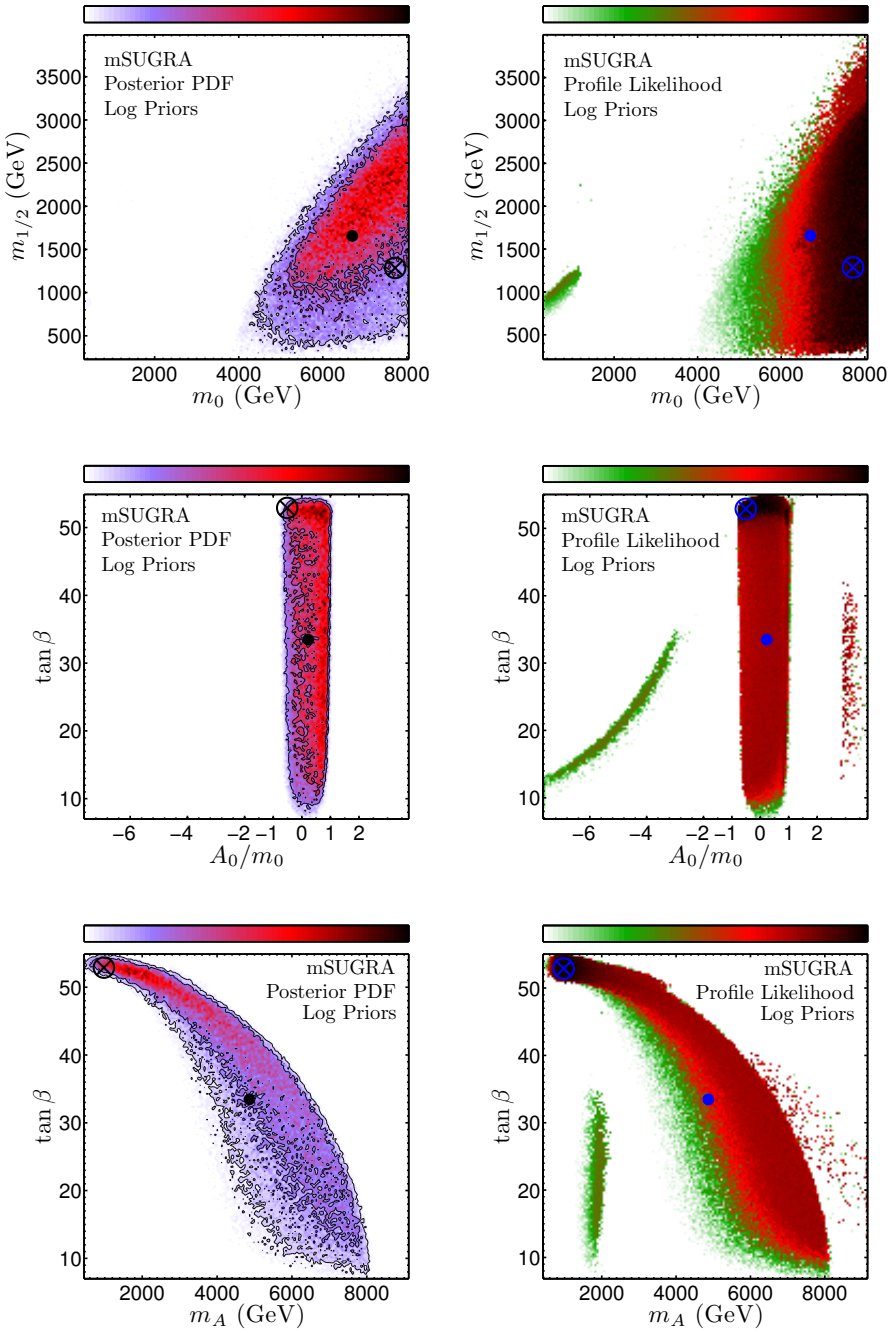


Figure 9.1: Left panels: plots of the 2D posterior probability densities, 1 σ and 2 σ contours are also drawn. Right panels: plots of the profile likelihoods. Top: in the $m_0 - m_{1/2}$ plane. Middle: in the $A_0/m_0 - \tan\beta$ plane. Bottom: in the $m_A - \tan\beta$ plane. The posterior mean is marked by a large dot while the best-fit point is shown by a circled 'X'. The color bar above the top panel gives the relative likelihood which increases left-to-right.

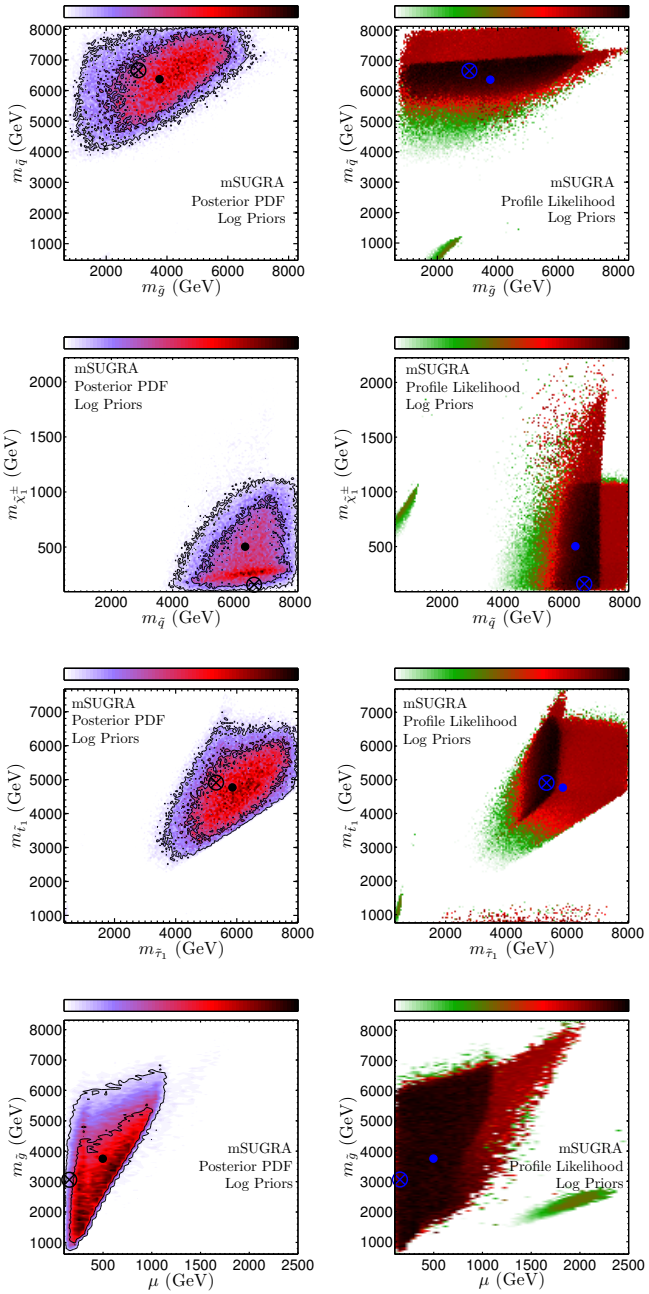


Figure 9.2: Left panels: plots of the 2D posterior probability densities, 1 σ and 2 σ contours are also drawn. Right panels: plots of the profile likelihoods. Top: in the $m_{\tilde{g}}$–$m_{\tilde{q}}$ plane. Upper-middle: in the $m_{\tilde{q}}$–$m_{\tilde{\chi}_1^\pm}$ plane. Lower-middle: in the $m_{\tilde{\tau}_1} - m_{\tilde{t}_1}$ plane. Bottom: in the $\mu - m_{\tilde{g}}$ plane. The posterior mean is marked by a large dot while the best-fit point is shown by a circled 'X'. The color bar above the top panel gives the relative likelihood which increases left-to-right.

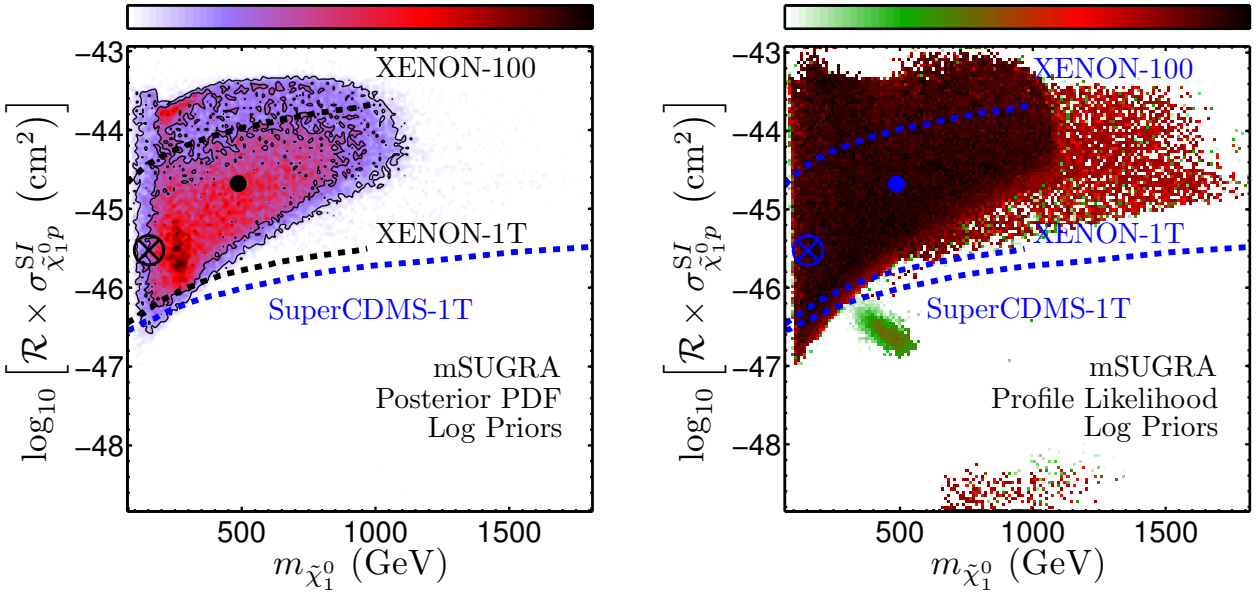


Figure 9.3: Plots of $\mathcal{R} \equiv (\Omega h^2) \,/\, (\Omega h^2)_{\rm WMAP}$ vs the neutralino mass $m_{\tilde{\chi}^0_1}$. The left panel presents the 2D posterior PDF, and the right panel presents the profile likelihood. The analysis shows that virtually all of credible region of mSUGRA will be probed by the SuperCDMS [112] and XENON-1T [111] experiments. The color bar above the panels gives the relative likelihood which increases left-to-right.

# Chapter 10

# Gluino-driven Radiative Breaking and Electroweak Supersymmetry

## 10.1 Introduction

We attempt to reconcile seemingly conflicting experimental results on the Higgs boson mass, the anomalous magnetic moment of the muon, null results in search for supersymmetry at the LHC within the 8 TeV data and results from B-physics, all within the context of supersymmetric grand unified theories. Specifically, we consider a supergravity grand unification model with non-universal gaugino masses where we take the $SU(3)_C$ gaugino field to be much heavier than the other gaugino and sfermion fields at the unification scale. This construction naturally leads to a large mass splitting between the slepton and squark masses, due to the mass splitting between the electroweak gauginos and the gluino. The heavy Higgs bosons and Higgsinos also follow the gluino toward large masses. We carry out a Bayesian Monte Carlo analysis of the parametric space and find that it can simultaneously explain the large Higgs mass, and the anomalous magnetic moment of the muon, while producing a negligible correction to

the Standard Model prediction for $\mathcal{B}r\left(B_s^0 \to \mu^+\mu^-\right)$. We also find that the model leads to an excess in the Higgs diphoton decay rate. A brief discussion of the possibility of detection of the light particles is given. Also discussed are the implications of the model for dark matter.

The CMS and ATLAS collaborations have discovered and measured [194–198] the mass of a new boson which is most likely the Higgs boson [12–15] responsible for breaking electroweak symmetry. In supersymmetry, one would identify this as the light CP-even Higgs boson [200, 204–209], $h^0$. Both experiments agree that the mass is between 125 and 126 GeV. It is quite remarkable that the observed Higgs boson mass lies close to the upper limit predicted in grand unified supergravity models [51–53, 101] which is roughly 130 GeV [200, 201, 208, 224–226]. (For a recent review of Higgs and supersymmetry see [227].) Because the mass of the $h^0$ boson in supersymmetry [54, 180, 202] is less than that of the Z boson at the tree level, a large loop correction is necessary to match the measured value. The dominant one-loop Higgs self energy correction arises from its coupling to the top supermultiplet so that

$$\Delta m_{h^0}^2 \simeq \frac{3m_t^4}{2\pi^2 v^2} \ln \frac{M_S^2}{m_t^2} + \frac{3m_t^4}{2\pi^2 v^2}\left(\frac{X_t^2}{M_S^2} - \frac{X_t^4}{12M_S^4}\right), \tag{10.1}$$

where $v = 246\,\text{GeV}$, $M_S$ is the average stop mass, $X_t = A_t - \mu \cot\beta$, $\mu$ is the Higgs mixing parameter and $A_t$ is the trilinear coupling (both at the electroweak scale), and $\tan\beta = \langle H_2\rangle/\langle H_1\rangle$, where $H_2$ gives mass to the up quarks while $H_1$ gives mass to the down quarks and leptons. Since $\Delta m_{h^0}^2$ has a logarithmic dependence of $M_S$, a sizable $\Delta m_{h^0}^2$ correction implies that the scale $M_S$ is high, lying in the several TeV region.

A high SUSY scale is also suggested by the ATLAS and CMS collaborations. So far, the LHC has delivered $5.3\,\text{fb}^{-1}$ and $23\,\text{fb}^{-1}$ of integrated luminosity [228] at 7 TeV and 8 TeV respectively to both CMS and ATLAS. Analysis of large portions of this data in search of supersymmetry has only yielded

null results, though it is important to note that the parametric exclusion limits provided are typically only on minimal or simplified models. Whenever one works with non-minimal models of supersymmetry, it is necessary to evaluate the signal efficiencies specific to one's model and determine the credible region. The null searches can be evaded obviously by just raising the masses of the superpartners, and thereby raising the scale of SUSY, but it can also be done by producing mass hierarchies and mass splittings that are atypical in minimal models.

The search for the rare decay $B_s^0 \to \mu^+\mu^-$ also has important implications for supersymmetry. The LHCb collaboration has recently observed [229] this rare decay, determining the branching ratio $\mathcal{B}r\left(B_s^0 \to \mu^+\mu^-\right) = (3.2^{+1.5}_{-1.2}) \times 10^{-9}$, which is in excellent agreement with the Standard Model, and thus requires the supersymmetric contribution [230–232] to this decay to be very small. This contribution is mediated by the neutral Higgs bosons and will involve a flavor-changing scalar quark loop. (It is also sensitive to CP violation [233, 234].) In the large $\tan\beta$ limit, the branching ratio is approximately [138, 235, 236]

$$\mathcal{B}r\left(B_s^0 \to \mu^+\mu^-\right) \simeq 3.5 \times 10^{-5} \left(\frac{\tau_{B_s}}{1.5\,\mathrm{ps}}\right) \left(\frac{f_{B_s}}{230\,\mathrm{MeV}}\right)^2 \times \left(\frac{\left|V_{ts}^{\mathrm{eff}}\right|}{0.040}\right)^2 \left(\frac{\tan\beta}{50}\right)^6 \left(\frac{m_t}{m_A}\right)^4 \frac{(16\pi^2)^2 \epsilon_Y^2}{(1+(\epsilon_0+\epsilon_Y y_t^2)\tan\beta)^2(1+\epsilon_0\tan\beta)^2}\,, \quad (10.2)$$

where $\tau_{B_s}$ is the mean lifetime, $f_{B_s}$ is the decay constant, and $V_{ts}^{\mathrm{eff}}$ is the effective CKM matrix element. The loop factors $\epsilon_0$ and $\epsilon_Y$ are given in terms of soft breaking parameters of the 3rd generation $m_{\widetilde{Q}}$, $m_{\widetilde{U}}$, $m_{\widetilde{D}}$, which are the masses of the left-handed squark, up-type squark, and down-type squark, as well as the gluino mass $m_{\widetilde{g}}$, the strong coupling constant $\alpha_s$, and the CP-odd Higgs mass $m_A$:

$$\epsilon_0 = -\frac{2\alpha_s}{3\pi}\frac{\mu}{m_{\widetilde{g}}} H(m_{\widetilde{Q}}^2/m_{\widetilde{g}}^2, m_{\widetilde{D}}^2/m_{\widetilde{g}}^2) \quad (10.3)$$

$$\epsilon_Y = \frac{1}{16\pi^2}\frac{A_t}{\mu} H(m_{\widetilde{Q}}^2/\mu^2, m_{\widetilde{U}}^2/\mu^2) \quad (10.4)$$

$$H(x_1, x_2) = \frac{x_1 \ln x_1}{(1-x_1)(x_1-x_2)} + \frac{x_2 \ln x_2}{(1-x_2)(x_2-x_1)}. \tag{10.5}$$

We note that the branching ratio given by Eq. (10.2) is suppressed by the factor $(m_t/m_A)^4$ and so a large weak scale of SUSY which implies a large $m_A$, naturally leads to a small contribution to $\mathcal{B}r\left(B_s^0 \to \mu^+\mu^-\right)$. Additionally, we see in Eq. (10.2) the factor $(\tan\beta/50)^6$, which implies that the SUSY contribution to $B_s^0 \to \mu^+\mu^-$ is further suppressed if $\tan\beta \lesssim 50$. Together these effects also reduce the SUSY contribution [236, 237] to $\mathcal{B}r\left(b \to s\gamma\right)$ to negligible value.

While the observation of a high Higgs boson mass, null results on the discovery of sparticles and the observation of no significant deviation in the $B_s^0 \to \mu^+\mu^-$ branching ratio from the Standard Model result all appear to indicate a high scale for SUSY, the opposite is indicated by the Brookhaven experiment E821 [238] which measures $a_\mu = \frac{1}{2}(g_\mu - 2)$ to deviate from the Standard Model prediction [223, 239] at the $3\,\sigma$ level. If this deviation is taken to arise from supersymmetry, then

$$a_\mu^{\rm SUSY} = \delta a_\mu = (287 \pm 80.) \times 10^{-11}\ . \tag{10.6}$$

The SUSY contribution [221, 240–246] arises from $\tilde{\chi}^\pm$–$\tilde{\nu}_\mu$ and $\tilde{\chi}^0$–$\tilde{\mu}$ loops. A rough estimate of the supersymmetric correction is

$$\delta a_\mu \simeq {\rm sgn}(M_2\mu)\left(130 \times 10^{-11}\right)\left(\frac{100\,{\rm GeV}}{M_{\rm SUSY}}\right)^2 \tan\beta\ , \tag{10.7}$$

where $M_{\rm SUSY}$ is the SUSY scale. In order to obtain a SUSY correction of size indicated by Eq. (10.6) the masses of sparticles in the loops, i.e., the masses of $\tilde{\chi}^\pm$, $\tilde{\chi}^0$, $\tilde{\mu}$, and $\tilde{\nu}_\mu$ must be only about a few hundred GeV.

Another result which may be a signal of SUSY concerns the excess seen in the diphoton decay rate of the Higgs, which is above the Standard Model prediction. This excess is parametrized by the signal

strength

$$R_{\gamma\gamma} = \frac{\sigma(pp \to H)_{obs}}{\sigma(pp \to H)_{SM}} \times \frac{\Gamma(H \to \gamma\gamma)_{obs}}{\Gamma(H \to \gamma\gamma)_{SM}} \tag{10.8}$$

and is reported as $R_{\gamma\gamma} = 1.6 \pm 0.4$ at CMS [194] and $R_{\gamma\gamma} = 1.8 \pm 0.5$ at ATLAS [198]. The excess is not statistically conclusive and can easily be attributed to a simple fluctuation or to QCD uncertainties [247]. Still it is worthwhile to consider how SUSY can contribute to this loop-induced decay (considering $h^0$ in place of $H$). The excess in the diphoton rate has been discussed in a variety of models by various authors (see, e.g., [207, 248, 249] and the references therein). Within the MSSM, the largest contributions would arise via a $\tilde{\tau}$ triangle, provided that its mass is not too high. (We discuss the calculation of $R_{\gamma\gamma}$ in more detail in Section 10.5.1.) So, if the diphoton result is real, we have another indication of low scale SUSY.

Assuming that the $g_\mu - 2$ and the diphoton rate hold up, one has apparently conflicting results for the weak scale of SUSY. On the one hand, the high Higgs boson mass, null results on the observation of sparticles at the LHC, and the lack of any significant deviation in the $\mathcal{B}r\left(B_s^0 \to \mu^+\mu^-\right)$ branching ratio from the Standard Model prediction point to a high SUSY scale, i.e., a SUSY scale lying in the several TeV range. On the other hand, the $3\,\sigma$ deviation in $a_\mu$ and a fledgling excess in the diphoton decay of the Higgs boson decay point to a low SUSY scale lying in the sub-TeV range. These results cannot be simultaneously satisfied in minimal models such as mSUGRA [250, 251] as they point to split scale SUSY with one scale governing the colored sparticle masses and the heavy Higgs boson masses, and the other SUSY scale governing the uncolored sparticle masses. To generate this split scale SUSY, we construct in this work a supergravity grand unified model [51–53] by introducing non-universalities in the gaugino sector with the feature that the gaugino mass in the $SU(3)_C$ sector is much larger than the other soft masses. In this model, radiative electroweak symmetry breaking [70–72] (for a review see [199]) is driven by the gluino mass. In this work, we label this model as $\tilde{g}$SUGRA. We will show that $\tilde{g}$SUGRA satisfies all of the experimental results simultaneously by exploiting a feature of the

renormalization group equations which leads to a splitting between the squarks, gluino, Higgs bosons, and Higgsinos which become very heavy, and the sleptons, bino and winos which are allowed to remain light at the electroweak scale. (The sfermion masses still unify at a high scale.) We will use a Bayesian Monte Carlo analysis of $\tilde{g}$SUGRA to show that it satisfies all experimental results and determine the credible regions in the parameters and sparticle masses.

The outline of the rest of the chapter is as follows: In Section 10.2, we discuss the general framework of non-universal SUGRA models with specific focus on $\tilde{g}$SUGRA where the gaugino mass in the $SU(3)_C$ color sector is much larger than other mass scales in the model. In Section 10.3, we discuss the statistical framework used in our Bayesian Monte Carlo analysis of a simplified parametric space for $\tilde{g}$SUGRA. In Section 10.4 we explore the impact of LHC searches for sparticles on $\tilde{g}$SUGRA using event-level data and signal simulations. The results of our analyses as well as the details of Higgs diphoton rate are presented in Section 10.5. Concluding remarks are given in Section 10.6.

## 10.2 The $\tilde{g}$SUGRA Model

Supergravity grand unification [51–53] is a broad framework which depends on three arbitrary functions: the superpotential, the Kähler potential, and the gauge kinetic energy function. Simplifying assumptions on the Kähler potential and the gauge kinetic energy function lead to universal boundary conditions for the soft parameters which is the basis of the model referred to as mSUGRA/CMSSM. The parameter space of mSUGRA is given by $m_0$, $m_{1/2}$, $A_0$, $\tan\beta$, and $\mathrm{sgn}(\mu)$, where $m_0$ is the universal scalar mass, $m_{1/2}$ is the universal gaugino mass, $A_0$ is the universal trilinear coupling, and $\tan\beta = \langle H_2\rangle/\langle H_1\rangle$. Here $H_2$ gives mass to the up quarks and $H_1$ gives mass to the down quarks and the leptons, and $\mu$ is the Higgs mixing parameter which enters in the superpotential as $\mu H_1 H_2$.

However, the supergravity grand unification framework does allow for non-universalities of the soft

parameters, i.e., non-universalities for the scalar masses, for the trilinear couplings and for the gaugino masses[1]. In $\tilde{g}$SUGRA, we consider supergravity grand unification with universal boundary conditions in all sectors except in the gaugino sector. In this sector, we specify that the $SU(3)_C$ gaugino mass, $M_3$, be much larger than the universal scalar mass and also much larger than the gaugino masses $M_2, M_1$ in the $SU(2)_L$, $U(1)_Y$ sectors, i.e.,

$$M_3 \gg m_0, M_1, M_2 \tag{10.9}$$

The constraints of Eq. (10.9) ensure that the radiative breaking of electroweak symmetry will be driven by the gluino (hence, $\tilde{g}$SUGRA). Now, the gluino mass enters in the renormalization group equations for the squark masses and thus the squark masses will be driven to values proportional to the gluino mass as we move down from the GUT scale toward the electroweak scale. Consequently, a gluino mass in the ten TeV region will also generate a squark mass in the several TeV region. On the other hand, the RGEs for the sleptons do not depend on the gluino mass at the one-loop level and if $m_0, M_1, M_2$ are $\mathcal{O}(100\,\text{GeV})$, the masses of the sleptons as well as the electroweak gauginos at the electroweak scale will likely remain this size. Thus the RG evolution creates a natural splitting of masses between the squarks and the sleptons at the electroweak scale even though they have a common mass at the grand unification scale. The renormalization of these soft masses for a sample point in $\tilde{g}$SUGRA is shown in Fig. 10.1. The huge mass splitting between the squark and slepton masses at low scales even though they are unified at high scales is reminiscent of the gauge coupling unification where the three gauge couplings $\alpha_i$ which are split at the electroweak scale but come together at the grand unification scale. We note that the split spectrum of $\tilde{g}$SUGRA is very different in nature from that of what is commonly called "split supersymmetry" [263], which consists of light Higgsinos $\widetilde{H}_{u,d}$, $\tilde{B}$, $\widetilde{W}$, $\tilde{g}$ and one Higgs doublet but does not allow for light sfermions.

[1]The literature on non-universalities in SUGRA models is enormous. For a sample of early and later works see [126, 127, 191, 252–261] and for a review see [262].

In GUT models, non-universal gaugino masses can arise from superfields that transform as a non-singlet IRs of the GUT group and get VEVs in the spontaneous breaking and give masses to the gauginos. The general form of the gaugino mass term in the Lagrangian is

$$-\frac{\langle F\rangle_{ab}}{M_{Pl}}\frac{1}{2}\lambda_a\lambda_b + \text{H.c.} \tag{10.10}$$

where $\langle F\rangle_{ab}$ is a non-zero VEV of mass dimension 2, and $M_{Pl}$ is the Planck mass. The $\lambda$'s belong to the adjoint of the GUT group: **24** for SU(5) and **45** for SO(10). Now only the symmetric product of the adjoints enters in the analysis. Thus for SU(5) one has $(\mathbf{24}\otimes\mathbf{24})_{sym} = \mathbf{1}\oplus\mathbf{24}\oplus\mathbf{75}\oplus\mathbf{200}$, while for SO(10) one has $(\mathbf{45}\otimes\mathbf{45})_{sym} = \mathbf{1}\oplus\mathbf{54}\oplus\mathbf{210}\oplus\mathbf{770}$. With the use of singlet and non-singlet breaking, one can produce a hierarchy in the gaugino masses so that Eq. (10.9) holds. We note that non-universalities of gaugino masses arise also in string based models, see, e.g., [264].

In our study of $\tilde{g}$SUGRA, we introduce gaugino sector non-universalities by having $m_{1/2} \to \widetilde{m}_{1/2} \equiv M_1 = M_2$ and $M_3 = 10\,\widetilde{m}_{1/2}$ as an illustrative example, so that at the unification scale, $M_1 : M_2 : M_3 = 1 : 1 : 10$. We now show how this choice can be constructed by combining singlet and non-singlet breaking in SU(5) and in SO(10). In SU(5) we consider the linear combination $\mathbf{1} + a\,\mathbf{24} + b\,\mathbf{75}$. Now the singlet breaking gives the ratio $M_1 : M_2 : M_3 = 1 : 1 : 1$, the 24-plet gives the ratio [259] $-1/2 : -3/2 : 1$ while the 75-plet gives the ratio [259] $-5 : 3 : 1$. Choosing $a = -8/11$ and $b = -1/11$ leads to the desired ratio $M_1 : M_2 : M_3 = 1 : 1 : 10$. This scheme also applies to SO(10) since $SU(5) \subset SO(10)$. However, for SO(10) we can also consider gaugino mass terms in representations of $SU(4)\times SU(2)_L \times SU(2)_R \subset SO(10)$ and label the breaking terms by $SU(4)\times SU(2)_R$ representations as subscripts. In this case we consider the breaking $\mathbf{1} + a\,\mathbf{210}_{(1,1)} + b\,\mathbf{210}_{(15,1)}$ where the $\mathbf{210}_{(1,1)}$ gives the gaugino mass ratio [259] of $-3/5 : 1 : 0$ and $\mathbf{210}_{(15,1)}$ gives the gaugino mass ratio [259] of $-4/5 : 0 : 1$. Thus we can choose $a = -3/4$ and $b = 3/2$ to get the desired $1 : 1 : 10$ ratio. We limit ourselves to this ratio for the rest of the analysis in this chapter. However, many features of this analysis will persist with

different ratios of $M_1 : M_2 : M_3$ as long as $M_3 \gg m_0, M_1, M_2$.

In $\tilde{g}$SUGRA, radiative electroweak symmetry breaking is dominated by the large gluino mass which is responsible for giving large masses to the squarks. We contrast this work with other recent works which have attempted to explain $g_\mu - 2$ in the context of a high Higgs boson mass. This is attempted in [248] with the assumption of a light slepton and heavy squark spectrum. The analysis also tries to correlate $g_\mu - 2$ with the diphoton rate. However, this model is not a high scale model and the analysis is limited to assumptions of the spectrum at the electroweak scale. In [265] the authors assumed a split family supersymmetry. The analysis of [266] uses non-universal gaugino masses in an SU(5) model but the details of the model are significantly different from the work presented here. The work [267] also addresses the issue of getting light uncolored and heavy colored particles but the analysis is within a gauge mediated supersymmetry breaking. Similar scenarios are studied in [268, 269] where the authors also attempt to reconcile the experimental results using non-universal gaugino masses.

The attractive feature of $\tilde{g}$SUGRA is that the relatively large value of $M_3$ automatically drives the squarks to be massive while the sleptons as well as the bino and the light wino are left alone. This is illustrated in Fig. 10.1 where we display the renormalization group flow for a sample point from our analysis. We wish to show that this simple feature automatically satisfies all of the empirical results that we have discussed here that hint at the supersymmetric spectrum. To this end, we perform a Bayesian Monte Carlo analysis of $\tilde{g}$SUGRA with the illustrative example of the $1 : 1 : 10$ gaugino mass ratio, which we discuss in the sections that follow.

## 10.3 Statistical Framework

We study here the parameter space of $\tilde{g}$SUGRA for the case where the ratio of the gaugino masses at the GUT scale is $1 : 1 : 10$. In this case, $\tilde{g}$SUGRA is parametrized by $m_0$, $\widetilde{m}_{1/2}$, $A_0$, and $\tan\beta$ (having

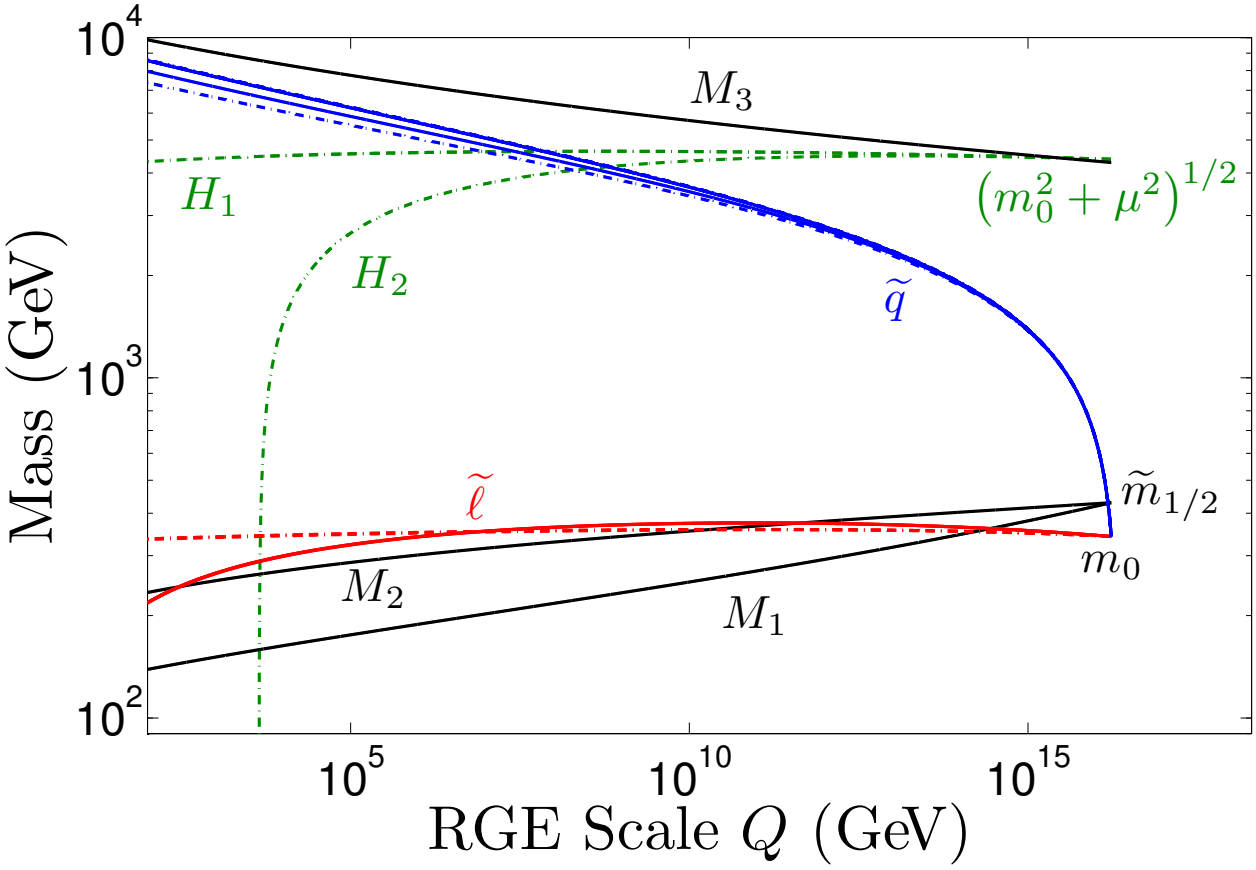


Figure 10.1: Two-loop renormalization group evolution of the soft parameters in g̃SUGRA. The input parameters used here are those of the best-fit point determined from our analysis in Section 10.3. The fields are labeled in the figure and also in color. The gaugino fields are presented in black and the Higgs fields are presented in green. The squarks and sleptons are in blue and red, where the left-handed fields are solid and the right-handed fields are dot-dashed. Additionally, $m_0$ is the soft mass for the scalars, $\widetilde{m}_{1/2}$ is the common mass of the $U(1)_Y$ and $SU(2)_L$ gaugino fields, and $\mu$ is the Higgs mixing parameter.

selected sgn $(\mu) = 1$). Here, $\widetilde{m}_{1/2} = M_1 = M_2$ while $M_3 = 10\,\widetilde{m}_{1/2}$. The dimensionful parameters $m_0$, $\widetilde{m}_{1/2}$, and $A_0$ are all specified at the GUT scale. The ratio of the two Higgs VEVs $\tan\beta = \langle H_2\rangle/\langle H_1\rangle$, is specified at $M_Z$. We further include four Standard Model nuisance parameters to create an 8D parameter space. Namely, we add the top quark pole mass, the running bottom quark mass, the strong

| Observable | Central value | Exp. Error | Theory Error | Distribution | Ref. |
|---|---|---|---|---|---|
| | | | SM Nuisance Parameters | | |
| $m_t^{pole}$ (GeV) | 173.5 | 1.0 | – | Gaussian | [218] |
| $m_b(m_b)^{\overline{MS}}$ (GeV) | 4.18 | 0.03 | – | Gaussian | [218] |
| $\alpha_s(M_Z)^{\overline{MS}}$ | 0.1184 | $7 \times 10^{-4}$ | – | Gaussian | [218] |
| $\alpha_{EM}^{-1}(M_Z)^{\overline{MS}}$ | 127.933 | 0.014 | – | Gaussian | [218] |
| | | | Measured | | |
| $\delta a_\mu \times 10^{11}$ | 287 | 80 | 10 | Gaussian | [223, 238, 239] |
| $\mathcal{B}r\left(B_s^0 \to \mu^+\mu^-\right) \times 10^9$ | 3.2 | 1.92 | 14% | Gaussian | [229] |
| $\mathcal{B}r\left(b \to s\gamma\right) \times 10^4$ | 3.55 | 0.26 | 0.21 | Gaussian | [270] |
| $\mathcal{B}r\left(B^+ \to \tau^+\nu\right) \times 10^4$ | 1.79 | 0.48 | 0.38 | Gaussian | [270] |
| $\omega_\chi$ | 0.1126 | 0.0036 | 10% | Upper-Gaussian | [271] |
| $h^0$ Mass (GeV) | 125.7 | 0.2 | 2.0 | Gaussian | [194, 198] |
| | | | 95% CL Particle Mass Limits (GeV) | | |
| $h^0$ | 122.5 | – | – | Lower – Step Func. | [272] |
| $h^0$ | 129 | – | – | Upper – Step Func. | [272] |
| $\tilde{\chi}_1^0$ | 46 | – | 5% | Lower – Error Func. | [218] |
| $\tilde{\chi}_2^0$ | 62.4 | – | 5% | Lower – Error Func. | [218] |
| $\tilde{\chi}_3^0$ | 99.9 | – | 5% | Lower – Error Func. | [218] |
| $\tilde{\chi}_4^0$ | 116 | – | 5% | Lower – Error Func. | [218] |
| $\tilde{\chi}_1^\pm$ | 94 | – | 5% | Lower – Error Func. | [218] |
| $\tilde{e}_R$ | 107 | – | 5% | Lower – Error Func. | [218] |
| $\tilde{\mu}_R$ | 94 | – | 5% | Lower – Error Func. | [218] |
| $\tilde{\tau}_1$ | 81.9 | – | 5% | Lower – Error Func. | [218] |
| $\tilde{b}_1$ | 89 | – | 5% | Lower – Error Func. | [218] |
| $\tilde{t}_1$ | 95.7 | – | 5% | Lower – Error Func. | [218] |
| $\tilde{g}$ | 500 | – | 5% | Lower – Error Func. | [218] |
| $\tilde{q}$ | 1100 | – | 5% | Lower – Error Func. | [218] |

Table 10.1: Summary of the observables used to construct the likelihood function. The distribution labeled "Upper-Gaussian" used for the $\omega_\chi$ observable means that there is only a decrease in likelihood for values larger than the central value. The 95% CL limits are evaluated using the complementary error function, as the bound is smeared by the theoretical uncertainty. Limits specified with a step function distribution indicate a hard cut, where points on the wrong side of the limit are assigned zero likelihood.

coupling, and the EM coupling. We create from these the parameter space $\mathbf{\Theta}$:

$$\mathbf{\Theta} = \left\{ m_0, \widetilde{m}_{1/2}, A_0, \tan\beta, m_t^{pole}, m_b(m_b)^{\overline{MS}}, \alpha_s(M_Z)^{\overline{MS}}, \alpha_{EM}^{-1}(M_Z)^{\overline{MS}} \right\} . \tag{10.11}$$

For each parameter $\theta_i \in \boldsymbol{\Theta}$, we begin by selecting uniform distributions in the allowed ranges prior to considering the experimental data. The prior distributions that we have selected for our parameters are uniform on either a linear or a log scale:

$$\begin{aligned} m_0 &\in [50, 5000]\ \text{GeV (log)} \\ \widetilde{m}_{1/2} &\in [50, 2500]\ \text{GeV (log)} \\ A_0 &\in [-50, 50]\ \text{TeV (linear)} \\ \tan\beta &\in [3, 60]\ \text{(linear)}\ . \end{aligned} \tag{10.12}$$

The nuisance parameters in $\boldsymbol{\Theta}$ are uniform in a $2\,\sigma$ range (linear scale) around the central values, which are specified in Section 10.2.

Next we collect the relevant observables into $\mathbf{D}$, which is a set of pairs of central values and uncertainties of experimental measurements. The observables include the precise measurements of the nuisance parameters, along with the results from flavor physics $\mathcal{B}r\left(B_s^0 \to \mu^+\mu^-\right)$ and $\mathcal{B}r\left(b \to s\gamma\right)$, the muon anomalous magnetic moment $\delta a_\mu$, the measured mass of the (ostensibly) light CP-even Higgs boson, as well as limits on superpartner masses. We further include the fit to the thermal relic density of dark matter, $\omega_\chi \equiv \Omega_\chi h^2$, from CMB temperature fluctuations measured by WMAP (9 year dataset) [273] and Planck (15.5 month dataset) [274]. In $\tilde{g}$SUGRA, the lightest neutralino is indeed a candidate for cold dark matter, but we wish to allow for multicomponent models of dark matter, and so we only consider the upper limit of $\omega_\chi$. The central values and uncertainties of $\mathbf{D}$ are specified in Section 10.2.

The goal now is to update our a priori guess for the probability distributions of the parameters in $\boldsymbol{\Theta}$ (given in Eq. (10.12)) with the empirical information in $\mathbf{D}$, giving the posterior probability distribution. This distribution can then be marginalized to determine the credible region of one or two parameters. The calculation of the posterior probability distribution is achieved using Bayesian inference, but we

first need to be able to compare a parametric point in our model to the empirical data in $\mathbf{D}$. This requires a set of mappings $\xi_i : \boldsymbol{\Theta} \to \mathtt{R}$ corresponding to each $d_i \in \mathbf{D}$, which just give the theoretical calculation for the observable corresponding to each $d_i$. These mappings are computed using numerical codes incorporated in our analysis software SusyKit [211].

Now we can move on to constructing the posterior probability distribution, which is given by Bayes' theorem

$$\mathtt{P}(\boldsymbol{\Theta}|\mathbf{D}) = \frac{\mathtt{P}(\mathbf{D}|\boldsymbol{\Theta})\mathtt{P}(\boldsymbol{\Theta})}{\mathtt{P}(\mathbf{D})} \,. \tag{10.13}$$

$\mathtt{P}(\boldsymbol{\Theta})$ is the prior distribution given in Eq. (10.12). The denominator is the so-called Bayesian evidence $\mathcal{Z} = \mathtt{P}(\mathtt{D})$, which can be used in model selection tests, but as we are only interested in parameter estimation, it serves as a normalization constant. The final factor is the likelihood function $\mathfrak{L} = \mathtt{P}(\mathbf{D}|\boldsymbol{\Theta})$, which is constructed by the "pulls" method

$$-2\ln\mathfrak{L} = \sum_{d_i \in \mathbf{D}} \frac{\left(\xi_i(\boldsymbol{\Theta}) - d_i\right)^2}{\sigma_i^2 + \tau_i^2} \tag{10.14}$$

where $\sigma_i$ and $\tau_i$ are the experimental and theoretical uncertainties, respectively. This is straightforward for the case that a measurement with precision is reported. In many cases only the 95% CL limits are given. In those cases, a smearing due to the implicit theoretical uncertainty in the computation is used and the likelihood is computed from the complementary error function. A hard cut on an observable can also be made by using a step function, i.e. assigning zero likelihood to points that are on the wrong side of a limit. The numerical values used to construct the likelihood function is given in Section 10.2.

Our analysis was performed using our software package SusyKit [211], which uses the efficient multi-modal ellipsoidal nested sampling algorithm implemented in the MultiNest [210, 212, 213] library. Additionally, SusyKit interfaces with several standard numerical codes such as SoftSUSY [132], MicrOMEGAs [87, 189], FeynHiggs [275, 276], and SuperIso Relic [277, 278]. SusyKit is written

entirely in C++11 and is largely inspired by the FORTRAN-90 code SuperBayes [214, 215].

We specify the MultiNest sampling parameters $n_{\text{live}} = 5{,}000$ and $\texttt{tol} = 0.01$. The analysis has required the evaluation of the likelihood function at 1.1 million points to sufficiently explore the parametric space. The result is a chain of 81,000 Monte Carlo sample points which is used to compute 1D and 2D marginalized distributions in our principal and derived parameters, and to establish credible regions in these parameters. We found that the credible regions entered areas that would be excluded by the LHC in minimal SUSY GUT models such as mSUGRA, so we found it necessary to evaluate the impact of LHC searches on $\tilde{g}$SUGRA.

## 10.4 LHC Analysis

In order to evaluate the impact of null results in the searches for supersymmetry at the LHC on $\tilde{g}$SUGRA, we construct an auxiliary likelihood function, $\mathfrak{L}_{\text{LHC}}$, based on the Monte Carlo event generation and detector simulation for our sample points.

We begin by generating 200,000 events for each sample point in our chain using PYTHIA [86, 279] considering $2 \to 2$ SUSY production processes with $\sqrt{s} = 8\,\text{TeV}$. We find that the total cross section for these processes is $\mathcal{O}(100\,\text{fb})$ and the dominant modes involve the production of $\tilde{\chi}_1^0$, $\tilde{\chi}_2^0$, $\tilde{\chi}_1^\pm$, $\tilde{\ell}$, $\tilde{\tau}_1$, $\tilde{\tau}_2$, and, $\tilde{\ell}$ and $\tilde{\nu}$. This is to be expected because in $\tilde{g}$SUGRA, the scalar quark fields all become heavy as they are renormalized to the electroweak scale, while the scalar leptons are allowed to remain light to produce contributions to $\delta a_\mu$ and the Higgs diphoton decay rate. By investigating the dominant decays of these particles, we decide that supersymmetry searches in leptonic final states are the most relevant to $\tilde{g}$SUGRA. We have used the $3\ell$ and same-sign $2\ell$ searches at CMS [280] using $9.2\,\text{fb}^{-1}$ at $\sqrt{s} = 8\,\text{TeV}$ to construct our $\mathfrak{L}_{\text{LHC}}$, in a manner similar to [251]. These searches are performed using 108 and 4 event bins respectively, which serve as counting experiments and are naturally Poisson

distributed. Therefore $\mathfrak{L}_{\text{LHC}}$ is computed by

$$\mathfrak{L}_{\text{LHC}} = \prod_{i \in \text{bins}} \mathfrak{L}_i \, . \tag{10.15}$$

Each $\mathfrak{L}_i$ would be a simple Poisson likelihood, except that one of the parameters to the Poisson distribution, the expected background yield, $b_i$, can have a large uncertainty, $\delta b_i$. Thus, it is necessary to convolve the Poisson distribution with a distribution for the background yield. Naïvely this would be a Gaussian distribution, however in the case that the relative error in the background yield is large, i.e., $\delta b_i / b_i \gtrsim 20\%$, then a non-trivial portion of the convolution is due to contributions from negative $b_i$, or even if the integration is limited to non-negative background, a large portion of the PDF may be omitted. Thus as a heuristic, we use the following definition for $\mathfrak{L}_i$:

$$\mathfrak{L}_i = \int_0^\infty \text{Pois}(s_i + \bar{b}; o_i) F(b_i, \delta b_i; \bar{b}) \, d\bar{b} \, , \tag{10.16}$$

where $i$ is the event bin, Pois is the Poisson probability mass function, $s_i$ is the expected signal yield, $o_i$ is the number of observed events, and as defined already $b_i$ is the expected background yield, and $\delta b_i$ is the uncertainty in the background. The function F is defined according to our heuristic

$$F(b_i, \delta b_i; \bar{b}) = \begin{cases} \mathcal{N}(b_i, \delta b_i; \bar{b}) \, , \, \delta b_i / b_i < 20\% \\ \\ \ln \mathcal{N}(b_i, \delta b_i; \bar{b}) \, , \, \delta b_i / b_i \geqslant 20\% \end{cases} \, , \tag{10.17}$$

where $\mathcal{N}$ is the Gaussian distribution and $\ln \mathcal{N}$ is the log-normal distribution. As a further heuristic, it is necessary to account for cases when either $b_i = 0$ or $\delta b_i = 0$. These cases are clearly oversights in the CMS *preliminary* analysis summary; still they must be addressed. We choose a sentinel value $\Delta = 10^{-6}$ and use $\delta b_i = \Delta$ if $\delta b_i$ is zero and we set $b_i = \delta b_i$ if $b_i$ is zero.

The expected signal yield $s_i$ is the product of the efficiency $\epsilon_i$ with the total SUSY cross section and the integrated luminosity. The efficiency $\epsilon_i$ is the proportion of the total generated events that would be counted in the $i^{th}$ bin, and is determined by running the events through a detector simulation, which we have carried out with PGS [117]. Jet objects were reconstructed using the anti-$k_T$ algorithm, with a distance parameter of 0.5. We implemented the cuts to place events into bins in a modified version of PARVICURSOR [281]. The object selection criteria, event vetoes, and geometrical cuts are reproduced as in [280].

To combine the likelihood from these searches to the likelihood function described in Section 10.3, we first compute the likelihood for the Standard Model according to this analysis by turning off the signal, $\mathfrak{L}_{SM} \equiv \mathfrak{L}_{LHC}\big|_{s=0}$. We then add the likelihood ratio statistic to the full likelihood function,

$$-2\ln\mathfrak{L} \to -2\ln\mathfrak{L} - 2\ln\left(\min\left\{\frac{\mathfrak{L}_{LHC}}{\mathfrak{L}_{SM}}, 1\right\}\right), \tag{10.18}$$

which is approximately $\chi^2$ distributed, and is a natural addition to the other "pull" terms in our likelihood function. Having computed the updated likelihood due to these CMS searches, it is necessary to re-weight the samples by a factor $\exp(\Delta\ln\mathfrak{L})$. We can now proceed to determine the marginalized posterior probability distributions within our parameters of interest.

## 10.5 Results

In this section we present the results from our Bayesian analysis. Given our likelihood function, we determine the Bayesian evidence of $\tilde{g}$SUGRA to be $\ln\mathcal{Z} = -11.9 \pm 0.042$. We provide this for reference, as we do not perform a model selection test. The best-fit point in our analysis is determined to have $\chi^2_{min} = 2.73$, and leaving out some of the nuisance parameters, is specified by $\left(m_0, \widetilde{m}_{1/2}, A_0, \tan\beta, m_t^{pole}\right) = (341, 429, 298, 9.73, 174)$ where the massive parameters are specified in GeV. This point illustrates the

general result of $\tilde{g}$SUGRA that high $h^0$ mass and $\delta a_\mu$ can be simultaneously satisfied. Additionally, the large scalar quark and gluino masses allow for consistency with $\mathcal{B}r\left(B_s^0 \to \mu^+\mu^-\right)$ and $\mathcal{B}r\left(b \to s\gamma\right)$. The credible regions in the masses of the heavier particles in $\tilde{g}$SUGRA are presented in the right panel of Fig. 10.2, and the light particles of $\tilde{g}$SUGRA that create the $\delta a_\mu$ contribution as well as the contribution to the diphoton Higgs decay are given in the left panel.

The 1 $\sigma$ and 2 $\sigma$ credible regions in our parameters of interest are given in Fig. 10.3, where we have chosen to use the dimensionless parameter $A_0/m_0$. The 1D posterior distributions in these parameters are given in the top panels of Fig. 10.4, though here we did give the distribution for the dimensionful parameter $A_0$.

While $\tilde{g}$SUGRA largely achieves the correct $h^0$ mass and $\delta a_\mu$ contribution as shown in the middle two lower panels of Fig. 10.4, the posterior distribution in the top mass is shifted up from the central value by 0.5 GeV to 174 GeV, which is evident in the lower left panel of Fig. 10.4. The tension between the top mass, the $h^0$ mass and $\delta a_\mu$ is clearly displayed in Fig. 10.7 where we have interpolated sample points from a slice in our likelihood function and presented level curves in "$\chi^2(\delta a_\mu)$" which is the contribution to $-2\ln\mathcal{L}$ due to $\delta a_\mu$. It is evident that the higher $h^0$ mass and $\delta a_\mu$ is best matched in $\tilde{g}$SUGRA for a slightly heavier top quark.

We point out that this tension is not overly significant in $\tilde{g}$SUGRA for two reasons. First, there is a large theoretical uncertainty in the calculation of the $h^0$ mass at the 2-loop level, which when considered does lift most of the tension. Next, we specified in $\tilde{g}$SUGRA $M_3 = 10\,\widetilde{m}_{1/2}$, where 10 is an arbitrary choice. Allowing the coefficient to be a new degree of freedom or simply selecting several different choices will likely resolve this tension as well.

In our Bayesian analysis, we have sampled the parameter space using the older WMAP7 value for $\omega_\chi$ in $\mathcal{L}$ but we can see from the fourth panel from the left in the bottom row of Fig. 10.4 that the slightly larger value indicated by WMAP9 and Planck would simply enlarge our credible region. Additionally,

we see in Fig. 10.6 that g̃SUGRA is not currently constrained by the best available limit on the direct detection of $\tilde{\chi}_1^0$ dark matter, and is slightly beyond the projected sensitivity of XENON1T and SuperCDMS1T, creating a sort of nightmare scenario for dark matter experiments, as our dark matter signal would be competing with the cosmic neutrino background. The LSP in our model is consistently a bino, and the $\tilde{\chi}_2^0$ is a wino. There is virtually no mixing with the Higgsino sector as the Higgsino mass parameter $\mu$ becomes very large due to the large $M_3$. The sensitivity to dark matter experiments can be increased by adjusting the ratio of $M_1$ to $M_2$ to allow for greater bino-wino mixing within the LSP state.

One of the exceptional aspects of g̃SUGRA is the presence of many light superpartners that have thus far evaded detection at the LHC. We concede that the searches that we considered here are not by any means comprehensive, but they are designed to constrain the production modes most prevalent in g̃SUGRA. The limits are evaded largely due to the stringent selection criteria and the difficulty in identifying $\tau$ leptons. Additionally, the mass hierarchy of g̃SUGRA limits the possibility of cascading decays.

We note that the parametric space of g̃SUGRA, naturally fits into the Hyperbolic Branch [96, 282, 283] of radiative breaking of the electroweak symmetry. This is due to the fact that the stop masses are driven to be large by the gluino, giving a large $Q = \sqrt{m_{\tilde{t}_1} m_{\tilde{t}_2}}$, and it was shown in [188, 284] that $Q \gtrsim 1$ TeV corresponds to a hyperbolic geometry of soft parameters that give radiative EWSB (a large SUSY scale in the tens of TeV also arises in a certain class of string motivated models [133, 285]). Still, g̃SUGRA as it stands produces a large value of $\mu$ with respect to the $Z$ mass. Specifically, a large value of $\mu$ is necessary to balance the large value of $M_3$ which enters in the corrections to the $H_2$ field mass.

### 10.5.1 Higgs Diphoton Decay

In the Standard Model, the loop-induced decay of the Higgs into two photons is mediated mainly by the $W$, top, and to a lesser extent, the bottom quark. The partial width reads [286]

$$\Gamma(H \to \gamma\gamma) = \frac{\alpha_{EM}^2 m_H^2}{256 v^2 \pi^3} \left| \sum_{f=t,b} N_{c,f} Q_f^2 A_{1/2}(\tau_f) + A_1(\tau_W) \right|^2 \tag{10.19}$$

where $\tau_i = 4m_i^2/m_H^2$, and the spin form factors are

$$A_{1/2}(\tau) = 2\tau\left(1 - (\tau - 1) f(\tau)\right) \tag{10.20}$$

$$A_1(\tau) = -\left(2 + 3\tau - 3\tau(\tau - 2) f(\tau)\right) \tag{10.21}$$

and the universal scaling function $f(\tau)$ is

$$f(\tau) = \begin{cases} \arcsin^2\left(\tau^{-1/2}\right) & : \tau \geqslant 1 \\ -\frac{1}{4}\left(\ln \frac{1 + \sqrt{1-\tau}}{1 - \sqrt{1-\tau}} - \imath\pi\right)^2 & : \tau < 1 \end{cases} . \tag{10.22}$$

Supersymmetry corrects this partial width [180] by factors involving the Higgs mixing angle $\alpha$ and $\beta$ arising from the two Higgs doublets. Additionally, new amplitudes are available mediated by the charged Higgs, charginos, and sfermions. The couplings to the charginos arise from Higgsino–gaugino mixing, but in $\tilde{g}$SUGRA the Higgsinos are very heavy thus the lighter chargino is always purely charged wino while the heavier one is purely charged Higgsino. This means that overall the chargino contribution is small either because the coupling is suppressed or because the mass is too large. The charged Higgs exchange is also suppressed due to its large mass. Thus the largest contributions can come only from the sfermion sector, which in $\tilde{g}$SUGRA is dominated by the staus.

In the decoupling limit where $M_A \gg M_Z$ which corresponds to $\alpha = \beta - \pi/2$, the Higgs coupling

to the staus is given by [248, 249]

$$g_{h^0\tilde{\tau}_i\tilde{\tau}_i} = I_3^\tau c_i \mp Q_\tau \sin^2\theta_W \cos 2\theta_{\tilde{\tau}} \mp \frac{m_\tau(A_\ell - \mu\tan\beta)}{2M_Z^2}\sin 2\theta_{\tilde{\tau}} - \frac{m_\tau^2}{M_Z^2} \tag{10.23}$$

with $c_1 = \cos^2\theta_{\tilde{\tau}}$, and $c_2 = \sin^2\theta_{\tilde{\tau}}$. The '$-$' case corresponds to $i = 1$, and the '$+$' case corresponds to $i = 2$. The partial width in $\tilde{g}$SUGRA including the amplitude due to staus then reads

$$\Gamma\left(h^0 \to \gamma\gamma\right) = \frac{\alpha_{EM}^2 m_H^2}{256v^2\pi^3}\left|\sum_{f=t,b} N_{c,f}Q_f^2 A_{1/2}(\tau_f) + A_1(\tau_W) + \sum_{i=1,2} g_{h^0\tilde{\tau}_1\tilde{\tau}_2}\frac{M_Z^2}{m_{\tilde{\tau}}^2}A_0(\tau_i)\right|^2 \tag{10.24}$$

and the spin zero form factor is

$$A_0(\tau) = -\tau(1 - \tau f(\tau)) \, . \tag{10.25}$$

We identify the ratio of this partial width to the Standard Model width given in Eq. (10.19) as $R_{\gamma\gamma}$. (We have taken the ratio of the theoretical and observed $h^0$ production to be unity.) We compute this ratio for each of our Monte Carlo samples and construct the 1D posterior PDF in this derived parameter which we present in Fig. 10.8. We find that $\tilde{g}$SUGRA generically produces a $\sim 20\%$ boost to this decay mode over the Standard Model case. The $2\,\sigma$ credible interval is $[1.03, 1.38]$, which is quite consistent with the preliminary results arriving from the LHC, but is also consistent with the SM prediction. As the Higgs boson couplings are studied with greater precision in the future, it will be useful to compute $R_{\gamma\gamma}$ with greater precision and estimate the uncertainty so that $R_{\gamma\gamma}$ may be used as an additional constraint on the parametric space.

## 10.6 Conclusion

The recent observation of the Higgs boson mass around 125 GeV points to large loop corrections which can be achieved with a large weak scale of SUSY. A large SUSY scale also explains the suppression of

SUSY contributions to the decay $B_s^0 \to \mu^+\mu^-$, to be consistent with the recently measured branching ratio for this process. On the other hand, the experimental observation of a $3\sigma$ effect in $\delta a_\mu$ and a possible excess in the diphoton rate $R_{\gamma\gamma}$ in the Higgs boson decay over the standard model prediction cannot be explained with a high SUSY scale. Thus the two sets of data point to a two scale SUSY spectrum, one a high scale consisting of colored particles, i.e., the squarks and the gluinos, and the Higgs bosons (aside from the lightest Higgs) and the other a low scale for masses of uncolored particles including sleptons and the electroweak gauginos.

In this work we discuss the high scale supergravity grand unified model, $\tilde{g}$SUGRA, which includes the feature of a two scale sparticle spectrum where the sparticle spectrum is widely split at the electroweak scale. This is accomplished within supergravity grand unification with non-universal gaugino masses such that $M_3 \gg M_1, M_2, m_0$. As an illustration we consider the specific case where $M_1 : M_2 : M_3 = 1 : 1 : 10$ at the unification scale, $M_1 = M_2 = \widetilde{m}_{1/2}$ and $M_3 \gg m_0$. This case is designed to be mainly illustrative and can be easily embedded within SU(5) and SO(10). Using a Bayesian Monte Carlo analysis, It is found that this construction simultaneously explains the high $h^0$ mass, null results for squarks and gluino searches at the LHC, a negligible correction to the branching ratio for $B_s^0 \to \mu^+\mu^-$, a $3\sigma$ deviation of $g_\mu - 2$ from the Standard Model prediction as well as the nascent excess in the Higgs diphoton signal.

The observable sparticle spectrum at the LHC in this model consists of light sleptons and light electroweak gauginos. However, sleptons and electroweak gauginos are typically difficult to observer at the LHC and thus far have evaded detection in multi-lepton searches in experiments at the ATLAS and the CMS detectors with the 7 TeV and 8 TeV data. The most promising $2 \to 2$ processes that can generate sparticles at the LHC in this model are $pp \to \tilde{\chi}_1^\pm \tilde{\chi}_1^\mp, \tilde{\chi}_2^0 \tilde{\chi}_1^\pm$. The identifying signatures of such processes will indeed be multi-leptons and missing energy. It is hoped that at increased energies and with larger luminosities such signals will lie in the observable region. However, a detailed analysis of

the signals is needed, requiring a knowledge of the backgrounds.

Another aspect of the simplified $\tilde{g}$SUGRA model relates to the spin-independent $\tilde{\chi}_1^0-p$ cross section. This cross section is found to be rather small for the case when the gaugino masses are chosen in the ratio $1:1:10$. The reason for this smallness is easily understood. The constraint $M_1 = M_2$ at the GUT scale, leads to an LSP which is essentially purely bino with very little Higgsino or wino content. The purely bino nature of the LSP leads to a suppressed $\tilde{\chi}_1^0 - p$ cross section (see e.g., [287]) which lies beyond the reach of the current and projected sensitivities for direct-detection experiments. However, the above result is very specific to the $M_1 : M_2 : M_3 = 1:1:10$ assumption and a modification of the above should allow $\tilde{\chi}_1^0 - p$ cross section within the observable range in the projected sensitivities for direct-detection experiments. We note that while our analysis was performed using the older WMAP7 measurement of the cold dark matter relic density, the newer measurements from WMAP9 and Planck (with 15.5 months of data) only slightly increase the measurement. As we only apply the upper limit from these measurements to allow for the possibility of multi-component theories of dark matter, the newer results would only expand the credible regions of our parameter space and either increase or not affect at all the likelihood of our best-fit point.

Finally, we note that the large squark masses in $\tilde{g}$SUGRA would also help stabilize the proton against decay from baryon and lepton number violating dimension five operators [284, 288, 289] (for a review see [166]).

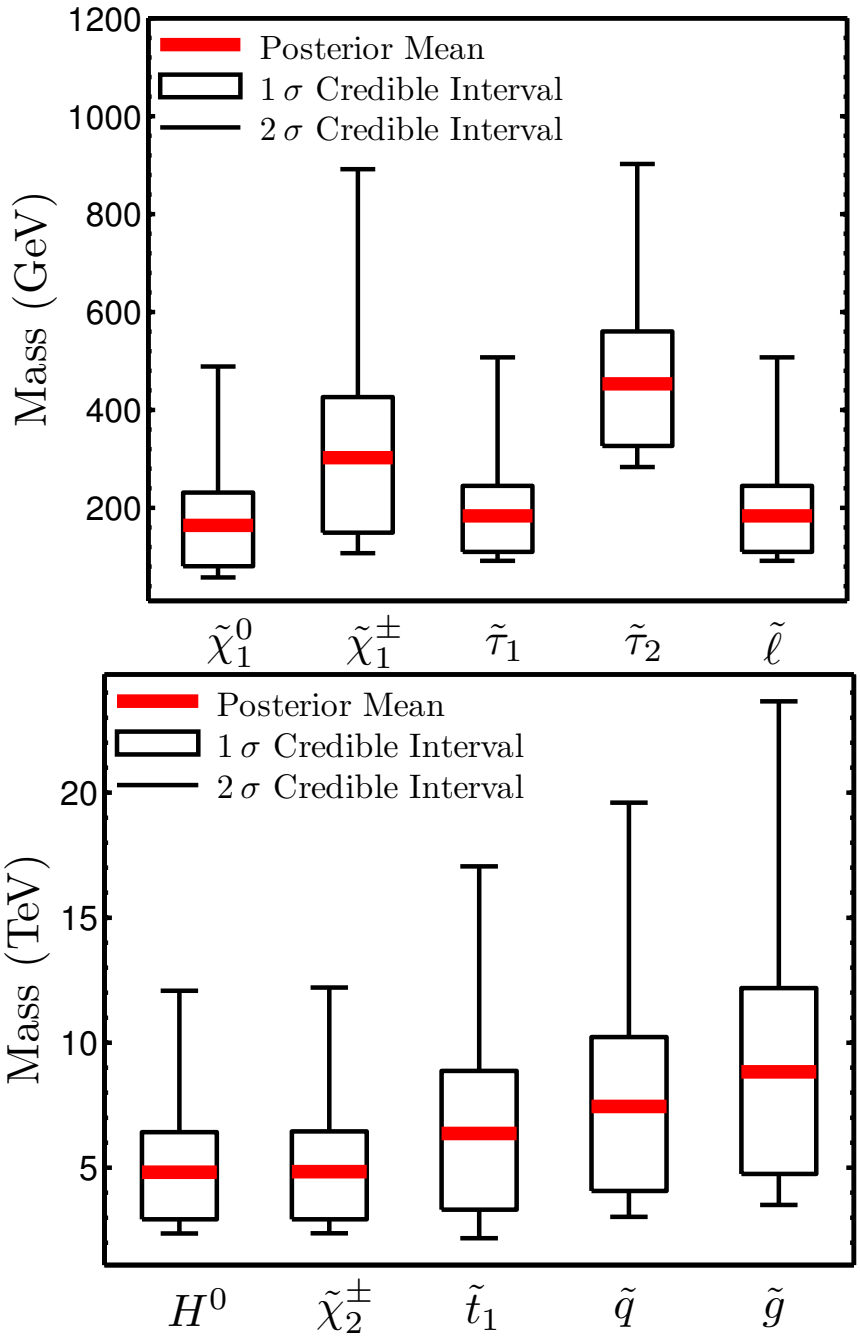


Figure 10.2: A display of the mass spectrum for sparticles and the Higgs boson with split scales, i.e., a low scale for $\tilde{\chi}_1^0$, $\tilde{\chi}_1^\pm$, $\tilde{\tau}_1$, $\tilde{\tau}_2$, $\tilde{\ell}$, and a high scale for $H^0$, $\tilde{\chi}_2^\pm$, $\tilde{t}_1$, $\tilde{q}$, $\tilde{g}$. Shown are the credible intervals in the superpartner masses from the Bayesian analysis of $\tilde{g}$SUGRA. The lighter superpartners are presented in the left panel, and the heavier are presented in the right panel. The posterior means are indicated in red.

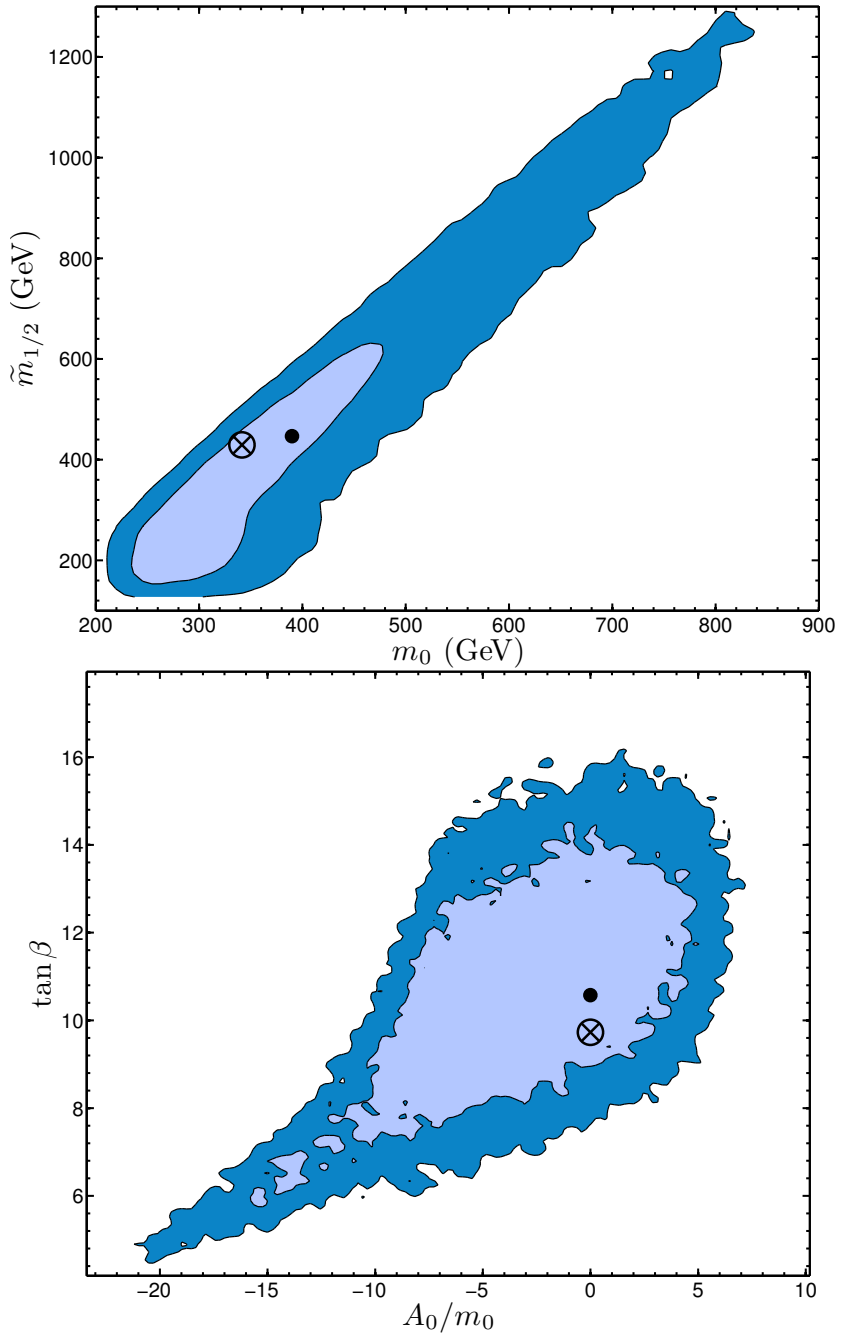


Figure 10.3: An exhibition of the 1 σ and 2 σ credible regions of the marginalized posterior probability distributions for the parameters of interest of g̃SUGRA. Left panel: the credible regions in $m_0$ and $\widetilde{m}_{1/2}$. Right panel: the credible regions in the dimensionless parameter $A_0/m_0$ and tan β. The location of the best-fit point is indicated by a circled 'X' and the posterior mean is given with a solid dot.

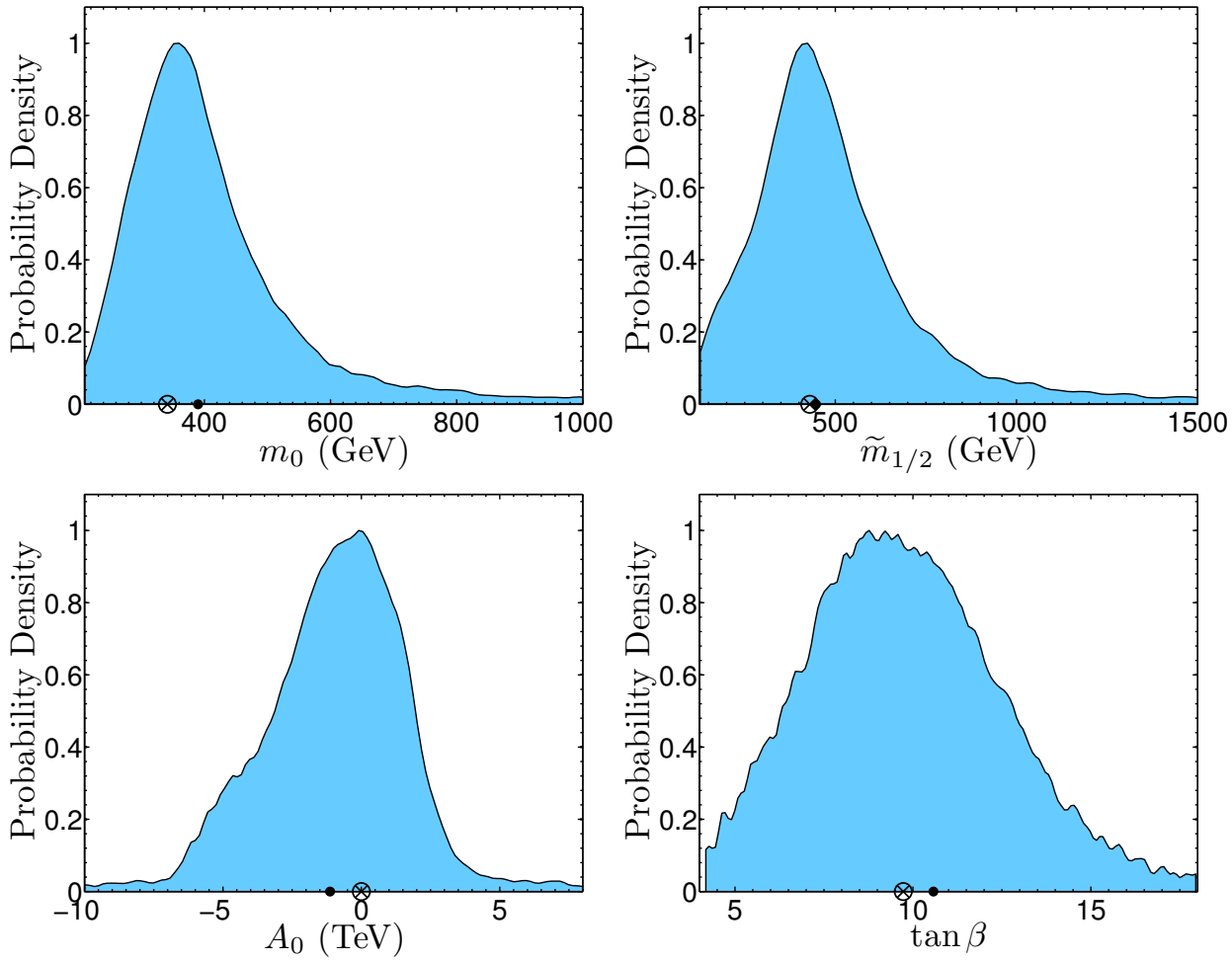


Figure 10.4: A display of the marginalized posterior probability distributions for g̃SUGRA in the parameters of interest as well as some important derived quantities. The top row (left to right) gives the posterior PDF for $m_0$, $\widetilde{m}_{1/2}$, $A_0$, and $\tan\beta$, and the bottom row (left to right) displays the same for the top quark mass, the light CP even Higgs boson mass, the contribution to $-2\ln\mathcal{L}$ due to the anomalous magnetic moment of the muon (which we have denoted as $\chi^2(\delta a_\mu)$, and the thermal relic density of cold dark matter, $\omega_\chi$. The location of the best-fit point is indicated by a circled 'X' and the posterior mean is given with a solid dot.

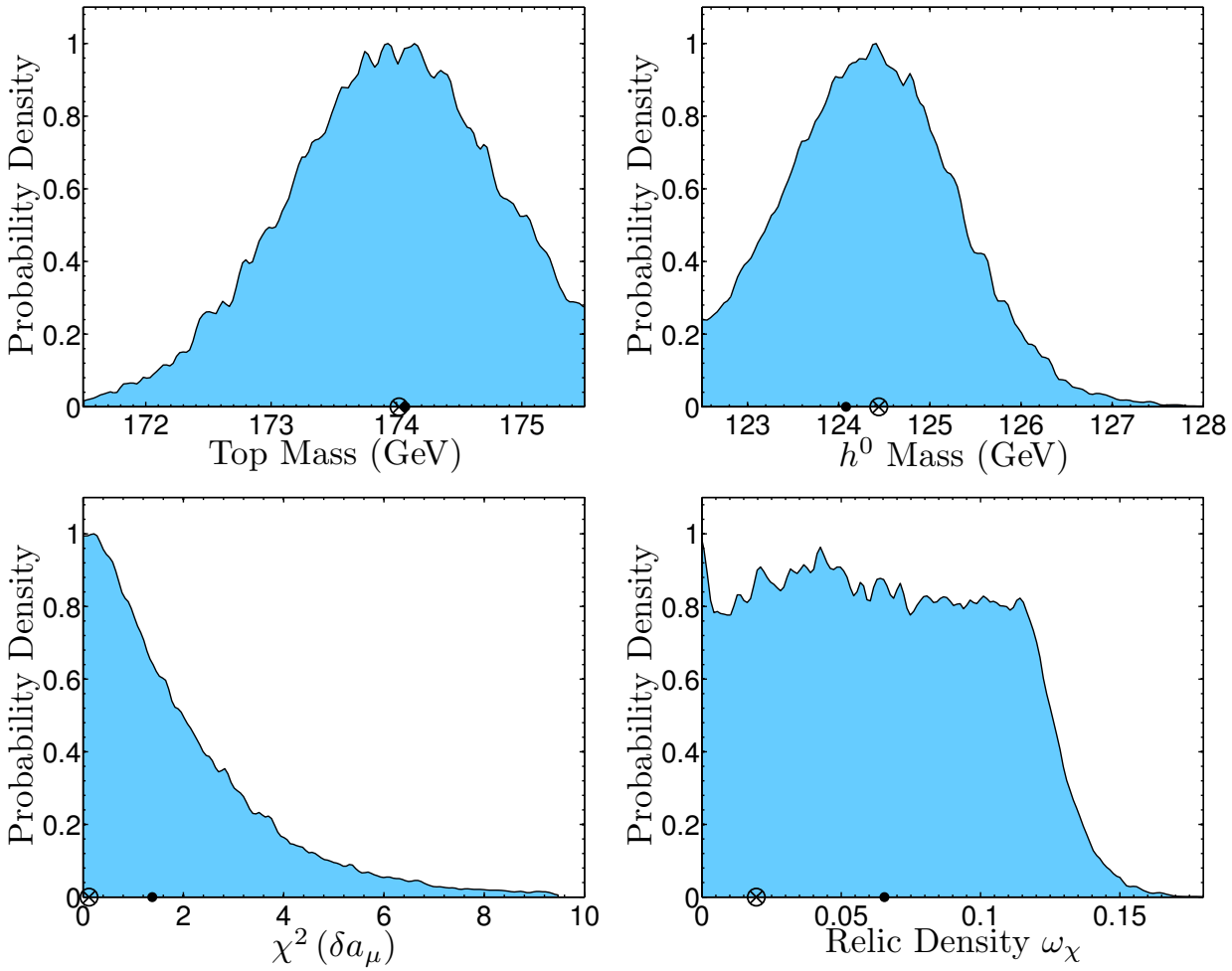


Figure 10.5: A display of the marginalized posterior probability distributions for g̃SUGRA in the parameters of interest as well as some important derived quantities. The top row (left to right) gives the posterior PDF for $m_0$, $\widetilde{m}_{1/2}$, $A_0$, and $\tan\beta$, and the bottom row (left to right) displays the same for the top quark mass, the light CP even Higgs boson mass, the contribution to $-2\ln\mathcal{L}$ due to the anomalous magnetic moment of the muon (which we have denoted as $\chi^2(\delta a_\mu)$, and the thermal relic density of cold dark matter, $\omega_\chi$. The location of the best-fit point is indicated by a circled 'X' and the posterior mean is given with a solid dot.

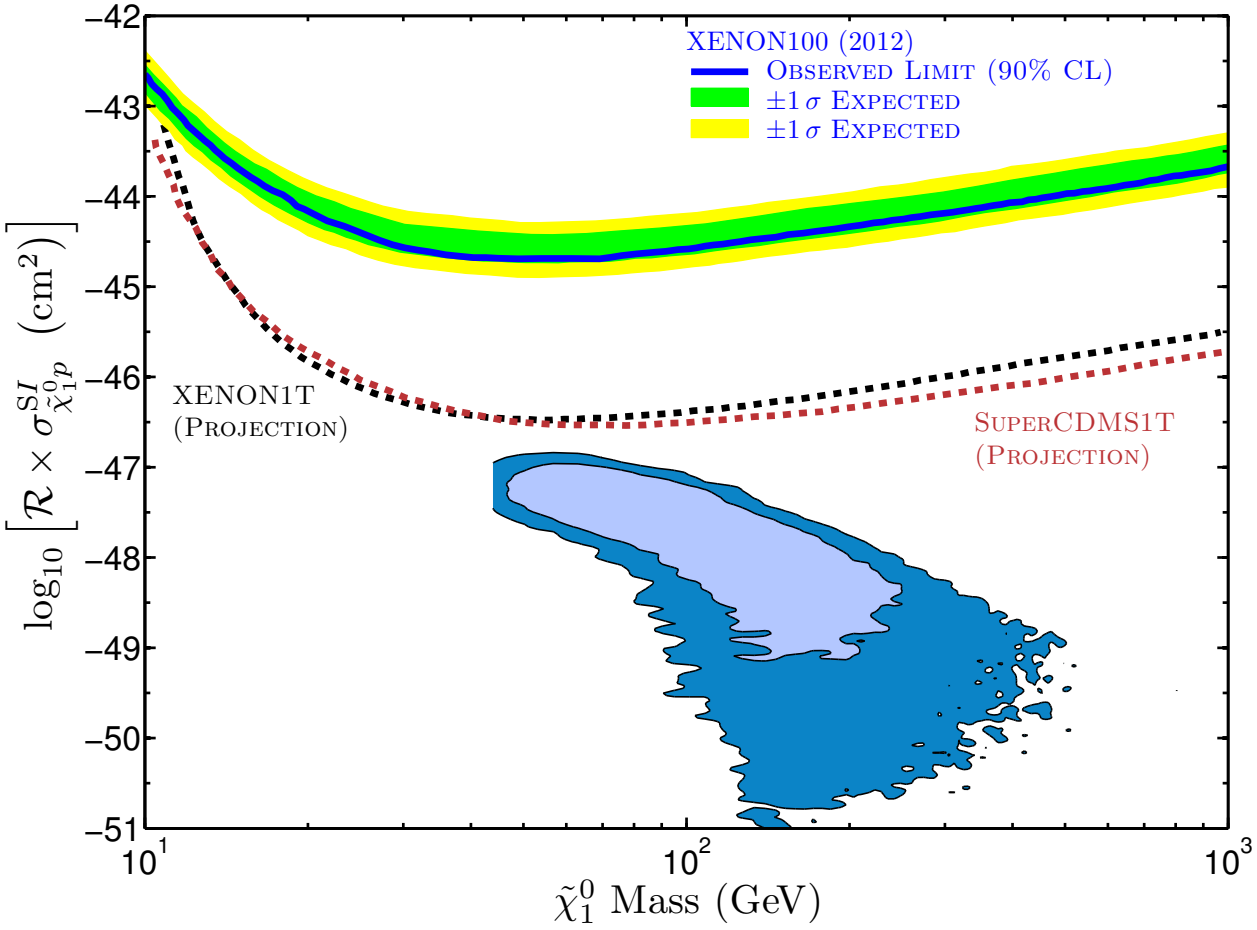


Figure 10.6: A display of the 1 σ and 2 σ credible regions of the marginalized posterior PDF of g̃SUGRA in the plane of the spin-independent p–$\tilde{\chi}_1^0$ cross section and the $\tilde{\chi}_1^0$ mass. The current limit from XENON100 is displayed as well as the projected sensitivities for XENON1T and SuperCDMS1T.

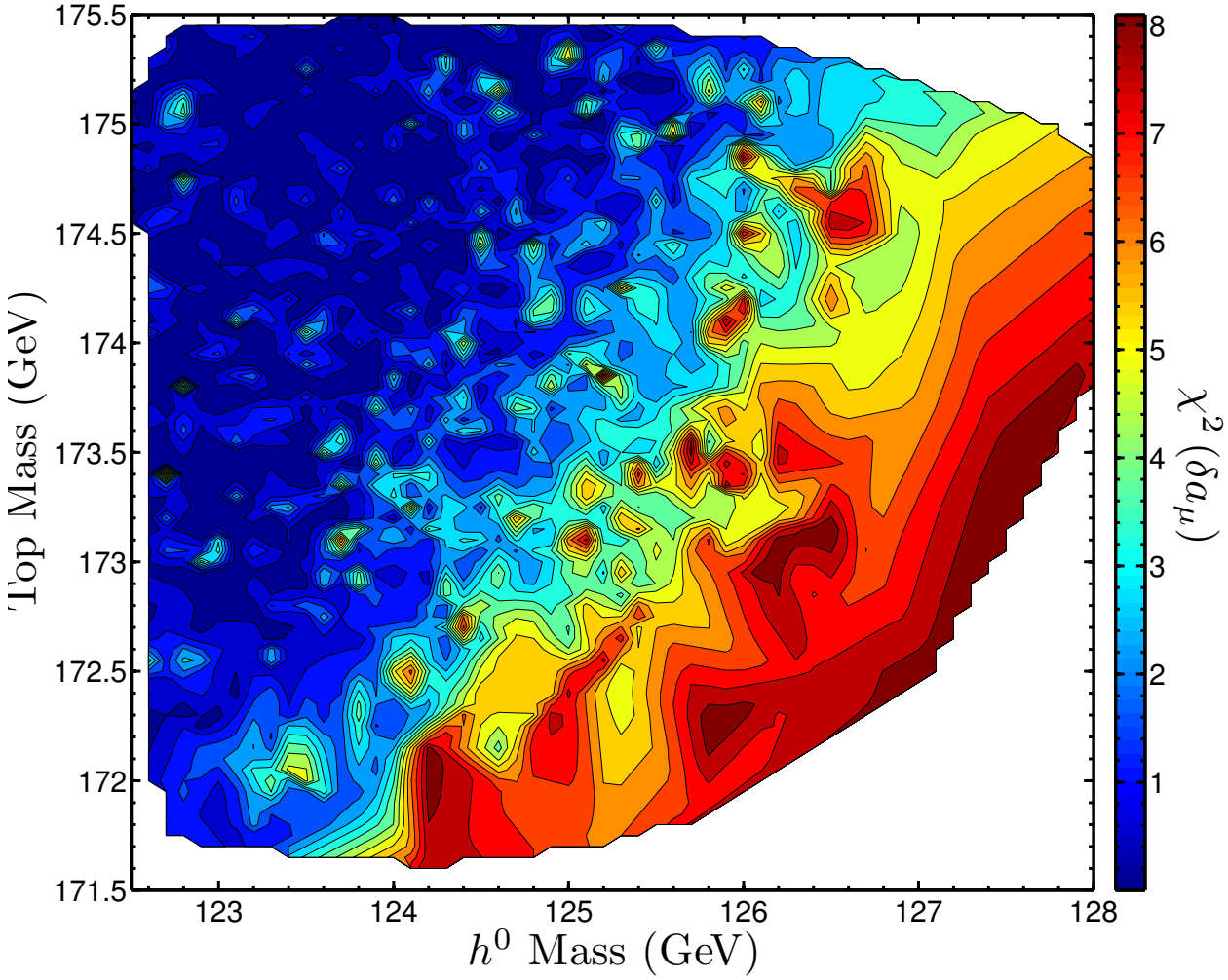


Figure 10.7: A display of level curves in the statistic $\chi^2\left(\delta a_\mu\right)$, which is the contribution to $-2\ln\mathfrak{L}$ due to $\delta a_\mu$. The level curves are given in the plane of the top mass and $h^0$ mass. The level curves are constructed by interpolating equally-weighted sample points. The interpolation is also colored by $\chi^2(\delta a_\mu)$ so that blue region indicates a good agreement with $\delta a_\mu$ and the red region indicates poor agreement.

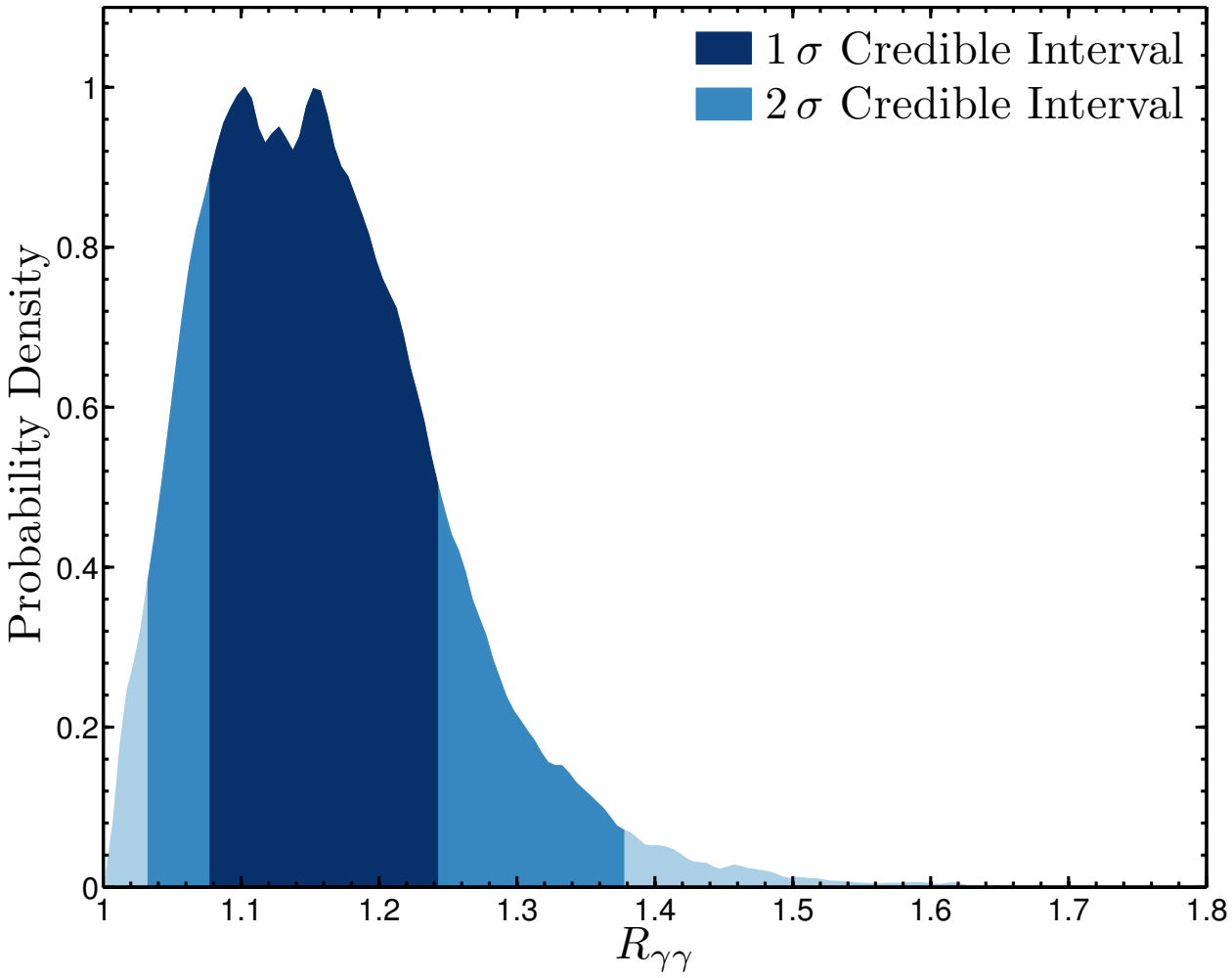


Figure 10.8: A display of the marginalized posterior probability density of $R_{\gamma\gamma}$ from our analysis. The 1 σ and 2 σ credible intervals are indicated in darker blues. We define $R_{\gamma\gamma}$ as the ratio of the diphoton partial width of the light CP-even Higgs boson to the corresponding width for a Standard Model Higgs of the same mass (see Eq. (10.8)).

# Chapter 11

# Conclusions

The focus of this dissertation was to examine supergravity grand unification models as viable candidates of beyond the Standard Model physics, in the context of this data-rich age in particles physics. With the conclusion of Run-I of the LHC operating at $\sqrt{s} = 7$ and 8 TeV, stringent limits on the minimal supergravity model have been placed, and lesser ones on supergravity grand unification models with non-universalities. We saw that initially, the region probed by the LHC was largely unavailable due to existing constraints from flavor measurements.

Meanwhile, the deep underground experiments searching for nuclear recoils with dark matter have continued to lower their limits on nuclear cross sections with WIMP dark matter. In models of supersymmetric dark matter, the LHC has provided a complementary probe, in some regions.

The major milestone was undoubtedly the discovery of the Higgs boson. The measured Higgs boson mass is among the most important constraints to be placed on all supersymmetry models, and the paradigm has rapidly become to account for it, and identify its impact on finding sparticles. We saw that the mass range of the Higgs boson as measured implies parameters of mSUGRA that are well beyond what the LHC has probed in all of Run-I.

Still, the question of naturalness has arisen. The simplest way to get the correct Higgs boson mass in mSUGRA and other SUGRA GUTs is to have very heavy scalars. This typically leads to a large value of $\mu$, the Higgsino mass parameter and thus requires tuning in order to preserve the Z boson mass. It was shown instead that within the Hyperbolic Branch, there are focal curve and focal surface solutions wherein the scalar sparticles can become heavier than $\gtrsim 10$ TeV and one still finds a much smaller value of $\mu$.

In SUSY models where the scalars are heavy, the overall scale of SUSY gets dragged up with them. This can make it difficult for SUSY to influence other aspects of electroweak physics. A striking example is the difficulty in explaining the discrepancy between experimental measurement and Standard Model prediction of the anomalous magnetic moment of the muon. This is because the sleptons necessary to provide the SUSY corrections are typically of the same order of magnitude in mass as the squarks. Since in GUT models the quarks and leptons belong to the same representation, it would not be attractive to simply separate their masses at the GUT scale in order to produce lighter sleptons and heavier squarks at the electroweak scale. Instead, we suggested the $\tilde{g}$SUGRA paradigm where just the gluino mass is taken to be heavier than the other parameters. Then, simply due to renormalization, the squark fields diverge from the slepton fields in mass as one approaches the electroweak scale, giving a splitting between squarks and sleptons, within a GUT framework. We demonstrated that this proves to be an excellent fit to both the Higgs boson mass and the anomalous muon magnetic moment, in addition to other results from flavor physics.

# Appendix A

# Conventions

## A.1 Metric, Spinors

This dissertation uses the "mostly minus" metric

$$\eta^{\mu\nu} = \eta_{\mu\nu} = \text{diag}(+1, -1, -1, -1) \, . \tag{A.1}$$

For an excellent review of two-component spinor techniques, please see [290] and also [38].

The Pauli matrices are given by

$$\sigma^{\mu}_{\alpha\dot{\beta}} = (\mathbb{1}, \sigma^1, \sigma^2, \sigma^3) \ \text{, and, } \ \bar{\sigma}^{\mu\dot{\alpha}\beta} = (\mathbb{1}, \bar{\sigma}^1, \bar{\sigma}^2, \bar{\sigma}^3) \quad \text{with} \tag{A.2}$$

$$\sigma^1 = -\bar{\sigma}^1 = \begin{pmatrix} 0 & 1 \\ 1 & 0 \end{pmatrix}, \ \sigma^2 = -\bar{\sigma}^2 = \begin{pmatrix} 0 & -i \\ i & 0 \end{pmatrix}, \ \sigma^3 = -\bar{\sigma}^3 = \begin{pmatrix} 1 & 0 \\ 0 & -1 \end{pmatrix} \, . \tag{A.3}$$

Any given Lorentz vector is packaged with spinor indices by

$$P_{\alpha\dot{\beta}} \equiv P_\mu \sigma^\mu_{\alpha\dot{\beta}} \text{ , so } P_{\alpha\dot{\beta}} = \begin{pmatrix} P_0 + P_3 & P_1 - iP_2 \\ P_1 + iP_2 & P_0 - P_3 \end{pmatrix} . \tag{A.4}$$

Notice then that

$$\det P_{\alpha\dot{\beta}} = P_0^2 - P_1^2 - P_2^2 - P_3^2 = P_\mu P^\mu \tag{A.5}$$

is invariant under $SL(2, C)$ transformations.

Spinor indices are raised and lowered by the rank-2 totally anti-symmetric symbol

$$\varepsilon^{\alpha\beta} = -\varepsilon_{\alpha\beta} = \begin{pmatrix} 0 & 1 \\ -1 & 0 \end{pmatrix} . \tag{A.6}$$

For a given spinor $\chi^\alpha$, transforming under the $(1/2, 0)$ representation of the Lorentz algebra

$$\chi^\alpha = \varepsilon^{\alpha\beta}\chi_\beta \text{ and } \chi_\alpha = \varepsilon_{\alpha\beta}\chi^\beta . \tag{A.7}$$

For a given spinor $\bar{\xi}_{\dot{\alpha}}$, transforming under the $(0, 1/2)$ representation of the Lorentz algebra

$$\bar{\xi}_{\dot{\alpha}} = \varepsilon_{\dot{\alpha}\dot{\beta}}\bar{\xi}^{\dot{\beta}} \text{ and } \bar{\xi}^{\dot{\alpha}} = \varepsilon^{\dot{\alpha}\dot{\beta}}\bar{\xi}_{\dot{\beta}} . \tag{A.8}$$

Products of spinors can be written without the contracted indices, bearing in mind a conventional order for the direction of the contracted indices. The convention is to have undotted indices falling and dotted indices rising as

$$\chi^\alpha{}_\alpha \text{ and } {}_{\dot{\alpha}}\bar{\xi}^{\dot{\alpha}} \tag{A.9}$$

thus without the indices we write

$$\xi\chi \equiv \xi^{\alpha}\chi_{\alpha} \text{ and } \bar{\xi}\bar{\chi} \equiv \bar{\xi}_{\dot{\alpha}}\bar{\chi}^{\dot{\alpha}} . \tag{A.10}$$

Since these are fermions, we obtain the nice relation

$$\xi\chi = \xi^{\alpha}\chi_{\alpha} = -\chi_{\alpha}\xi^{\alpha} = +\chi^{\alpha}\xi_{\alpha} = \chi\xi . \tag{A.11}$$

However, when a Lorentz index is included

$$\bar{\xi}\bar{\sigma}^{\mu}\chi = \bar{\xi}_{\dot{\alpha}}\bar{\sigma}^{\mu\dot{\alpha}\beta}\chi_{\beta} = -\chi_{\beta}\bar{\sigma}^{\mu\dot{\alpha}\beta}\bar{\xi}_{\dot{\alpha}} = -\chi^{\beta}\sigma^{\mu}_{\dot{\alpha}\beta}\bar{\xi}^{\dot{\alpha}} = -\chi\sigma^{\mu}\xi . \tag{A.12}$$

We also define

$$\sigma^{\mu\nu} \equiv \frac{1}{2}\left(\sigma^{\mu}\bar{\sigma}^{\nu} - \sigma^{\nu}\bar{\sigma}^{\mu}\right) \quad \text{and} \quad \bar{\sigma}^{\mu\nu} \equiv \frac{1}{2}\left(\bar{\sigma}^{\mu}\sigma^{\nu} - \bar{\sigma}^{\nu}\sigma^{\mu}\right) . \tag{A.13}$$

## A.2 Grassmann Coordinates

An extensive and formal review of supergroups, superalgebras, and supermanifolds can be found in [291], and the most relevant results can be found in [35, 37, 38].

In the $\mathcal{N} = 1$ superspace formulation, we have two Grassmann coordinates $\theta_1$ and $\theta_2$, and their conjugates, $\bar{\theta}_1$ and $\bar{\theta}_2$. Any Grassmann coordinate $\eta$ (such as $\theta_1$, $\bar{\theta}_1$, etc.) satisfies

$$\{\eta, \eta\} = 0 \iff \eta^2 = 0 . \tag{A.14}$$

The derivative is $\frac{\partial}{\partial\eta}\eta = 1$ as expected, but the integration is defined by the Berezin rules

$$\int d\eta = 0 \quad \text{and} \quad \int d\eta\,\eta = 1\,. \tag{A.15}$$

In the $\mathcal{N} = 1$ superspace, these Grassmann coordinates are arranged into Weyl spinors which span the fermionic subspace

$$\theta^\alpha = (\theta_1, \theta_2) \ \text{, and} \ \ \bar{\theta}_{\dot{\alpha}} = (\bar{\theta}_1, \bar{\theta}_2) \ . \tag{A.16}$$

Making use of the spinor conventions from Appendix A.1, we write

$$\theta^2 = \theta^\alpha\theta_\alpha = \varepsilon^{\alpha\beta}\theta_\beta\theta_\alpha = 2\theta_2\theta_1 \tag{A.17}$$

$$\bar{\theta}^2 = \bar{\theta}_{\dot{\alpha}}\bar{\theta}^{\dot{\alpha}} = \varepsilon^{\dot{\alpha}\dot{\beta}}\bar{\theta}_{\dot{\alpha}}\bar{\theta}_{\dot{\beta}} = 2\bar{\theta}_1\bar{\theta}_2\,. \tag{A.18}$$

All cubic and higher terms in either of the $\theta^\alpha$ and $\theta_{\dot{\alpha}}$ spinors *separately* are equal to zero but we define the non-zero

$$\theta^4 \equiv \theta^2\bar{\theta}^2\,. \tag{A.19}$$

The derivatives of the spinors are given by

$$\frac{\partial}{\partial\theta^\alpha}\theta^\beta = \delta_\alpha{}^\beta, \quad \frac{\partial}{\partial\bar{\theta}_{\dot{\alpha}}}\bar{\theta}_{\dot{\beta}} = \delta^{\dot{\alpha}}{}_{\dot{\beta}} \ \text{, and} \ \ \frac{\partial}{\partial\theta^\alpha}\bar{\theta}^{\dot{\beta}} = \frac{\partial}{\partial\bar{\theta}_{\dot{\alpha}}}\theta^\beta = 0\,. \tag{A.20}$$

For integration, we first scale the measures to normalize the integrals

$$d^2\theta \equiv -\frac{1}{4}d\theta^\alpha d\theta_\alpha = -\frac{1}{4}\varepsilon_{\alpha\beta}d\theta^\alpha d\theta^\beta \tag{A.21}$$

$$d^2\bar{\theta} \equiv -\frac{1}{4}d\theta_{\dot{\alpha}}d\theta^{\dot{\alpha}} = -\frac{1}{4}\varepsilon^{\dot{\alpha}\dot{\beta}}d\theta_{\dot{\alpha}}d\theta_{\dot{\beta}} \tag{A.22}$$

$$d^4\theta \equiv d^2\theta d^2\bar{\theta} \tag{A.23}$$

so that the integrals

$$\int d^2\theta\, \theta^2 = \int d^2\bar{\theta}\, \bar{\theta}^2 = \int d^4\theta\, \theta^4 = 1\ . \tag{A.24}$$

# Bibliography


[1] P. A. M. Dirac, "Quantum theory of emission and absorption of radiation", *Proc. Roy. Soc. Lond. A* **114** (1927) 243.

[2] P. A. M. Dirac, "Quantized Singularities in the Electromagnetic Field", *Proc. Roy. Soc. Lond. A* **133** (1931) 60–72.

[3] S. Glashow, "Partial Symmetries of Weak Interactions", *Nucl. Phys.* **22** (1961) 579–588.

[4] S. Weinberg, "A Model of Leptons", *Phys. Rev. Lett.* **19** (1967) 1264–1266.

[5] A. Salam, "Weak and Electromagnetic Interactions", in *Elementary Particle Theory*, N. Svartholm, ed., p. 367. Almquist & Wiksell, Stockholm, 1968.

[6] G. 't Hooft, "Renormalization of Massless Yang-Mills Fields", *Nucl. Phys. B* **33** (1971) 173–199.

[7] D. J. Gross and F. Wilczek, "Ultraviolet Behavior of Nonabelian Gauge Theories", *Phys. Rev. Lett.* **30** (1973) 1343–1346.

[8] H. D. Politzer, "Reliable Perturbative Results for Strong Interactions?", *Phys. Rev. Lett.* **30** (1973) 1346–1349.

[9] P. Ramond, "Journeys Beyond the Standard Model". Frontiers in Physics. Westview Press, Boulder, 2003.

[10] S. Novaes, "Standard model: An Introduction", `arXiv:hep-ph/0001283`.

[11] C. Burgess and G. Moore, "The Standard Model: A Primer". Cambridge University Press, Cambridge, 2006.

[12] F. Englert and R. Brout, "Broken Symmetry and the Mass of Gauge Vector Mesons", *Phys. Rev. Lett.* **13** (1964) 321–323.

[13] P. W. Higgs, "Broken symmetries, massless particles and gauge fields", *Phys. Lett.* **12** (1964) 132–133.

[14] P. W. Higgs, "Broken Symmetries and the Masses of Gauge Bosons", *Phys. Rev. Lett.* **13** (1964) 508–509.

[15] G. Guralnik, C. Hagen, and T. Kibble, "Global Conservation Laws and Massless Particles", *Phys. Rev. Lett.* **13** (1964) 585–587.

[16] Y. Nambu, "Quasiparticles and Gauge Invariance in the Theory of Superconductivity", *Phys. Rev.* **117** (1960) 648–663.

[17] J. Goldstone, "Field Theories with Superconductor Solutions", *Nuovo Cim.* **19** (1961) 154–164.

[18] J. Goldstone, A. Salam, and S. Weinberg, "Broken Symmetries", *Phys. Rev.* **127** (1962) 965–970.

[19] P. Ramond, "Dual Theory for Free Fermions", *Phys. Rev. D* **3** (1971) 2415–2418.

[20] A. Neveu and J. H. Schwarz, "Factorizable dual model of pions", *Nucl. Phys. B* **31** (1971) 86–112.

[21] J.-L. Gervais and B. Sakita, "Field Theory Interpretation of Supergauges in Dual Models", *Nucl. Phys. B* **34** (1971) 632–639.

[22] Y. A. Gol'fand and E. P. Likhtman, "Extension of the Algebra of Poincaré Group Generators and Violation of p Invariance", *JETP Lett.* **13** (1971) 323–326.

[23] J. Wess and B. Zumino, "Supergauge Transformations in Four-Dimensions", *Nucl. Phys. B* **70** (1974) 39–50.

[24] D. Volkov and V. Akulov, "Is the Neutrino a Goldstone Particle?", *Phys. Lett. B* **46** (1973) 109–110.

[25] A. Salam and J. A. Strathdee, "Supergauge Transformations", *Nucl. Phys. B* **76** (1974) 477–482.

[26] R. Haag, J. T. Łopuszański, and M. Sohnius, "All Possible Generators of Supersymmetries of the S Matrix", *Nucl. Phys. B* **88** (1975) 257.

[27] S. R. Coleman and J. Mandula, "All Possible Symmetries of the S-Matrix", *Phys. Rev.* **159** (1967) 1251–1256.

[28] P. Van Nieuwenhuizen, "Supergravity", *Phys. Rept.* **68** (1981) 189–398.

[29] J. Wess and J. Bagger, "Supersymmetry and Supergravity". Princeton University Press, Princeton, 1992.

[30] D. Z. Freedman and A. Van Proeyen, "Supergravity". Cambridge University Press, Cambridge, 2012.

[31] P. West, "Introduction to Supersymmetry and Supergravity". World Scientific, Singapore, 1990.

[32] S. Weinberg, "The Quantum Theory of Fields", volume 3. Cambridge University Press, Cambridge, 2000.

[33] E. D'Hoker and D. Z. Freedman, "Supersymmetric gauge theories and the AdS / CFT correspondence", in *TASI 2001: Strings, Branes and Extra Dimensions*, pp. 3–158. World Scientific, Singapore, 2002. arXiv:hep-th/0201253. doi:10.1142/5495.

[34] J. Terning, "Modern Supersymmetry: Dynamics and Duality". Oxford University Press, Oxford, 2006.

[35] M. Drees, R. M. Godbole, and P. Roy, "Theory and phenomenology of sparticles: An account of four-dimensional N=1 supersymmetry in high energy physics". World Scientific, Singapore, 2004.

[36] H. Baer and X. Tata, "Weak scale supersymmetry: From superfields to scattering events",.

[37] S. P. Martin, "A Supersymmetry primer", arXiv:hep-ph/9709356.

[38] J. Thaler, Z. Thomas, and D. Bertolini, "Super-Tricks for Superspace", in *TASI 2012: Searching for New Physics at Small and Large Scales*, pp. 421–496. World Scientific, Singapore, 2013. arXiv:1302.6229. doi:10.1142/8906.

[39] P. C. West, "The Supersymmetric Effective Potential", *Nucl. Phys. B* **106** (1976) 219.

[40] D. Capper and M. Ramon Medrano, "Spontaneous Symmetry Breaking and PseudoGoldstone Bosons in Supersymmetry Theories", *J. Phys. G* **2** (1976) 269.

[41] S. Weinberg, "Ambiguous Solutions of Supersymmetric Theories (f1)", *Phys. Lett. B* **62** (1976) 111.

[42] E. Witten, "Dynamical Breaking of Supersymmetry", *Nucl. Phys. B* **188** (1981) 513.

[43] L. O'Raifeartaigh, "Spontaneous Symmetry Breaking for Chiral Scalar Superfields", *Nucl. Phys. B* **96** (1975) 331.

[44] P. Fayet and J. Iliopoulos, "Spontaneously Broken Supergauge Symmetries and Goldstone Spinors", *Phys. Lett. B* **51** (1974) 461–464.

[45] S. Ferrara, L. Girardello, and F. Palumbo, "A General Mass Formula in Broken Supersymmetry", *Phys. Rev. D* **20** (1979) 403.

[46] P. Nath and R. L. Arnowitt, "Generalized Supergauge Symmetry as a New Framework for Unified Gauge Theories", *Phys. Lett. B* **56** (1975) 177.

[47] R. L. Arnowitt, P. Nath, and B. Zumino, "Superfield Densities and Action Principle in Curved Superspace", *Phys. Lett. B* **56** (1975) 81.

[48] D. Z. Freedman, P. van Nieuwenhuizen, and S. Ferrara, "Progress Toward a Theory of Supergravity", *Phys. Rev. D* **13** (1976) 3214–3218.

[49] S. Deser and B. Zumino, "Consistent Supergravity", *Phys. Lett. B* **62** (1976) 335.

[50] E. Cremmer, B. Julia, J. Scherk et al., "Spontaneous Symmetry Breaking and Higgs Effect in Supergravity Without Cosmological Constant", *Nucl. Phys. B* **147** (1979) 105.

[51] A. H. Chamseddine, R. L. Arnowitt, and P. Nath, "Locally Supersymmetric Grand Unification", *Phys. Rev. Lett.* **49** (1982) 970.

[52] P. Nath, R. L. Arnowitt, and A. H. Chamseddine, "Gauge Hierarchy in Supergravity Guts", *Nucl. Phys. B* **227** (1983) 121.

[53] L. J. Hall, J. D. Lykken, and S. Weinberg, "Supergravity as the Messenger of Supersymmetry Breaking", *Phys. Rev. D* **27** (1983) 2359–2378.

[54] P. Nath, R. L. Arnowitt, and A. H. Chamseddine, "Applied $\mathcal{N} = 1$ Supergravity", volume 1 of *ICTP Series in Theoretical Physics*. World Scientific, Singapore, 1984.

[55] W. Rarita and J. Schwinger, "On a theory of particles with half integral spin", *Phys. Rev.* **60** (1941) 61.

[56] G. Lopes Cardoso and B. A. Ovrut, "Supersymmetric calculation of mixed Kahler gauge and mixed Kahler-Lorentz anomalies", *Nucl. Phys. B* **418** (1994) 535–570, arXiv:hep-th/9308066.

[57] J. A. Bagger, T. Moroi, and E. Poppitz, "Anomaly mediation in supergravity theories", *JHEP* **0004** (2000) 009, arXiv:hep-th/9911029.

[58] J. A. Bagger, T. Moroi, and E. Poppitz, "Quantum inconsistency of Einstein supergravity", *Nucl. Phys. B* **594** (2001) 354–368, arXiv:hep-th/0003282.

[59] M. K. Gaillard and B. D. Nelson, "Quantum induced soft supersymmetry breaking in supergravity", *Nucl. Phys. B* **588** (2000) 197–212, arXiv:hep-th/0004170.

[60] P. Binetruy, G. Girardi, and R. Grimm, "Supergravity couplings: A Geometric formulation", *Phys. Rept.* **343** (2001) 255–462, arXiv:hep-th/0005225.

[61] R. L. Arnowitt and P. Nath, "Supersymmetry and Supergravity: Phenomenology and Grand Unification", arXiv:hep-ph/9309277.

[62] R. Arnowitt, A. Chamseddine, and P. Nath, "The Development of Supergravity Grand Unification: Circa 1982-85", *Int. J. Mod. Phys. A* **27** (2012) 1230028, arXiv:1206.3175.

[63] J. C. Pati and A. Salam, "Is Baryon Number Conserved?", *Phys. Rev. Lett.* **31** (1973) 661–664.

[64] J. C. Pati and A. Salam, "Lepton Number as the Fourth Color", *Phys. Rev. D* **10** (1974) 275–289.

[65] H. Georgi and S. Glashow, "Unity of All Elementary Particle Forces", *Phys. Rev. Lett.* **32** (1974) 438–441.

[66] H. Georgi, "The State of the Art - Gauge Theories", in *Particles and Fields*, C. E. Carlson, ed., p. 575. AIP, New York, 1975.

[67] H. Fritzsch and P. Minkowski, "Unified Interactions of Leptons and Hadrons", *Annals Phys.* **93** (1975) 193–266.

[68] S. Dimopoulos and H. Georgi, "Softly Broken Supersymmetry and SU(5)", *Nucl. Phys. B* **193** (1981) 150.

[69] N. Sakai, "Naturalness in Supersymmetric Guts", *Z. Phys. C* **11** (1981) 153.

[70] K. Inoue, A. Kakuto, H. Komatsu et al., "Aspects of Grand Unified Models with Softly Broken Supersymmetry", *Prog. Theor. Phys.* **68** (1982) 927.

[71] L. E. Ibanez and G. G. Ross, "SU(2)-L x U(1) Symmetry Breaking as a Radiative Effect of Supersymmetry Breaking in Guts", *Phys. Lett. B* **110** (1982) 215–220.

[72] L. Alvarez-Gaume, J. Polchinski, and M. B. Wise, "Minimal Low-Energy Supergravity", *Nucl. Phys. B* **221** (1983) 495.

[73] S. R. Coleman and E. J. Weinberg, "Radiative Corrections as the Origin of Spontaneous Symmetry Breaking", *Phys. Rev. D* **7** (1973) 1888–1910.

[74] S. Weinberg, "Perturbative Calculations of Symmetry Breaking", *Phys. Rev. D* **7** (1973) 2887–2910.

[75] CMS Collaboration, "Search for Supersymmetry in pp Collisions at 7 TeV in Events with Jets and Missing Transverse Energy", *Phys. Lett. B* **698** (2011) 196–218, arXiv:1101.1628.

[76] Atlas Collaboration, "Search for supersymmetry using final states with one lepton, jets, and missing transverse momentum with the ATLAS detector in sqrts = 7 TeV pp", *Phys. Rev. Lett.* **106** (2011) 131802, arXiv:1102.2357.

[77] Atlas Collaboration, "Search for squarks and gluinos using final states with jets and missing transverse momentum with the ATLAS detector in sqrt(s) = 7 TeV proton-proton collisions", *Phys. Lett. B* **701** (2011) 186–203, arXiv:1102.5290.

[78] J. L. Feng, J.-F. Grivaz, and J. Nachtman, "Searches for Supersymmetry at High-Energy Colliders", *Rev. Mod. Phys.* **82** (2010) 699–727, arXiv:0903.0046.

[79] H. Baer, V. Barger, A. Lessa et al., "Capability of LHC to discover supersymmetry with $\sqrt{s} = 7$ TeV and 1 fb$^{-1}$", *JHEP* **1006** (2010) 102, arXiv:1004.3594.

[80] B. Altunkaynak, M. Holmes, P. Nath et al., "SUSY Discovery Potential and Benchmarks for Early Runs at $\sqrt{s} = 7$ TeV at the LHC", *Phys. Rev. D* **82** (2010) 115001, arXiv:1008.3423.

[81] N. Chen, D. Feldman, Z. Liu et al., "Low Mass Gluino within the Sparticle Landscape, Implications for Dark Matter, and Early Discovery Prospects at LHC-7", *Phys. Rev. D* **83** (2011) 035005, arXiv:1011.1246.

[82] ATLAS Collaboration, "Expected Performance of the ATLAS Experiment - Detector, Trigger and Physics", arXiv:0901.0512.

[83] ATLAS Collaboration, https://atlas.web.cern.ch/Atlas/GROUPS/PHYSICS/PAPERS/SUSY-2010-05/.

[84] A. Djouadi, J.-L. Kneur, and G. Moultaka, "SuSpect: A Fortran code for the supersymmetric and Higgs particle spectrum in the MSSM", *Comput. Phys. Commun.* **176** (2007) 426–455, arXiv:hep-ph/0211331.

[85] J. Alwall, P. Demin, S. de Visscher et al., "MadGraph/MadEvent v4: The New Web Generation", *JHEP* **0709** (2007) 028, arXiv:0706.2334.

[86] T. Sjostrand, S. Mrenna, and P. Z. Skands, "PYTHIA 6.4 Physics and Manual", *JHEP* **0605** (2006) 026, arXiv:hep-ph/0603175.

[87] G. Belanger, F. Boudjema, P. Brun et al., "Indirect search for dark matter with micrOMEGAs2.4", *Comput. Phys. Commun.* **182** (2011) 842–856, arXiv:1004.1092.

[88] M. Misiak, H. Asatrian, K. Bieri et al., "Estimate of B(anti-B $\to$ X(s) gamma) at O(alpha(s)**2)", *Phys. Rev. Lett.* **98** (2007) 022002, arXiv:hep-ph/0609232.

[89] N. Chen, D. Feldman, Z. Liu et al., "SUSY and Higgs Signatures Implied by Cancellations in $b \to s\gamma$", *Phys. Lett. B* **685** (2010) 174–181, arXiv:0911.0217.

[90] Particle Data Group, "Review of particle physics", *J. Phys. G* **37** (2010) 075021.

[91] A. Djouadi, M. Drees, and J.-L. Kneur, "Updated constraints on the minimal supergravity model", *JHEP* **0603** (2006) 033, arXiv:hep-ph/0602001.

[92] CDF Collaboration, "Search for $B_s^0 \to \mu^+\mu^-$ and $B_d^0 \to \mu^+\mu^-$ decays with $2fb^{-1}$ of $p\bar{p}$ collisions", *Phys. Rev. Lett.* **100** (2008) 101802, arXiv:0712.1708.

[93] Heavy Flavor Averaging Group, "Averages of b–hadron and c–hadron Properties at the End of 2007", arXiv:0808.1297.

[94] WMAP Collaboration, "Seven-Year Wilkinson Microwave Anisotropy Probe (WMAP) Observations: Cosmological Interpretation", *Astrophys. J. Suppl.* **192** (2011) 18, arXiv:1001.4538.

[95] N. Jarosik, C. Bennett, J. Dunkley et al., "Seven-Year Wilkinson Microwave Anisotropy Probe (WMAP) Observations: Sky Maps, Systematic Errors, and Basic Results", *Astrophys. J. Suppl.* **192** (2011) 14, arXiv:1001.4744.

[96] K. L. Chan, U. Chattopadhyay, and P. Nath, "Naturalness, weak scale supersymmetry and the prospect for the observation of supersymmetry at the Tevatron and at the CERN LHC", *Phys. Rev. D* **58** (1998) 096004, arXiv:hep-ph/9710473.

[97] R. L. Arnowitt and P. Nath, "Loop corrections to radiative breaking of electroweak symmetry in supersymmetry", *Phys. Rev. D* **46** (1992) 3981–3986.

[98] J. L. Feng, K. T. Matchev, and T. Moroi, "Multi-TeV scalars are natural in minimal supergravity", *Phys. Rev. Lett.* **84** (2000) 2322–2325, arXiv:hep-ph/9908309.

[99] P. Nath and R. L. Arnowitt, "Predictions in SU(5) supergravity grand unification with proton stability and relic density constraints", *Phys. Rev. Lett.* **70** (1993) 3696–3699, arXiv:hep-ph/9302318.

[100] D. Feldman, K. Freese, P. Nath et al., "Predictive Signatures of Supersymmetry: Measuring the Dark Matter Mass and Gluino Mass with Early LHC data", *Phys. Rev. D* **84** (2011) 015007, arXiv:1102.2548.

[101] R. L. Arnowitt and P. Nath, "SUSY mass spectrum in SU(5) supergravity grand unification", *Phys. Rev. Lett.* **69** (1992) 725–728.

[102] S. Akula, N. Chen, D. Feldman et al., "Interpreting the First CMS and ATLAS SUSY Results", *Phys. Lett. B* **699** (2011) 377–382, arXiv:1103.1197.

[103] XENON100 Collaboration, "Dark Matter Results from 100 Live Days of XENON100 Data", *Phys. Rev. Lett.* **107** (2011) 131302, arXiv:1104.2549.

[104] XENON100 Collaboration, "Likelihood Approach to the First Dark Matter Results from XENON100", *Phys. Rev. D* **84** (2011) 052003, arXiv:1103.0303.

[105] XENON100 Collaboration, "First Dark Matter Results from the XENON100 Experiment", *Phys. Rev. Lett.* **105** (2010) 131302, arXiv:1005.0380.

[106] CDMS-II Collaboration, "Dark Matter Search Results from the CDMS II Experiment", *Science* **327** (2010) 1619–1621, arXiv:0912.3592.

[107] CDMS Collaboration, "Search for Weakly Interacting Massive Particles with the First Five-Tower Data from the Cryogenic Dark Matter Search at the Soudan Underground Laboratory", *Phys. Rev. Lett.* **102** (2009) 011301, arXiv:0802.3530.

[108] G. Gamberini, G. Ridolfi, and F. Zwirner, "On Radiative Gauge Symmetry Breaking in the Minimal Supersymmetric Model", *Nucl. Phys. B* **331** (1990) 331–349.

[109] D. M. Pierce, J. A. Bagger, K. T. Matchev et al., "Precision corrections in the minimal supersymmetric standard model", *Nucl. Phys. B* **491** (1997) 3–67, arXiv:hep-ph/9606211.

[110] S. P. Martin and M. T. Vaughn, "Two loop renormalization group equations for soft supersymmetry breaking couplings", *Phys. Rev. D* **50** (1994) 2282, arXiv:hep-ph/9311340.

[111] XENON1T collaboration, "The XENON1T Dark Matter Search Experiment", arXiv:1206.6288.

[112] SuperCDMS Collaboration, "SuperCDMS Development Project", (April, 2005). Fermilab Program Advisory Committee.

[113] U. Chattopadhyay, T. Ibrahim, and P. Nath, "Effects of CP violation on event rates in the direct detection of dark matter", *Phys. Rev. D* **60** (1999) 063505, arXiv:hep-ph/9811362.

[114] J. R. Ellis, A. Ferstl, and K. A. Olive, "Reevaluation of the elastic scattering of supersymmetric dark matter", *Phys. Lett. B* **481** (2000) 304–314, arXiv:hep-ph/0001005.

[115] J. R. Ellis, K. A. Olive, Y. Santoso et al., "Update on the direct detection of supersymmetric dark matter", *Phys. Rev. D* **71** (2005) 095007, arXiv:hep-ph/0502001.

[116] J. R. Ellis, K. A. Olive, and C. Savage, "Hadronic Uncertainties in the Elastic Scattering of Supersymmetric Dark Matter", *Phys. Rev. D* **77** (2008) 065026, arXiv:0801.3656.

[117] J. Conway, "PGS 4: Pretty Good Simulation of high energy collisions", http://physics.ucdavis.edu/~conway/research/software/pgs/pgs4-general.htm.

[118] G. L. Kane, E. Kuflik, R. Lu et al., "Top Channel for Early SUSY Discovery at the LHC", *Phys. Rev. D* **84** (2011) 095004, arXiv:1101.1963.

[119] D0 Collaboration, "Search for the rare decay $B_s^0 \to \mu^+\mu^-$", *Phys. Lett. B* **693** (2010) 539–544, arXiv:1006.3469.

[120] L. E. Ibanez and D. Lust, "Duality anomaly cancellation, minimal string unification and the effective low-energy Lagrangian of 4-D strings", *Nucl. Phys. B* **382** (1992) 305–364, arXiv:hep-th/9202046.

[121] V. Kaplunovsky and J. Louis, "Field dependent gauge couplings in locally supersymmetric effective quantum field theories", *Nucl. Phys. B* **422** (1994) 57–124, arXiv:hep-th/9402005.

[122] U. Chattopadhyay, A. Corsetti, and P. Nath, "WMAP data and recent developments in supersymmetric dark matter", *Phys. Atom. Nucl.* **67** (2004) 1188–1194, arXiv:hep-ph/0310228.

[123] D. Feldman, Z. Liu, and P. Nath, "Light Higgses at the Tevatron and at the LHC and Observable Dark Matter in SUGRA and D Branes", *Phys. Lett. B* **662** (2008) 190–198, arXiv:0711.4591.

[124] M. Holmes and B. D. Nelson, "Non-Universal Gaugino Masses, CDMS, and the LHC", *Phys. Rev. D* **81** (2010) 055002, arXiv:0912.4507.

[125] B. S. Acharya, G. Kane, E. Kuflik et al., "Theory and Phenomenology of $\mu$ in M theory", *JHEP* **1105** (2011) 033, arXiv:1102.0556.

[126] P. Nath and R. L. Arnowitt, "Nonuniversal soft SUSY breaking and dark matter", *Phys. Rev. D* **56** (1997) 2820–2832, arXiv:hep-ph/9701301.

[127] J. R. Ellis, K. A. Olive, and Y. Santoso, "The MSSM parameter space with nonuniversal Higgs masses", *Phys. Lett. B* **539** (2002) 107–118, arXiv:hep-ph/0204192.

[128] M. K. Gaillard, B. D. Nelson, and Y.-Y. Wu, "Gaugino masses in modular invariant supergravity", *Phys. Lett. B* **459** (1999) 549–556, arXiv:hep-th/9905122.

[129] B. Kors and P. Nath, "Hierarchically split supersymmetry with Fayet-Iliopoulos D-terms in string theory", *Nucl. Phys. B* **711** (2005) 112–132, arXiv:hep-th/0411201.

[130] J. D. Wells, "PeV-scale supersymmetry", *Phys. Rev. D* **71** (2005) 015013, arXiv:hep-ph/0411041.

[131] L. E. Ibanez, C. Lopez, and C. Munoz, "The Low-Energy Supersymmetric Spectrum According to N=1 Supergravity Guts", *Nucl. Phys. B* **256** (1985) 218–252.

[132] B. Allanach, "SOFTSUSY: a program for calculating supersymmetric spectra", *Comput. Phys. Commun.* **143** (2002) 305–331, arXiv:hep-ph/0104145.

[133] D. Feldman, G. Kane, E. Kuflik et al., "A new (string motivated) approach to the little hierarchy problem", *Phys. Lett. B* **704** (2011) 56–61, arXiv:1105.3765.

[134] ATLAS Collaboration, "Search for squarks and gluinos using final states with jets and missing transverse momentum with the ATLAS detector in sqrts = 7 TeV proton-proton collisions", Technical Report ATLAS-CONF-2011-086, CERN, Geneva, (Jun, 2011).

[135] ATLAS Collaboration, "Search for squarks and gluinos using final states with jets and missing transverse momentum with the ATLAS detector in $\sqrt{s} = 7$ TeV proton-proton collisions", *Phys. Lett. B* **710** (2012) 67–85, arXiv:1109.6572.

[136] ATLAS Collaboration, "Search for new phenomena in final states with large jet multiplicities and missing transverse momentum using $\sqrt{s} = 7$ TeV pp collisions with the ATLAS detector", *JHEP* **1111** (2011) 099, arXiv:1110.2299.

[137] S. Akula, D. Feldman, Z. Liu et al., "New Constraints on Dark Matter from CMS and ATLAS Data", *Mod. Phys. Lett. A* **26** (2011) 1521–1535, arXiv:1103.5061.

[138] S. Akula, D. Feldman, P. Nath et al., "Excess Observed in CDF $B_s^0 \to \mu^+\mu^-$ and SUSY at the LHC", *Phys. Rev. D* **84** (2011) 115011, arXiv:1107.3535.

[139] CMS and LHCb Collaborations, "Search for the rare decay $B_s^0 \to \mu^+\mu^-$ at the LHC with the CMS and LHCb experiments", Technical Report CMS-PAS-BPH-11-019. CERN-LHCb-CONF-2011-047, CERN, Geneva, (Aug, 2011). Linked to LHCb-ANA-2011-039.

[140] M. Farina, M. Kadastik, D. Pappadopulo et al., "Implications of XENON100 and LHC results for Dark Matter models", *Nucl. Phys. B* **853** (2011) 607–624, arXiv:1104.3572.

[141] B. Allanach, "Impact of CMS Multi-jets and Missing Energy Search on CMSSM Fits", *Phys. Rev. D* **83** (2011) 095019, arXiv:1102.3149.

[142] S. Scopel, S. Choi, N. Fornengo et al., "Impact of the recent results by the CMS and ATLAS Collaborations at the CERN Large Hadron Collider on an effective Minimal Supersymmetric extension of the Standard Model", *Phys. Rev. D* **83** (2011) 095016, arXiv:1102.4033.

[143] O. Buchmueller, R. Cavanaugh, D. Colling et al., "Implications of Initial LHC Searches for Supersymmetry", *Eur. Phys. J. C* **71** (2011) 1634, arXiv:1102.4585.

[144] M. Guchait and D. Sengupta, "Event-shape selection cuts for supersymmetry searches at the LHC with 7 TeV energy", *Phys. Rev. D* **84** (2011) 055010, arXiv:1102.4785.

[145] P. Bechtle, B. Sarrazin, K. Desch et al., "What if the LHC does not find supersymmetry in the $\sqrt{s} = 7$ TeV run?", *Phys. Rev. D* **84** (2011) 011701, arXiv:1102.4693.

[146] D. S. Alves, E. Izaguirre, and J. G. Wacker, "Where the Sidewalk Ends: Jets and Missing Energy Search Strategies for the 7 TeV LHC", *JHEP* **1110** (2011) 012, arXiv:1102.5338.

[147] B. Allanach, T. Khoo, C. Lester et al., "The impact of the ATLAS zero-lepton, jets and missing momentum search on a CMSSM fit", *JHEP* **1106** (2011) 035, arXiv:1103.0969.

[148] S. Profumo, "The Quest for Supersymmetry: Early LHC Results versus Direct and Indirect Neutralino Dark Matter Searches", *Phys. Rev. D* **84** (2011) 015008, arXiv:1105.5162.

[149] O. Buchmueller, R. Cavanaugh, D. Colling et al., "Supersymmetry and Dark Matter in Light of LHC 2010 and Xenon100 Data", *Eur. Phys. J. C* **71** (2011) 1722, arXiv:1106.2529.

[150] G. Bertone, D. G. Cerdeno, M. Fornasa et al., "Global fits of the cMSSM including the first LHC and XENON100 data", *JCAP* **1201** (2012) 015, arXiv:1107.1715.

[151] D. Grellscheid, J. Jaeckel, V. V. Khoze et al., "Direct SUSY Searches at the LHC in the light of LEP Higgs Bounds", *JHEP* **1203** (2012) 078, arXiv:1111.3365.

[152] U. Ellwanger, G. Espitalier-Noel, and C. Hugonie, "Naturalness and Fine Tuning in the NMSSM: Implications of Early LHC Results", *JHEP* **1109** (2011) 105, arXiv:1107.2472.

[153] S. Cassel, D. Ghilencea, and G. Ross, "Testing SUSY at the LHC: Electroweak and Dark matter fine tuning at two-loop order", *Nucl. Phys. B* **835** (2010) 110–134, arXiv:1001.3884.

[154] M. Papucci, J. T. Ruderman, and A. Weiler, "Natural SUSY Endures", *JHEP* **1209** (2012) 035, arXiv:1110.6926.

[155] I. Gogoladze, M. U. Rehman, and Q. Shafi, "Amelioration of Little Hierarchy Problem in SU(4)(c) x SU(2)(L) x SU(2)(R)", *Phys. Rev. D* **80** (2009) 105002, arXiv:0907.0728.

[156] D. Feldman, Z. Liu, and P. Nath, "Sparticles at the LHC", *JHEP* **0804** (2008) 054, arXiv:0802.4085.

[157] D. Feldman, Z. Liu, and P. Nath, "The Landscape of Sparticle Mass Hierarchies and Their Signature Space at the LHC", *Phys. Rev. Lett.* **99** (2007) 251802, arXiv:0707.1873.

[158] C. F. Berger, J. S. Gainer, J. L. Hewett et al., "Supersymmetry Without Prejudice", *JHEP* **0902** (2009) 023, arXiv:0812.0980.

[159] H. Baer, K. Hagiwara, and X. Tata, "Gauginos as a Signal for Supersymmetry at p anti-p Colliders", *Phys. Rev. D* **35** (1987) 1598.

[160] P. Nath and R. L. Arnowitt, "Supersymmetric Signals at the Tevatron", *Mod. Phys. Lett. A* **2** (1987) 331–341.

[161] H. Baer, C.-h. Chen, F. Paige et al., "Trileptons from chargino - neutralino production at the CERN Large Hadron Collider", *Phys. Rev. D* **50** (1994) 4508–4516, arXiv:hep-ph/9404212.

[162] E. Accomando, R. L. Arnowitt, and B. Dutta, "Trilepton signal of grand unified models at the Tevatron", *Phys. Lett. B* **475** (2000) 176–183, arXiv:hep-ph/9811300.

[163] Z. Sullivan and E. L. Berger, "Trilepton production at the CERN LHC: Standard model sources and beyond", *Phys. Rev. D* **78** (2008) 034030, arXiv:0805.3720.

[164] S. Bornhauser, M. Drees, H. Dreiner et al., "CP Asymmetries in the Supersymmetric Trilepton Signal at the LHC", *Eur. Phys. J. C* **72** (2012) 1887, arXiv:1110.6131.

[165] A. Djouadi, M. Muhlleitner, and M. Spira, "Decays of supersymmetric particles: The Program SUSY-HIT (SUspect-SdecaY-Hdecay-InTerface)", *Acta Phys. Polon. B* **38** (2007) 635–644, arXiv:hep-ph/0609292.

[166] P. Nath and P. Fileviez Perez, "Proton stability in grand unified theories, in strings and in branes", *Phys. Rept.* **441** (2007) 191–317, arXiv:hep-ph/0601023.

[167] F. Gianotti, on behalf of the ATLAS Collaboration, "Update on the Standard Model Higgs searches in ATLAS", http://indico.cern.ch/getFile.py/access?contribId=0&resId=1&materialId=slides&confId=164890.

[168] G. Tonelli, on behalf of the CMS Collaboration, "Update on the Standard Model Higgs searches in CMS", http://indico.cern.ch/getFile.py/access?contribId=1&resId=0&materialId=slides&confId=164890.

[169] P. Nath, R. L. Arnowitt, and A. H. Chamseddine, "Gravity Induced Symmetry Breaking and Ground State of Local Supersymmetric GUTs", *Phys. Lett. B* **121** (1983) 33.

[170] D. Feldman, Z. Liu, and P. Nath, "Connecting the Direct Detection of Dark Matter with Observation of Sparticles at the LHC", *Phys. Rev. D* **81** (2010) 095009, arXiv:0912.4217.

[171] Y. Okada, M. Yamaguchi, and T. Yanagida, "Upper bound of the lightest Higgs boson mass in the minimal supersymmetric standard model", *Prog. Theor. Phys.* **85** (1991) 1–6.

[172] J. R. Ellis, G. Ridolfi, and F. Zwirner, "Radiative corrections to the masses of supersymmetric Higgs bosons", *Phys. Lett. B* **257** (1991) 83–91.

[173] H. E. Haber and R. Hempfling, "Can the mass of the lightest Higgs boson of the minimal supersymmetric model be larger than m(Z)?", *Phys. Rev. Lett.* **66** (1991) 1815–1818.

[174] H. E. Haber, R. Hempfling, and A. H. Hoang, "Approximating the radiatively corrected Higgs mass in the minimal supersymmetric model", *Z. Phys. C* **75** (1997) 539–554, arXiv:hep-ph/9609331.

[175] G. L. Kane, C. F. Kolda, and J. D. Wells, "Calculable upper limit on the mass of the lightest Higgs boson in any perturbatively valid supersymmetric theory", *Phys. Rev. Lett.* **70** (1993) 2686–2689, arXiv:hep-ph/9210242.

[176] J. Casas, J. Espinosa, M. Quiros et al., "The Lightest Higgs boson mass in the minimal supersymmetric standard model", *Nucl. Phys. B* **436** (1995) 3–29, arXiv:hep-ph/9407389.

[177] M. S. Carena, M. Quiros, and C. Wagner, "Effective potential methods and the Higgs mass spectrum in the MSSM", *Nucl. Phys. B* **461** (1996) 407–436, arXiv:hep-ph/9508343.

[178] J. R. Espinosa and R.-J. Zhang, "Complete two loop dominant corrections to the mass of the lightest CP even Higgs boson in the minimal supersymmetric standard model", *Nucl. Phys. B* **586** (2000) 3–38, arXiv:hep-ph/0003246.

[179] M. S. Carena, P. H. Chankowski, S. Pokorski et al., "The Higgs boson mass as a probe of the minimal supersymmetric standard model", *Phys. Lett. B* **441** (1998) 205–214, arXiv:hep-ph/9805349.

[180] A. Djouadi, "The Anatomy of electro-weak symmetry breaking. II. The Higgs bosons in the minimal supersymmetric model", *Phys. Rept.* **459** (2008) 1–241, arXiv:hep-ph/0503173.

[181] B. Allanach, A. Djouadi, J. Kneur et al., "Precise determination of the neutral Higgs boson masses in the MSSM", *JHEP* **0409** (2004) 044, arXiv:hep-ph/0406166.

[182] H. Baer, V. Barger, P. Huang et al., "Implications of a high mass light MSSM Higgs scalar for SUSY searches at the LHC", *Phys. Rev. D* **84** (2011) 091701, arXiv:1109.3197.

[183] I. Gogoladze, Q. Shafi, and C. S. Un, "Higgs Boson Mass from t-b-$\tau$ Yukawa Unification", *JHEP* **1208** (2012) 028, arXiv:1112.2206.

[184] K. Tobe and J. D. Wells, "Higgs boson mass limits in perturbative unification theories", *Phys. Rev. D* **66** (2002) 013010, arXiv:hep-ph/0204196.

[185] N. Arkani-Hamed, S. Dimopoulos, G. Giudice et al., "Aspects of split supersymmetry", *Nucl. Phys. B* **709** (2005) 3–46, arXiv:hep-ph/0409232.

[186] K. Babu, I. Gogoladze, M. U. Rehman et al., "Higgs Boson Mass, Sparticle Spectrum and Little Hierarchy Problem in Extended MSSM", *Phys. Rev. D* **78** (2008) 055017, arXiv:0807.3055.

[187] D. Feldman, Z. Liu, P. Nath et al., "Multicomponent Dark Matter in Supersymmetric Hidden Sector Extensions", *Phys. Rev. D* **81** (2010) 095017, arXiv:1004.0649.

[188] S. Akula, M. Liu, P. Nath et al., "Naturalness, Supersymmetry and Implications for LHC and Dark Matter", *Phys. Lett. B* **709** (2012) 192–199, arXiv:1111.4589.

[189] G. Belanger, F. Boudjema, A. Pukhov et al., "Dark matter direct detection rate in a generic model with micrOMEGAs 2.2", *Comput. Phys. Commun.* **180** (2009) 747–767, arXiv:0803.2360.

[190] B. Altunkaynak, B. D. Nelson, L. L. Everett et al., "Landscape of Supersymmetric Particle Mass Hierarchies in Deflected Mirage Mediation", *Eur. Phys. J. Plus* **127** (2012) 2, arXiv:1011.1439.

[191] D. Feldman, Z. Liu, and P. Nath, "Gluino NLSP, Dark Matter via Gluino Coannihilation, and LHC Signatures", *Phys. Rev. D* **80** (2009) 015007, arXiv:0905.1148.

[192] CMS Collaboration, "Observation of a new boson at a mass of 125 GeV with the CMS experiment at the LHC", *Phys. Lett. B* (2012) arXiv:1207.7235.

[193] ATLAS Collaboration, "Observation of a new particle in the search for the Standard Model Higgs boson with the ATLAS detector at the LHC", arXiv:1207.7214.

[194] CMS Collaboration, "A new boson with a mass of 125 GeV observed with the CMS experiment at the Large Hadron Collider", *Science* **338** (2012) 1569–1575.

[195] CMS Collaboration, "Observation of a new boson with mass near 125 GeV in pp collisions at sqrt(s) = 7 and 8 TeV", arXiv:1303.4571.

[196] CMS Collaboration, "Observation of a new boson at a mass of 125 GeV with the CMS experiment at the LHC", *Phys. Lett. B* **716** (2012) 30–61, arXiv:1207.7235.

[197] ATLAS Collaboration, "Observation of a new particle in the search for the Standard Model Higgs boson with the ATLAS detector at the LHC", *Phys. Lett. B* **716** (2012) 1–29, arXiv:1207.7214.

[198] ATLAS Collaboration, "A particle consistent with the Higgs Boson observed with the ATLAS Detector at the Large Hadron Collider", *Science* **338** (2012) 1576–1582.

[199] L. Ibanez and G. Ross, "Supersymmetric Higgs and radiative electroweak breaking", *Comptes Rendus Physique* **8** (2007) 1013–1028, arXiv:hep-ph/0702046.

[200] S. Akula, B. Altunkaynak, D. Feldman et al., "Higgs Boson Mass Predictions in SUGRA Unification, Recent LHC-7 Results, and Dark Matter", *Phys. Rev. D* **85** (2012) 075001, arXiv:1112.3645.

[201] A. Arbey, M. Battaglia, A. Djouadi et al., "The Higgs sector of the phenomenological MSSM in the light of the Higgs boson discovery", arXiv:1207.1348.

[202] M. S. Carena and H. E. Haber, "Higgs boson theory and phenomenology", *Prog. Part. Nucl. Phys.* **50** (2003) 63–152, arXiv:hep-ph/0208209.

[203] Tevatron New Physics Higgs Working Group, DØCollaboration, and CDF Collaboration, "Updated Combination of CDF and D0 Searches for Standard Model Higgs Boson Production with up to 10.0 $\text{fb}^{-1}$ of Data", arXiv:1207.0449.

[204] H. Baer, V. Barger, and A. Mustafayev, "Implications of a 125 GeV Higgs scalar for LHC SUSY and neutralino dark matter searches", *Phys. Rev. D* **85** (2012) 075010, arXiv:1112.3017.

[205] A. Arbey, M. Battaglia, A. Djouadi et al., "Implications of a 125 GeV Higgs for supersymmetric models", *Phys. Lett. B* **708** (2012) 162–169, arXiv:1112.3028.

[206] P. Draper, P. Meade, M. Reece et al., "Implications of a 125 GeV Higgs for the MSSM and Low-Scale SUSY Breaking", *Phys. Rev. D* **85** (2012) 095007, arXiv:1112.3068.

[207] M. "Carena, S. Gori, N. R. Shah et al., "A 125 GeV SM-like Higgs in the MSSM and the $\gamma\gamma$ rate", *JHEP* **1203** (2012) 014, arXiv:1112.3336.

[208] S. Akula, P. Nath, and G. Peim, "Implications of the Higgs Boson Discovery for mSUGRA", *Phys. Lett. B* **717** (2012) 188–192, arXiv:1207.1839.

[209] C. Strege, G. Bertone, F. Feroz et al., "Global Fits of the cMSSM and NUHM including the LHC Higgs discovery and new XENON100 constraints", arXiv:1212.2636.

[210] F. Feroz, M. Hobson, and M. Bridges, "MultiNest: an efficient and robust Bayesian inference tool for cosmology and particle physics", *Mon. Not. Roy. Astron. Soc.* **398** (2009) 1601–1614, arXiv:0809.3437.

[211] S. Akula, "SusyKit", http://freeboson.org/software/.

[212] F. Feroz and M. Hobson, "Multimodal nested sampling: an efficient and robust alternative to MCMC methods for astronomical data analysis", *Mon. Not. Roy. Astron. Soc.* **384** (2008) 449, arXiv:0704.3704.

[213] F. Feroz, K. Cranmer, M. Hobson et al., "Challenges of Profile Likelihood Evaluation in Multi-Dimensional SUSY Scans", *JHEP* **1106** (2011) 042, arXiv:1101.3296.

[214] R. R. de Austri, R. Trotta, and L. Roszkowski, "A Markov chain Monte Carlo analysis of the CMSSM", *JHEP* **0605** (2006) 002, arXiv:hep-ph/0602028.

[215] R. R. de Austri, R. Trotta, and F. Feroz, "SuperBayes", http://superbayes.org/.

[216] A. Lewis and S. Bridle, "Cosmological parameters from CMB and other data: A Monte Carlo approach", *Phys. Rev. D* **66** (2010) 103511, arXiv:astro-ph/0205436.

[217] Y. Akrami, P. Scott, J. Edsjo et al., "A Profile Likelihood Analysis of the Constrained MSSM with Genetic Algorithms", *JHEP* **1004** (2010) 057, arXiv:0910.3950.

[218] Particle Data Group, "Review of Particle Physics (RPP)", *Phys. Rev. D* **86** (2012) 010001.

[219] CMS Collaboration, "Combined results of searches for the standard model Higgs boson in pp collisions at sqrt(s) = 7 TeV", *Phys. Lett. B* **710** (2012) 26–48, arXiv:1202.1488.

[220] XENON100 Collaboration, "Dark Matter Results from 225 Live Days of XENON100 Data", arXiv:1207.5988.

[221] T. Yuan, R. L. Arnowitt, A. H. Chamseddine et al., "Supersymmetric Electroweak Effects on G-2 (mu)", *Z. Phys. C* **26** (1984) 407.

[222] A. Hoecker, "The Hadronic Contribution to the Muon Anomalous Magnetic Moment and to the Running Electromagnetic Fine Structure Constant at MZ - Overview and Latest Results", *Nucl. Phys. Proc. Suppl.* **218** (2011) 189–200, arXiv:1012.0055.

[223] K. Hagiwara, R. Liao, A. D. Martin et al., "$(g-2)_\mu$ and $\alpha(M_Z^2)$ re-evaluated using new precise data", *J. Phys. G* **38** (2011) 085003, arXiv:1105.3149.

[224] J. Ellis and K. A. Olive, "Revisiting the Higgs Mass and Dark Matter in the CMSSM", *Eur. Phys. J. C* **72** (2012) 2005, arXiv:1202.3262.

[225] O. Buchmueller, R. Cavanaugh, A. De Roeck et al., "Higgs and Supersymmetry", *Eur. Phys. J. C* **72** (2012) 2020, arXiv:1112.3564.

[226] H. Baer, V. Barger, P. Huang et al., "Post-LHC7 fine-tuning in the mSUGRA/CMSSM model with a 125 GeV Higgs boson", arXiv:1210.3019.

[227] P. Nath, "Higgs Physics and Supersymmetry", arXiv:1210.0520.

[228] "LHC Performance and Statistics", https://lhc-statistics.web.cern.ch/LHC-Statistics/.

[229] LHCb Collaboration, "First evidence for the decay $B_s \to \mu^+\mu^-$", *Phys. Rev. Lett.* **110** (2013) 021801, arXiv:1211.2674.

[230] S. R. Choudhury and N. Gaur, "Dileptonic decay of B(s) meson in SUSY models with large tan Beta", *Phys. Lett. B* **451** (1999) 86–92, arXiv:hep-ph/9810307.

[231] K. Babu and C. F. Kolda, "Higgs mediated $B^0 \to \mu^+\mu^-$ in minimal supersymmetry", *Phys. Rev. Lett.* **84** (2000) 228–231, arXiv:hep-ph/9909476.

[232] C. Bobeth, T. Ewerth, F. Kruger et al., "Analysis of neutral Higgs boson contributions to the decays $\bar{B}_s \to \ell^+\ell^-$ and $\bar{B} \to K\ell^+\ell^-$", *Phys. Rev. D* **64** (2001) 074014, arXiv:hep-ph/0104284.

[233] T. Ibrahim and P. Nath, "CP violation effects on $B^0_{s,d} \to l^+l^-$ in supersymmetry at large tan $\beta$", *Phys. Rev. D* **67** (2003) 016005, arXiv:hep-ph/0208142.

[234] T. Ibrahim and P. Nath, "CP Violation From Standard Model to Strings", *Rev. Mod. Phys.* **80** (2008) 577–631, arXiv:0705.2008.

[235] A. J. Buras, P. H. Chankowski, J. Rosiek et al., "Correlation between $\Delta M_s$ and $B^0_{s,d} \to \mu^+\mu^-$ in supersymmetry at large tan $\beta$", *Phys. Lett. B* **546** (2002) 96–107, arXiv:hep-ph/0207241.

[236] G. Degrassi, P. Gambino, and P. Slavich, "QCD corrections to radiative B decays in the MSSM with minimal flavor violation", *Phys. Lett. B* **635** (2006) 335–342, arXiv:hep-ph/0601135.

[237] S. Bertolini, F. Borzumati, A. Masiero et al., "Effects of supergravity induced electroweak breaking on rare B decays and mixings", *Nucl. Phys. B* **353** (1991) 591–649.

[238] Muon G-2 Collaboration, "Final Report of the Muon E821 Anomalous Magnetic Moment Measurement at BNL", *Phys. Rev. D* **73** (2006) 072003, arXiv:hep-ex/0602035.

[239] M. Davier, A. Hoecker, B. Malaescu et al., "Reevaluation of the Hadronic Contributions to the Muon g-2 and to alpha(MZ)", *Eur. Phys. J. C* **71** (2011) 1515, arXiv:1010.4180.

[240] D. A. Kosower, L. M. Krauss, and N. Sakai, "Low-Energy Supergravity and the Anomalous Magnetic Moment of the Muon", *Phys. Lett. B* **133** (1983) 305.

[241] J. L. Lopez, D. V. Nanopoulos, and X. Wang, "Large (g-2)-mu in SU(5) x U(1) supergravity models", *Phys. Rev. D* **49** (1994) 366–372, arXiv:hep-ph/9308336.

[242] U. Chattopadhyay and P. Nath, "Probing supergravity grand unification in the Brookhaven g-2 experiment", *Phys. Rev. D* **53** (1996) 1648–1657, arXiv:hep-ph/9507386.

[243] T. Moroi, "The Muon anomalous magnetic dipole moment in the minimal supersymmetric standard model", *Phys. Rev. D* **53** (1996) 6565–6575, arXiv:hep-ph/9512396.

[244] T. Ibrahim and P. Nath, "Effects of large CP violating phases on g(muon) - 2 in MSSM", *Phys. Rev. D* **62** (2000) 015004, arXiv:hep-ph/9908443.

[245] S. Heinemeyer, D. Stockinger, and G. Weiglein, "Two loop SUSY corrections to the anomalous magnetic moment of the muon", *Nucl. Phys. B* **690** (2004) 62–80, arXiv:hep-ph/0312264.

[246] A. Sirlin and A. Ferroglia, "Radiative Corrections in Precision Electroweak Physics: a Historical Perspective", arXiv:1210.5296.

[247] J. Baglio, A. Djouadi, and R. Godbole, "The apparent excess in the Higgs to di-photon rate at the LHC: New Physics or QCD uncertainties?", *Phys. Lett. B* **716** (2012) 203–207, arXiv:1207.1451.

[248] G. F. Giudice, P. Paradisi, A. Strumia et al., "Correlation between the Higgs Decay Rate to Two Photons and the Muon g - 2", *JHEP* **1210** (2012) 186, arXiv:1207.6393.

[249] W.-Z. Feng and P. Nath, "Higgs diphoton rate and mass enhancement with vector-like leptons and the scale of supersymmetry", arXiv:1303.0289.

[250] J. Cao, Z. Heng, D. Li et al., "Current experimental constraints on the lightest Higgs boson mass in the constrained MSSM", *Phys. Lett. B* **710** (2012) 665–670, arXiv:1112.4391.

[251] A. Fowlie, M. Kazana, K. Kowalska et al., "The CMSSM Favoring New Territories: The Impact of New LHC Limits and a 125 GeV Higgs", *Phys. Rev. D* **86** (2012) 075010, arXiv:1206.0264.

[252] J. R. Ellis, K. Enqvist, D. V. Nanopoulos et al., "GAUGINO MASSES AND GRAND UNIFICATION", *Phys. Lett. B* **155** (1985) 381.

[253] M. Drees, "PHENOMENOLOGICAL CONSEQUENCES OF N=1 SUPERGRAVITY THEORIES WITH NONMINIMAL KINETIC ENERGY TERMS FOR VECTOR SUPERFIELDS", *Phys. Lett. B* **158** (1985) 409.

[254] G. Anderson, H. Baer, C.-h. Chen et al., "The Reach of Fermilab Tevatron upgrades for SU(5) supergravity models with nonuniversal gaugino masses", *Phys. Rev. D* **61** (2000) 095005, arXiv:hep-ph/9903370.

[255] K. Huitu, Y. Kawamura, T. Kobayashi et al., "Phenomenological constraints on SUSY SU(5) GUTs with nonuniversal gaugino masses", *Phys. Rev. D* **61** (2000) 035001, arXiv:hep-ph/9903528.

[256] A. Corsetti and P. Nath, "Gaugino mass nonuniversality and dark matter in SUGRA, strings and D-brane models", *Phys. Rev. D* **64** (2001) 125010, arXiv:hep-ph/0003186.

[257] U. Chattopadhyay and P. Nath, "b - tau unification, g(mu) - 2, the $b \to s + \gamma$ constraint and nonuniversalities", *Phys. Rev. D* **65** (2002) 075009, arXiv:hep-ph/0110341.

[258] U. Chattopadhyay, A. Corsetti, and P. Nath, "Supersymmetric dark matter and Yukawa unification", *Phys. Rev. D* **66** (2002) 035003, arXiv:hep-ph/0201001.

[259] S. P. Martin, "Non-universal gaugino masses from non-singlet F-terms in non-minimal unified models", *Phys. Rev. D* **79** (2009) 095019, arXiv:0903.3568.

[260] I. Gogoladze, F. Nasir, and Q. Shafi, "Non-Universal Gaugino Masses and Natural Supersymmetry", arXiv:1212.2593.

[261] M. A. Ajaib, I. Gogoladze, Q. Shafi et al., "A Predictive Yukawa Unified SO(10) Model: Higgs and Sparticle Masses", arXiv:1303.6964.

[262] P. Nath, B. D. Nelson, H. Davoudiasl et al., "The Hunt for New Physics at the Large Hadron Collider", *Nucl. Phys. Proc. Suppl.* **200-202** (2010) 185–417, arXiv:1001.2693.

[263] N. Arkani-Hamed and S. Dimopoulos, "Supersymmetric unification without low energy supersymmetry and signatures for fine-tuning at the LHC", *JHEP* **0506** (2005) 073, arXiv:hep-th/0405159.

[264] B. L. Kaufman, B. D. Nelson, and M. K. Gaillard, "Mirage Models Confront the LHC: I. Kahler-Stabilized Heterotic String Theory", arXiv:1303.6575.

[265] M. Ibe, T. T. Yanagida, and N. Yokozaki, "Muon g-2 and 125 GeV Higgs in Split-Family Supersymmetry", arXiv:1303.6995.

[266] S. Mohanty, S. Rao, and D. Roy, "Reconciling the Muon g-2 and Dark Matter Relic Density with the LHC Results in Nonuniversal Gaugino Mass Models", arXiv:1303.5830.

[267] G. Bhattacharyya, B. Bhattacherjee, T. T. Yanagida et al., "A natural scenario for heavy colored and light uncolored superpartners", arXiv:1304.2508.

[268] T. Cheng, J. Li, T. Li et al., "Electroweak Supersymmetry around the Electroweak Scale", *Eur. Phys. J. C* **73** (2013) 2322, arXiv:1202.6088.

[269] M. Endo, K. Hamaguchi, S. Iwamoto et al., "Muon g-2 vs LHC in Supersymmetric Models", arXiv:1303.4256.

[270] Heavy Flavor Averaging Group, "Averages of B-Hadron, C-Hadron, and tau-lepton properties as of early 2012", arXiv:1207.1158.

[271] WMAP Collaboration, "Seven-Year Wilkinson Microwave Anisotropy Probe (WMAP) Observations: Cosmological Interpretation", *Astrophys. J. Suppl.* **192** (2011) 18, arXiv:1001.4538.

[272] CMS Collaboration, "Combined results of searches for the standard model Higgs boson in pp collisions at $\sqrt{s} = 7$ TeV", *Phys. Lett. B* **710** (2012) 26–48, arXiv:1202.1488.

[273] WMAP Collaboration, "Nine-Year Wilkinson Microwave Anisotropy Probe (WMAP) Observations: Cosmological Parameter Results", arXiv:1212.5226.

[274] Planck Collaboration, "Planck 2013 results. I. Overview of products and scientific results", arXiv:1303.5062.

[275] S. Heinemeyer, W. Hollik, and G. Weiglein, "FeynHiggs: A Program for the calculation of the masses of the neutral CP even Higgs bosons in the MSSM", *Comput. Phys. Commun.* **124** (2000) 76–89, arXiv:hep-ph/9812320.

[276] T. Hahn, S. Heinemeyer, W. Hollik et al., "FeynHiggs 2.7", *Nucl. Phys. Proc. Suppl.* **205-206** (2010) 152–157, arXiv:1007.0956.

[277] F. Mahmoudi, "SuperIso v3.0, flavor physics observables calculations: Extension to NMSSM", *Comput. Phys. Commun.* **180** (2009) 1718–1719.

[278] A. Arbey and F. Mahmoudi, "SuperIso Relic v3.0: A program for calculating relic density and flavour physics observables: Extension to NMSSM", *Comput. Phys. Commun.* **182** (2011) 1582–1583.

[279] T. Sjostrand, S. Mrenna, and P. Z. Skands, "A Brief Introduction to PYTHIA 8.1", *Comput. Phys. Commun.* **178** (2008) 852–867, arXiv:0710.3820.

[280] "Search for direct EWK production of SUSY particles in multilepton modes with 8 TeV data", Technical Report CMS-PAS-SUS-12-022, (2012).

[281] B. Altunkaynak, "Parvicursor", http://gluino.net/heptools.html.

[282] U. Chattopadhyay, A. Corsetti, and P. Nath, "WMAP constraints, SUSY dark matter and implications for the direct detection of SUSY", *Phys. Rev. D* **68** (2003) 035005, arXiv:hep-ph/0303201.

[283] H. Baer, C. Balazs, A. Belyaev et al., "Updated reach of the CERN LHC and constraints from relic density, $b \to s\gamma$ and $a(\mu)$ in the mSUGRA model", *JHEP* **0306** (2003) 054, arXiv:hep-ph/0304303.

[284] M. Liu and P. Nath, "Higgs Boson Mass, Proton Decay, Naturalness and Constraints of LHC and Planck Data", arXiv:1303.7472.

[285] B. S. Acharya, K. Bobkov, G. L. Kane et al., "The G(2)-MSSM: An M Theory motivated model of Particle Physics", *Phys. Rev. D* **78** (2008) 065038, arXiv:0801.0478.

[286] A. Djouadi, "The Anatomy of electro-weak symmetry breaking. I: The Higgs boson in the standard model", *Phys. Rept.* **457** (2008) 1–216, arXiv:hep-ph/0503172.

[287] D. Feldman, Z. Liu, and P. Nath, "Low Mass Neutralino Dark Matter in the MSSM with Constraints from $B_s \to \mu^+\mu^-$ and Higgs Search Limits", *Phys. Rev. D* **81** (2010) 117701, arXiv:1003.0437.

[288] R. L. Arnowitt and P. Nath, "Testing Supergravity Grand Unification at Future Accelerator and Underground Experiments", *Phys. Rev. D* **49** (1994) 1479–1485, arXiv:hep-ph/9309252.

[289] J. Hisano, D. Kobayashi, T. Kuwahara et al., "Decoupling Can Revive Minimal Supersymmetric SU(5)", arXiv:1304.3651.

[290] H. K. Dreiner, H. E. Haber, and S. P. Martin, "Two-component spinor techniques and Feynman rules for quantum field theory and supersymmetry", *Phys. Rept.* **494** (2010) 1–196, arXiv:0812.1594.

[291] F. A. Berezin, “Introduction To Superanalysis”, volume 9 of *Mathematical Physics and Applied Mathematics*. D. Reidel, Dordrecht, 1987.